

# **A New Experimental Approach to Study Helicopter Blade-Vortex Interaction Noise**

by

Sudarshan N. Koushik

Dissertation submitted to the Faculty of the Graduate School of the  
University of Maryland, College Park in partial fulfillment  
of the requirements for the degree of  
Doctor of Philosophy  
2007

Advisory Committee:

Professor Fredric H. Schmitz, Chair/Advisor  
Professor James Baeder  
Professor Inderjit Chopra  
Professor Christopher Cadou  
Professor Amr Baz

# ABSTRACT

Title of dissertation:      **A New Experimental Approach to Study Helicopter  
Blade-Vortex Interaction Noise**

Sudarshan N. Koushik, Doctor of Philosophy, 2007

Dissertation directed by:   Professor Fredric H. Schmitz  
Department of Aerospace Engineering

A unique and novel experimental approach has been developed to study the aerodynamics and acoustics of the helicopter Blade-Vortex Interaction in a controlled hover environment. This is achieved by having a non-lifting single-bladed rotor with a rigid hub interact with a carefully controlled gust disturbance that replicates the essential characteristics of the vortex velocity. This experimental approach termed the Blade-Controlled Disturbance-Interaction or the BCDI, decouples the rotor parameters from the characteristics of the incident disturbance velocity, thus providing an ideal setup for studying the blade's aerodynamics and acoustic response in detail. Moreover, the angle of interaction between the disturbance field and the rotor blade can be controlled by orienting the gust, providing the ability to study both parallel and oblique interactions. The noise data was recorded at thirty different microphone locations.

A series of experiments at various rotor tip Mach numbers and interaction angles, replicating many of the conditions of helicopter BVI, were performed. The results show that the directionality of the BVI noise is strongly determined by the interaction angle. A small change in interaction angle results in the radiation of noise over a larger azimuthal area compared to the parallel interaction. Moreover, as the interaction becomes more oblique, the peak noise elevation angle approaches closer to the rotor plane.

A linear unsteady lifting-line aerodynamic theory (corrected for chord-wise non-compactness) was used to estimate the blade aerodynamics during the interaction and hence the radiated noise. Although the theory under-predicted the noise levels for most of the cases, and did not replicate exactly the general pulse shape, the general directionality trends were predicted reasonably well. The theory was used to separate the contribution to the acoustics, from different spanwise blade sections, providing significant insights into the phasing mechanism of BVI noise.

© Copyright by  
Sudarshan N. Koushik  
2007

## DEDICATION

To My Parents and Kripa and Priya. Your love and support has made this possible.

# Acknowledgements

I am grateful to a lot of people for without their support and help this thesis would not have come to fruition.

First and foremost, I would like to thank my advisor, Prof. Fredric Schmitz, for accepting to work with me, for keeping his faith in me throughout and for providing guidance – both academic as well as practical. Even though he was not always physically present owing to his health, he was always available over the phone irrespective of where in the country he was to provide the guidance, and practical and moral support through the various stages of this thesis. I have learnt an immense lot from him during the past few years.

Special thanks are due to my parents for teaching and strengthening my fundamentals through my younger years, and inculcating in me the thirst for research. It was by their encouragement and guidance that I started on my thesis in the first place, and their and my sisters' love and faith which saw me through the thesis. Thanks also to my friends Shaju and Gunjan for understanding what I was going through during my “down times” and bringing out of it every time, by encouraging me

and helping me put things in perspective.

I also owe thanks to my friends and fellow graduate students at the Rotorcraft center at the University of Maryland, for the various discussions on my research. Many of them helped me at various times during the setting of the experiment with their time and labor, without which the thesis would not have been what it is – Ben Sim, Manikandan, Shreyas, Shaju, Arun, Anand, Vinit, Beerinder, Jaina, Karthik, Eric Greenwood, Rick Sickenberger, Cal Sargent, Gaurav, Andy Drysdale . . . and the list goes on. Thanks also go to my friends outside of school, Shaju, Rahul, Rajagopal, Srikant, Anuj, Gunjan, Marylin, Ashok, and many others, who made the past few years enjoyable, for those times when a little change from academics proved to be incalculably enriching both for academics as well as the larger perspective of life.

# Table of Contents

<b>List of Tables</b>	<b>ix</b>
<b>List of Figures</b>	<b>x</b>
<b>List of Symbols</b>	<b>xviii</b>
<b>1 Introduction</b>	<b>1</b>
1.1 Sources of Helicopter Noise . . . . .	4
1.2 Blade-Vortex Interaction Noise . . . . .	9
1.3 BVI Noise: Challenges and Prior Art . . . . .	19
1.3.1 Unsteady Aerodynamics . . . . .	20
1.3.2 Aeroacoustics . . . . .	22
1.3.3 Experimental Approaches . . . . .	27
1.4 Objectives of Current Research . . . . .	32



<b>2</b>	<b>Approach</b>	<b>36</b>
2.1	Experimental BVI Simulation — The BCDI Experiment . . . . .	36
2.2	The Assembled Experimental Setup . . . . .	44
2.3	Experimental Design and Calibration . . . . .	44
2.3.1	The Gust Generator . . . . .	48
2.3.2	Comparison of Gust to Vortex Induced Velocity Profile . . . . .	52
2.3.3	Rotor Test Stand and Operation . . . . .	57
2.3.4	Acoustic Chamber . . . . .	58
2.3.5	Microphone Measurement System . . . . .	62
2.3.6	Data Acquisition and Reduction Technique . . . . .	62
2.4	Experimental Cases Studied . . . . .	65
2.4.1	Case 1 — Parallel BCDI . . . . .	65
2.4.2	Oblique BCDI . . . . .	66
<b>3</b>	<b>Experimental Results</b>	<b>70</b>
3.1	Data Quality . . . . .	71
3.1.1	Background Noise . . . . .	71
3.1.2	Acoustic Pulse Reflection . . . . .	72
3.1.3	Repeatability of Acoustic Data . . . . .	73
3.2	Noise radiation due to nozzle presence . . . . .	73
3.2.1	Case 1 — Parallel BCDI . . . . .	73
3.2.2	Case 2 — 3.3° Oblique BCDI . . . . .	78

3.2.3	Case 3 — 8.8° Oblique BCDI . . . . .	78
3.2.4	Case 4 —15.3° Oblique BCDI . . . . .	81
3.3	BCDI Acoustic Data — Parallel BCDI . . . . .	85
3.3.1	Acoustic Time Histories . . . . .	88
3.3.2	Frequency Spectrum . . . . .	91
3.3.3	Effect of tip Mach number . . . . .	94
3.4	Oblique BCDI . . . . .	94
3.4.1	Case 2 — 3.3° Oblique Interaction . . . . .	94
3.4.2	Case 3 — 8.8° Oblique Interaction . . . . .	102
3.4.3	Case 4 — 15.3° Oblique Interaction . . . . .	103
3.5	Effect of Interaction Angle on Noise Levels . . . . .	111
3.6	Effect of tip Mach number on Case 4 (15.3°) Oblique BCDI . . . . .	112
<b>4</b>	<b>Theoretical Comparison</b>	<b>118</b>
4.1	Theoretical Approach . . . . .	118
4.1.1	Linear Unsteady Indicial Aerodynamics . . . . .	119
4.1.2	The Acoustics Formulation . . . . .	121
4.2	Comparison with Experiment — Parallel Interaction . . . . .	125
4.3	Oblique Interactions . . . . .	132
4.3.1	Case 2 — 3.3° Oblique BCDI . . . . .	132
4.3.2	Case 3 — 8.8° Oblique BCDI . . . . .	139
4.3.3	Case 4 — 15.3° Oblique BCDI . . . . .	146

4.4	Summary of Results . . . . .	150
<b>5</b>	<b>Summary and Conclusions</b>	<b>153</b>
5.1	The BCDI Facility . . . . .	154
5.2	BCDI Experimental Findings . . . . .	155
5.3	Indicial Aerodynamics and Acoustic Predictions . . . . .	156
5.4	Recommendations for Further Research . . . . .	157
<b>A</b>	<b>Gust Generator Fabrication and Operational Details</b>	<b>160</b>
<b>B</b>	<b>Rotor Test Stand Dynamics</b>	<b>168</b>
<b>C</b>	<b>Effect of Nozzle Interference on the Acoustic Time Histories</b>	<b>170</b>
<b>D</b>	<b>Comparison Between Compact and Non-Compact Acoustic Formulations</b>	<b>175</b>
<b>E</b>	<b>Comparison of Frequency Spectrum Between Theory and Experiment</b>	<b>180</b>
<b>F</b>	<b>Scaling of the Acoustics Data</b>	<b>185</b>
F.1	Choice of Scaling Origin . . . . .	185
	<b>References</b>	<b>191</b>

## List of Tables

2.1	Some key characteristics of the rotor . . . . .	59
2.2	Tip Mach numbers tested . . . . .	65
4.1	Coefficients of the Indicial gust function, $\phi_g$ . . . . .	120

## List of Figures

1.1	Source of helicopter noise [4] . . . . .	5
1.2	Frequency spectrum of radiated noise from a typical hovering helicopter [5] . . . . .	6
1.3	Preferred radiation directions of some noise sources [13] . . . . .	9
1.4	A 4-bladed rotor undergoing BVI . . . . .	10
1.5	Top view of helicopter in BVI . . . . .	11
1.6	Side view of helicopter BVI . . . . .	12
1.7	Two-dimensional schematic of the BVI . . . . .	13
1.8	Locus of possible blade-vortex interactions for two-bladed rotor for two different advance ratios ( $\mu = 0.1$ and $\mu = 0.164$ ) . . . . .	15
1.9	Trace Mach number of BVI . . . . .	16
1.10	Directivity patterns obtained from wave tracing and $M_{TR}$ approach ( $\mu = 0.164, M_T =$ $0.664$ ) . . . . .	18
1.11	In-flight acoustic measurement technique [8] . . . . .	28
1.12	A schematic of the BVI experiment by Leverton . . . . .	31
1.13	A schematic of the wind tunnel experimental setup used by Kitaplioglu et al [84] . . . . .	33

2.1	Helicopter BVI geometry for a two-bladed rotor . . . . .	38
2.2	Two-dimensional schematic of the BVI . . . . .	39
2.3	Typical vortex induced velocity profile and its gradient . . . . .	39
2.4	Sectional lift coefficient induced by a vortex on the airfoil . . . . .	40
2.5	Schematic of the experiment . . . . .	42
2.6	Trace Mach Number of BVI . . . . .	43
2.7	Layout of the different components inside the acoustic chamber . . . . .	45
2.8	Schematic of the final assembled experimental setup . . . . .	46
2.9	Photograph of a portion of the experimental setup inside the chamber . . . . .	47
2.10	Schematic of experimental setup . . . . .	48
2.11	Schematic showing different sections of the “Gust Generator” . . . . .	49
2.12	Schematic of the final nozzle design . . . . .	51
2.13	Variation of velocity distribution across the span of the nozzle . . . . .	53
2.14	Variation of velocity distribution with height above the nozzle . . . . .	54
2.15	Comparison of measured gust and vortex induced velocity . . . . .	56
2.16	Schematic of the setup showing the relative positions of the gust and the rotor blade during interaction . . . . .	58
2.17	Reflection characteristics of chamber prior to treatment . . . . .	60
2.18	Reflection characteristics of chamber after acoustic treatment . . . . .	61
2.19	Top view of microphone measurement locations . . . . .	63
2.20	Side view of microphone measurement locations . . . . .	64

2.21	Comparison of the parallel interaction in the experiment with a real BVI . . . . .	67
2.22	Schematic of the oblique interaction angles and corresponding trace Mach number profiles ( $M_T = 0.702$ ) . . . . .	68
3.1	Power spectrum of the gust flow noise . . . . .	71
3.2	Ratio of main acoustic pulse to the first reflected pulse . . . . .	72
3.3	Revolution-to-Revolution fidelity of the rotor setup . . . . .	74
3.4	SPL trends of noise radiation due to the nozzle — parallel BCDI . . . . .	75
3.5	SPL trends with gust strength . . . . .	76
3.6	Acoustic time history comparison with and without the gust, showing the effect of the nozzle . . . . .	77
3.7	SPL trends of noise radiation due to the nozzle — Case 2 . . . . .	79
3.8	Acoustic time history comparison with and without the gust, for Case 2 at $\psi = 120.9^\circ$ ( $M_T = 0.702$ ) . . . . .	80
3.9	SPL trends of noise radiation due to the nozzle — Case 3 . . . . .	81
3.10	Acoustic time history comparison with and without the gust, for Case 3 at $\psi = 120.9^\circ$ ( $M_T = 0.702$ ) . . . . .	82
3.11	SPL trends of noise radiation due to the nozzle — Case 4 . . . . .	83
3.12	Acoustic time history comparison with and without the gust, for Case 4 at $\psi = 120.9^\circ$ ( $M_T = 0.702$ ) . . . . .	84
3.13	Top view of acoustic wavefronts radiating from the parallel interaction . . . . .	85
3.14	Unaveraged data for two revolutions for the parallel interaction at $\psi = 120.9^\circ$ . . . . .	86

3.15	Acoustic time histories at the various microphones in terms of Acoustic Pressure (in Pa) vs. Rotor Azimuth (in Deg) ( $M_T = 0.702$ — Parallel Interaction) . . . . .	90
3.16	Directionality trends at $0.702M_T$ for the Parallel Interaction . . . . .	92
3.17	Frequency spectrum of noise at various microphones — Sound pressure in dB vs. Single-blade rotor harmonics ( $M_T = 0.702$ — Parallel Interaction) . . . . .	93
3.18	Variation of peak-to-peak noise level with tip Mach number — Parallel BCDI . . . . .	95
3.19	Variation of peak-to-peak level with increase in tip Mach number for the parallel BCDI at $\psi = 107^\circ$ . . . . .	96
3.20	Top view of acoustic wavefronts for Case 2 oblique BCDI . . . . .	97
3.21	Acoustic time histories at the various microphones in terms of Acoustic Pressure (in Pa) vs. Rotor Azimuth (in Deg) — Case 2 ( $3.3^\circ$ Oblique Interaction $M_T = 0.702$ ) . . . . .	98
3.22	Frequency spectrum of noise at various microphones — Sound pressure in dB vs. Single-blade rotor harmonics — Case 2 ( $3.3^\circ$ Oblique Interaction $M_T = 0.702$ ) . . . . .	99
3.23	Directionality trends for Case 2 ( $3.3^\circ$ Oblique Interaction) at $M_T = 0.702$ . . . . .	101
3.24	Top view of acoustic of the wavefronts for Case 3 oblique BCDI . . . . .	103
3.25	Acoustic time histories at the various microphones in terms of Acoustic Pressure (in Pa) vs. Rotor Azimuth (in Deg) — Case 3 ( $8.8^\circ$ Oblique Interaction $M_T = 0.702$ ) . . . . .	104
3.26	Frequency spectrum of noise at various microphones — Sound pressure in dB vs. Single-blade rotor harmonics — Case 3 ( $8.8^\circ$ Oblique Interaction $M_T = 0.702$ ) . . . . .	105
3.27	Directionality trends for Case 3 ( $M_T = 0.702$ ) . . . . .	106
3.28	Top view of acoustic of the wavefronts for Case 4 oblique BCDI . . . . .	107



3.29	Acoustic time histories at the various microphones in terms of Acoustic Pressure (in Pa) vs. Rotor Azimuth (in Deg) — Case 4 (15.3° Oblique Interaction $M_T = 0.702$ )	109
3.30	Frequency spectrum of noise at various microphones — Sound pressure in dB vs. Single-blade rotor harmonics — Case 4 (15.3° Oblique Interaction $M_T = 0.702$ )	110
3.31	Directionality trends for Case 4 ( $M_T = 0.702$ )	111
3.32	Variation of peak-to-peak noise levels with interaction angle ( $M_T = 0.702$ )	113
3.33	Variation of trace Mach number as function of tip Mach number — Case 4 oblique BCDI	115
3.34	Acoustic directivity variation with tip Mach number — Case 4 (15.3° Oblique BCDI)	116
3.34	(Cont'd) Acoustic directivity variation with tip Mach number — Case 4 (15.3° Oblique BCDI)	117
4.1	Weissinger-L lifting line model for the rotor blade	121
4.2	Comparison between compact and non-compact chord approaches — Parallel In- teraction at $M_T = 0.702$ ( $\psi = 107^\circ$ & $\theta = 53.75^\circ$ )	124
4.3	Difference in peak-to-peak sound pressure between compact and non-compact ap- proaches — Case 1 parallel BCDI at $M_T = 0.702$	126
4.4	Difference in sound pressure between compact and non-compact approaches — Case 4 (15.3° Oblique BCDI) at $M_T = 0.702$	127
4.5	Acoustic time histories at the various microphones in terms of Acoustic Pressure (in Pa) vs. Rotor Azimuth (in Deg) ( $M_T = 0.702$ — Parallel Interaction)	129

4.6	Comparison of the directionality trends between theory and experiment for the parallel interaction ( $M_T = 0.702$ ) . . . . .	130
4.7	Spanwise acoustic phasing effect for the parallel interaction ( $M_T = 0.702$ ) . . . . .	133
4.8	Acoustic time histories at the various microphones in terms of Acoustic Pressure (in Pa) vs. Rotor Azimuth (in Deg) — Case 2 (3.3° Oblique BCDI; $M_T = 0.702$ ) . . . . .	135
4.9	Comparison of the directionality trends between theory and experiment — Case 2 (3.3° Oblique BCDI; $M_T = 0.702$ ) . . . . .	136
4.10	Spanwise acoustic phasing effect — Case 2 (3.3° Oblique BCDI) at $M_T = 0.702$ . . . . .	137
4.11	Trace Mach number along the radiation direction for Case 2 (3.3° Oblique BCDI) . . . . .	139
4.12	Acoustic time histories at the various microphones in terms of Acoustic Pressure (in Pa) vs. Rotor Azimuth (in Deg) (Case 3 – 8.8° Oblique BCDI) at $M_T = 0.702$ . . . . .	141
4.13	Comparison of the directionality trends between theory and experiment — Case 3 (8.8° Oblique BCDI) at $M_T = 0.702$ . . . . .	142
4.14	Spanwise acoustic phasing effect — Case 3 (8.8° Oblique BCDI; $M_T = 0.702$ ) . . . . .	144
4.15	Trace Mach number along the radiation direction for Case 3 (8.8° Oblique BCDI) . . . . .	145
4.16	Acoustic time histories at the various microphones in terms of Acoustic Pressure (in Pa) vs. Rotor Azimuth (in Deg) — Case 4 (15.3° Oblique BCDI; $M_T = 0.702$ ) . . . . .	147
4.17	Comparison of the directionality trends between theory and experiment — Case 4 (15.3° Oblique BCDI; $M_T = 0.702$ ) . . . . .	148
4.18	Spanwise acoustic phasing effect — Case 4 (15.3° Oblique BCDI; $M_T = 0.702$ ) . . . . .	149
4.19	Trace Mach number along the radiation direction for Case 4 (15.3° Oblique BCDI) . . . . .	151

A.1	Schematic of early nozzle design . . . . .	162
A.2	Velocity profile obtained from the first nozzle design . . . . .	163
A.3	RMS variation of velocities across nozzle width . . . . .	165
A.4	Frequency distribution of turbulence at various locations . . . . .	167
B.1	Resonant frequencies associated with the RTS . . . . .	169
C.1	Acoustic time history due to nozzle alone (No gust) ( $M_T = 0.702$ — Parallel In- teraction) . . . . .	171
C.2	Acoustic time history due to nozzle alone (No gust) ( $M_T = 0.702$ — Case 2) . . . .	172
C.3	Acoustic time history due to nozzle alone (No gust) ( $M_T = 0.702$ — Case 3) . . . .	173
C.4	Acoustic time history due to nozzle alone (No gust) ( $M_T = 0.702$ — Case 4) . . . .	174
D.1	Comparison between Compact and Non-compact chord formulations ( $M_T = 0.702$ — Parallel Interaction) . . . . .	176
D.2	Comparison between Compact and Non-compact chord formulations ( $M_T = 0.702$ — Case 2) . . . . .	177
D.3	Comparison between Compact and Non-compact chord formulations ( $M_T = 0.702$ — Case 3) . . . . .	178
D.4	Comparison between Compact and Non-compact chord formulations ( $M_T = 0.702$ — Case 4) . . . . .	179
E.1	Acoustic time histories at the various microphones in terms of Acoustic Pressure (in Pa) vs. Rotor Azimuth (in Deg) ( $M_T = 0.702$ — Parallel Interaction) . . . . .	181

E.2	Acoustic time histories at the various microphones in terms of Acoustic Pressure (in Pa) vs. Rotor Azimuth (in Deg) ( $M_T = 0.702$ — Case 2) . . . . .	182
E.3	Acoustic time histories at the various microphones in terms of Acoustic Pressure (in Pa) vs. Rotor Azimuth (in Deg) ( $M_T = 0.702$ — Case 3) . . . . .	183
E.4	Acoustic time histories at the various microphones in terms of Acoustic Pressure (in Pa) vs. Rotor Azimuth (in Deg) ( $M_T = 0.702$ — Case 4) . . . . .	184
F.1	Directionality trends for parallel BCDI when scaled about 0.8R ( $M_T = 0.702$ ) . . .	187
F.2	Directionality trends for parallel BCDI when scaled about the hub ( $M_T = 0.702$ ) .	187
F.3	Directionality trends for the 3.3° oblique BCDI when scaled about 0.8R ( $M_T = 0.702$ )	188
F.4	Directionality trends for the 3.3° oblique BCDI when scaled about the hub ( $M_T =$ 0.702) . . . . .	188
F.5	Directionality trends for the 8.8° oblique BCDI when scaled about 0.8R ( $M_T = 0.702$ )	189
F.6	Directionality trends for the 8.8° oblique BCDI when scaled about the hub ( $M_T =$ 0.702) . . . . .	189
F.7	Directionality trends for the 15.3° oblique BCDI when scaled about 0.8R ( $M_T =$ 0.702) . . . . .	190
F.8	Directionality trends for the 15.3° oblique BCDI when scaled about the hub ( $M_T =$ 0.702) . . . . .	190

## List of Symbols

$(\dot{\phantom{x}})$	Derivative with respect to source time
$\alpha_{TPP}$	Rotor tip path plane angle
$\beta$	Glauert's factor, $=\sqrt{1-M_\infty^2}$
$\Delta C_P$	Differential pressure on the airfoil
$\Gamma$	Vortex circulation, $m^2/s$
$\gamma$	Interaction angle
$\mu$	Advance Ratio of the helicopter
$\Omega$	Rotor angular velocity, $rad/s$
$\phi$	Azimuth location with respect to rotor hub, $deg$
$\phi_g$	Indicial response function
$\psi_b$	Azimuthal location of the blade tip, $rad$
$\psi_w$	Azimuthal location of a vortex, $rad$
$\rho_0$	Density of quiescent medium, $kg/m^3$
$\sigma$	Rotor Solidity
$\theta$	Elevation above rotor plane, $deg$

$a$	Local speed of sound, m/s
$a_0$	Speed of sound in the medium, m/s
$C_l$	Lift coefficient
$C_t$	Thrust coefficient
$G_1, G_2, g_1, g_2$	Indicial coefficients
$L$	Length of nozzle, m
$l$	Sectional blade load
$l_r$	Component of sectional load along observer direction
$M_r$	Mach number along direction of observer
$M_T$	Tip Mach number
$M_{TR}$	Trace Mach number (in the rotor plane)
$N_b$	Number of blades
$n_j$	Local surface normal
$p$	Observed acoustic pressure
$p_L$	Acoustic pressure due to loading term
$P_{ij}$	Surface pressure
$R$	Blade radius, m
$r$	Blade radial station
$r_c$	Distance from center of vortex, non-dimensionalized by $c$
$r_{obs}$	Distance between observer and source, m/s
$s$	Reduced chord

$T_{ij}$	Lighthill's stress tensor
$U_m$	Mean horizontal velocity
$u_m$	Horizontal component of gust velocity, m/s
$V$	Velocity, m/s
$V_\theta$	Tangential velocity induced by a vortex, m/s
$v_n$	Velocity component normal to surface, m/s
$v_z$	Vertical component of velocity, m/s
$V_{TR}$	Trace Velocity
$w_g$	Vertical component of gust velocity, m/s
$W_m$	Mean vertical velocity
$w_m$	Vertical component of gust velocity, m/s
$x_c$	Horizontal distance from vortex center, non-dimensionalized by c
$x_i, x_j$	Space coordinates
$x_{tip}, y_{tip}$	Coordinates of the tip vortex
$z_c$	Vertical distance from vortex center, non-dimensionalized by c

# Chapter 1

## Introduction

Mankind has had a fascination for flying vehicles for centuries, and helicopter flight was among the first forms of flight envisioned by man. The ancient Chinese played with a hand-spun top that rose upwards when revolved rapidly and as early as 1490 Leonardo da Vinci made drawings of a machine that resembles the modern helicopter. One of the main reasons for the keen interest in rotary winged flight is also one of its biggest advantages compared to fixed wing, namely vertical take-off and landing. This ability combined with the capability to hover almost motionless has made the rotorcraft indispensable to the military and in certain civilian applications. Although, people were experimenting with various rotorcraft design even before the Wright-Flyer, it was not until 1939 that the first practical helicopter flew. Even to this day, rotorcraft advancement has lagged behind their fixed wing counterparts.

Despite various innovations, the present day helicopters are noisy and suffer from aeromechanical and vibration issues. The noise and vibrations cause passenger discomfort and increase annoyance levels around communities as well as reduce military effectiveness of helicopters in



enemy territories. Over the last few decades, considerable effort has gone into mitigating rotorcraft noise and making it a smoother ride. However, these efforts have only had limited success. This is because the fundamental principles governing rotorcraft are very complex, and the essential technical aspects and physics governing the aerodynamics are not completely understood. Another significant issue with rotor noise is the fact, that it is inherent to any lifting rotor system.

In a fixed wing aircraft most of the noise is due to the engine, with some additional noise coming from the airframe and control surfaces. In general, an increase in thrust causes an increase in engine noise, while increasing the velocity and performing maneuvers results in increase in noise radiation from the airframe and the control surfaces. Since the engine and the control surfaces are, for the most part functionally unrelated, changes can be made to reduce noise on a component by component basis, without significantly affecting the low-noise design of other components or the overall performance. Moreover, improving the efficiency of the engine (in small to moderate sized aircraft such as the 737), through increase in by-pass ratios, has also resulted in the reduction of noise. In the case of the rotorcraft, the main source of noise is the helicopter main and tail rotors which perform the functions of providing lift and thrust, as well as controlling and maneuvering the aircraft. The various components in the helicopter are much more tightly coupled than in the case of the fixed wing aircraft. Thus the decoupling of the noise problem from the “overall efficiency” of the helicopter is next to impossible, and any effort to reduce helicopter noise has to be made with a particular eye towards not affecting the performance adversely.

The distinctive nature of helicopter noise calls attention to it even when the radiated noise levels are somewhat low by community standards [1]. The characteristic impulsive “*Wop-Wop*”

*Wop*” sound from the main rotor, the propeller like noise from the tail rotor or the whine of the Fenestron cause an awareness to nearby rotorcraft operation and increases annoyance. Excessive noise levels near community heliports are among the main impediments to increasing civilian use of helicopters. Noise reduction is also important from a militaristic standpoint. Stealth in a military offensive is desirable when the element of surprise can be used to a tactical advantage. Helicopter noise reduction, though traditionally not a design driver has been gaining prominence off late. Performance metrics have almost always superseded acoustic considerations of annoyance and stealth in traditional rotorcraft design, but acoustics is becoming an increasingly important design and operational criteria for operators and manufacturers [2, 3].

Many efforts have been directed at understanding helicopter noise sources and in developing techniques to reduce external noise. One of the more persistent sources, which has evaded significant abatement is what is termed “Blade-Vortex Interaction” or BVI noise. Unlike in fixed wing aircraft or even propellers, where the trailed tip vortices from the wing or propeller tip are convected behind when the aircraft moves forward, the trailed tip vortices from the tip of the helicopter’s main rotor blades are convected below the main rotor. Most operating conditions of the helicopter result in these tip vortices coming close to the main rotor, resulting in an interaction between the vortex and the oncoming rotor blade. The tip vortex induces a sharp change in the effective angle-of-attack observed by the interacting blade leading to a sudden change in pressure on the blade surface. This rapid pressure change radiates out from the rotor in the form of an impulsive noise referred to as BVI.

This thesis provides a novel, carefully controlled experimental approach to study the helicopter

BVI problem in order to develop deeper insights into the physics of noise radiations of the rotor blade as it moves through a vortex, and to help develop techniques and/or specially tailored blades to help reduce BVI noise. In this chapter an overview of the various sources of helicopter noise, along with the accompanying physics is presented. This is followed by a discussion on the noise reduction techniques deployed by previous researchers with a particular emphasis on Blade-Vortex Interaction Noise.

## 1.1 Sources of Helicopter Noise

Noise is primarily the propagation of pressure fluctuations in a medium like air. Changes in pressure on the aerodynamic surface, associated with lift or drag radiates as noise to an observer moving with respect to the surface. The helicopter main rotor, the tail rotor and the engine along with the rest of the body contribute to the noise. The helicopter main rotor is the primary source by virtue of the complex aerodynamic phenomena. Even during normal flight conditions, the helicopter rotor undergoes various unsteady aerodynamic phenomena (Fig. 1.1). These, including dynamic stall, interaction between the main rotor and the wake system, transonic flow resulting in shocks on the blade surface, and the complex interaction between the main rotor wake and the tail rotor. Many of these phenomena lead to vibration and noise radiation.

Fig. 1.2 shows the typical frequency spectrum of the noise radiated by a hovering helicopter [5]. The lower frequencies (0-100Hz) are dominated by the main rotor harmonics of revolution. The mid-frequencies (60-200) are dominated by the tail rotor harmonics. At higher frequencies the noise is more broad-band (less tonal) and the main contributions are possibly due to the interac-

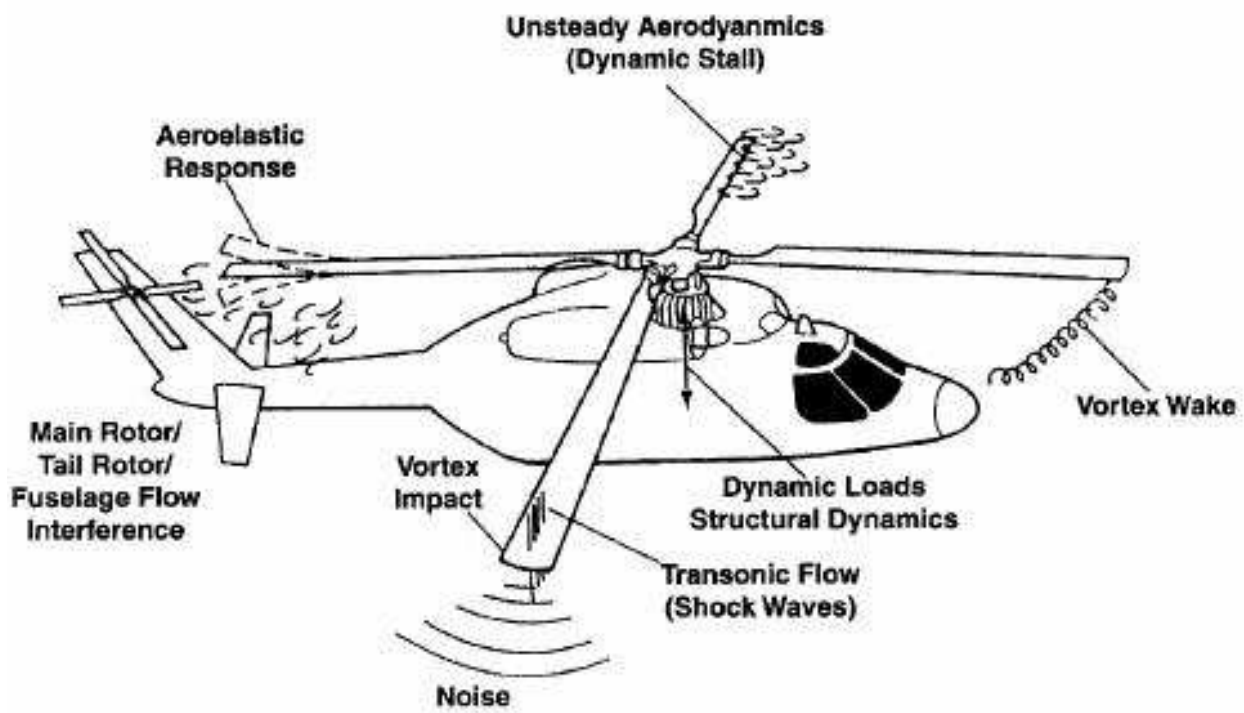


Figure 1.1: Source of helicopter noise [4]

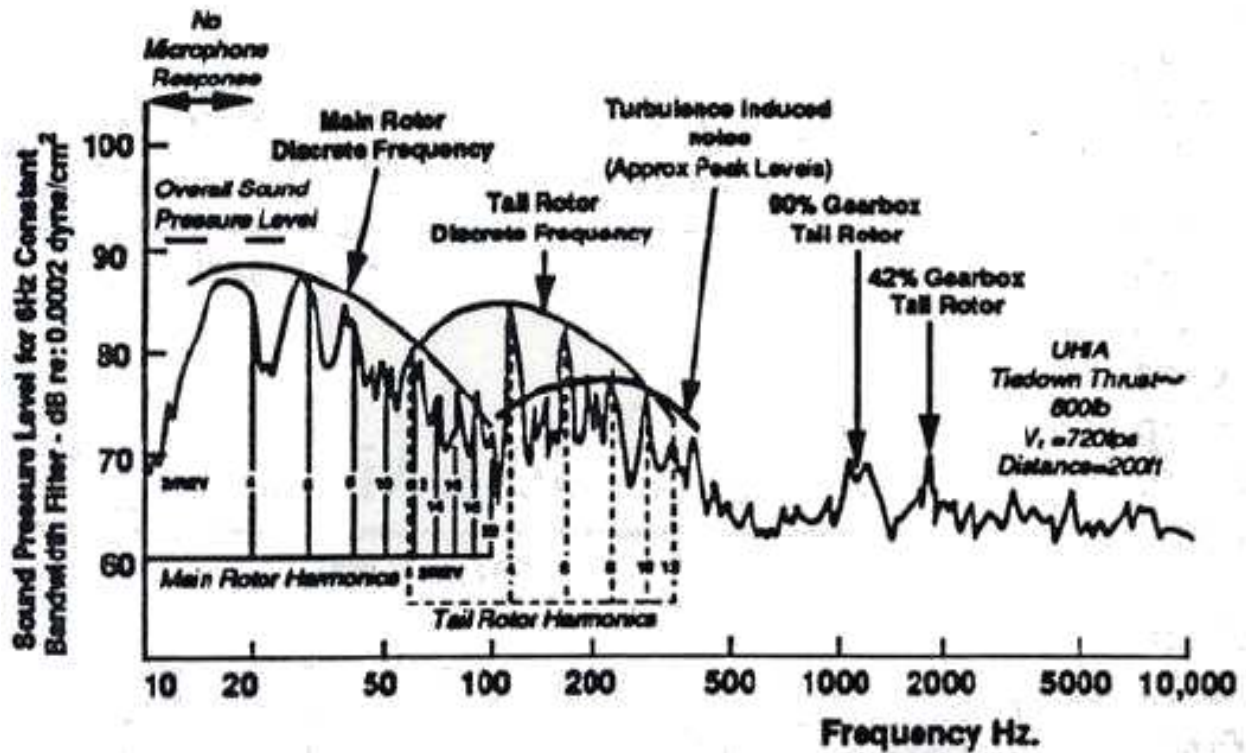


Figure 1.2: Frequency spectrum of radiated noise from a typical hovering helicopter [5]

tion of the rotor with the turbulence, and due to the gearbox and engine. In general, the relative importance of each of these sources depends on the specific rotor design.

When the helicopter moves into forward flight, the unsteady aerodynamic blade loads, including BVI contribute to the lower and mid-frequency spectrum. Other unsteady phenomena such as dynamic stall and interaction of the tail rotor with the wake of the main rotor might also generate broadband noise. The important noise sources on a helicopter in forward flight, each possess distinct characteristics and have preferred propagation directions. The noise sources can broadly be classified into the following:

- **Main rotor noise**

- **Main rotor thickness noise** — The thickness noise is a result of the displacement of the fluid around the blade as it passes through the medium and is present in both hover and forward flight. The noise sources on the rotor blade can be represented by a series of sources and sinks (monopoles) [6] and results in noise radiation mostly in the plane of the rotor (Fig. 1.3).
- **Main rotor harmonic noise** — This is a result of the steady and unsteady loading on the main rotor and is strongly influenced by the constantly changing loads of a helicopter rotor in forward flight. This source of noise is usually modelled as a series of dipoles distributed over the blade. The loading noise due to the steady and unsteady lift radiates mostly below the rotor plane (Fig. 1.3), while the noise due to steady and unsteady drag radiates more in the plane of the rotor.
- **Main rotor High Speed Impulsive (HSI) Noise** — This source of noise occurs mostly in high speed forward flight and is an extreme case of “thickness noise” discussed above. This very intense pulse is strongly influenced by the transonic effects on the blade surface. At very high transonic tip Mach numbers, the shock formed on the blade surface, can extend past the rotor blade tip and can propagate into the far-field. This phenomenon known as “delocalization” [6, 7] of the shock results in a particularly impulsive sound referred to as High-Speed Impulsive (HSI) Noise. This source of noise typically observed in older “Huey Helicopters”, can be mitigated to some extent by operating the helicopter at low advancing tip Mach numbers. Since the “delocalized”

shock wave tends to radiate in-plane, this sound source is mostly focused in and slightly below the plane of the rotor and is particularly important for military detection. In the recent past, several flight tests [8] and pioneering experiments conducted in wind tunnels and hover chambers [6, 7, 9] have been conducted to characterize and understand this particular source. Some of the solutions including lower rotor tip speeds and/or innovative blade designs, like the BERP tip [10] have been incorporated in modern helicopters. Moreover, theoretical predictions of HSI noise signature using “state-of-the-art” codes has reached a reasonably good level of accuracy [11].

– **Main rotor Blade-Vortex Interaction (BVI) Noise** — It is the typical “popping” or “slapping” sound heard most often when the observer is in front and to the advancing-blade side of the helicopter, or to the rear and retreating-blade side of the helicopter. This particular phenomenon has been a topic of extensive research for the past decades [12]. As discussed earlier, this impulsive noise mostly occurs when the wake of the main rotor passes near the rotor tip path plane. The primary radiation direction is to front and below the rotor (Fig. 1.3).

- **Tail rotor harmonic noise** — Occurs due to the steady & unsteady airloads on the tail rotor. It is similar in nature to the rotor harmonic noise, but of a higher frequency as the RPM of the tail rotor is a higher than that of the main rotor as can be seen from Fig. 1.2.
- **Other noise sources** — The gearbox of the transmission system, engine and airframe also contribute to some broadband noise. These sources are however, significantly lower in magnitude than the main rotor noise sources, as can be seen from Fig. 1.2.

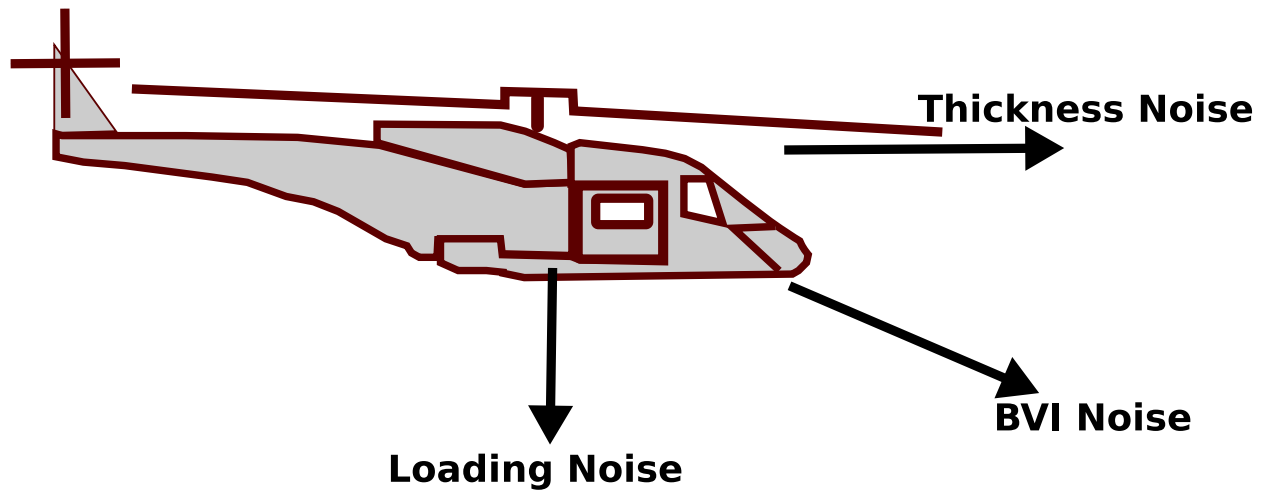


Figure 1.3: Preferred radiation directions of some noise sources [13]

## 1.2 Blade-Vortex Interaction Noise

Blade-Vortex Interaction noise mainly occurs during low speed descending flight, low speed turning descents and during some maneuvering flights [14]. These conditions are conducive to the rotor blade passing close to a vortex that is trailed from previous blades (Fig 1.4). The induced velocity of each tip vortex essentially induces a sharp change in effective angle of attack observed by the interacting blade, leading to a sharp change in surface pressure. This rapid pressure change radiates out in the form of the impulsive noise known as Blade-Vortex Interaction or BVI noise.

BVI noise is known to be highly directional and quite sensitive to flight conditions. The fact that most of the acoustic energy is concentrated in the frequency range from 75Hz to 1500Hz (5 rotor harmonics to 100 rotor harmonics) makes it quite annoying as the human ear is very sensitive to sound at the higher end of the frequency range. The noise generation itself is a complex aero-acoustic phenomenon and depends on a variety of factors encompassing rotor design, operational



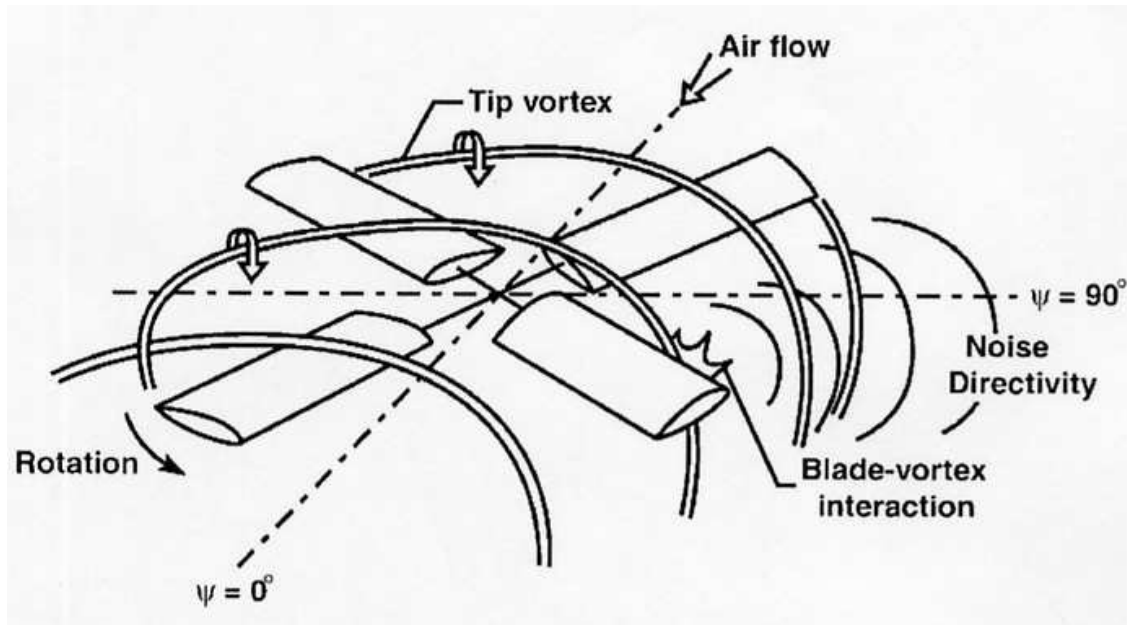


Figure 1.4: A 4-bladed rotor undergoing BVI

conditions and even atmospheric conditions. The nature and strength of the effective BVI noise sources, the associated propagation mechanisms and the geometry of the interaction determine the BVI noise radiation to the far-field.

Fig. 1.5 shows the geometry of two-bladed rotor undergoing BVI as seen from the top view. As is apparent from the figure, each blade intersects the vortices trailed from the blade tips at earlier times. Even for a two-bladed rotor, several interactions are possible and are dependant on the trajectory of the tip vortex. The strength of the tip vortex and its trajectory, in turn, are dependant on various rotor parameters including rotor tip Mach number and advance ratio. Under most flight conditions such as hover or steady level flight, the tip vortices are mostly below the plane of the rotor as seen in Fig. 1.6(a) and the interaction between the blade and vortices do not lead to significant noise radiation. However, certain flight conditions such as low speed descent,

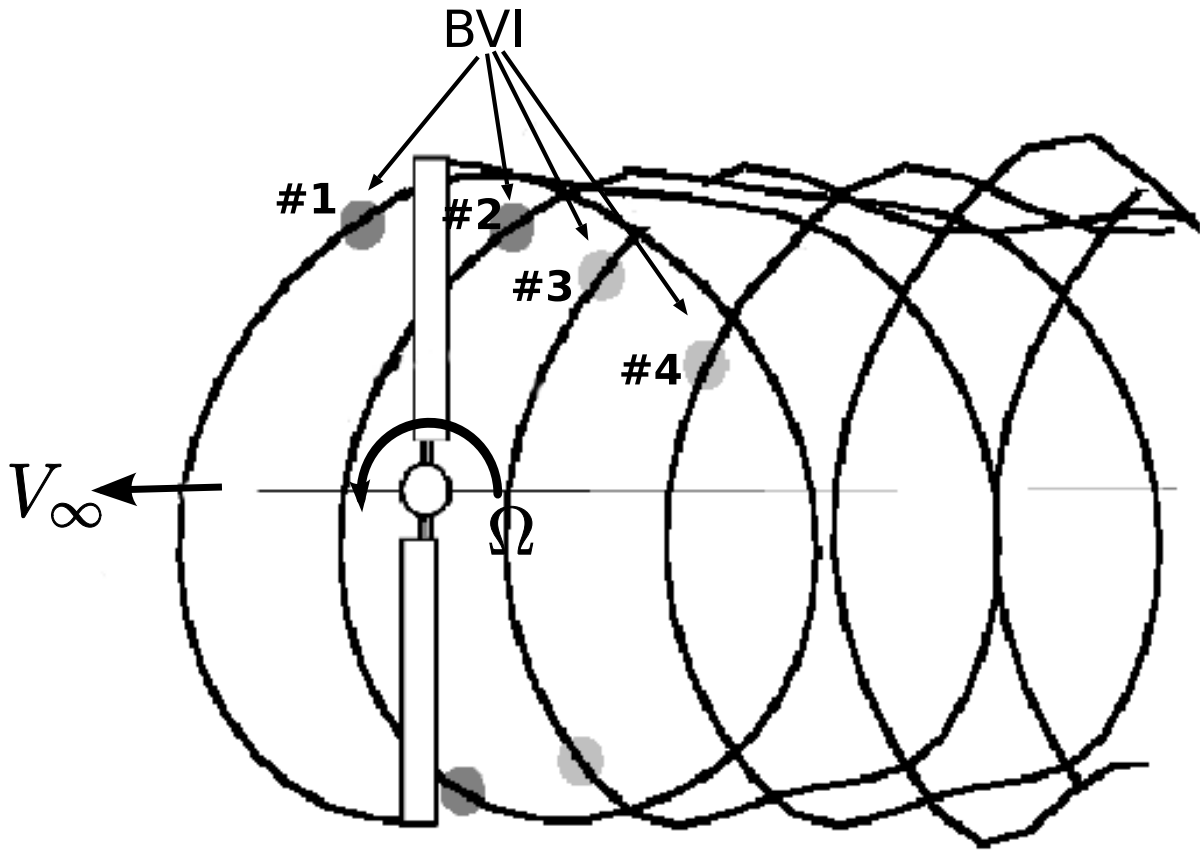
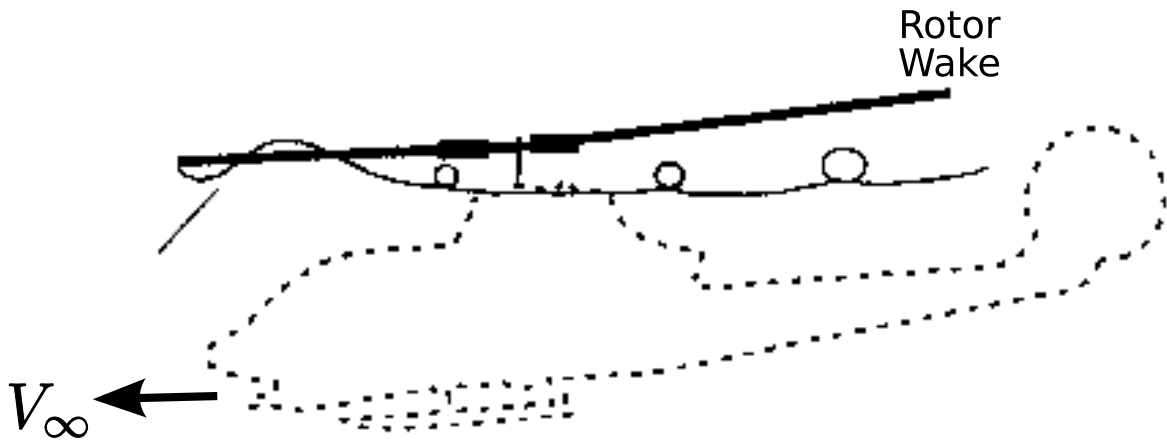


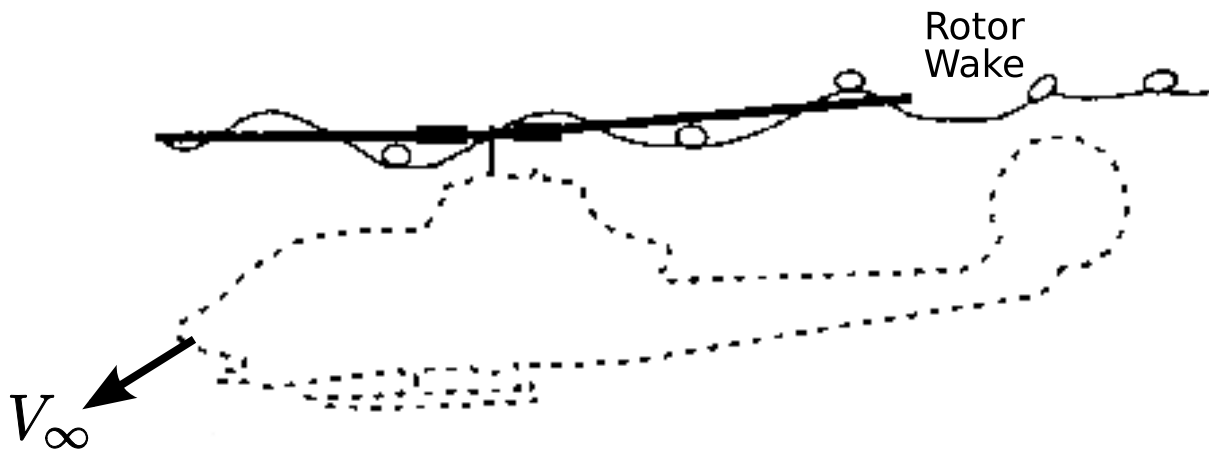
Figure 1.5: Top view of helicopter in BVI

lead to the tip vortices passing close to rotor plane (Fig. 1.6(b)). The closer the tip vortices are to the rotor plane, the stronger and more impulsive is the noise radiated.

Certain interactions, for example BVI #3 in Fig. 1.5, are such that the interacting tip vortex filament with the blade is nearly parallel to the rotor blade. The resulting interaction can then be idealized as a series of two-dimensional interactions between the blade section and a two-dimensional vortex. A two-dimensional section of the rotor blade airfoil undergoing BVI is shown as a schematic in Fig. 1.7 along with the typical vortex induced velocity. The velocity induced by



(a) Helicopter in steady level flight



(b) Helicopter in low speed descent

Figure 1.6: Side view of helicopter BVI

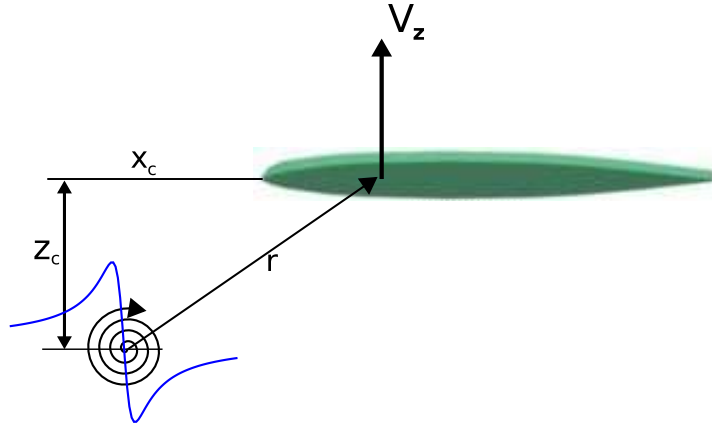


Figure 1.7: Two-dimensional schematic of the BVI

an idealized vortex on the blade is given by the Biot-Savart law:

$$V_{\theta} = \frac{\Gamma}{2\pi r} \quad (1.1)$$

where  $V_{\theta}$  is the tangential velocity induced by the vortex,  $\Gamma$  is the vortex strength and  $r$  is the radial distance from the vortex center. The blade surface pressure and hence the lift is most affected by the vertical component of the induced velocity and is given by

$$V_z = \frac{\Gamma}{2\pi} \frac{x_c}{r_c^2 - (z_c^2 + x_c^2)} \quad (1.2)$$

where  $V_z$  is the vertical component of the velocity induced at the quarter chord location of an airfoil which is separated vertically by a distance  $z_c$  and horizontally by a distance  $x_c$  from the vortex.

The unsteadiness of the induced surface pressures, and hence the strength of the radiated noise depends quite strongly on the vertical “miss-distance ( $z_c$ )” between the blade and the vortex, the strength ( $\Gamma$ ) and core radius ( $r_c$ ) of the vortex.

A relatively simple analysis can be performed to estimate the tip-vortex trajectory for a rotor in steady forward flight. Assuming that the tip vortex convects along with the rotor downwash

and is undistorted in the rotor tip path plane, the tip vortex coordinates can be obtained using the following equations [15]:

$$\begin{aligned}\frac{x_{tip}}{R} &= \cos(\psi_b - \psi_w) + \mu\psi_w \\ \frac{y_{tip}}{R} &= \sin(\psi_b - \psi_w)\end{aligned}\quad (1.3)$$

where  $x_{tip}$  and  $y_{tip}$  are the coordinates of the tip vortex filament,  $R$  is the blade radius,  $\psi_b$  and  $\psi_w$  are the azimuthal angles of the blade and the tip vortex filament under consideration, respectively and  $\mu$  is the advance ratio of the helicopter. This basic equation although possibly over-simplified, captures the essential parameters affecting the BVI. Moreover, this set of equations also helps predict the locations of important BVIs. The locus of possible BVIs for an  $N_b$ -bladed rotor, in a rotor fixed reference frame, can then be determined by solving the following two equations, simultaneously:

$$\begin{aligned}r \cos\left(\psi_b - \frac{2\pi(i-1)}{N_b}\right) &= \cos(\psi_b - \psi_w) + \mu\psi_w \\ r \sin\left(\psi_b - \frac{2\pi(i-1)}{N_b}\right) &= \sin(\psi_b - \psi_w)\end{aligned}\quad (1.4)$$

Fig. 1.8 shows the locus of possible BVIs for a two bladed helicopter at two different advance ratios of 0.1 and 0.164 obtained from the rigid wake (Eqn. 1.4), in the rotor fixed reference frame. It should be noted that a rigid wake model is not entirely accurate as the rotor downwash and interaction between the individual shed vortices causes the wake to modify even during steady flight conditions. Nevertheless, the trajectory described by the rigid wake model provides an important understanding of the interaction geometry and in identifying the important interactions for BVI noise radiation.

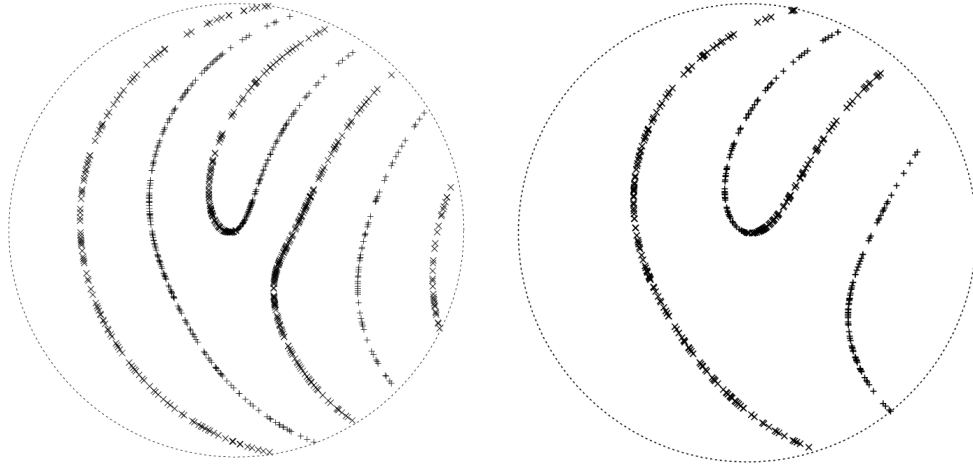


Figure 1.8: Locus of possible blade-vortex interactions for two-bladed rotor for two different advance ratios ( $\mu = 0.1$  and  $\mu = 0.164$ )

If one were to consider the instantaneous interaction point between the tip vortex and the blade as the noise source, then the trajectory of the source in the undisturbed medium is obtained from the tip vortex trajectory depicted in Fig. 1.8. Confining this trajectory to lie in a plane parallel to the rotor disk causes the aerodynamic loading and the resulting acoustics of the BVI to be predominantly dependant on the basic top-view geometry of the BVI process. The controlling parameters are the advance ratio ( $\mu$ ) and the hover tip Mach number ( $M_T$ ) of the rotor [16]. From these two parameters, a third parameter called the trace Mach number [17] can be obtained (Eqn. 1.5). The trace Mach number ( $M_{TR}$ ) is the speed ( $V_{TR}$  in Fig. 1.9) of the locus of the interaction geometry, with respect to the undisturbed medium, non-dimensionalized by the speed of sound.

$$M_{TR} = \frac{\Omega r(\mu + \sin \psi_b)}{a_0 \sin \gamma} \quad (1.5)$$

Both the three-dimensional interaction geometry and the trace Mach number determine the

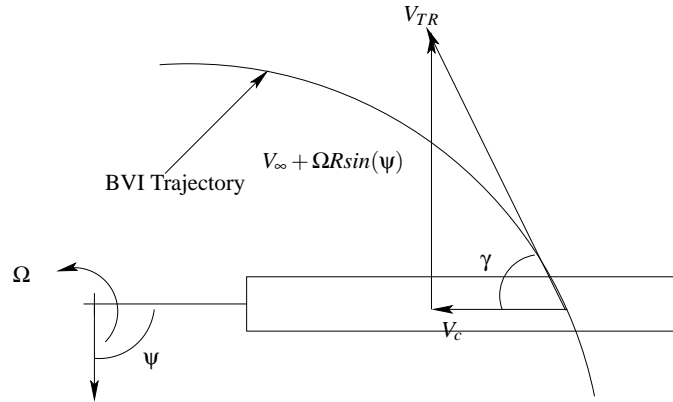


Figure 1.9: Trace Mach number of BVI

phasing of the acoustic events and hence the directionality of the BVI noise radiation [18, 19, 20, 21, 22]. When viewed in a medium fixed frame of reference, the BVI trajectory can be treated as a single acoustic source (of varying strength) moving along the epi-cycloidal tip vortex trajectory at a non-dimensionalized speed given by the trace Mach number. At each instant in time, this acoustic source triggers an acoustic disturbance (BVI wavelet) that propagates away from the blade surface at the speed of sound. If the trace Mach number at points along the trajectory becomes large, a series of these acoustic disturbances can group together with the undesirable effect of strong noise focusing and amplification. The noise focusing is directly related to the trace Mach number.

For a parallel BVI, the interaction angle  $\gamma$ , in Fig. 1.9 is zero resulting in a trace Mach number of infinity (from Eqn. 1.5). Physically, this is because all the acoustic sources along the BVI trajectory are triggered simultaneously. The wavefront resulting from the summing of these acoustic waves propagates almost perpendicular to the initial interaction. A schematic of the wavefront for a helicopter undergoing near-parallel (slightly curved) BVI is shown in Fig. 1.10(a) and the corresponding trace Mach number profile in Fig. 1.10(b). This interaction — corresponding to

BVI #3 in Fig. 1.5 — has an infinite trace Mach number for most of the interaction, resulting in a simultaneous summing of the BVI wavelets. Such interactions are typically the strongest, with most of the acoustic energy focused in front and to the advancing side of the rotor.

Oblique BVIs tend to be of a lesser magnitude due to summing of the waves from the acoustic source as the blade sweeps the tip vortex trajectory. For the oblique BVI, the trace Mach number being finite, results in non-simultaneous summing of the acoustic waves. This results in an entirely different azimuthal directionality of noise radiation. A schematic of a helicopter undergoing oblique BVI (corresponding to BVI #2 in Fig. 1.5) is shown in Fig. 1.10(c). This interaction has a decelerating trace Mach number profile as shown in Fig. 1.10(d). Most of the acoustic energy in this case is directed towards the front of the rotor.

From the discussion so far, it is apparent that the helicopter BVI is a strong function of the helicopter wake.

Significant research effort has been directed at reducing BVI noise in the past decades. Various blade and/or rotor design modifications including active and passive approaches, X-Force control and flight path management have been attempted with success. However, they require significant modifications to the helicopter airframe. A significant portion of the problem has been the lack of understanding of the real cause and effect. For instance, changes in blade planform affects the tip vortex characteristics which in turn modifies the unsteady induced loads. However, the change in blade planform also affects the trace Mach number profile of the interaction as the blade sweeps over the tip vortex, thus affecting the phasing and hence directionality of the acoustic energy. Given that the tip vortex trajectory is far more complex than is represented by Eqn. 1.3 the real effect of



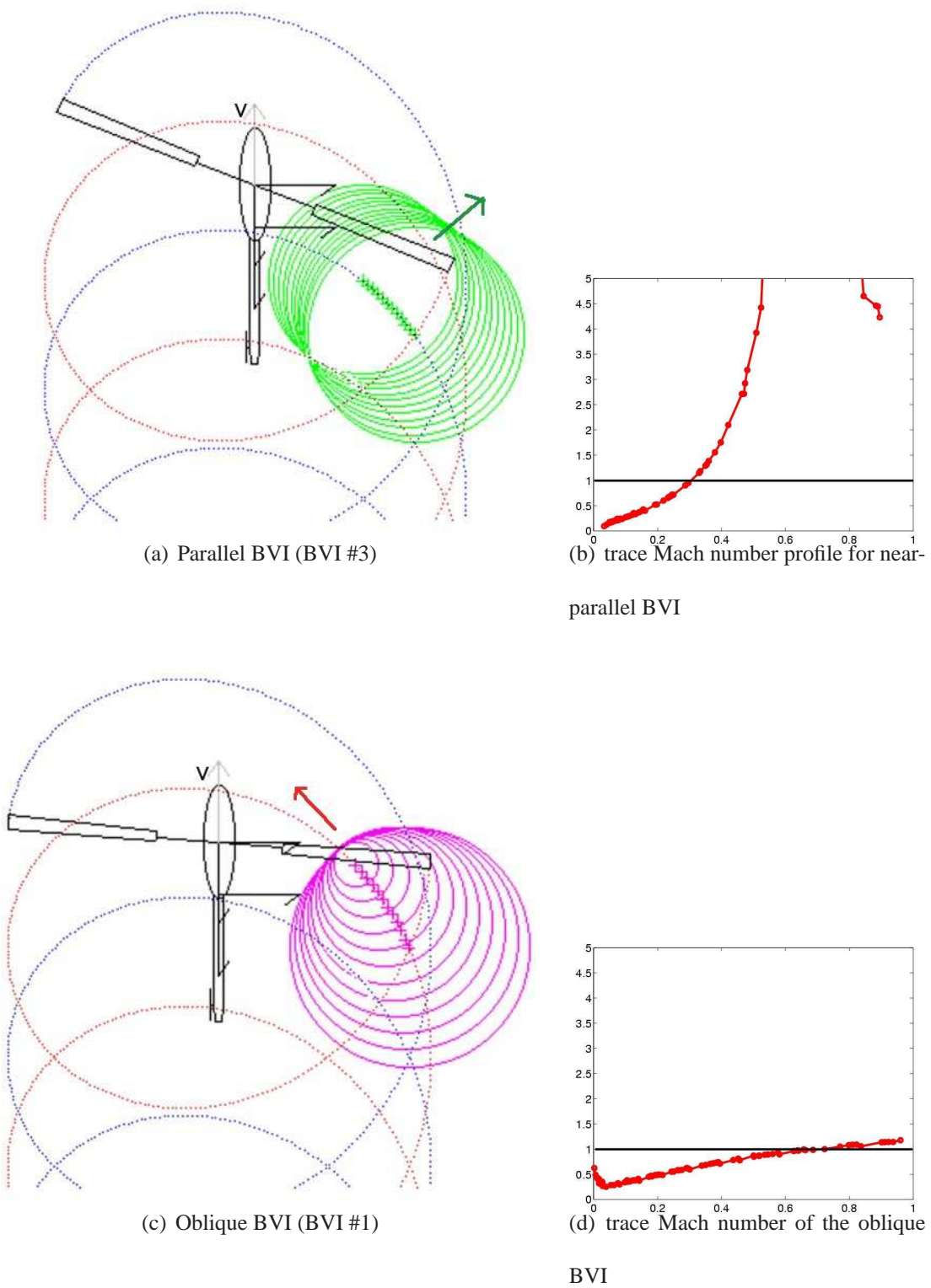


Figure 1.10: Directivity patterns obtained from wave tracing and  $M_{TR}$  approach ( $\mu = 0.164, M_T =$

the blade design change is hard to predict and control. Similar coupled effects occur with almost all rotor parameter changes making BVI noise reduction a real challenge.

### **1.3 BVI Noise: Challenges and Prior Art**

Accurate prediction of helicopter BVI noise is a difficult challenge that has yet to be accomplished. BVI noise prediction requires good estimates of the rotor trim state and very accurate estimates of the vortex strength, trajectory and vortex structure, blade aerodynamics and aeroelasticity.

In predicting rotorcraft noise on the ground, therefore, there are typically two challenges involved:

- Estimate the blade loads and blade surface pressure distribution at a given operating condition. This requires a very detailed knowledge of the wake dynamics, especially the vortex locations and the evolution characteristics to sufficiently high degree of resolution. Moreover, the turbulence and near shed-wake dynamics also contribute to some of the acoustics. The complexity of the wake and unsteadiness of the whole system makes this a very challenging task.
- Once the aerodynamic environment is known, experimentally or computationally, Eqn. 1.6 or other suitable equations can be applied to calculate the noise radiated to the ground. Even at this stage, the non-linearities involved at high transonic tip Mach numbers, make accurate noise prediction complicated

A brief review of previous work undertaken by researchers in understanding these challenges is provided below.

### **1.3.1 Unsteady Aerodynamics**

Beginning with Theodersen's [23] analysis of two-dimensional oscillating airfoils, various theories have been put forward for understanding unsteady aerodynamics, including heaving and pitching airfoils [24, 25] and airfoils moving through gusts [26]. Wagner first proposed the in-dicial approach, whereby the empirically estimated the airfoil response to a step change in angle of attack is integrated using the Duhamel integral to obtain the airfoil response to arbitrary unsteady angle of attack changes. This approach has been extended by various researchers to other airfoil motions including pitching and heaving. Beddoes [27] and, later Leishman [28] extended the approach for the motion of an airfoil through a gust. Leishman obtained the airfoil response to a sharp-edged gust using an two-dimensional unsteady Reynolds Averaged Navier-Stokes (RANS) CFD solution, which was then used to estimate the airfoil loads for an arbitrary gust. Such techniques when tailored for specific Mach number regimes can account for compressibility effects to some extent, and have been used with a reasonable degree of accuracy to predict BVI noise [29]. However, all the above theories being based on potential flow are truly valid only for sufficiently low Mach numbers and relatively small changes in aerodynamic character.

While the above approaches mostly concern airfoil-gust interactions and are essentially two-dimensional in nature, Widnall and Chu [30] and later Martinez and Widnall [31] attempted the development of a theoretical model for the interaction of an infinite wing with an oblique gust.

While this approach helped solidify the trace Mach number concept proposed by Widnall [17], comparison with experiment [32, 33] was not satisfactory due to the assumptions of low reduced frequency and moderate tip Mach numbers.

BVI induced loads are of very high frequency in nature and can cause acceleration of the flow to transonic Mach numbers. Since BVI far-field acoustics is more a function of the rate of change of loads than the level of the loads itself, the radiated noise predicted using these aerodynamic models tend to be wrong. Moreover, they very quickly lose validity at higher Mach numbers.

These potential theories, nevertheless have been used in three dimensional calculations for various helicopter maneuvers. Vortex based models have been used to represent the wake behind the helicopter, and the induced blade loads. Prescribed wake methods [34, 35], where the wake structure is modelled *a priori* or is obtained from empirical estimates, and free wake methods [36, 37], where the wake structures evolves as a part of the solution have been developed. These techniques, although successful to some extent in predicting the wake dynamics, precise location of BVIs require extremely high level of resolution of the wake, thus increasing the computational time by orders of magnitudes.

With the advent of cheaper and faster computers, full-fledged solutions of the Navier-Stokes equation for the flow field surrounding the rotor has become possible. Datta et al [38] present a detailed review of the development of CFD based approaches used by researches in the last decade. The main advantage of this approach is the accurate description of the flow field around the rotor blade. With sufficient resolution in grids and using the right discretization, the formation of vorticity on the surface of the rotor blades, its convection into the trailing vortex sheet, and

rollup into one or more vortex structures can be calculated accurately. However, they require very fine grid resolution in order to prevent numerical dissipation of the vortex structures. Some hybrid formulations which use the Lagrangian free-vortex approach (or prescribed wake in some cases) approach for the far-field wake and solve the flow equations in the near field have been used to work around this problem [39]. Computationally more intensive techniques such as direct wake capturing scheme [40, 41] and vorticity confinement techniques [42] have also been applied to the problem. These computational techniques are under active development and might prove very useful for the simulation of the rotor wake aerodynamics problem. However, they are still in the infancy and lot more research is needed before they can be used in full fledged rotorcraft comprehensive codes.

### **1.3.2 Aeroacoustics**

Acoustic pressure in the far-field is simply the aerodynamic perturbation pressure that radiates a net energy from the source. Thus in theory, one expects that a solution to the full Navier-Stokes equations over the entire flow field (including the observer), would provide the desired solution. However, this approach for practical problems is beyond any currently available computing capacity and will be so in the foreseeable future [43]. However, once the aerodynamic field around a rotor blade has been estimated, the application of the appropriate acoustic propagation equation can yield the acoustic pressure at the observer location [44].

Some of the earliest acoustics research with regards to rotating systems was focused on the propeller. By the late 1930s it was known that for rotating blades, both loading and the blade thickness

could generate noise by different mechanisms. The first estimate of harmonic loading noise due to the steady loading on the blade was obtained by Gutin [45]. This early theory though based on simple aerodynamic estimates of the loading brought out the extremely directional nature of the loading noise and its dipole nature. Demming [46] and Ernsthausen [47] worked independently on the problem of thickness noise in propellers. These loading and thickness noise estimates were derived for propellers that were simply rotating in one place. Garrick and Watkins [48] extended Gutin's results to the propeller in forward flight in the early fifties.

By the 1960s the noise of helicopters became an important issue. It was realized that unsteady blade loading in addition to steady loading was a significant contributor to the discrete and broad-band noise of the helicopter rotors. However, the acoustic theories developed earlier for propellers were only applicable to helicopters in hover or axial climb, because they did not account for the unsteady blade loading during the helicopter's forward flight. Some of the first noise prediction theories applied specifically to helicopter rotors were developed by Lawson [49] and Wright [50]

Lighthill's [51, 52] paper where he recast the Navier-Stokes equation as a wave equation propagating pressure was among the first to mathematically model pure aerodynamic sources (other than monopoles and dipoles). This approach termed the "acoustic analogy", was originally derived for jet noise and is not directly applicable to the rotor noise problem.

Working on similar lines as the Lighthill's analogy, and using generalized functions, the Navier-Stokes equation was recast into a non-homogeneous wave equation, which can be applied to any arbitrary surface by Ffowcs-Williams and Hawkings [53]. This equation, now called the "Ffowcs-Williams and Hawkings Equation" is more general than other rotorcraft acoustic modelling and has

been used extensively for the rotor noise problem. The classic derivation assumes an impermeable surface and the solution is derived using the Green's function over free unbounded space. The acoustic pressure can be expressed in tensor notation:

$$\begin{aligned}
p(x,t) = & - \underbrace{\frac{\partial}{\partial x_i} \iint \left[ \frac{P_{ij} n_j}{r|1-M_r|} \right] dS}_{\text{Loading (dipole) term}} \\
& + \underbrace{\frac{\partial}{\partial t} \iint \left[ \frac{\rho_0 v_n}{r|1-M_r|} \right] dS}_{\text{Thickness (monopole) term}} \\
& + \underbrace{\frac{\partial^2}{\partial x_i \partial x_j} \iiint \left[ \frac{T_{ij}}{r|1-M_r|} \right] dV}_{\text{Quadrupole term}}
\end{aligned} \tag{1.6}$$

where,  $p$  represents the acoustic pressure at the observer,  $r$  is the distance between the acoustic source and the observer,  $M_r$  is the Mach number of the source along the direction of the observer,  $P_{ij}$  and  $T_{ij}$  are the local pressure and stress tensors respectively and  $n_j$  represents the local normal to the surface containing the acoustic sources. Finally, the terms within the square brackets are evaluated at the right retarded time (time of acoustic emission from the source).

The acoustic pressure,  $p$ , in the far-field is given as the sum of three terms: the loading term, the thickness term and the quadrupole term. The ‘‘loading’’ term, also a surface integral, accounts for the steady and unsteady aerodynamic forces of lift and drag on the surface. This term is dipole in nature and radiates in a double-dumbbell shaped pattern perpendicular to the rotor plane for noise due to lift and parallel to the rotor plane for noise due to drag. The ‘‘thickness’’ term, a surface integral, accounts for the displacement of the medium due to the thickness of the surface. It is a monopole term and in the case of the helicopter, results in radiation mostly in the plane of the rotor. The third term, a volume integral, is simply termed as a quadrupole and accounts for all

other sources including non-linearities at transonic Mach numbers, turbulence and aerodynamic stresses produced in the flow-field. This term can be extremely complicated to compute and most initial researchers either dropped this term all together or developed formulations which reduced the complexity of the computation involved.

The Ffowcs-Williams Hawkins equation (Eqn. 1.6) itself has been the subject of significant research in the past two decades and recast into more useful forms. Notable among them are Farassat's formulations [54, 55] which are used in many comprehensive rotorcraft codes including WOPWOP [56].

While the “dipole” (loading) term and “monopole” (thickness) term relate directly to far-field radiated noise due to airloads on the rotor blade, the “quadrupole” term encompasses the entire flow-field, including the aerodynamics of the rotor wake along with turbulent fluctuations and other non-linearities all the way out to the observer. The quadrupole term is really a manifestation of choosing a linear solution formulation of the rotor acoustic problem. This term also accounts for non-linearities due to local variations in speed of sound induced by compressibility. Unfortunately, this term is extremely complicated to calculate accurately and truly requires a full-blown CFD estimation of the important flow-field variables. The effect of the non-linearities is usually very small far away from the rotor blade and are neglected, and most formulations only try to capture the quadrupole term near the blade. Although this term does play an important role in BVI noise generation, particularly at higher tip Mach numbers [57], it is neglected in most preliminary calculations.

Farassat and Myers [58, 59] developed the Kirchoff surface formulation to eliminate the need



to estimate the quadrupole source term. The Kirchoff surface encloses the blade and the near field wake so that the primary contribution of the quadrupole term is contained within the surface. CFD methods are then used to compute the flow inside this surface [44], and to estimate the flow velocities and pressure, and their spatial and temporal derivatives. These values are then input into the acoustic propagation formulations to compute the far-field noise. Lyrintzis et al [43] provide a good review of approaches and methods of implementation of the Kirchoff surface to rotor problems. The Kirchoff surface can either surround the entire rotor and be fixed with respect to the flow-field of interest, or it can encompass a single blade and rotate in the medium. Although both these methods and the conventional method of dropping the effect of the quadrupole term provide very similar results for low speed problems, in the transonic flow regime the non-rotating Kirchoff surface is seen to give better results.

The impermeable Kirchoff [60] surface formulation is valid only in the region where the linear wave propagation governs the flow. In regions close to the blade, where non-linear acoustic phenomena dominate, unphysical solutions have been obtained by this method [4]. Also it has been shown that the Kirchoff surface can give unreliable results in situations with vorticity transporting across the surface. This is particularly important for rotor problems. di Fransescantonio [61] revised the Ffowcs-Williams Hawkins (Eqn. 1.6) equation using a permeable surface boundary condition. Recently many researchers have been employing the permeable surface formulation for the rotor noise problem as it helps better capture the noise radiation due to aerodynamic non-linearities around the blade [62, 63].

Caradonna et al [64] presented a comparison of various computational methodologies, to ex-

perimental results of BVI induced blade loads and noise. Full-fledged CFD, indicial methods using blade element theory and aeroacoustics formulation using experimental blade pressures [65] were compared to a controlled parallel blade vortex interaction. It was observed that most theoretical approaches predicted blade loads reasonably well, when vortex parameters and blade motion were accurately known. However, there were discrepancies in the noise prediction. Most approaches over-predicted the magnitude and/or the pulse-width.

### **1.3.3 Experimental Approaches**

Flight tests have been performed for a very long time to estimate helicopter noise for research purposes, community noise acceptance studies and certification [66]. Microphones mounted on the ground, or on tall poles or cranes [67] are used to obtain far-field noise information. The effect of atmospheric absorption can be accounted for and studies can be conducted for different flight maneuvers. However, using this technique it is hard to accurately measure the noise when the noise signature or directivity changes during a flyby. Certain flight segments such as high speed flight preclude averaging of the data and hence pose difficulties in accurate noise measurements.

The In-Flight Rotor Acoustic Program (IRAP) at NASA Ames developed by Schmitz and Boxwell [9, 8, 68] consists of a fixed wing aircraft flying in formation with the helicopter being tested (Fig. 1.11). The fixed wing aircraft acts as an instrumented “flying platform” for making acoustic measurements. This approach has two distinct advantages over ground based measurement approaches. The periodic data obtained can be ensemble averaged and tied to discrete aerodynamic events on the helicopter rotor. Moreover, the “flying platform” can be flown at different

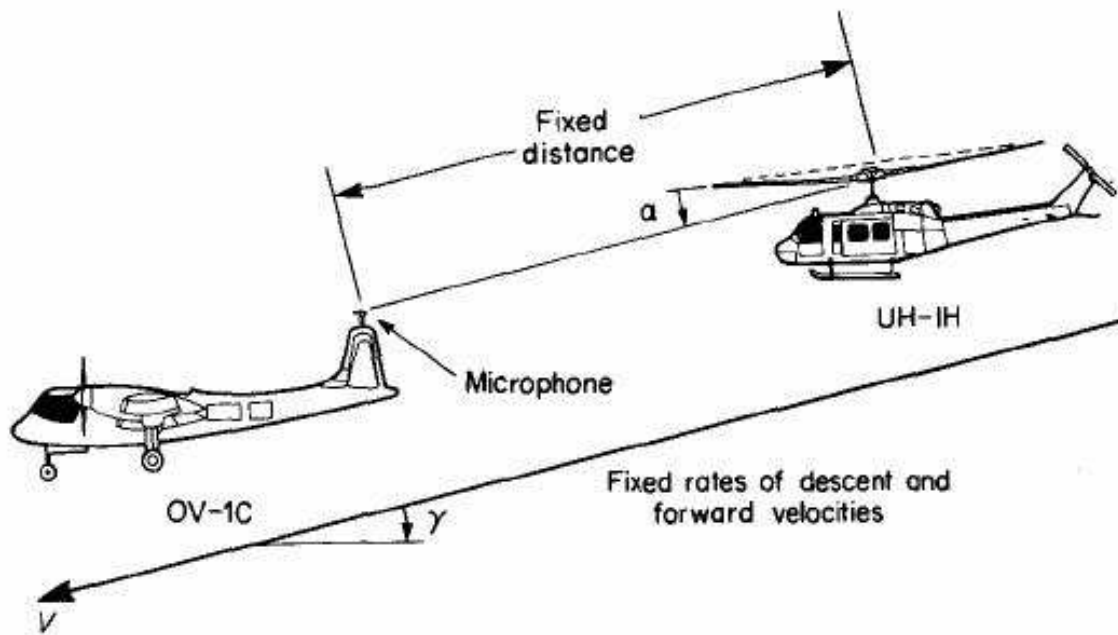


Figure 1.11: In-flight acoustic measurement technique [8]

azimuth and elevation angles at a fixed distance from the helicopter to obtain directivity information.

A Mohawk (OV-1C) instrumented with microphones was flown in formation with a UH-1H helicopter (Fig.1.11), positioning the helicopter to obtain periodic noise at the microphone on the OV-1C. This was the first successful attempt at characterizing the full-scale impulsive noise of this helicopter. This flight test also showed that the helicopter cabin noise measurements are not necessarily indicative of noise radiated outside, particularly for High-Speed Impulsive (HSI) noise. Later, an instrumented Y0-3A was used to measure noise characteristics of the AH-1S and the UH-1H. Tests were performed at different advance ratios and moderate rates of sink. It was shown that BVI noise radiated mostly forward and below the main rotor.

Experiments conducted by Boxwell et al [16] suggested that the main non-dimensional parameters are the advance ratio ( $\mu$ ), the thrust coefficient ( $C_T$ ), rotor tip-path plane angle ( $\alpha_{TPP}$ ), and hover tip Mach number ( $M_T$ ). The study also showed that when these parameters are matched, full-scale flight BVI acoustics are comparable to experimental wind-tunnel BVIs for low to moderate advance ratios. These non-dimensional parameters affect the radiated noise, primarily by altering the vortex characteristics and wake structure. The change in thrust coefficient and tip path plane angle affects the miss-distance and strength of the vortex thus affecting the induced pressure on the blade surface. The hover tip Mach number and the advance ratio affect the basic vortex characteristics as well the trajectory of the tip vortices, changing the interaction geometry.

Several wind tunnel tests have further explored the effect of these parameters on BVI noise. Burley and Martin [69] present detailed time histories of BVI noise associated with a model BO-105 helicopter in the DNW wind tunnel on a ground plane under the scaled rotor. It was implicitly assumed that the model rotor acoustics were similar to the full-scale BO-105. The researchers extensively covered the effect of tip path plane angle and advance ratio and concluded that BVI noise peaks in a narrow range of tip-path plane angles and that this range reduces as the advance ratio decreases.

The Higher Harmonics Control Aeroacoustic Rotor Test (HART) [70, 71, 72] program at the DNW wind tunnel, tested an instrumented BO-105 rotor for various operating conditions with and without applying Higher-Harmonic control (HHC). The wake geometry (including the vortex strength and structure) was also measured using Particle Imaging Velocimetry (PIV) and Laser Doppler Velocimetry (LDV). Several computational approaches have used these results for validat-

ing the acoustics and near wake aerodynamic predictions [73, 74, 75]. These experiments however, in simulating a full BVI problem had the same rotor-wake coupling issue discussed earlier. The wake geometry and blade motions were reported to have a very important effect on the acoustics predictions.

The in-flight measurement approach was used once again by Yamauchi [76] to study the acoustic characteristics of the S-76 and perform comparisons with full-scale wind tunnel tests. Comparisons at low advance ratios between the time histories of wind tunnel and flight tests were reasonable. However, at higher advance ratios ( $\mu > 0.25$ ) the wind tunnel measurements showed much higher blade-to-blade and revolution-to-revolution variability, and slightly different pulse shapes compared to flight data, possibly due to wind tunnel turbulence. It was observed that peak BVI noise radiation increased with increasing tip-path plane angle until it reached a maximum value for a given advance ratio. Further increases in the tip-path plane angle resulted in a reduction in peak BVI noise.

Sim and Schmitz [77] conducted a series of flight test experiments to establish the relation between the azimuthal directivity of BVI and flight conditions such as rate-of-sink and forward speed. A microphone instrumented boom was mounted on the helicopter while flying it at various flight conditions. This set of experiments provides a particularly useful dataset as it allowed to keep the microphones at precisely known location with respect to the main rotor during flight. Efforts are also underway to instrument the helicopter with tip path plane measurement system to quantify its role as a fundamental parameter for BVI noise radiation.

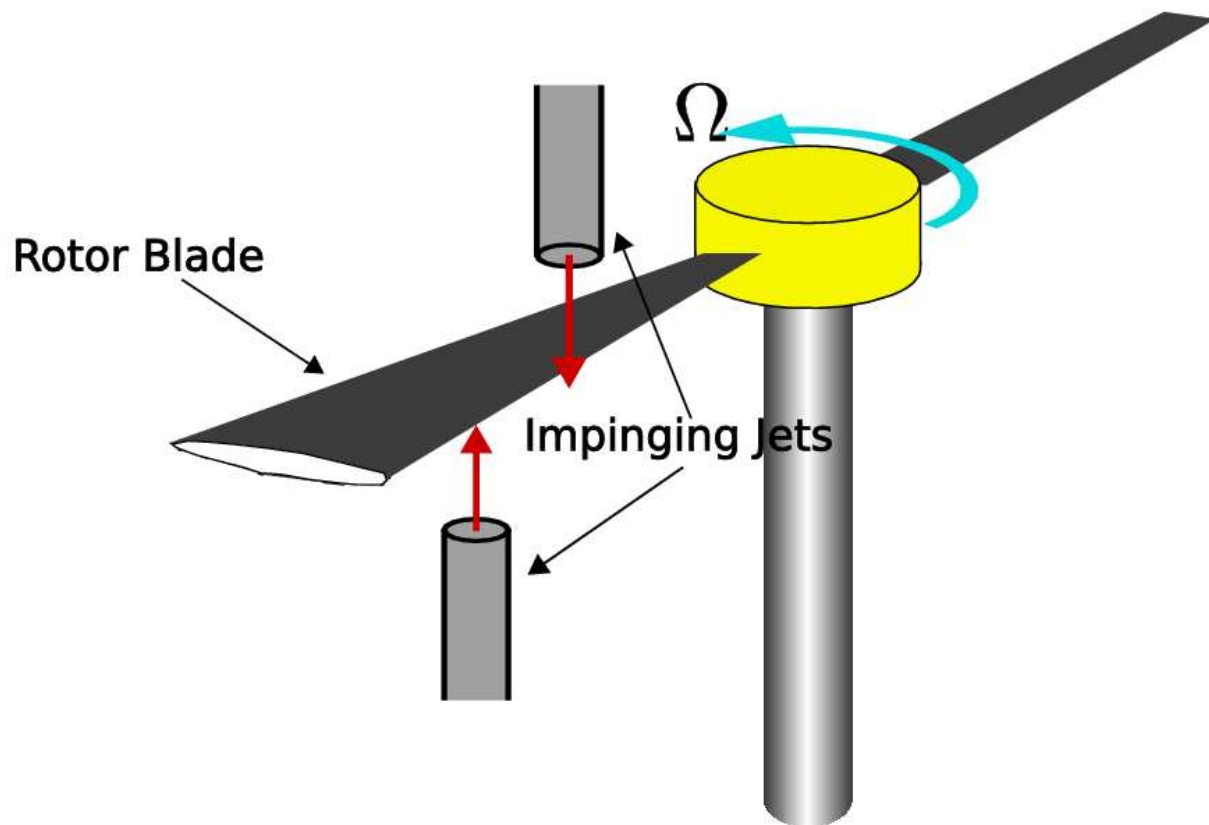


Figure 1.12: A schematic of the BVI experiment by Leverton

### Experimental Simulations of BVI Noise

Among the first experimental studies of the BVI noise was performed by Leverton [78, 79]. He used a series of jets impinging on a rotating blade while measuring the radiated noise (Fig. 1.12). Although this experiment had several limitations, it was successful in establishing the general origin of BVI noise as occurring due to a vortex interaction.

McCormick and Surendraiah [80] were the first to conduct controlled experiments with a stationary vortex. A semi-span wing mounted in a wind tunnel was used to generate a tip vortex, which when convected downstream underwent a parallel interaction with a two-bladed rotor. The

rotor itself was non-lifting so that it did not generate any noticeable tip vortices. The strength of the vortex and the miss distance could be controlled by changing the angle of attack and by moving the wing-tip relative to the rotor system. An independantly generated vortex provided known parameters for the blade-vortex interaction and significantly reduced the complexity, enabling a parametric study of unsteady loads and acoustics. However, the upstream vortex strength was not strong enough to be representative of full-scale BVI.

Several experiments have since been performed to study the Blade-Vortex interaction [81, 82, 83]. One particularly important experiment was a parallel Blade-Vortex Interaction conducted by Kitaplioglu et al [84, 85]. A vortex shed from a fixed-wing tip interacted with a scaled OLS blade further downstream in the  $80 \times 120$  ft wind tunnel (Fig. 1.13). Blade surface pressures at various spanwise locations were recorded simultaneously with far-field as well as near-field noise. This experiment has since been the validation point for almost all BVI simulation methodologies developed. However, the vortex size was about 15% of the rotor chord which is on the larger side of typically encountered vortices during BVI. Thus it contained a lower frequency content than is typical. Although the setup had the capability to move the rotor with respect to the vortex trajectory it was not performed and no oblique BVI interaction cases were studied to determine the noise radiation characteristics of the rotor.

## 1.4 Objectives of Current Research

Although significant amount of research has gone into studying the BVI noise problem in the recent past, quiet rotor designs are hard to come by in the real world. Accurately predicting the

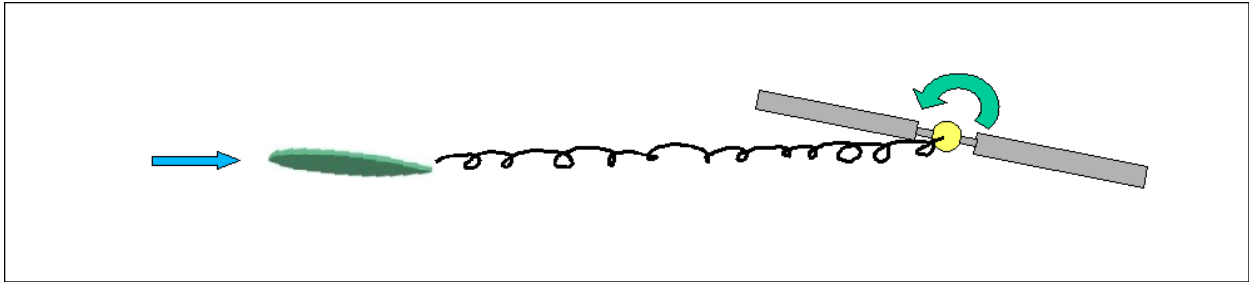


Figure 1.13: A schematic of the wind tunnel experimental setup used by Kitaplioglu et al [84]

airloads and the resulting rotor noise has been a challenging problem owing to the complex wake structure behind the rotor. Past experience has shown that accurately predicting BVI noise depends strongly on the tip vortex characteristics like vortex core size, peak swirl velocity of the vortex and the tip vortex geometry during the interaction [71]. Another key parameter determining accurate noise prediction is the blade aeroelastic deflection [74]. Modifications to the rotor characteristics such as the tip Mach number, blade planform etc. result in significant changes to the tip vortex characteristics and hence further complicate the accuracy of the prediction.

Approaches to study the simplified BVI problem in a controlled environment by decoupling the interacting vortex from the rotor parameters and blade geometry have been useful, albeit limited in their scope. Most previous experiments have been focused on the parallel BVI situation. Moreover, the vortex generated in the wind-tunnel is somewhat larger compared to the typical tip vortex undergoing BVI, resulting in lower frequency content. These experiments have mostly focused on the peak noise direction, and have not covered azimuthal variation.

The primary objective of the present study is to simulate BVI through the interaction between the rotor blade and controlled gust which replicates the key features and governing param-



eters of the vortex induced velocity in a hover environment. This Blade-Controlled Disturbance-Interaction, termed the BCDI, is the primary focus of the present study. The experimental facility needed to achieve this objective is built from the ground up. The controlled disturbance is provided in the form of a gust field with a velocity profile tailored to replicate that of a typical tip vortex. The first objective therefore, is to design and fabricate a “gust generator” that outputs a disturbance field that replicates the impulsiveness and the induced velocity profile of a typical tip vortex. The gust field needs to be well-characterized and have a relatively low turbulence to ensure repeatability. The nozzle should also be orientable at any angle with respect to the rotor blade to simulate oblique interactions and to match realistic trace Mach number.

The rotor stand built for the experiment consists of a single-bladed, non-lifting to reduce the complexity of the problem. It has the capability to spin at full-scale tip Mach numbers in order to accurately scale the acoustic phenomena. The large acoustic chamber present at the University of Maryland is used for the experiment. A set of tests were conducted to check the reflection characteristics within the chamber. The chamber was then treated with acoustic material to improve the sound absorbing characteristics of the wall for the frequency range expected.

The ultimate objective is to study in detail the acoustics of the BCDI at different tip Mach numbers and interaction angles and identify the radiation characteristics, including directionality for different trace Mach numbers. This will help identify the key parameters affecting the noise radiation. As mentioned earlier, in order to achieve oblique interaction angles, the nozzle of the gust generator is orientable with respect to the blade. Furthermore, to obtain the detailed directionality information acoustic data is recorded at several microphone locations around the chamber.

Another objective of the present research is to study the effect of spanwise phasing on the radiated noise and directionality trends. In order to study contribution of the spanwise blade sections a lifting line approach combined with unsteady indicial aerodynamics and Farassat's formulation 1A for calculating the acoustics is used. This approach will be useful in helping design quieter rotor blades.

## Chapter 2

### Approach

#### 2.1 Experimental BVI Simulation — The BCDI Experiment

This chapter explains in detail the fundamental ideas behind the experimental approach used in this study along with the experimental setup and the associated theoretical modeling to understand the fundamental physics behind the BVI acoustics.

As described in the previous chapter, predicting BVI noise involves two steps:

1. Estimating the unsteady aerodynamic loads on the blade due to the tip vortex interaction and
2. Estimating the radiated acoustics resulting from the changes in blade aerodynamic loads.

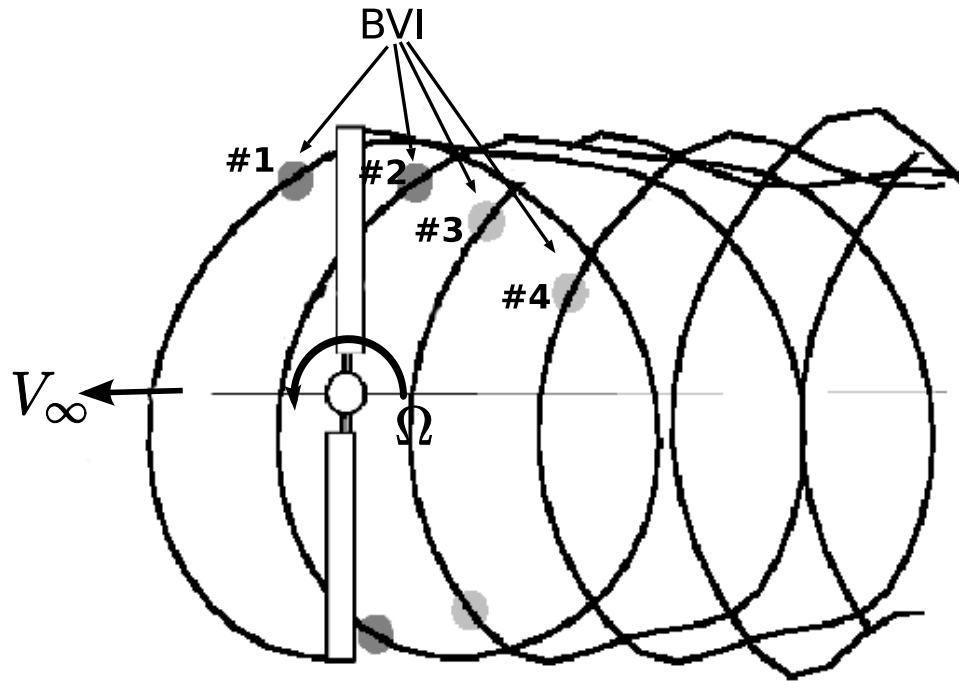
The first step of the approach enumerated above is extremely complicated owing to the tightly coupled nature of the helicopter blade aerodynamics to the wake structure.

The approach detailed in this dissertation is to study the BVI problem by decoupling the vortex characteristics from the rotor characteristics. This simplifies the problem significantly and allows

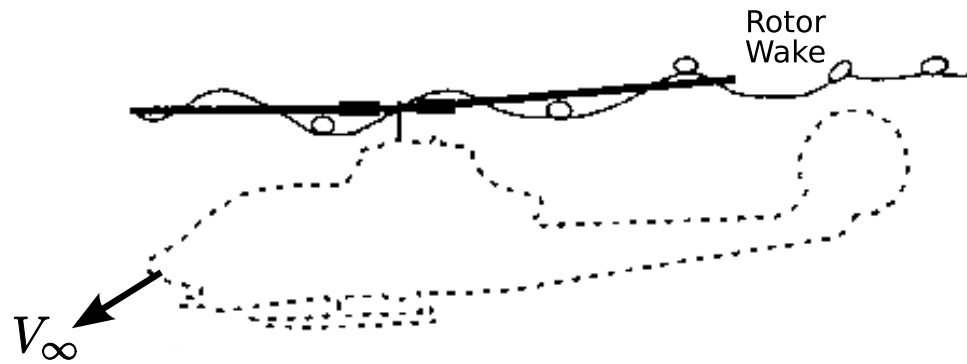
studying the blade response to a fixed velocity field that simulates a vortex of known characteristics. This in turn, allows the comparison of the acoustic response of the rotor blade to changes in blade planform and other features. In the present experiment the tip vortex is simulated by an independently controlled velocity field which is not dependent on the characteristics of the rotor being tested. This controlled velocity field is tailored so as to match the essential tip vortex characteristics responsible for BVI. A crucial hypothesis this approach is based on is that the unsteady blade aerodynamic response to the controlled velocity field is similar in character to the response during an interaction with a real tip vortex. This simulated BVI experiment is thus referred to in the dissertation as the Blade Controlled-Disturbance Interaction or BCDI.

Fig 2.1 shows the top and side view of a two bladed helicopter rotor exhibiting blade-vortex interaction. The top view (Fig. 2.1(a)) clearly suggests that the rotor blade passes near multiple vortices during one revolution and that each interaction is strongly dependant on the angle the blade makes with the interaction vortex. This interaction angle, combined with the tip Mach number of the blade and the advance ratio determines the three-dimensional geometry of the interaction, and hence plays a crucial role in the BVI noise generation process [22, 86]. The side view of the schematic (Fig. 2.1(b)) shows the vertical distance between the vortex and the rotor blade — usually referred to as the miss distance. The miss distance determines the velocity field induced by the vortex on the rotor blade section, and hence the unsteady aerodynamics during the interaction. In experimentally simulating a blade-vortex interaction it is important to faithfully replicate the both the induced velocity field as well as the overall three-dimensional geometry of the interaction.

If one were to consider a near parallel interaction, the BVI aerodynamics is mostly two-



(a) Top View of a Helicopter In BVI



(b) Side View of a Helicopter in BVI

Figure 2.1: Helicopter BVI geometry for a two-bladed rotor

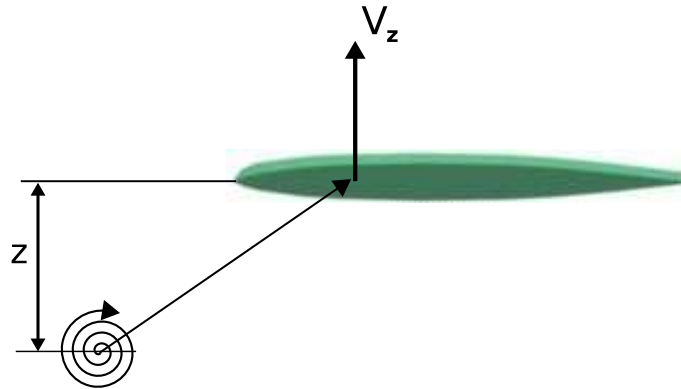


Figure 2.2: Two-dimensional schematic of the BVI

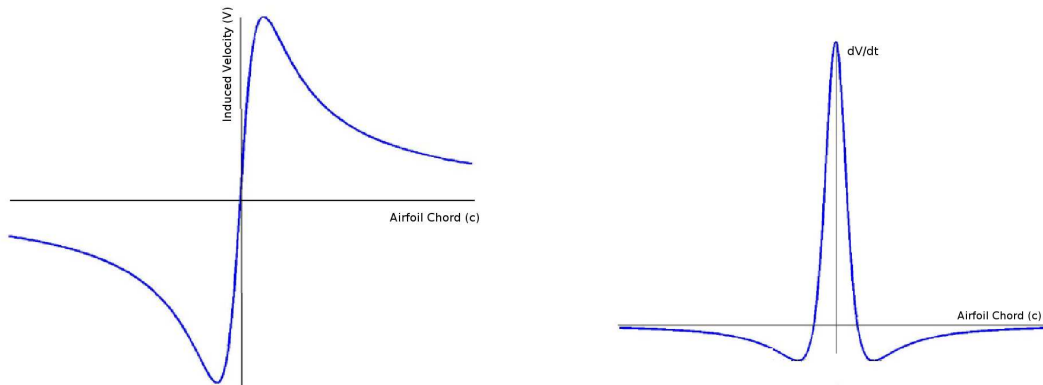


Figure 2.3: Typical vortex induced velocity profile and its gradient

dimensional (Fig. 2.2) inboard from tip of the blade. A sketch of the two-dimensional chord-wise cross-section of a typical vortex induced velocity profile at the quarter chord location along with the gradient of the velocity profile with time is shown in Fig. 2.3. A rapid change in induced velocity occurs as the blade passes near the vortex and results in sharp changes in blade aerodynamic loads (Fig. 2.4). This sharp change induces a reactionary changing pressure on the fluid as per the loading term of the Ffowcs-Williams and Hawking's equation (Eqn. 1.6 on pg. 24). A part of this changing pressure propagates outwards as a radiated impulsive pressure pulse.

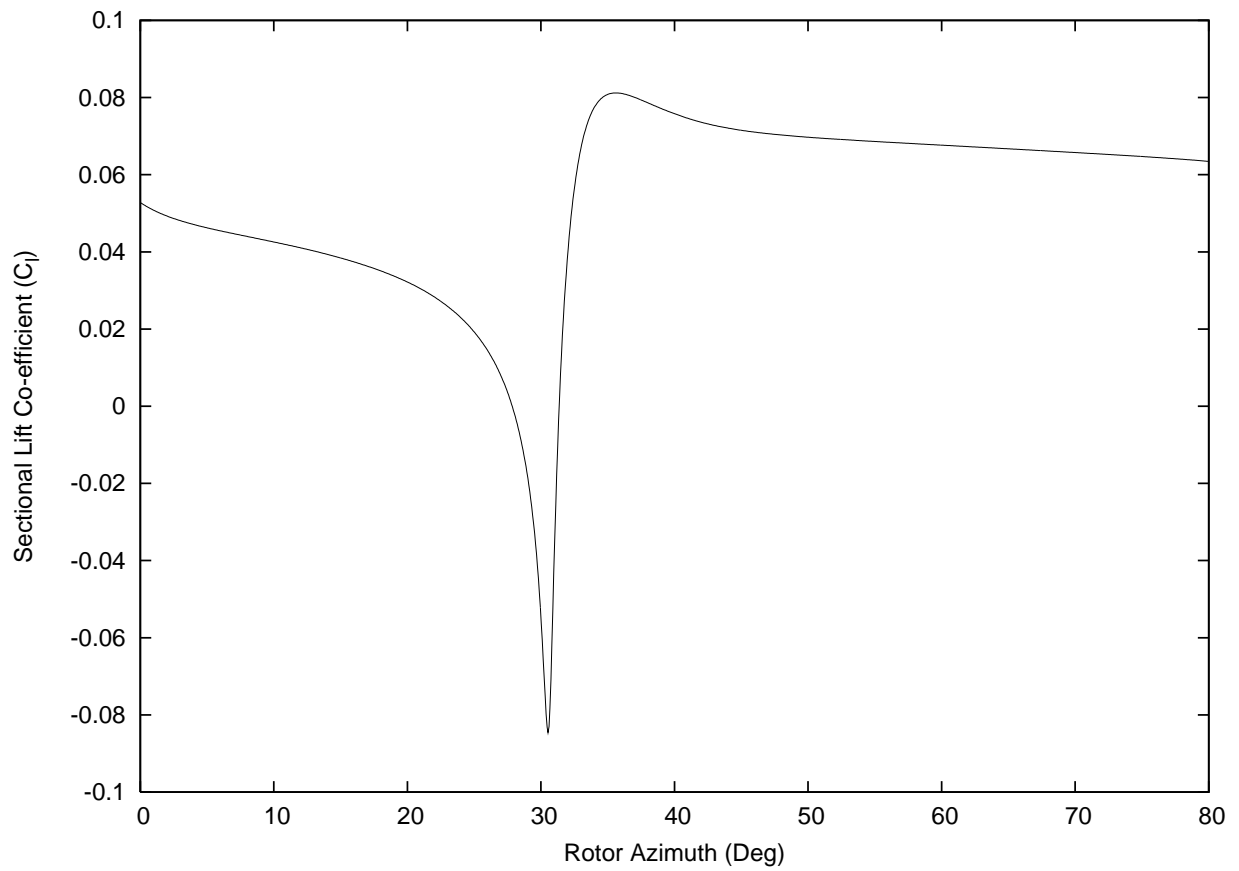


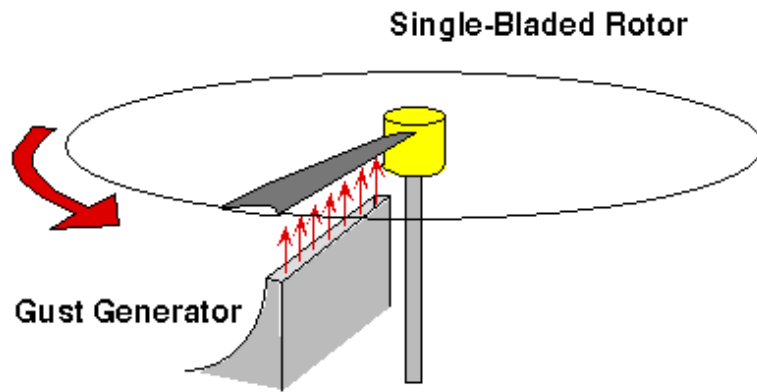
Figure 2.4: Sectional lift coefficient induced by a vortex on the airfoil

Since BVI noise is primarily a result of the unsteady lift – which is caused by the vertical component of the vortex induced velocity – only the component perpendicular to the rotor plane has been simulated at this time in the BCDI experiment. The important characteristics required to replicate the impulsiveness of the problem are: (i) the magnitude of the peak induced velocity and (ii) the gradient of the induced velocity. In the present BCDI approach, a controlled vertical velocity field is provided in the form of a gust located at a fixed azimuthal position with respect to the rotor (Fig. 2.5(a)).

The nozzle of the gust generator is designed so that the key vortex velocity characteristics, viz. the vertical velocity gradient (which defines the impulsiveness of the problem) and the peak velocity, are replicated. Unfortunately, in this simulation approach it is not possible to replicate the negative portion of the vortex induced velocity. However, the fundamental nature of the problem remains unchanged as the impulsiveness can still be sufficiently replicated. The three-dimensional geometry of the interaction is matched by orienting the gust at different angles with respect to the blade. The gust when oriented parallel to the blade replicates a parallel Blade-Vortex Interaction, while an oblique interaction with a straight line vortex is replicated by orienting the gust at an angle with the blade. However, it should be noted that in a real BVI, the tip vortex filament undergoing the interaction with the blade is curved (Fig. 2.1(a)) and not straight. This can be achieved by using a curved nozzle and is left for future work (Fig. 2.5(b)).

Apart from the vortex vertical velocity characteristics and geometry, it is also important to match the rotor characteristics to scale the phenomenon faithfully. In real BVI conditions the helicopter is almost always in forward flight and most often in mild descent. As discussed earlier, in

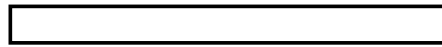




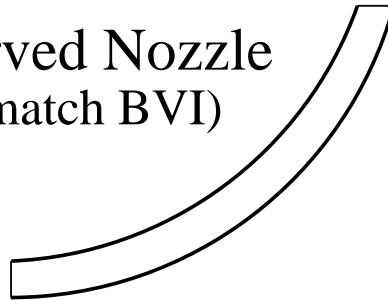
(a) The BCDI approach

## TOP VIEW

Straight Nozzle



Curved Nozzle  
(to match BVI)



(b) Straight and curved interaction with different nozzle shapes

Figure 2.5: Schematic of the experiment

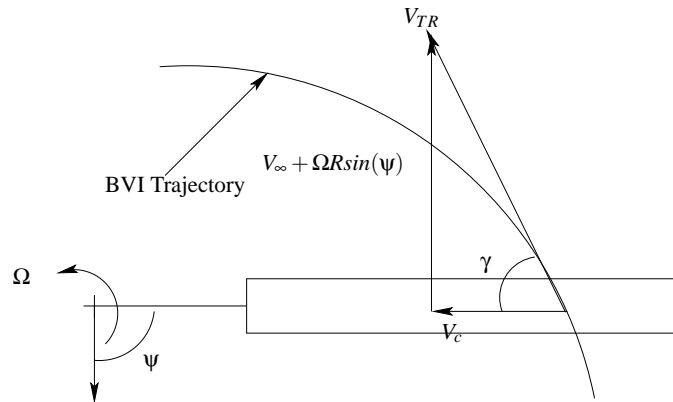


Figure 2.6: Trace Mach Number of BVI

order to carefully control the interaction parameters, the present experiment is conducted in hover. Thus it is difficult to precisely match the spanwise variation in velocity during the interaction. However, for problems that depend on wave collection processes, it is very important to match the tip Mach number of the blade. Therefore, the tip Mach number of the hovering rotor in the experiment has to be matched to the advancing tip Mach number of the rotor in forward flight undergoing BVI. An important point to remember is that the interaction geometry resulting from the epi-cycloid like pattern laid out by the tip vortices in space, is a result of the forward speed combined with the hover tip Mach number of the rotor. When the rotor blade sweeps over the tip vortex (Fig. 2.6), it can be considered as a series of two-dimensional interactions, each of which radiate noise in the medium. The rate at which these “sectional acoustic sources” sum in the medium is critical to the resulting phasing and hence the strength and directionality of the radiated noise. The velocity of these “sectional sources” non-dimensionalized with respect to the speed of sound is termed the trace Mach number. The trace Mach number is given by the following

equation:

$$M_{TR} = \frac{\Omega r(\mu + \sin \psi_b)}{a_0 \sin \gamma} \quad (2.1)$$

While the acoustic phasing along the rotor plane is determined by the trace Mach number profile, the actual three-dimensionality of aerodynamics is determined by the interaction geometry.

## 2.2 The Assembled Experimental Setup

Fig. 2.7 shows the layout of the experiment along with the additional acoustic treatment (melamine wedges) and microphone positions inside the chamber. The rotor stand is positioned to one side of the chamber in order to maximize the distance from the rotor hub to the microphone locations. The fan-blower of the Gust Generator is placed outside the chamber to reduce extraneous noise sources inside the chamber. The nozzle of the Gust Generator is placed vertically below the rotor stand as seen in Fig. 2.8.

## 2.3 Experimental Design and Calibration

The experimental setup consists of many components (see Fig. 2.9), each of which was developed and tested, including the “Gust Generator”, the Rotor Test Stand, and the Acoustic Chamber alongwith their respective instrumentation. The following sections describe in detail the various components of the setup.

A schematic of the hardware necessary to perform this experimental BVI simulation is shown in Fig. 2.10. The hovering rotor stand along with the gust generator is placed in an acoustic chamber.

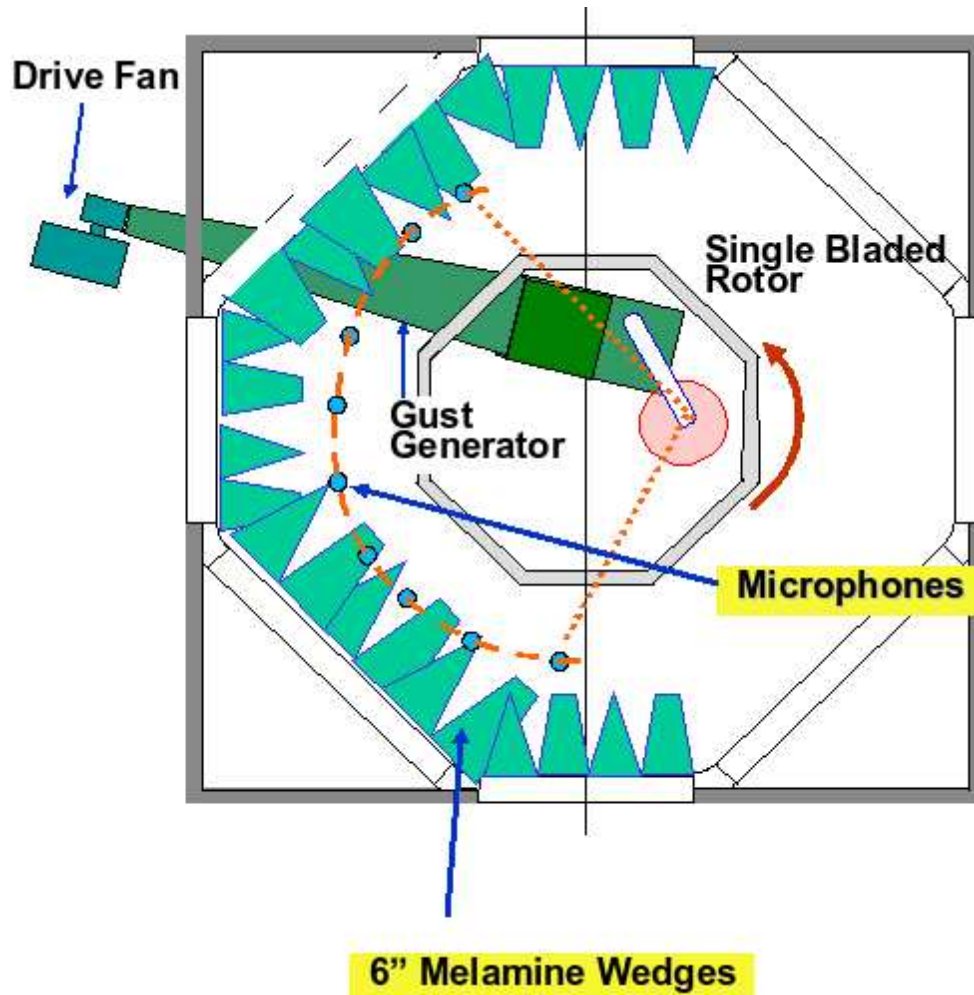


Figure 2.7: Layout of the different components inside the acoustic chamber

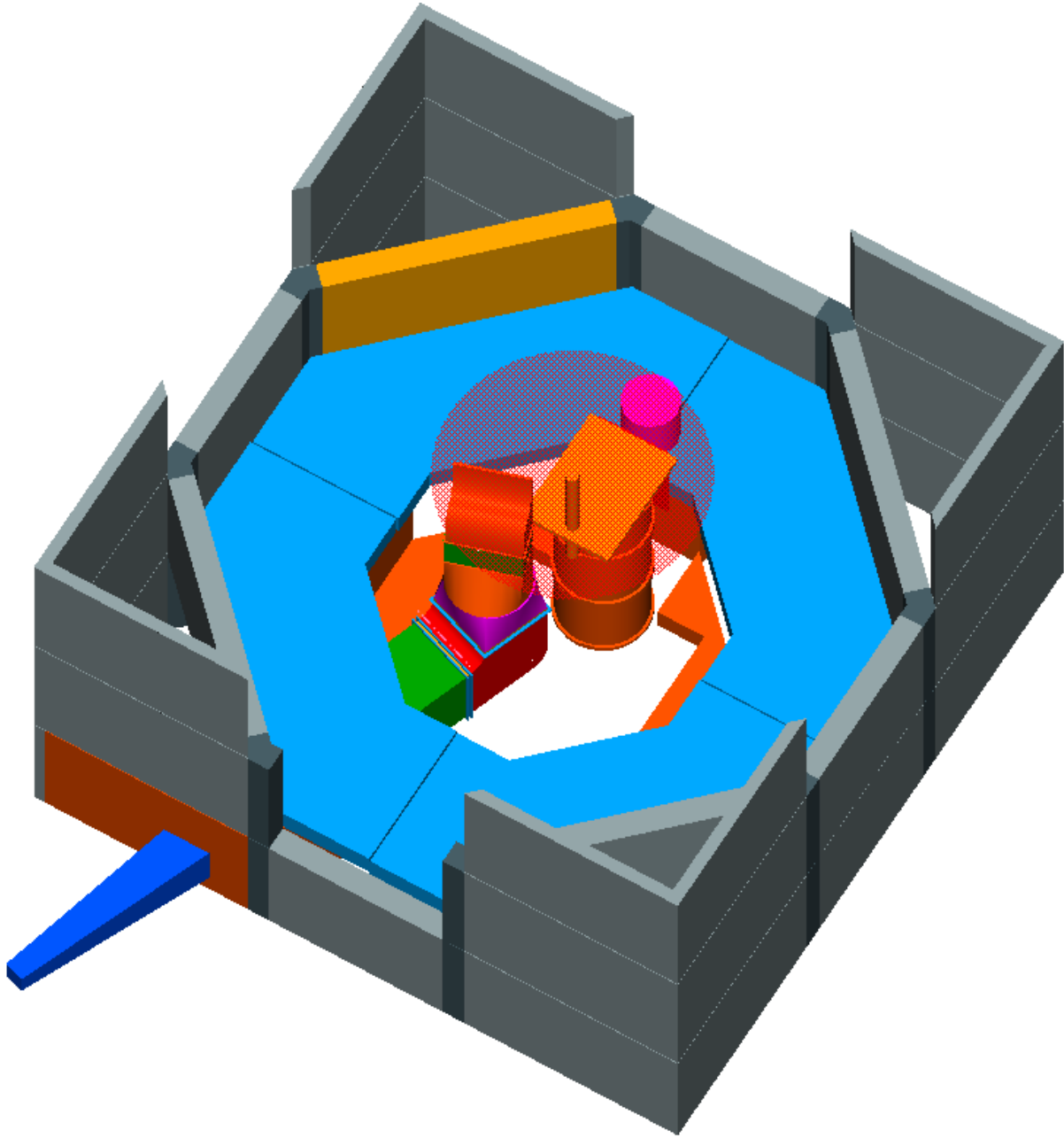


Figure 2.8: Schematic of the final assembled experimental setup

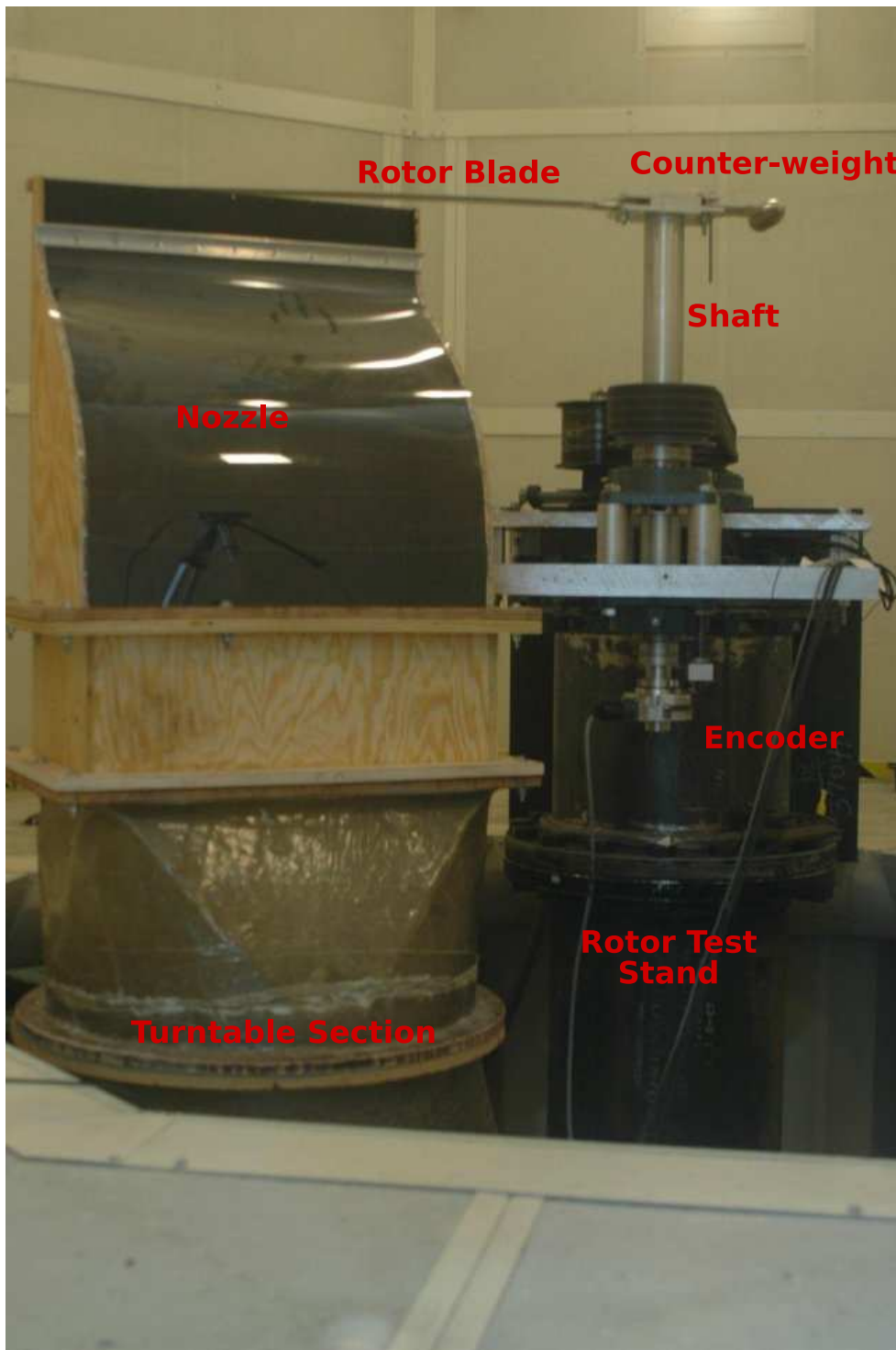


Figure 2.9: Photograph of a portion of the experimental setup inside the chamber

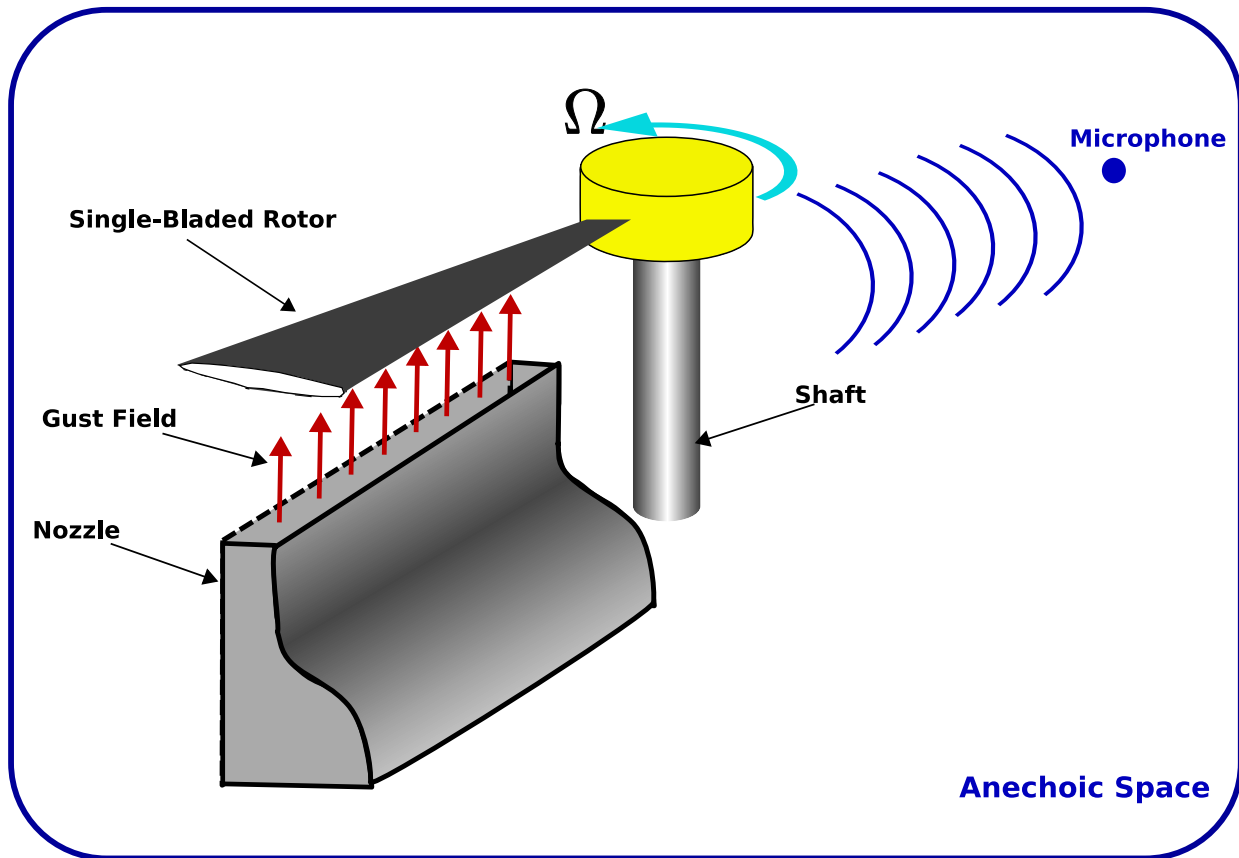


Figure 2.10: Schematic of experimental setup

While the acoustic chamber was already available at the beginning the program, the other critical components have been developed and tested in-house as a part of this experiment.

### 2.3.1 The Gust Generator

The “Gust Generator” shown in Fig. 2.11 is a critical part of the BCDI setup. It is basically an open jet wind-tunnel with a specially designed nozzle so that the obtained velocity profile at the blade-passage section mimics a vortex induced profile. The gust generator consists of various sections, each performing a certain function in obtaining a specially tailored low turbulence jet at

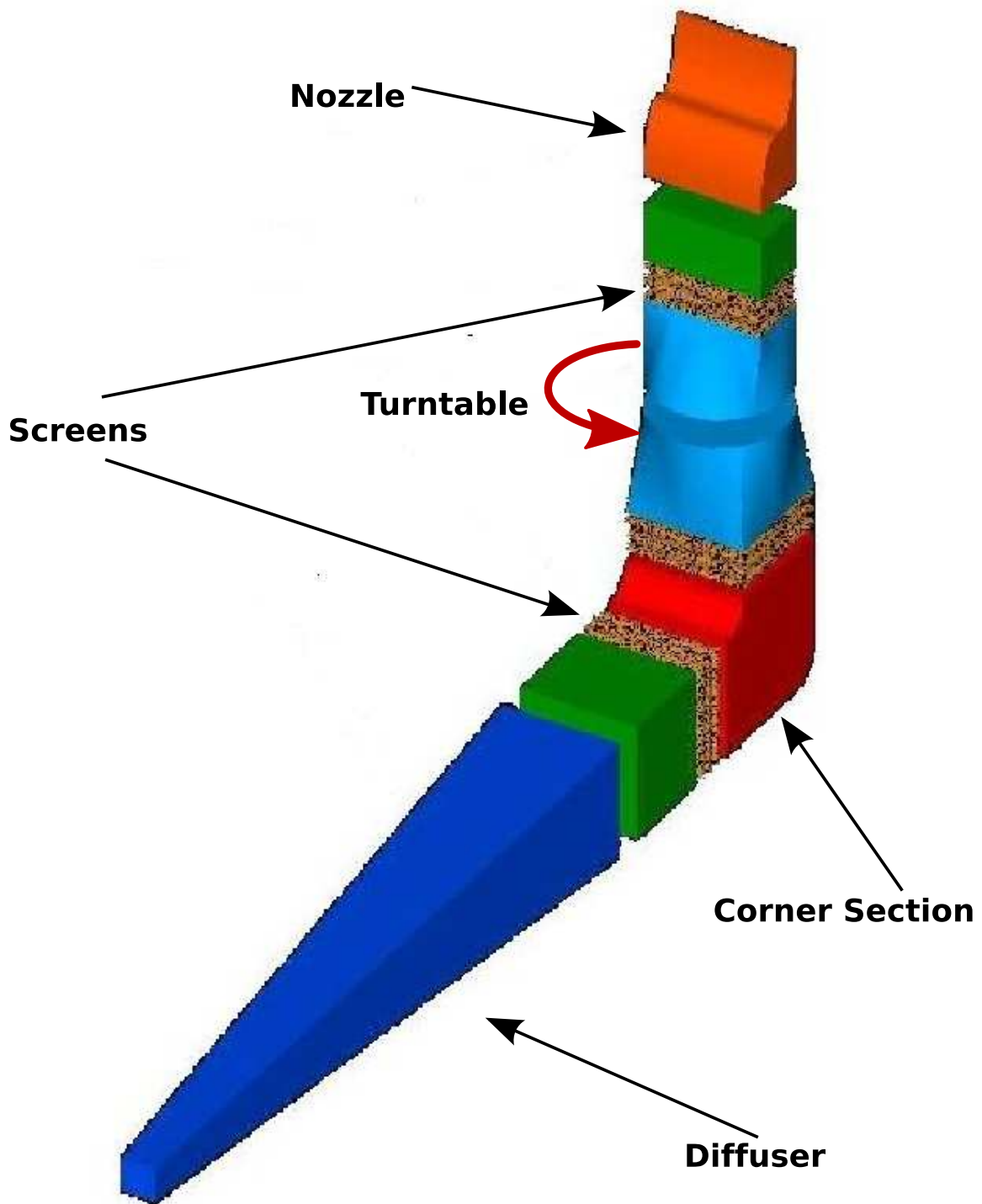


Figure 2.11: Schematic showing different sections of the “Gust Generator”



the blade passage location. An important requirement was the ability to orient the nozzle at any angle with respect to the interacting blade to simulate oblique interactions. This is achieved with the help of the turn-table sections which share a circular cross-section. The details of the key parts of the “Gust Generator” are given in Appendix A.

The most important section of the gust generator is the nozzle, which has been designed based on the concept of free jet mixing. As mentioned previously, the nozzle simulates the vertical velocity field of the vortex by attempting to replicate the asymmetry of the vertical velocity component. To provide vertical flow-field asymmetry, the curved wall was built shorter than the flat wall, as shown in Fig. 2.12. This results in greater mixing on the curved wall, thus smoothing out the flow and resulting in a reduction of the velocity gradient on the curved side. For a free jet, the jet width is proportional to  $1/l$ , where  $l$  is the mixing length. As the mixing width on the curved side is greater than that on the flat wall of the nozzle, the flow diffuses and spreads out to a greater extent on the curved side than on the flat side, resulting in an asymmetric flow profile as seen in Fig. 2.13(a). Since the main feature of the flow is the sharp rising edge, the classical technique of boundary layer suction was employed to control the velocity gradient on the flat side. Slots were made on the flat side (Fig. 2.12) to provide boundary layer suction, further increasing the gradient of the velocity on the flat wall side.

### **Mean Flow Characteristics**

A set of measurements were performed at three positions along the length of the nozzle, viz.  $y = 0.25L$ ,  $y = 0.5L$  and  $y = 0.75L$  to ensure the uniformity of the flow across the nozzle

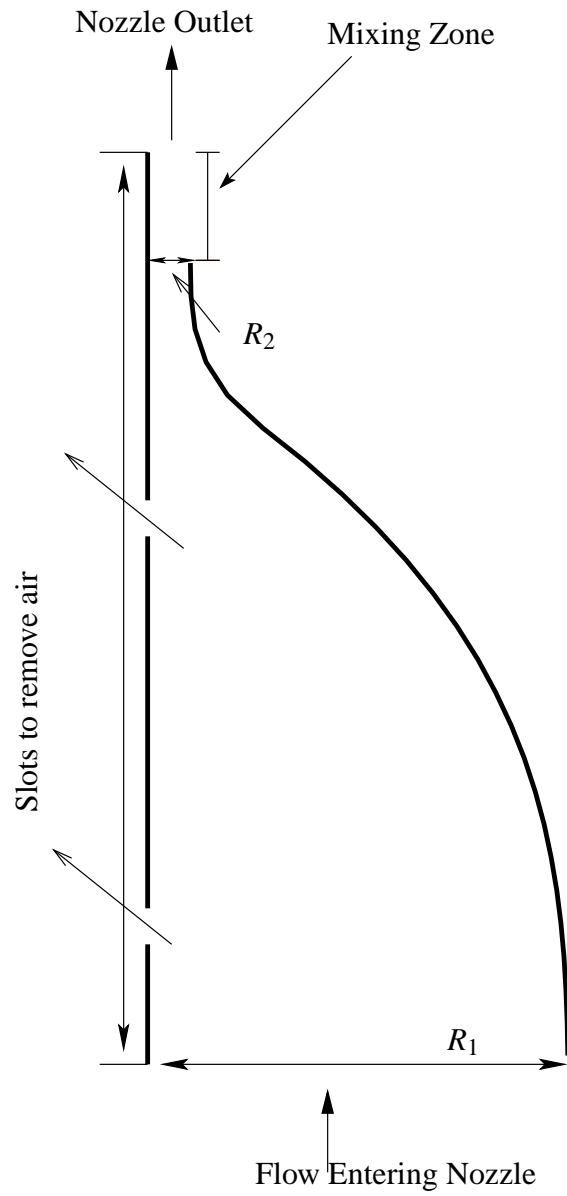


Figure 2.12: Schematic of the final nozzle design

length. Fig. 2.13 shows the mean vertical and chordwise velocity components ( $w_m$  and  $u_m$ , resp.) measured at each location. A second set of measurements were performed at different heights above the nozzle at the mid-point locations ( $y = 0.5L$ ), viz  $z = 0.625$ inches,  $0.875$ inches and  $1.275$ inches (Fig. 2.14). These data were taken with a calibrated two-component hotwire probe. The main character of the flow-field necessary for replicating BVI is clearly shown. The span-wise variation in velocity is seen to be almost negligible. As the height of blade passage location above the nozzle increases, the flow starts diverging on the flat side of the nozzle, decreasing the slope of the rising edge of the velocity profile. This suggests that an optimal height exists for simulating a chosen BVI.

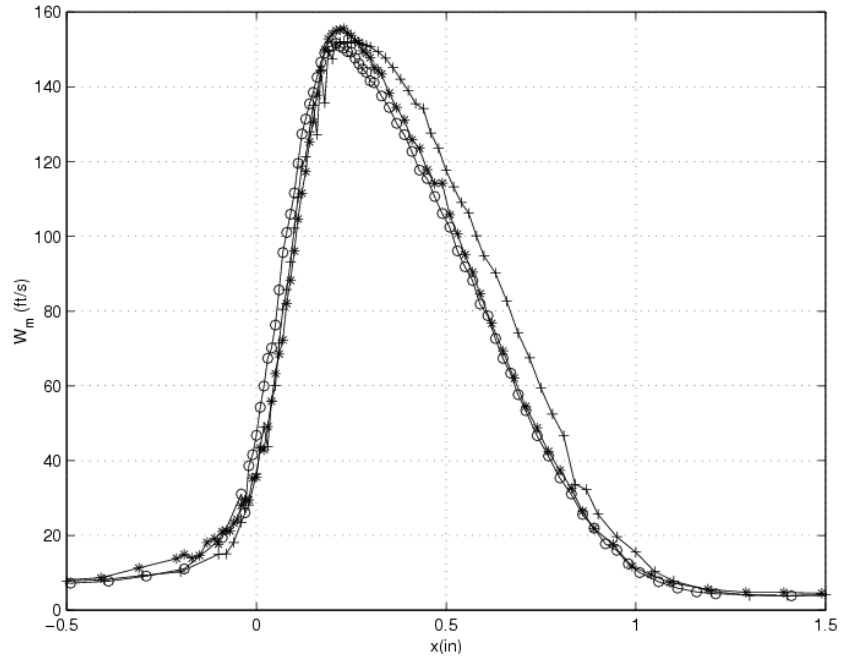
The various other sections constituting the gust generator along with detailed turbulence measurements of the flow are described in Appendix A

### 2.3.2 Comparison of Gust to Vortex Induced Velocity Profile

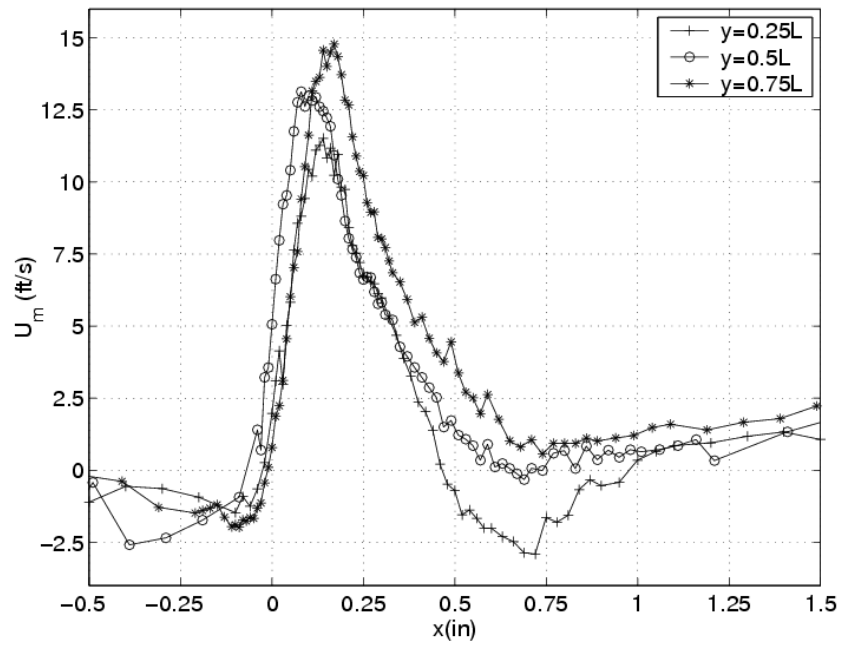
To complete the comparison, it is useful to know the type of BVI and the equivalent vortex characteristics being simulated by the present B-CD-I experiment. For the present nozzle, the event that is chosen to set the strength of the vertical velocity field is a parallel BVI.

The following analysis can be used to establish some of the equivalent vortex characteristics that are simulated. Using Biot-Savart Law, we know that for a parallel BVI, the induced velocity on the blade is given as,

$$w = \frac{\Omega R C_t}{\pi \sigma} \frac{z_h}{z_h^2 + r_c^2} \times \left( \frac{\frac{x}{z_h}}{1 + \left(\frac{x}{z_h}\right)^2} \right) \quad (2.2)$$

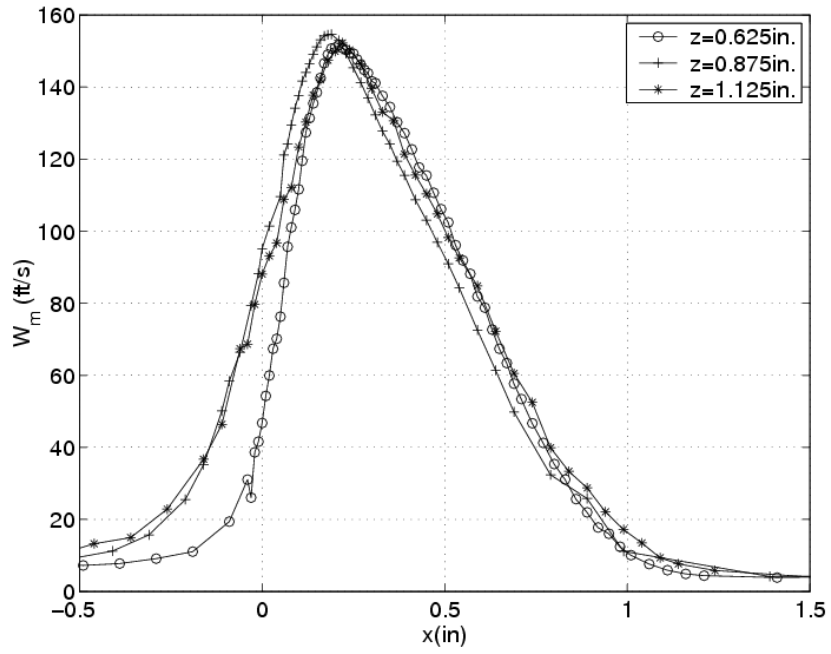


(a) Vertical velocity component( $W_m$ )

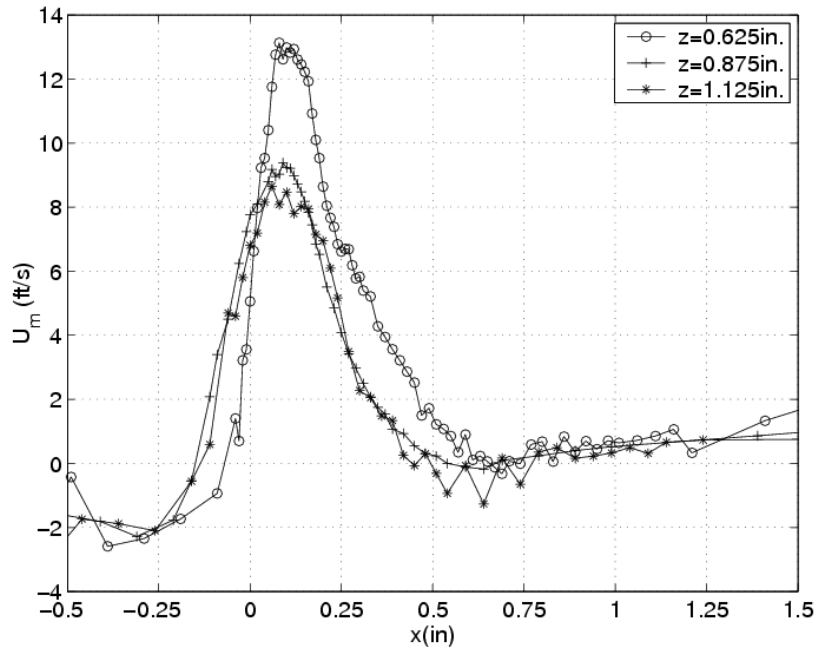


(b) Chord-wise velocity component( $U_m$ )

Figure 2.13: Variation of velocity distribution across the span of the nozzle



(a) Vertical velocity component ( $W_m$ )



(b) Chord-wise velocity component ( $U_m$ )

Figure 2.14: Variation of velocity distribution with height above the nozzle

Differentiating Eqn. 2.2 and equating to zero, we get  $x_p$ , the point where  $w$  peaks as,

$$x_p = z_h \quad (2.3)$$

This gives,

$$w_p = \frac{\Omega R C_t}{\pi \sigma} \frac{z_h}{z_h^2 + r_c^2} \quad (2.4)$$

Since we are trying to achieve equivalence between the interaction in the hover experiment and the real BVI events, we can idealize the velocity obtained with the nozzle at the blade passage location to be represented by Eqn.2.2. For the gust generator case, the peak velocity from Fig. 2.13(a) is 155.4ft/s, and occurs at  $x_p = 0.0572$  (non-dimensionalized w.r.t the blade chord). This is equivalent to a miss distance of 7% and the core radius of 5% of the blade chord signifying a strong BVI. It is possible to modify these equivalent vortex parameters by changing the gust peak velocity and by adjusting the height of blade passage above the nozzle. Fig. 2.15 compares the measured gust vertical velocity with the induced velocity due to such a vortex. It is observed that the peak and gradient of the vortex induced velocity and the gust match closely. However, the tail of the gust falls off more rapidly than the vortex induced velocity. The impulsive noise from the BVI primarily results from the rising edge of the velocity profile. Since this is closely replicated in the gust velocity field, it is assured that the main acoustic peak will be captured in the experiment. However, the steeper falling edge in the gust velocity field will result in a change in the character of the acoustic pulse.

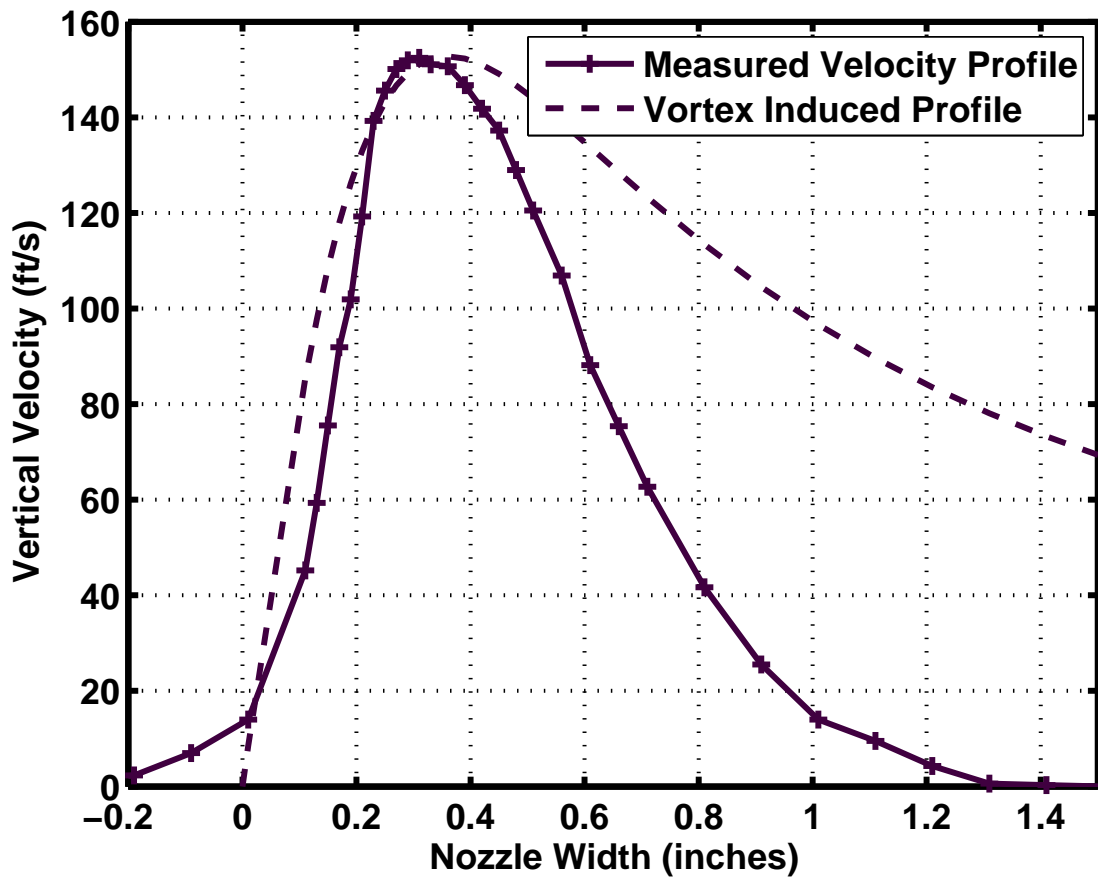


Figure 2.15: Comparison of measured gust and vortex induced velocity

### 2.3.3 Rotor Test Stand and Operation

The rotor (shown in Fig. 2.9) is a rigid single-bladed counter-weighted 1:7 scale, untwisted, model UH-1H blade with the ability to spin to high RPMs. Having a single blade greatly reduces the chances of rotor-to-rotor aerodynamic interference, providing a cleaner experimental setup. Further, the blade is run at a small pitch angle ( $2^\circ$ ), resulting in a very small thrust in order to prevent the blade's wake from staying in the rotor plane. The blade is positioned to pass 1.62 inches above the outlet of the nozzle, close enough to maintain the simulated vortex characteristic, but far enough to minimize the interference effects of the nozzle. The whole setup is oriented so that the tip of the blade passes well within the gust field and hence is free of the three-dimensionality associated with the outer edge of the nozzle (Fig. 2.16). The inboard half of the blade, contributes little to the acoustic field as the Mach number is very small. Moreover, if the nozzle extended inboard, these blade sections could experience a high angle of attack resulting in stall. In order to avoid such complications, the inner edge of the nozzle is located at the 48% spanwise section of the blade.

The rotor stand is also instrumented with thermocouples on the bearings and accelerometers. The signals from these sensors are sampled 10 times every second and are constantly monitored to ensure the safety of the system. A magnet attached to the shaft of the rotor stand triggers a hall-switch once every revolution. There is also a 10bit quadrature encoder that provides 1024 pulses every revolution. Since this signal perfectly phase-locked to the shaft it is used to estimate the blade location accurately at any given time instant. Accelerometer recordings when striking the rotor test stand with an impact hammer were used to establish safe operating conditions. In particular, it was



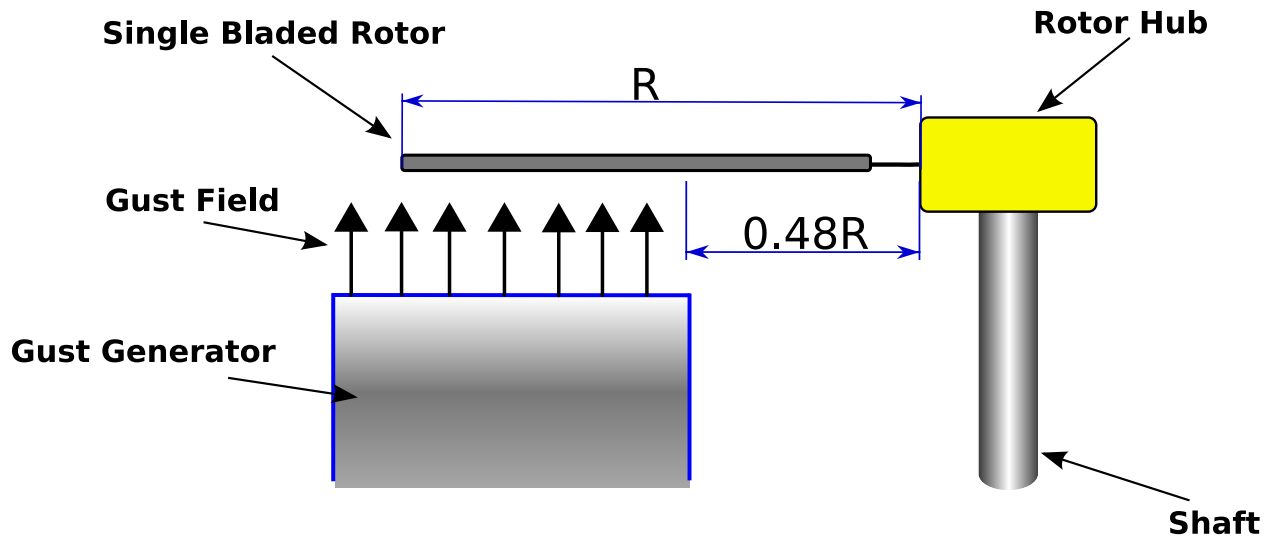


Figure 2.16: Schematic of the setup showing the relative positions of the gust and the rotor blade during interaction

found that the operating close to 2500RPM resulted in some vibrations in the rotor, and hence was avoided for the experiment (see Appendix B). A summary of the rotor operational characteristics is presented in table 2.1.

### 2.3.4 Acoustic Chamber

The acoustic chamber is an octagonal chamber that is 20ft×20ft wide and 30ft tall. The walls of the chamber consist of 8inches of fiber glass sandwiched between two metal plates. The metal plate on the inside of the chamber is porous. This construction is mainly designed to prevent external noise from contaminating the acoustic environment, but also has limited acoustic treatment (the fiber glass) to minimize wall reflections within the chamber. The relatively small size of the chamber implies that it is not ideal for testing low-frequency noise sources. The thickness of the

1:7 scale untwisted UH-1H single-bladed rotor	
Blade airfoil	NACA 0009
Airfoil chord	3 inches
Blade radius	38.75 inches
Blade pitch angle	-2°
Max. rotor RPM	2640 RPM
Max. tip Mach number	0.77

Table 2.1: Some key characteristics of the rotor

fiber-glass filled chamber walls result in a cutoff frequency of about 500Hz. While this frequency is acceptable for the BVI experiment, it was also found that the walls were not sufficiently absorptive and tended to reflect significant amount of the impulsive noise.

A test was designed to estimate the amount of sound reflected by a high frequency noise pulse with the aim of improving the chamber characteristics. A speaker was placed close to the expected interaction location and an impulsive signal generated by a function generator was fed to it through an amplifier. The fed signal was chosen to match the frequency range expected from simulating the BVI experiment – 200Hz to 2000Hz.

Fig. 2.17 shows a representative example of the direct and the reflected acoustic pulses measured at one microphone location. The acoustic pressure measured at the microphone has been normalized by the maximum observed pressure, since we are only interested in relative magnitudes. The first reflection off the wall behind the microphone shows only a 33% (~2.5dB) reduction in peak-to-peak value. For a good acoustic experiment we require at least a factor of

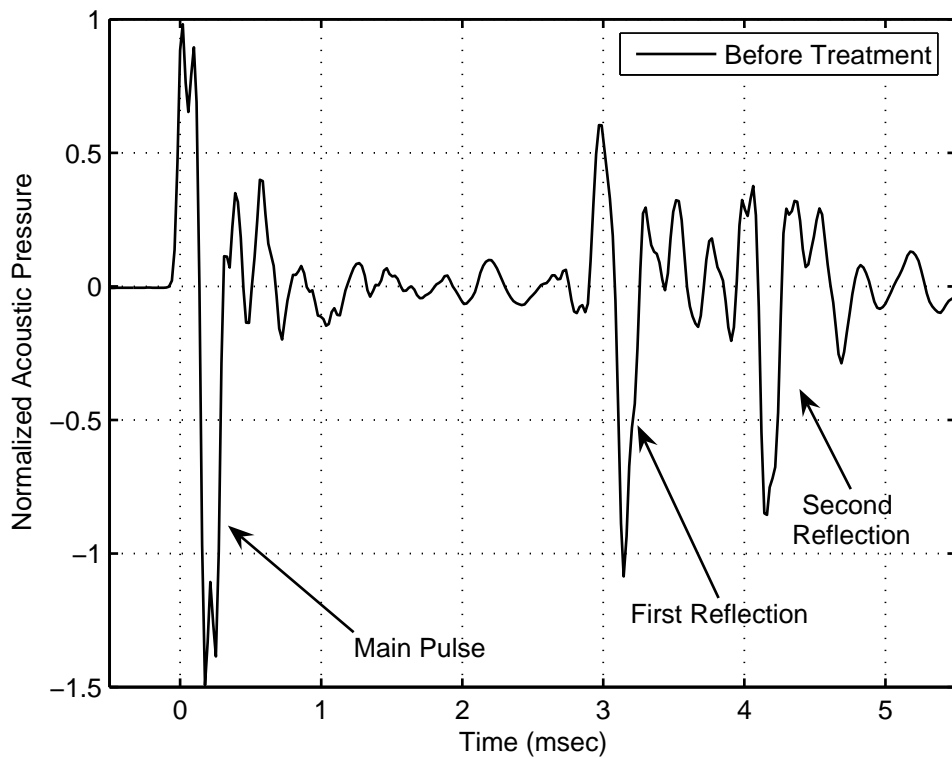


Figure 2.17: Reflection characteristics of chamber prior to treatment

three ( $\sim 9.5\text{dB}$ ) between the main signal and any reflected signals or background noise. In order to improve the absorption characteristic of the chamber various sound absorbing materials were tested on the chamber wall to decide on the ideal treatment option. Fiber glass panels of different thickness varying from two inches to six inches and two different types of foam with and without wedge shapes were tested. Finally, the six inch deep melamine foam wedges were chosen because they had the best absorption characteristic providing a ratio 5 ( $\sim 14\text{dB}$ ) between the main pulse and the reflected pulse (Fig. 2.18). It was decided not use deeper wedges as it would overly reduce the measurement space available in the chamber.

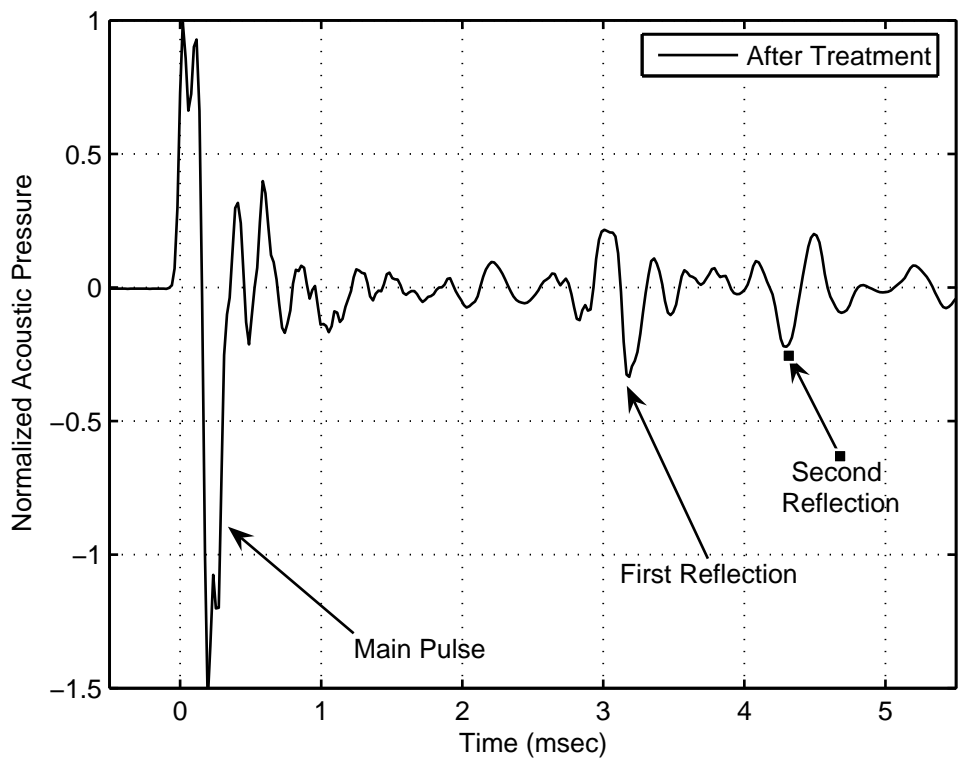


Figure 2.18: Reflection characteristics of chamber after acoustic treatment

### **2.3.5 Microphone Measurement System**

The chamber is instrumented with a vertical microphone array consisting of four 0.5 inch B&K microphones placed at various elevation angles. The microphones are mounted on a traverse that can be moved to different azimuthal locations, with respect to the rotor hub, allowing the measurement of the directional nature of the acoustic field. Figs. 2.19 and 2.20 shows the top and front view of different microphone locations used to obtain data during the course of the experiment. It is known that for a parallel interaction the peak azimuthal directivity of the noise is about a perpendicular line drawn from the 75% span section of the rotor blade at the interaction. This is close to 104° azimuth microphone location. The other microphones were placed about 10°–15° apart from each other one either side of the peak azimuth location. The microphones vary from 2.8R to 3.5R in distance from the hub and can be considered to be in acoustic far-field for the experiment. It should, however, be noted that this distance is not ideal, but acceptable because the BCDI events occur only over half the blade span.

### **2.3.6 Data Acquisition and Reduction Technique**

The data for the four microphones were obtained simultaneously using a 16 bit data acquisition system sampled at 50kHz and triggered by a 1/rev hall sensor mounted on the rotor stand. The 1024 pulses per revolution signal from the encoder mounted on the rotor shaft is also simultaneously recorded. As mentioned earlier this can be used to provide the azimuthal location of the blade at any instant of time to 0.35° accuracy.

For each microphone data is recorded for close to 100 rotor revolutions after an initial start up

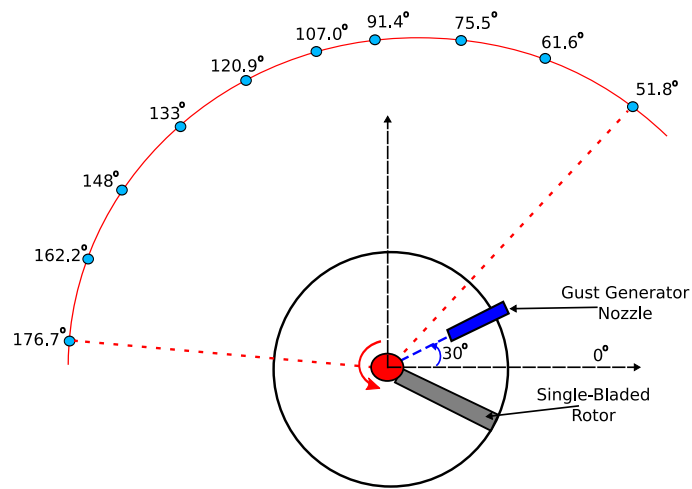


Figure 2.19: Top view of microphone measurement locations

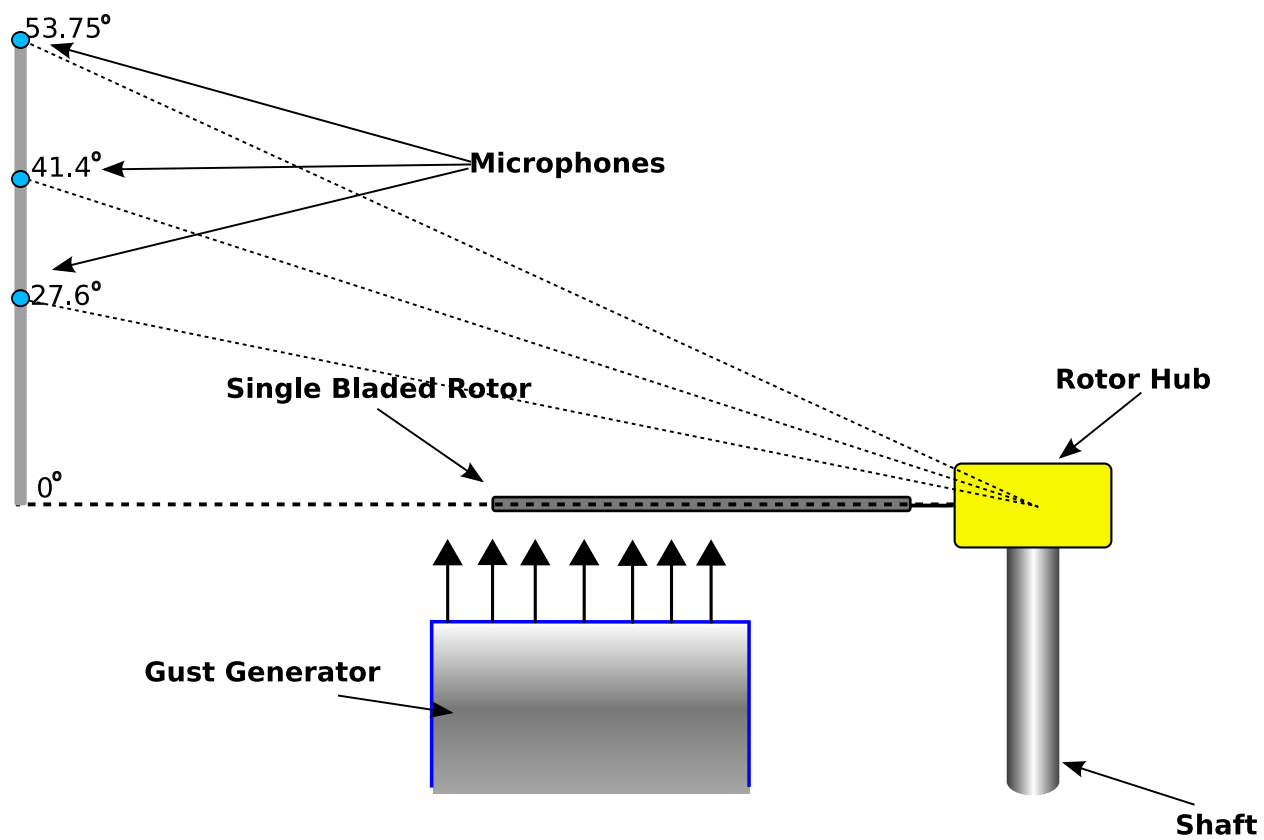


Figure 2.20: Side view of microphone measurement locations

Rotor RPM	1950	2108	2260	2410	2640
tip Mach Number	0.569	0.614	0.659	0.702	0.768

Table 2.2: Tip Mach numbers tested

period to let the flow transients die down. However, because power fluctuations and the accuracy of the motor controller, the rotor RPM is not always constant over this time period. The fluctuation in RPM is  $\pm 2$  RPM about the nominal value. In order to perform the averaging the 1024 pulse per revolution signal is used to add the acoustic time history corresponding to the correct blade location. This is very accurate since the encoder is fixed to shaft and records the variations in RPM faithfully. The microphone data corresponding to time samples in between two successive pulses are obtained by interpolation. The correct acoustic time histories are then summed over 80 such revolutions and averaged.

## 2.4 Experimental Cases Studied

A controlled experiment such as this one, offers the possibility of wide variation in parameters. A total of five rotor tip Mach numbers (Table 2.2) were studied. At each of these tip Mach numbers four different interaction geometries (discussed below as Cases 1-4) were studied.

### 2.4.1 Case 1 — Parallel BCDI

The first set of experiments performed were for the parallel interaction (Fig. 2.21(a)). Although perfect parallel Blade-Vortex interactions do not occur in a helicopter because of the curvature of



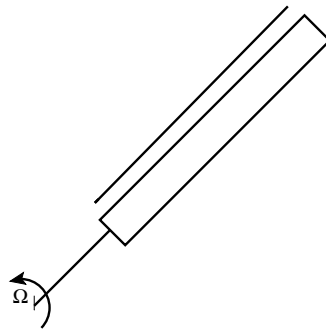
the tip vortex trajectory, near parallel interactions (Fig. 2.21(b)), where the trace Mach number is well above supersonic (Fig. 2.21(c)) over most of the blade span do occur and have very similar acoustic radiation characteristics to the parallel interaction.

The parallel BCDI performed in the acoustic chamber using the straight nozzle has an infinite trace Mach number through the entire blade span. Thus, it is more impulsive than the near-parallel (slightly curved) BVI. The testing with a slight curved nozzle to match the right trace Mach number profile for the near-parallel BVI is left for a future effort.

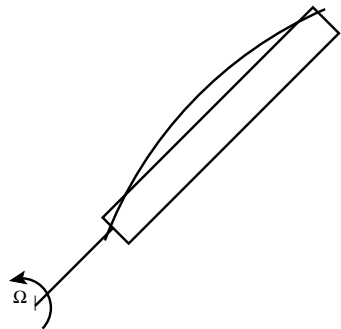
## **2.4.2 Oblique BCDI**

Most of the previous experiments on BVI in conducted in wind tunnels [64] have focused primarily on parallel BVIs. The experiment described in this dissertation takes the understanding of BVIs a step further with the ability to study oblique interactions. As mentioned earlier, the interactions are conducted with a straight nozzle. The oblique interactions in the current experimental setup are obtained simply by orienting the nozzle at the required angle with respect to the blade. This is achieved with the help of the two sections of the gust generator that share a circular cross-section (see Fig. 2.11) so that the top three sections including the nozzle can be rotated without affecting the flow through the nozzle.

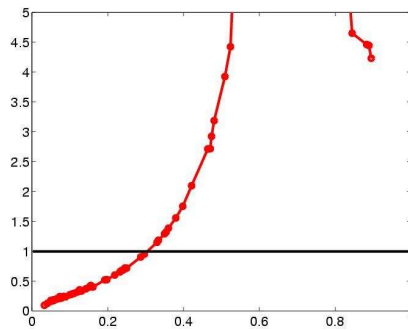
A set of three oblique interactions have been studied and are presented here. All the interactions start at the tip of the blade and sweep in-board as shown in the schematics. The result of this orientation is a decelerating trace Mach number profile, similar to the oblique interaction in Figs. 1.10(c) & 1.10(d) in Chapter 1. The trace Mach number variation determines the speed of



(a) Schematic of the parallel interaction in the experiment



(b) Schematic of a near-parallel BVI in the real helicopter



(c) trace Mach number profile for near-parallel BVI

Figure 2.21: Comparison of the parallel interaction in the experiment with a real BVI

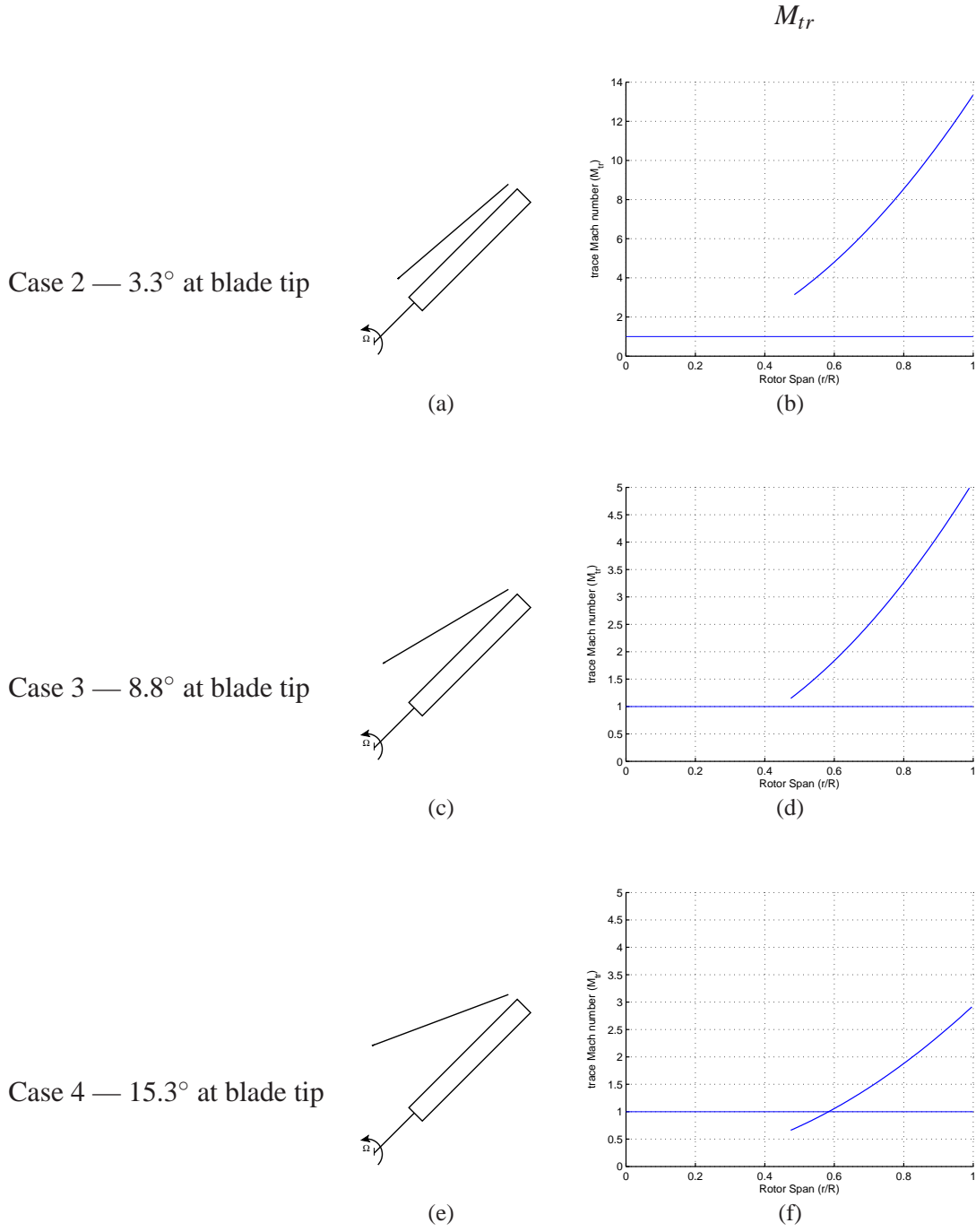


Figure 2.22: Schematic of the oblique interaction angles and corresponding trace Mach number profiles ( $M_T = 0.702$ )

the acoustic sources in the medium, and hence the phasing of the waves from these sources. This affects the radiation patterns in the plane of the rotor. For the real helicopter BVI, the trace Mach number profiles contain within them information about the advance ratio of the helicopter ( $\mu$ ) and the tip Mach number of the rotor. While the experiment is performed in hover, the trace Mach number profiles obtained by orienting the nozzle match similar conditions as in helicopter forward flight case.

## **Chapter 3**

### **Experimental Results**

The previous chapter discussed the experimental setup in detail. The number of possible parameter variations in this experiment is quite extensive. For the present dissertation, the parameter variations has been restricted to values that are closer to those that occur in real helicopter BVI situations. As discussed earlier, in the real BVI case, the trajectory of the interaction follows an epicycloid-like geometry, the nozzle in this experiment that is used to simulate the vortex induced velocity is not curved. However, the interaction between the rotor blade and straight gust captures most of the relevant physics with regards to the aerodynamics as well as the acoustics. This chapter covers the experimental results obtained during the study, beginning with parallel interaction and later discussing the oblique interaction angles.

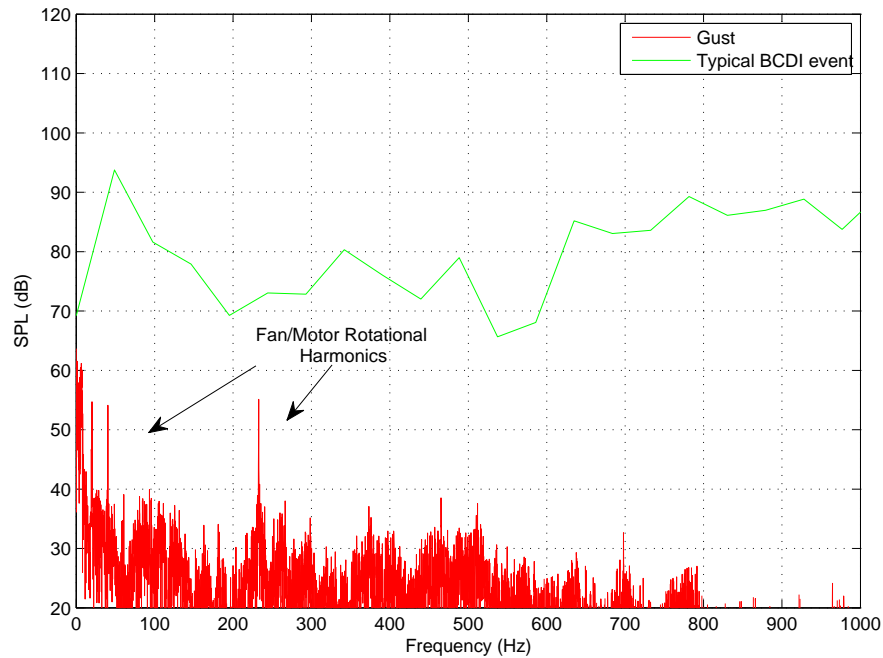


Figure 3.1: Power spectrum of the gust flow noise

## 3.1 Data Quality

### 3.1.1 Background Noise

Fig. 3.1 shows the acoustic power spectrum of the noise due to the gust flow from the nozzle inside the chamber at the microphone azimuth and elevation of  $129^\circ$  and  $53.75^\circ$ , respectively. The fan/motor powering the gust is spinning at close to 1210 revolutions per minute, resulting in a few harmonics associated with this frequency. Prominent are the first (20.22Hz), second (40.44Hz) and the eleventh (222.42Hz) harmonic, the last one being present because the fan has eleven blades. The total noise generated is less than 80dB. This is more than 20dB less than the noise of a typical BCDI pulse shown in the figure.

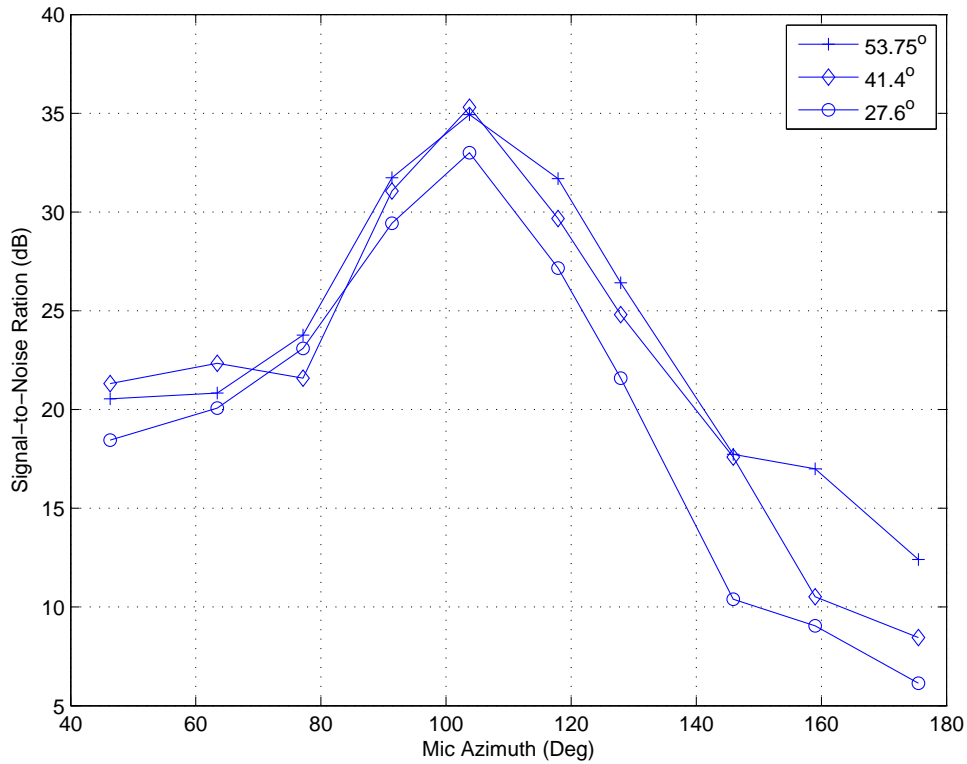


Figure 3.2: Ratio of main acoustic pulse to the first reflected pulse

### 3.1.2 Acoustic Pulse Reflection

Once the entire setup was assembled inside, the chamber was re-evaluated to check for unacceptable reflections at every microphone location used for the experiment using the method outlined in section 2.3.4. Figure 3.2 shows the ratio of peak-to-peak amplitudes of the direct acoustic pulse and the first reflection for each microphone. Except for the extreme azimuthal locations of the microphones ( $\psi > 140^\circ$ ) the ratio of the direct acoustic pulse to the first reflected pulse is greater than 15dB. Even at the highest azimuthal location the ratio is more than 10dB for the topmost microphone and the data at that location is therefore, quite reliable. Moreover, since the experiment

is run with a single-bladed rotor, the acoustic pulse reflected off the wall does not overlap with the acoustic pulse corresponding to the interaction event.

### **3.1.3 Repeatability of Acoustic Data**

Fig. 3.3 shows the revolution-to-revolution variation in the measured noise for the parallel interaction case at the topmost ( $53.75^\circ$  elevation) microphone placed at  $104^\circ$  azimuth at  $0.612 M_T$ . The figure shows instantaneous data from 80 revolutions plotted on top of each other along with the ensemble averaged data. The total variation in magnitude of noise from revolution to revolution is less than 5%. Moreover, azimuthal variation of the event is less than  $0.2^\circ$  corresponding to the time interval between successive samples recorded by the data acquisition system.

## **3.2 Noise radiation due to nozzle presence**

The presence of the nozzle very close to blade (1.62 inches below) results in some radiation of impulsive noise even without the gust turned on, as the blade passes over it. This noise radiation is most likely because of the fluid that is dragged along by the blade having to accelerate over the nozzle wall.

### **3.2.1 Case 1 — Parallel BCDI**

Figure 3.4 shows the SPL trends for radiated noise, with the rotor running over the nozzle — without the gust turned on — for all the 30 microphone locations for the parallel BCDI. The peak noise is about 108dB. As can also be seen from the figure the radiation reduces when the



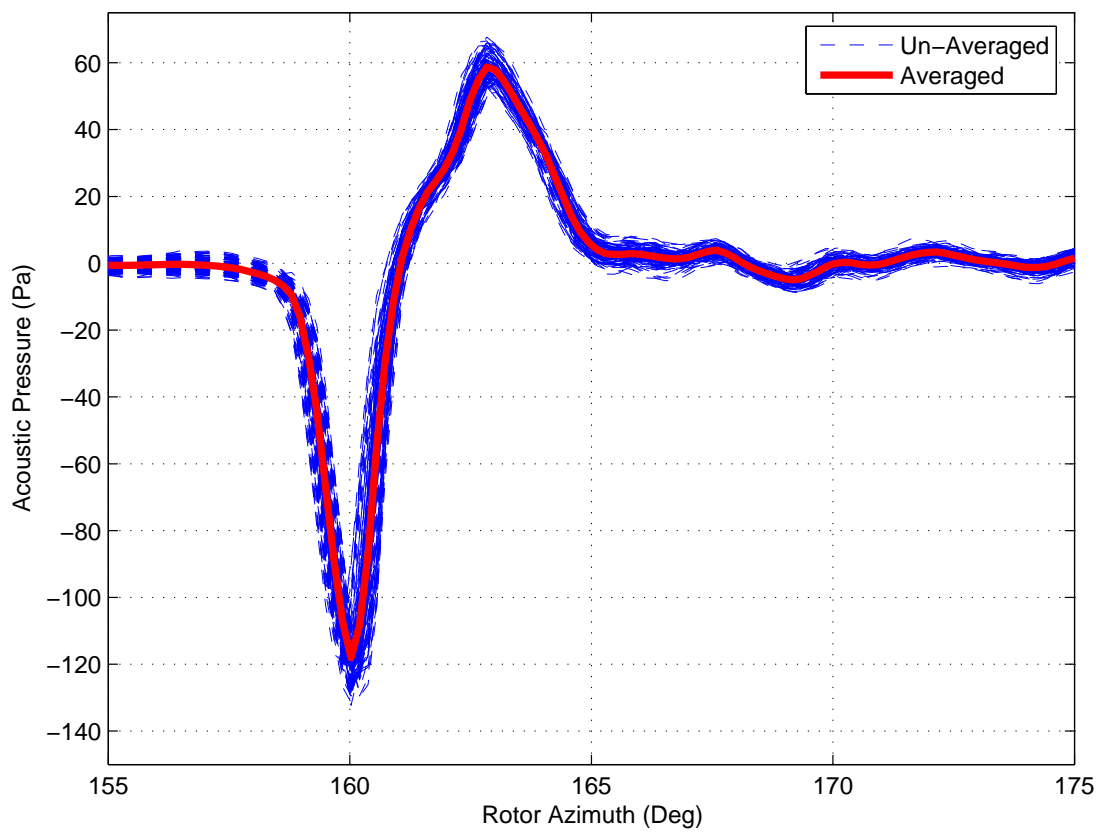


Figure 3.3: Revolution-to-Revolution fidelity of the rotor setup

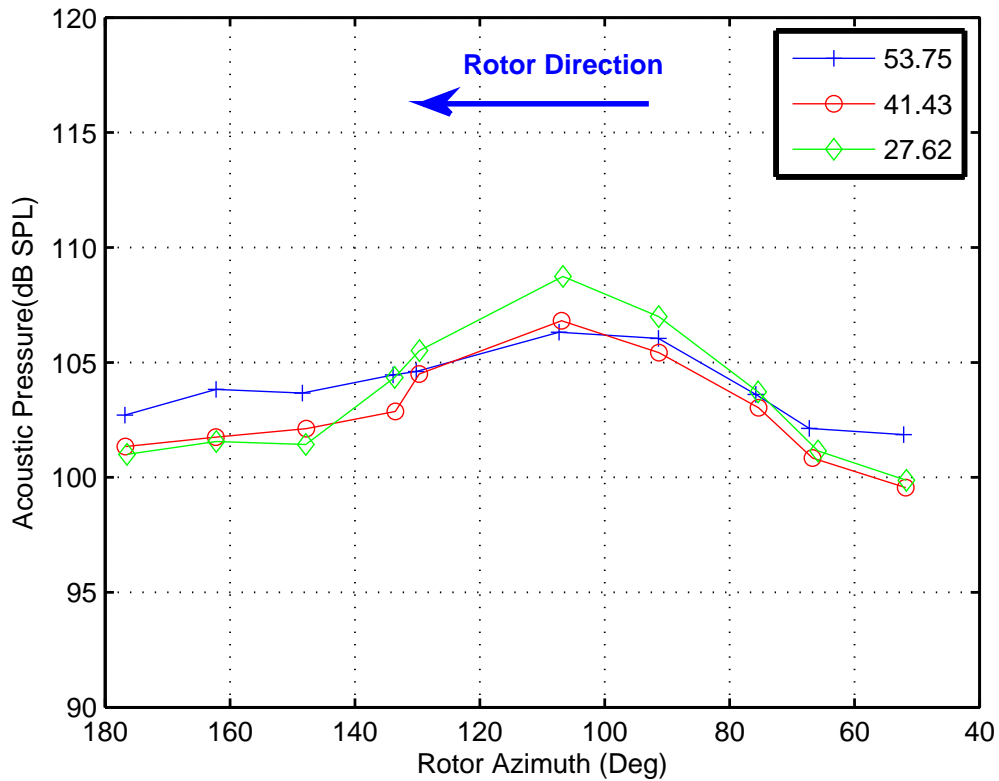


Figure 3.4: SPL trends of noise radiation due to the nozzle — parallel BCDI

microphone elevation angle increases, unlike the BVI situation where the noise increases as the microphone elevation increases. Moreover, there is not much azimuthal variation in the noise. The azimuthal variation is only about 7dB for the lower microphone elevation, while for the topmost microphone it is less than 5dB.

Figure 3.5 shows the variation of sound pressure level at the  $107^\circ$  azimuth microphones as a function of the peak gust velocity as the gust strength is increased. At the first non-zero gust velocity ( 80ft/s) shown in the graph, the sound pressure levels are almost equal for the three elevations. At the highest gust strength (corresponding to a peak gust velocity of 160ft/s), the difference be-

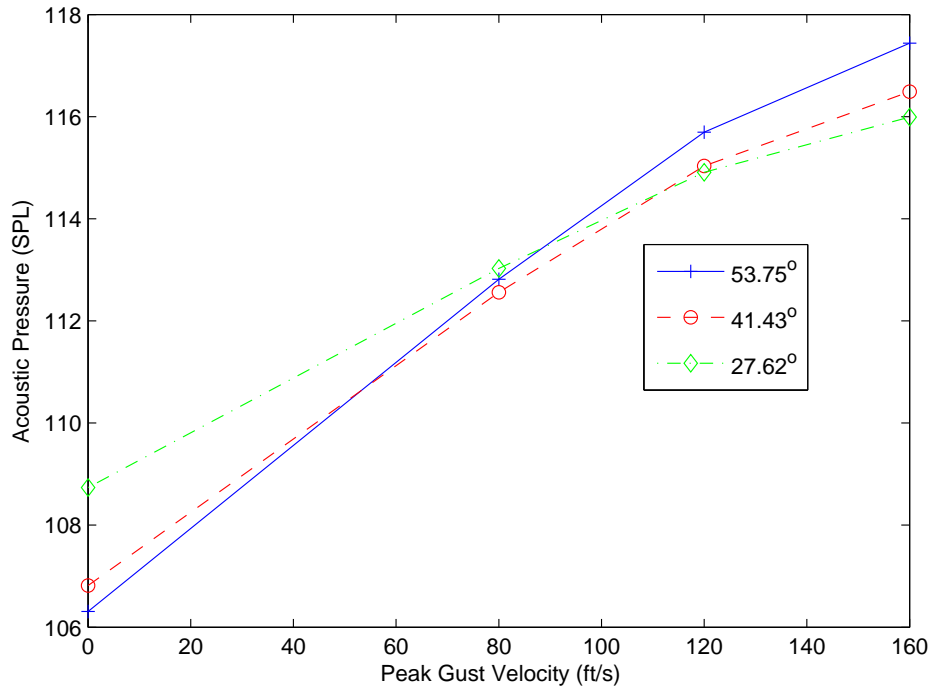
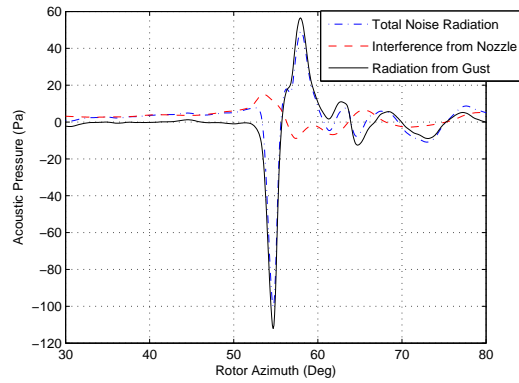


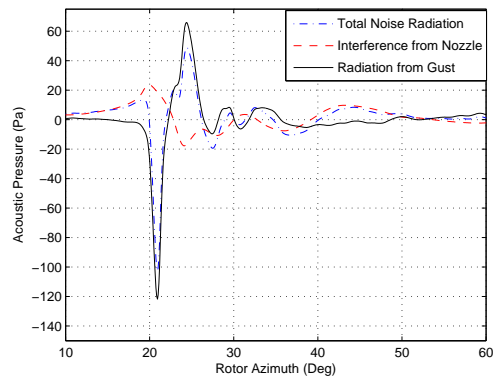
Figure 3.5: SPL trends with gust strength

tween the gust-on and the gust-off (0ft/s) case is about 12dB for the topmost microphone and 8dB for the lowest. Moreover, the velocity profile at the highest peak velocity case matches closely with the original design point discussed previously in Sec. 2.3.2.

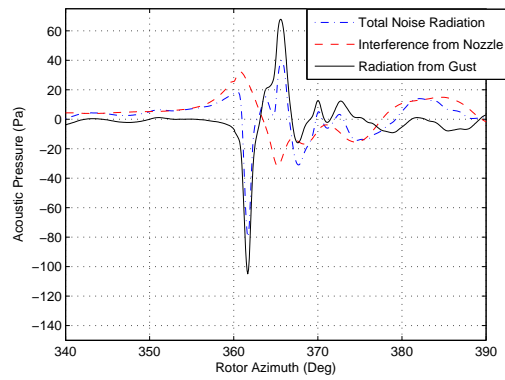
Figure 3.6 shows the time history recorded at the three microphones at the 107° azimuth. The figure shows the acoustic pressure time histories for the three microphone elevations with and without the simulated vortex velocity profile. The noise recorded at the microphones without the gust turned on, is impulsive and occurs over the same azimuthal range as the main BCDI event, confirming that it is due to the proximity of the nozzle. Moreover, the pulse radiated by the nozzle interaction is of opposite sign compared to the BCDI event. However, the noise radiation from the blade due to the nozzle presence alone is significantly lower than total noise radiated when the gust



(a) Microphone elevation =  $53.75^\circ$



(b) Microphone elevation =  $41.43^\circ$



(c) Microphone elevation =  $27.62^\circ$

Figure 3.6: Acoustic time history comparison with and without the gust, showing the effect of the

is turned on. In order to remove the effect of the nozzle from the acoustic data, the noise from the nozzle alone (without any flow) is subtracted from the total noise radiated. This not only removes the effect of the nozzle on the acoustics, but also eliminates the thickness noise and steady loading noise from the blade as it is of equal magnitude in both the situations. All further results presented are with the effect of the nozzle subtracted from the data and with the peak gust velocity at 160ft/s.

### **3.2.2 Case 2 — 3.3° Oblique BCDI**

Fig. 3.7 shows the noise levels due to the nozzle interference at all the microphone locations. The microphones at the lower elevation record more noise than at the higher elevation angles for most of the microphone azimuths. The radiation from the nozzle is opposite in sign to the total noise radiation, as can be seen from Fig. 3.8. However, the noise radiated due to the interference effect from the nozzle is significantly lower than the total noise radiated at all the microphone locations.

### **3.2.3 Case 3 — 8.8° Oblique BCDI**

Fig. 3.9 shows the noise levels due to the nozzle interference at all the microphone locations. The microphones at the lower elevation record more noise than at the higher elevation angles for most of the microphone azimuths. The radiation from the nozzle is opposite in sign to the total noise radiation, as can be seen from Fig. 3.10. However, the noise radiated due to the interference effect from the nozzle is significantly lower than the total noise radiated at all the microphone locations. Moreover, the noise levels for this interaction angle are lower than the previous interactions.

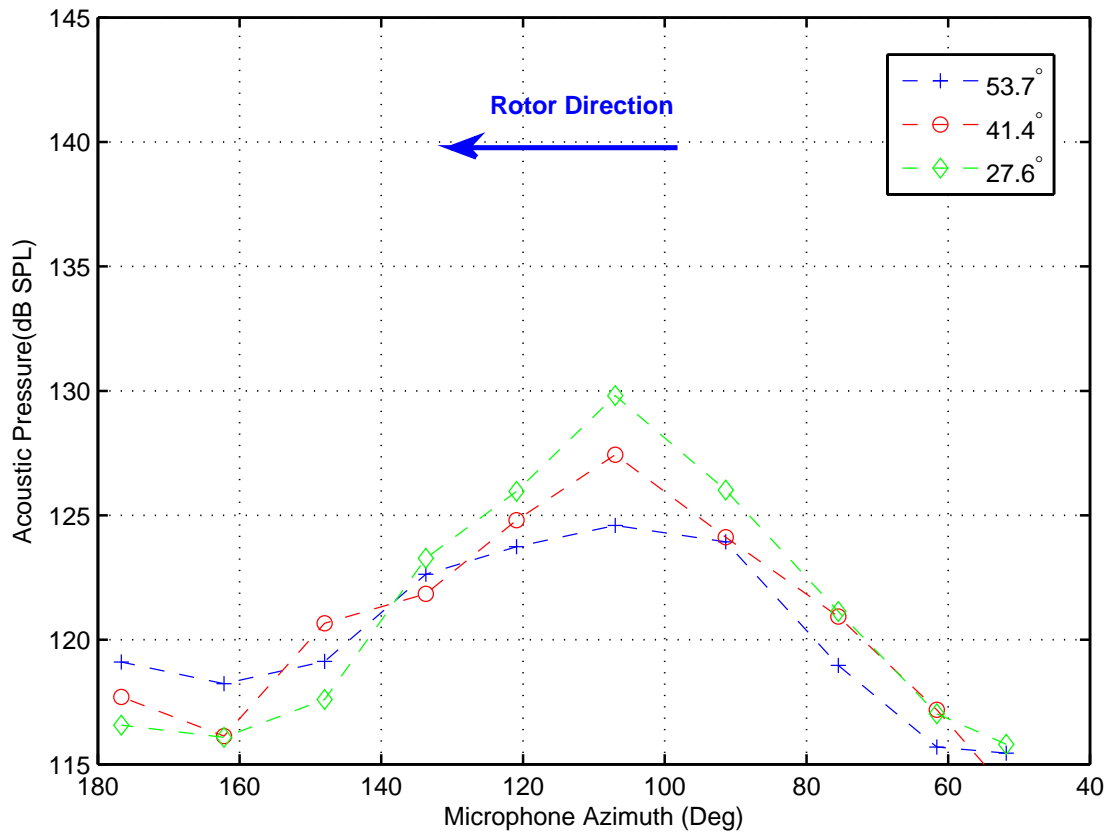
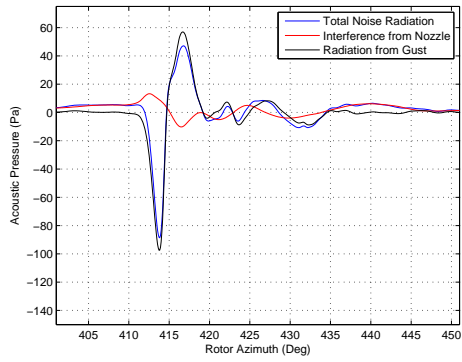
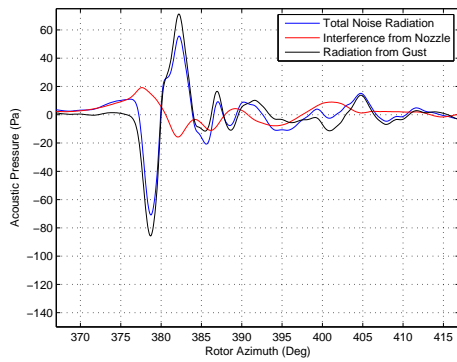


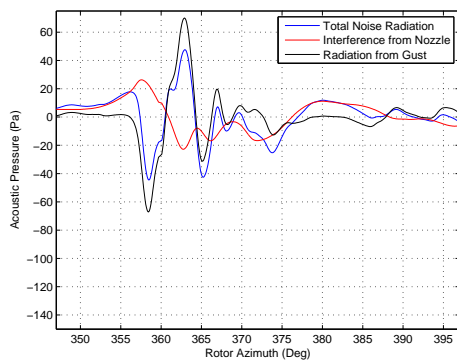
Figure 3.7: SPL trends of noise radiation due to the nozzle — Case 2



(a) Microphone elevation =  $53.75^\circ$



(b) Microphone elevation =  $41.43^\circ$



(c) Microphone elevation =  $27.62^\circ$

Figure 3.8: Acoustic time history comparison with and without the gust, for Case 2 at  $\psi = 120.9^\circ$

( $M_T = 0.702$ )

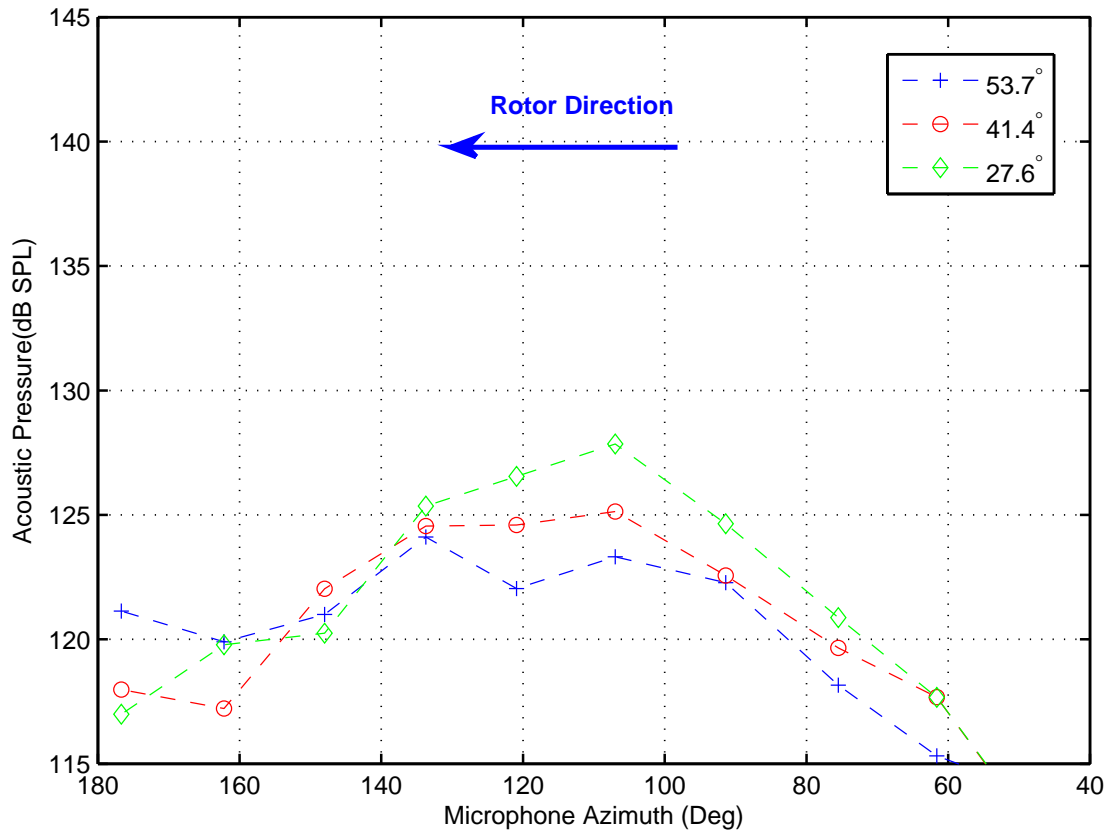
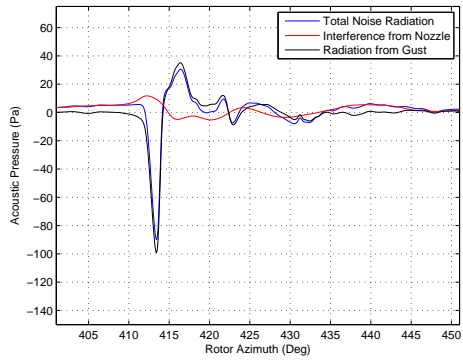


Figure 3.9: SPL trends of noise radiation due to the nozzle — Case 3

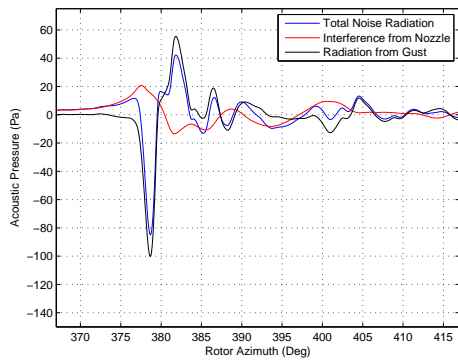
### 3.2.4 Case 4 — 15.3° Oblique BCDI

Fig. 3.11 shows the noise levels due to the nozzle interference at all the microphone locations. The microphones at the lower elevation record more noise than at the higher elevation angles for most of the microphone azimuths. The radiation from the nozzle is opposite in sign to the total noise radiation, as can be seen from Fig. 3.12. However, the noise radiated due to the interference effect from the nozzle is significantly lower than the total noise radiated at all the microphone

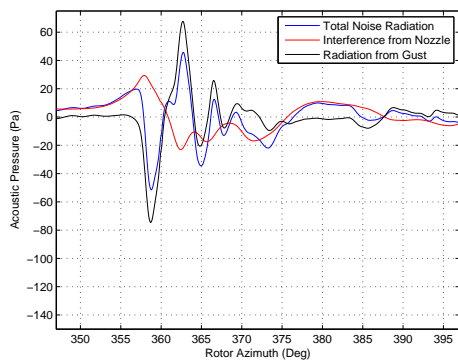




(a) Microphone elevation =  $53.75^\circ$



(b) Microphone elevation =  $41.43^\circ$



(c) Microphone elevation =  $27.62^\circ$

Figure 3.10: Acoustic time history comparison with and without the gust, for Case 3 at  $\psi = 120.9^\circ$

( $M_T = 0.702$ )

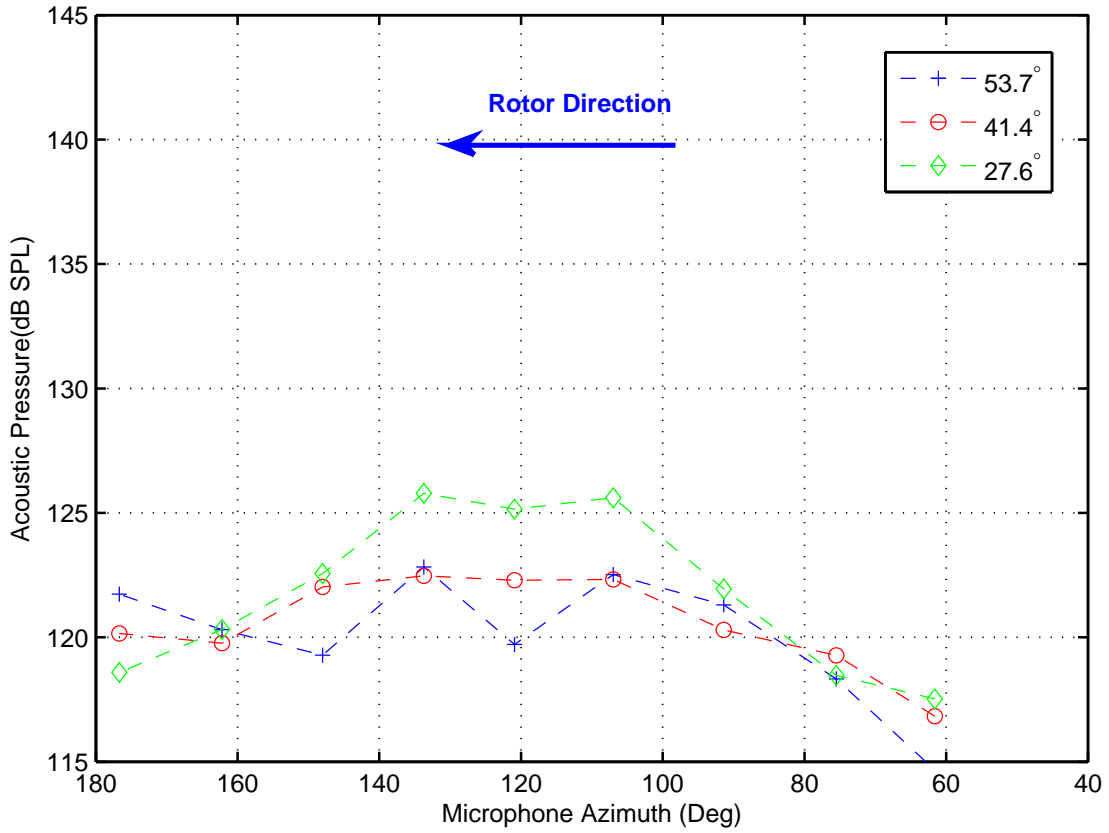
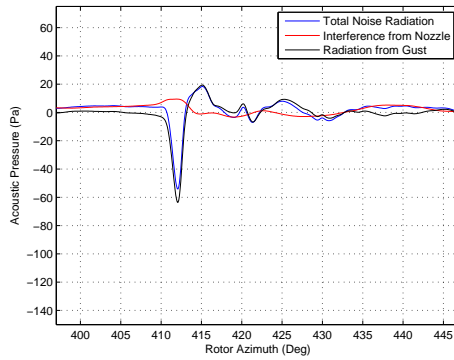


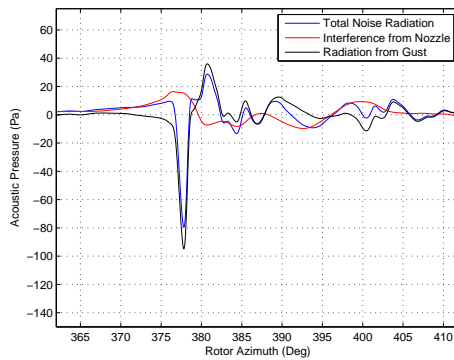
Figure 3.11: SPL trends of noise radiation due to the nozzle — Case 4

locations. The noise levels for this interaction angle are significantly lower than the previous interactions, and there is a greater difference between the total radiation with the gust on and the interference due to the nozzle.

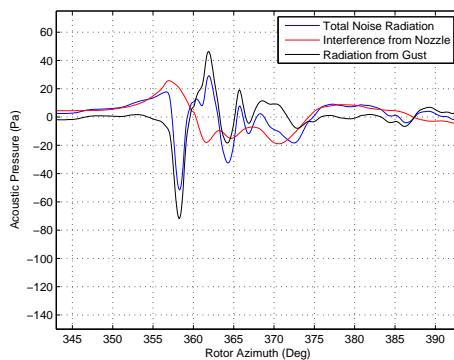
For complete acoustic time histories of the effect of the nozzle at other azimuthal angles, please see Appendix C.



(a) Microphone elevation =  $53.75^\circ$



(b) Microphone elevation =  $41.43^\circ$



(c) Microphone elevation =  $27.62^\circ$

Figure 3.12: Acoustic time history comparison with and without the gust, for Case 4 at  $\psi = 120.9^\circ$

( $M_T = 0.702$ )

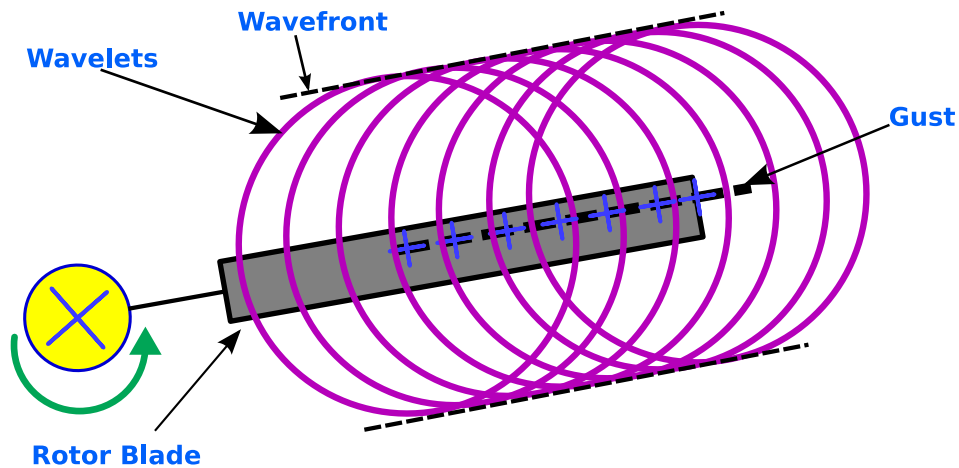
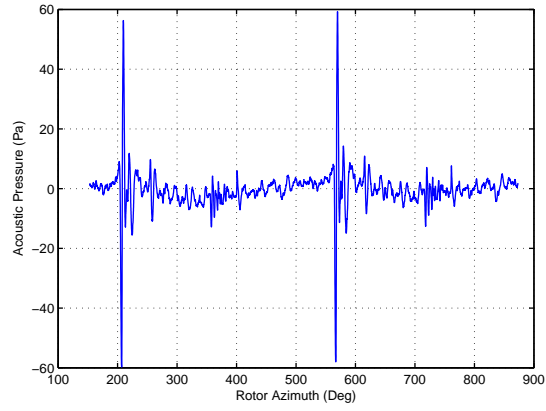


Figure 3.13: Top view of acoustic wavefronts radiating from the parallel interaction

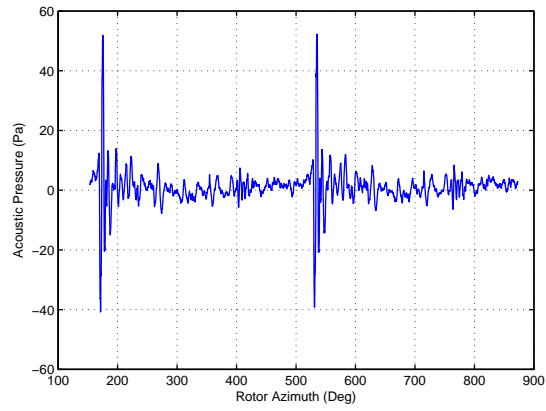
### 3.3 BCDI Acoustic Data — Parallel BCDI

As mentioned earlier, the parallel interaction has a trace Mach number of infinity. This results in the span-wise acoustic sources being triggered simultaneously (Fig. 3.13), and arrive in-phase at the far-field observer position assumed to be perpendicular to mid-span of the interaction, leading to significant noise radiation. Typically, this case results in maximum noise radiation from the helicopter. These near-parallel interactions occur close to  $60^\circ$  azimuth on the advancing side of the rotor (for a two-bladed helicopter) and tend to radiate most of noise to the starboard side of the helicopter, around a perpendicular line drawn from the 80% blade span location at the time of the interaction. This corresponds to a microphone azimuthal angle of  $107^\circ$  in the BCDI experiment.

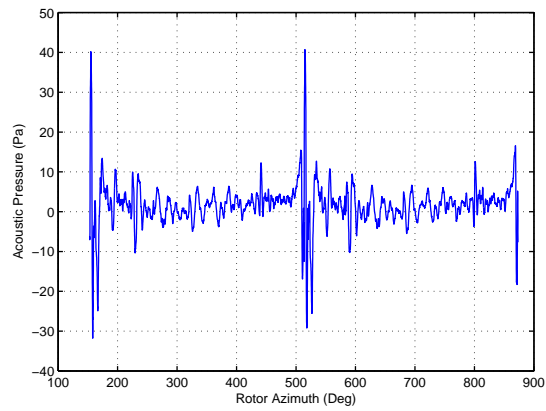
Fig. 3.14 shows the unaveraged data for two revolutions of the rotor at the microphones at  $\psi = 120.9^\circ$  for the parallel interaction at 0.702 tip Mach number. It should be noted that the data in these figures have not been scaled with different microphone locations. Thus the amount of



(a) Microphone elevation =  $53.75^\circ$



(b) Microphone elevation =  $41.43^\circ$



(c) Microphone elevation =  $27.62^\circ$

Figure 3.14: Unaveraged data for two revolutions for the parallel interaction at  $\psi = 120.9^\circ$

spherical spreading of the acoustic waves from the source to the microphone is different for each of the microphones. Firstly, it is obvious that there are quite a few reflections recorded by the microphones. However, they are significantly lesser in magnitude than the main pulse due to the interaction. Secondly, it also seen that the pulses are slightly different from revolution to revolution. This is mostly, of the turbulence levels in the gust and to a lesser extent due to recirculation setup in the room.

In order to study the directionality characteristics, it would be ideal to position microphones at a fixed distance from the acoustic source, and distribute the microphones on the surface of a sphere. However, this is not possible within the constraints of the chamber, and so the spherical spreading of the noise from the interaction is different for different microphones. In order to compare the noise across microphones, this effect needs to be normalized. It was decided to normalize the all the microphone pressure data to a distance of  $3R$  from the hub of the rotor. This would be equivalent to distributing the microphones on a sphere with radius  $3R$  and centered at the rotor hub. Ideally, this sphere should be centered about the acoustic source. However, in the case of the experiment, there is no single point of origin for the noise. While for the parallel interaction most of the acoustic activity occurs close to the 80% blade span, when comparing the acoustics across different interaction angles there is no particular fixed point in space to choose as the center of the sphere. Thus, in order to be able to compare the results across the various parameters, it was decided to normalize the microphone pressure data at a fixed distance about the rotor hub. Moreover, changing the center of scaling to the 80% blade span section during at the interaction, does not result in significant changes to the relative noise levels and the directionality for different

interaction angles. For some results and discussion with regards to this, please refer to Appendix F. The distance of  $3R$  was chosen because it is in between the range of microphone distances used in the experiment. The acoustic pressure data are normalized using a far-field solution to an acoustic point source and are divided by the distance of the microphone from the rotor hub. All the data presented here onwards is for microphones whose distances have been normalized to a distance of  $3R$  from the rotor hub.

The infinite trace Mach number along the blade span essentially means that all the acoustic sources along that the blade span are triggered simultaneously, and are perfectly in phase when they radiate from the rotor blade. However, the directional characteristics of this interaction is decided by the arrival times of these acoustic pulses at different observer locations. The microphone location where the important pulses add in phase records the maximum noise. This peak noise azimuthal location is close to a perpendicular line drawn from the 80% blade span location at the time of the interaction. For the parallel interaction, elevation angle does not affect the phasing of the acoustic signals. The variation of noise across the elevation above the rotor plane is determined by the dipole nature of the acoustic sources and hence are expected to increase up to a certain microphone elevation ( $\sim 60^\circ$ ) and reduce thereafter. In the present experimental setup, the highest microphone is at  $53.75^\circ$ — close to the  $60^\circ$  angle.

### **3.3.1 Acoustic Time Histories**

Fig. 3.15 shows the acoustic time histories for the parallel interaction at most of the microphones, after subtracting the effect of the nozzle from the time histories. The plots are truncated in

time to show only the acoustics of the interaction event. It is observed from these plots, that there are two strong peaks — a negative peak followed by a positive one. The first negative peak is a result of the velocity gradient in the gust velocity field, while the positive peak is caused by the negative velocity gradient of the gust field. The asymmetry in the gust (higher positive velocity gradient compared to the negative velocity gradient) results in a higher negative peak in the acoustics. This is most easily observable at the  $107^\circ$  azimuth microphones, where most of the span-wise acoustic disturbances arrive almost in-phase resulting in a distinct pulse, and hence high frequency noise.

At the microphones at lower azimuthal angles ( $\psi < 107^\circ$ ), the acoustic disturbances from the tip of the blade arrive earlier than from further inboard of the blade. The first pulse arriving from towards the blade tip results in the initial negative gradient in the acoustics. The following pulses from further in board of the blade, arrive a little later in time, resulting in a broadening of the positive peak in the acoustics. At even lower microphone azimuths, the span-wise acoustic pulses become more out of phase and result in almost no positive peak.

For microphones at azimuth larger than  $107^\circ$ , the opposite is true. The acoustic pulses from the in board blade locations arrive earlier than from the tip of the blade. This results in out-of-phase summation in the negative peak of the acoustic pulse and hence a lowering of the magnitude of the negative peak relative to the positive peak. As the microphone azimuth is increased ( $\psi > 133.7^\circ$ ), particularly at the lower microphone elevations, the typical shape of pulse is almost completely lost.

Figure 3.16 shows the variation in sound pressure level with azimuth and elevation for a tip



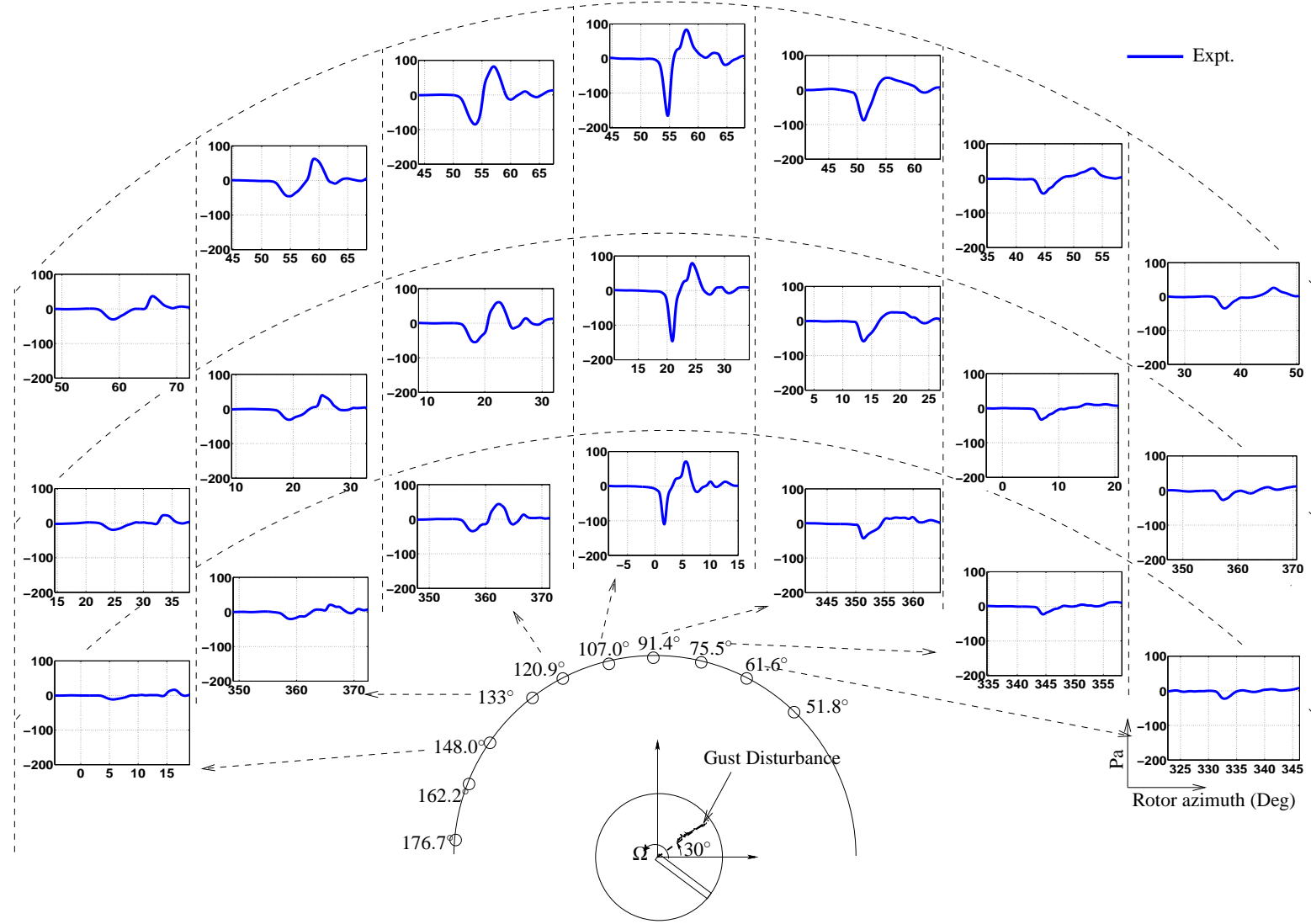


Figure 3.15: Acoustic time histories at the various microphones in terms of Acoustic Pressure (in Pa) vs. Rotor Azimuth (in Deg)

( $M_T = 0.702$  — Parallel Interaction)

Mach number of 0.702. The peak noise levels occurs at the  $\psi = 107^\circ$  microphone location. This is to be expected — as explained earlier — as this microphone location is perpendicular to blade around the 80% blade span location when the interaction occurs. As expected the SPL values increase with increasing microphone elevation due to the dipole nature of the loading during the interaction. The radiated noise has a sharp peak in the azimuthal direction close to  $107^\circ$  and falls quite rapidly on either side. The asymmetry about the peak noise azimuth observed can be attributed to the choice of the rotor hub as the center of normalizing the spherical spreading. Most of the acoustic energy is concentrated close to the blade tip. Since the microphones at higher azimuthal angle are farther away from the interaction, they end up being scaled to a greater distance than the microphones closer to the interaction. An appropriate choice of the scaling center ( $\sim 80\%$  blade span at the interaction) would reduce this asymmetry for the parallel interaction, however, as explained earlier, this would make it difficult to compare the results across different interaction angles.

### 3.3.2 Frequency Spectrum

Fig. 3.17 shows the frequency spectrum of the noise recorded at most of the microphone locations. The microphones recording high amplitudes ( $> 60\text{dB}$ ) at frequencies as high as 200 rotor harmonics are at  $\psi = 107^\circ$ . This corresponds to the strong narrow time history of the pulse (see Fig. 3.15). As the microphones are moved to azimuths away from the peak noise location, the time histories exhibit wider waveforms and correspondingly lower magnitude at these high frequencies.

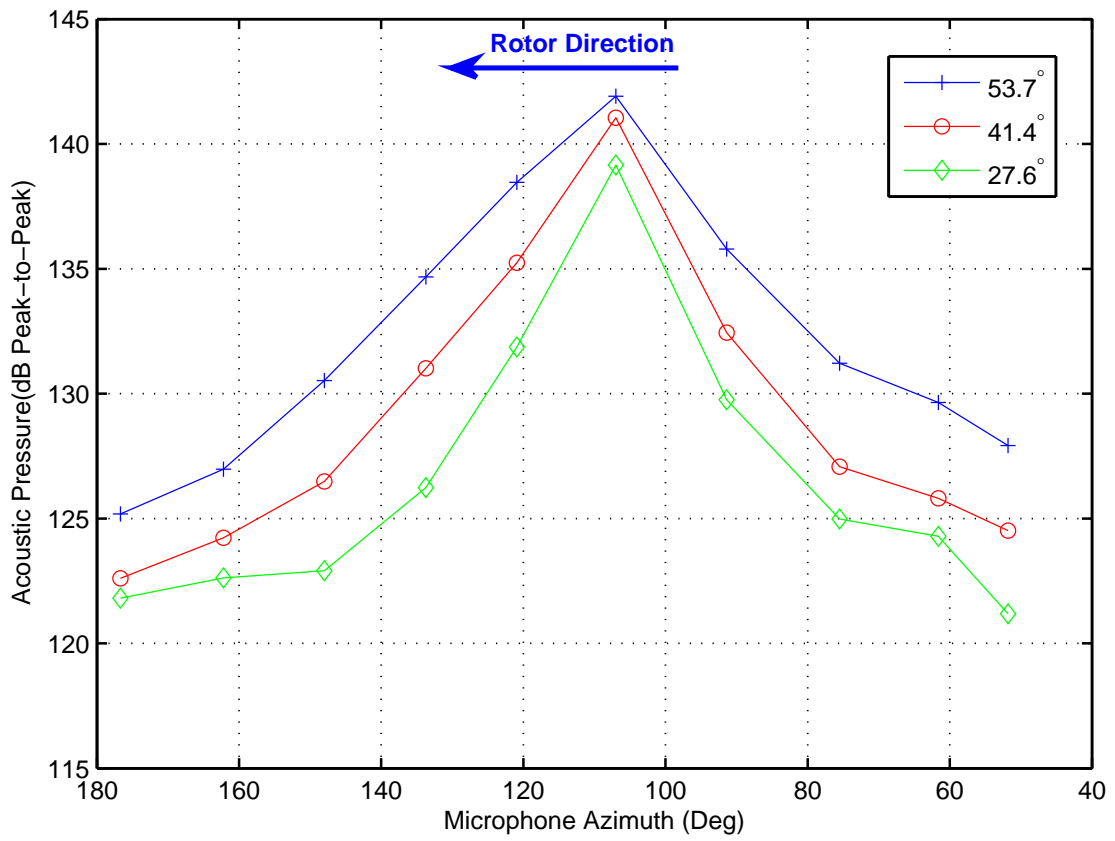


Figure 3.16: Directionality trends at  $0.702M_T$  for the Parallel Interaction

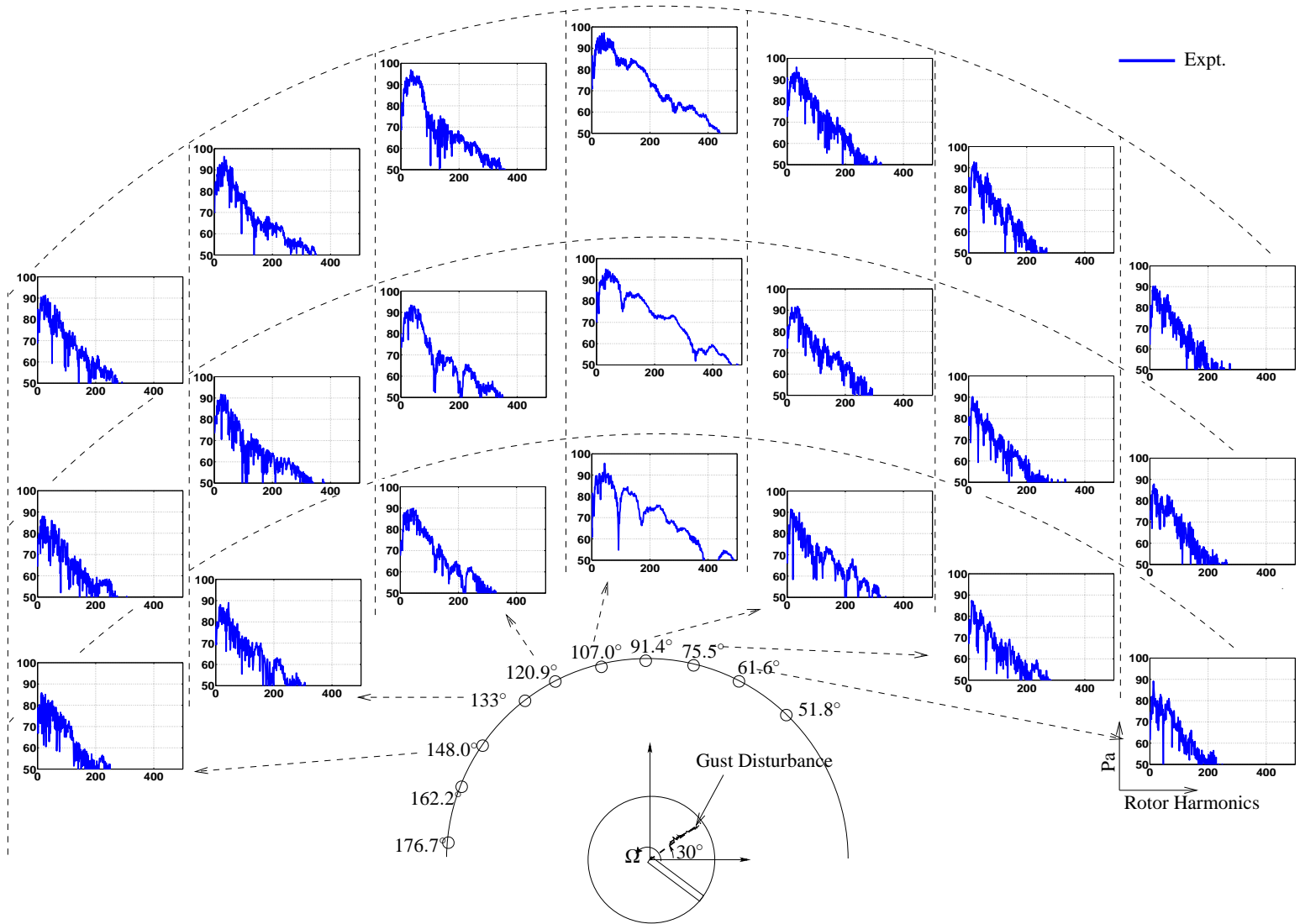


Figure 3.17: Frequency spectrum of noise at various microphones — Sound pressure in dB vs. Single-blade rotor harmonics

( $M_T = 0.702$  — Parallel Interaction)

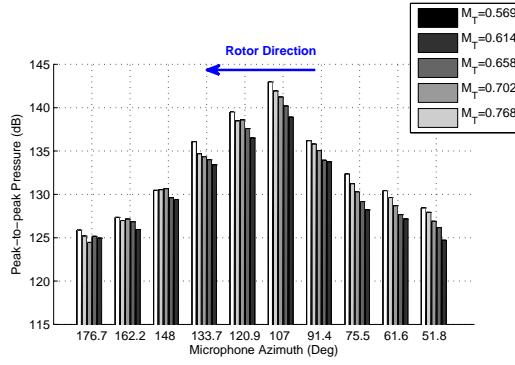
### 3.3.3 Effect of tip Mach number

Fig. 3.18 shows the variation of the peak-to-peak noise observed at the various microphones as a function of the rotor tip Mach number. Clearly, as the tip Mach number increases, the noise level also goes up. It is also observed that the noise levels increase almost monotonically with increase in tip Mach number. While this increase occurs for the microphones close to the peak microphone locations, this is not true for all microphone azimuths. In particular for the lowest microphone positions at  $\psi = 61.6^\circ$  and  $\psi = 148^\circ$ . This is probably due to reflections from the gust generator affecting the former microphone, while reflections off of the rotor stand itself affecting the latter. For the peak noise microphone location at the  $107^\circ$  azimuthal location, Fig. 3.19 shows the peak-to-peak variation with rotor tip Mach number. As can be seen, the noise level increases almost linearly up to a tip Mach number of about 0.65. At the higher tip Mach numbers the noise level increases slower than the linear increase rate, particularly for the lower microphone location.

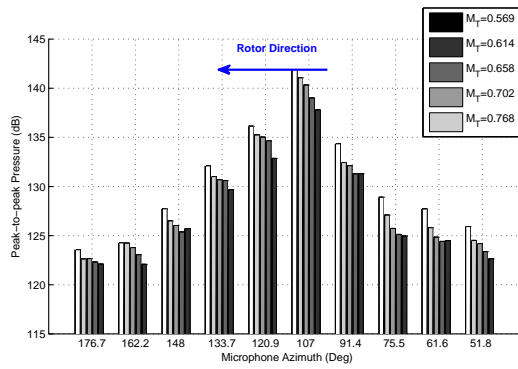
## 3.4 Oblique BCDI

### 3.4.1 Case 2 — $3.3^\circ$ Oblique Interaction

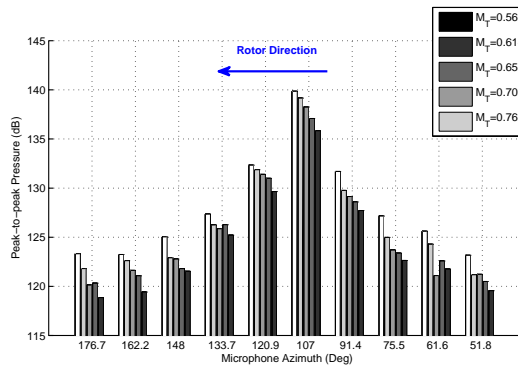
The first interaction angle (starting with  $3.3^\circ$  at the blade tip) studied is shown in Fig. 2.22(a). The interaction starts out at the tip of the blade at a small  $3.3^\circ$  angle and sweeps inboard. This near-parallel interaction has a completely supersonic trace Mach number profile(Fig. 2.22(b)). This implies that the noise sources are triggered very rapidly creating the in-plane acoustic wave pattern shown in Fig. 3.20. In effect the BCDI summation process can be viewed as a decelerating super-



(a) Microphone elevation =  $53.75^\circ$



(b) Microphone elevation =  $41.43^\circ$



(c) Microphone elevation =  $27.62^\circ$

Figure 3.18: Variation of peak-to-peak noise level with tip Mach number — Parallel BCDI

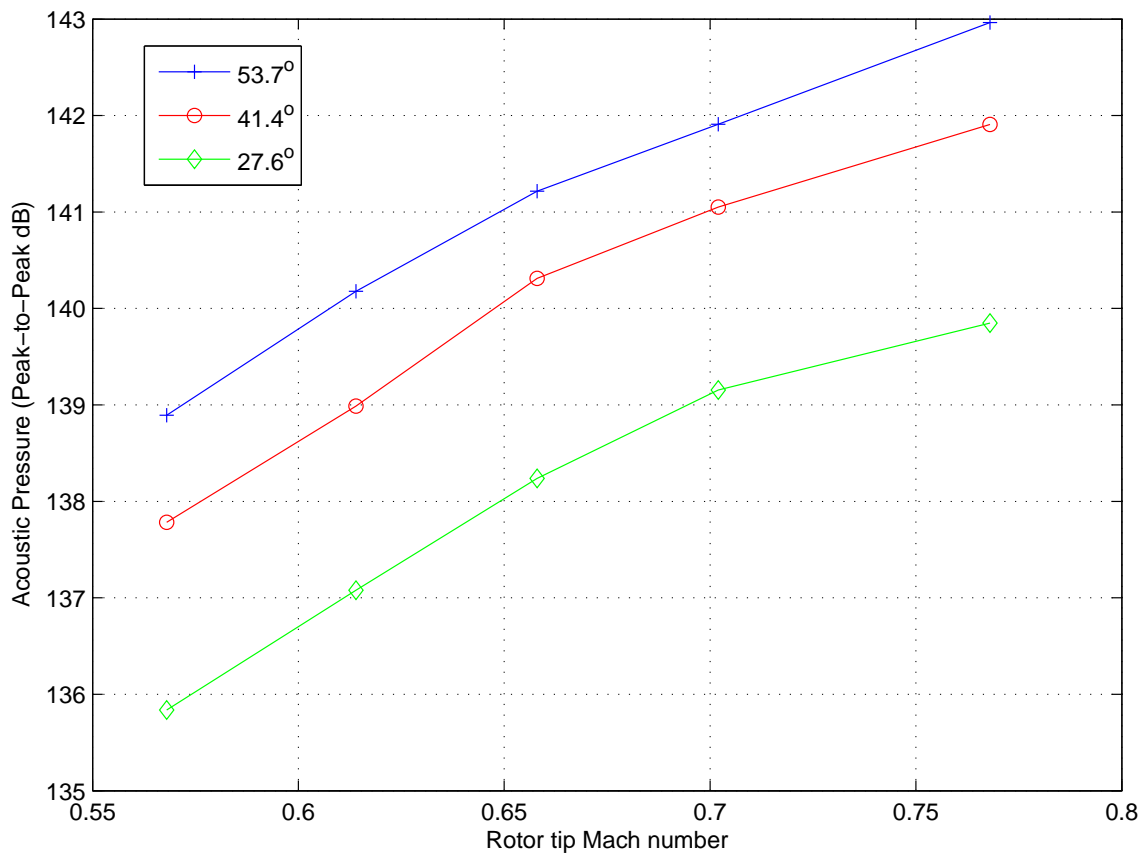


Figure 3.19: Variation of peak-to-peak level with increase in tip Mach number for the parallel BCDI at  $\psi = 107^\circ$

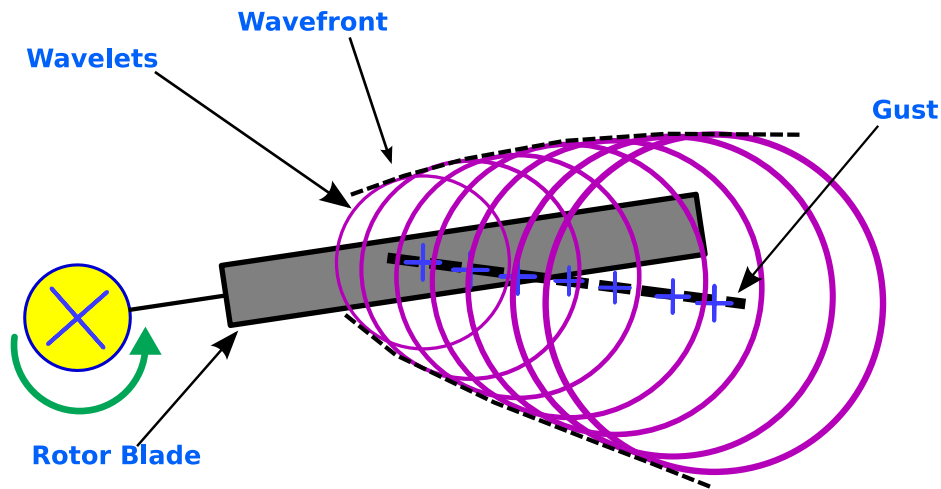


Figure 3.20: Top view of acoustic wavefronts for Case 2 oblique BCDI

sonic unit acoustic source. The envelope of this wave pattern shows the grouping of the waves that contribute to the peak levels of radiated noise in the rotor plane.

Fig. 3.21 shows the time history of the noise at most of the microphone locations for the  $3.3^\circ$  oblique angle at a tip Mach number equal to 0.702. It is interesting to note that while the pulse shapes close to the peak noise azimuth ( $\psi = 120.9^\circ$  to  $\psi = 91.4^\circ$ ) are similar to that during the parallel interaction, the pulse shapes at higher microphone azimuth angles are also still preserved, unlike for the parallel interaction case (Fig. 3.15). At higher microphone azimuths the phasing of the spanwise sources results in less destructive interference of the sources originating at the most inboard location as well the tip of the blade, leading to a strong and well-defined pulse shape with higher noise levels.

The small change in interaction angle results in a significant change in the phasing relation between the spanwise acoustic sources, and hence the resulting radiation pattern. This can be seen



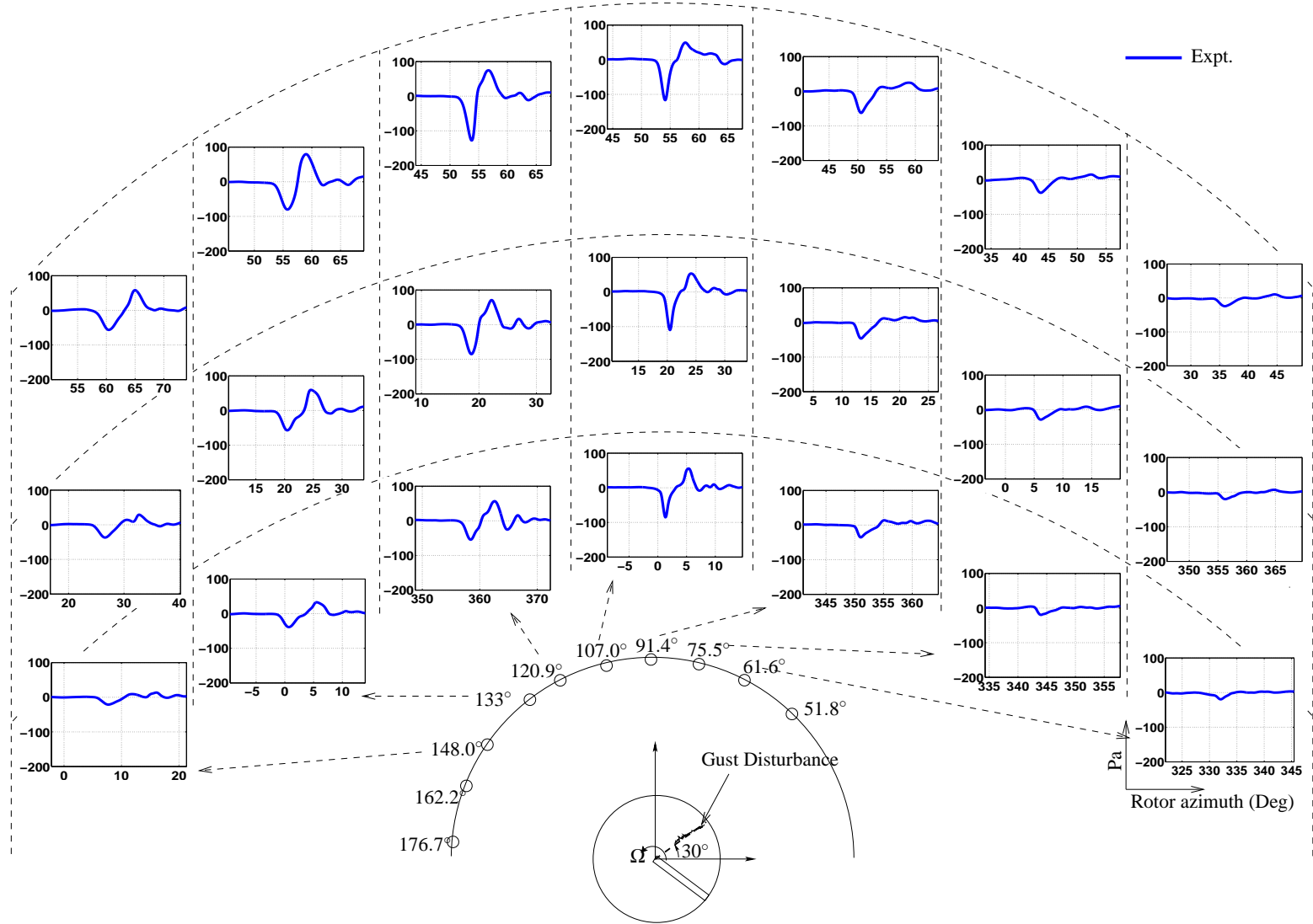


Figure 3.21: Acoustic time histories at the various microphones in terms of Acoustic Pressure (in Pa) vs. Rotor Azimuth (in Deg)

— Case 2 ( $3.3^\circ$  Oblique Interaction  $M_T = 0.702$ )

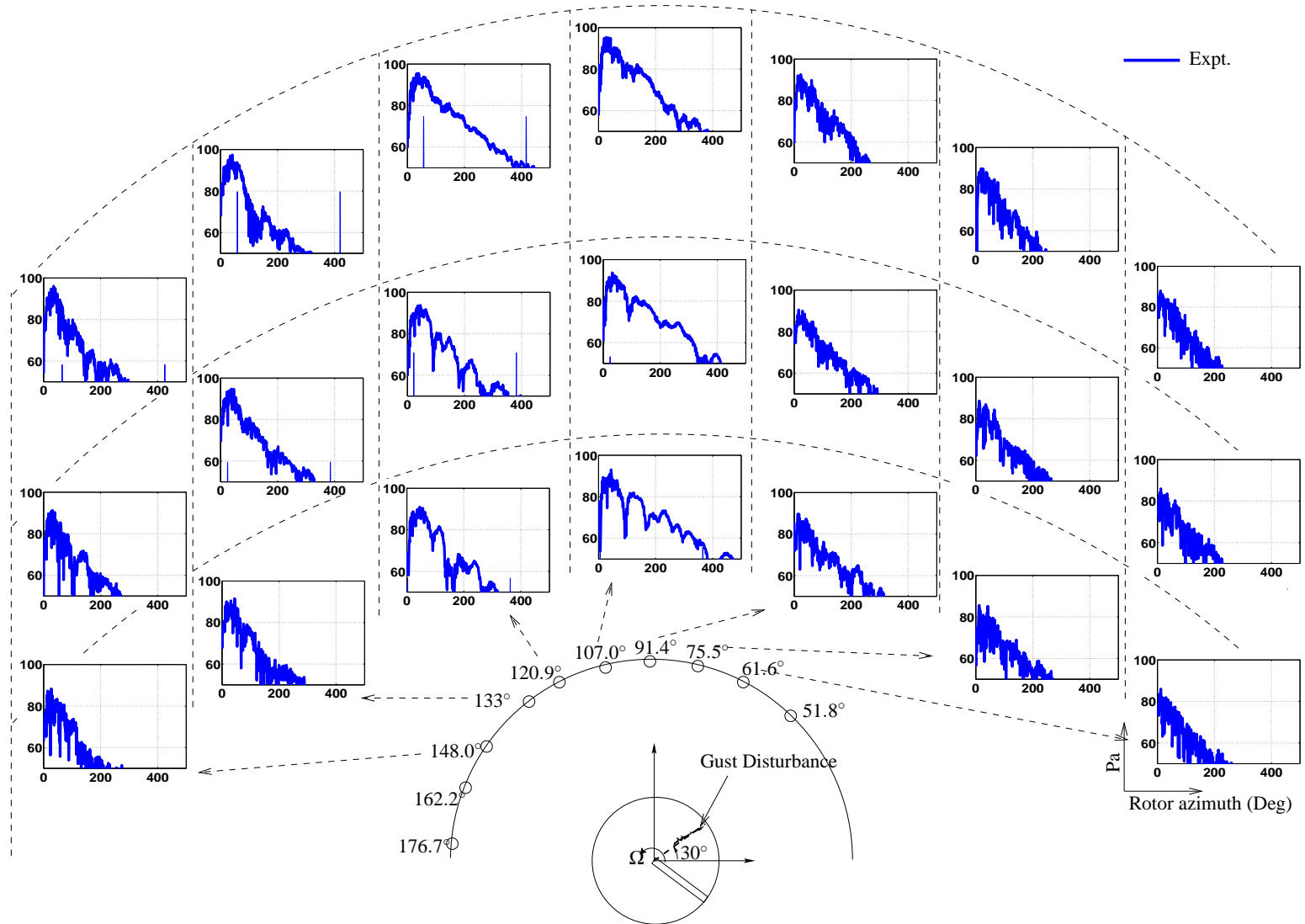


Figure 3.22: Frequency spectrum of noise at various microphones — Sound pressure in dB vs. Single-blade rotor harmonics —  
Case 2 ( $3.3^\circ$  Oblique Interaction  $M_T = 0.702$ )

in the sketch of the wavefronts radiation from the blade for the parallel (Fig. 3.13) and the  $3.3^\circ$  oblique interaction (Fig. 3.20). The in-phase summing of the spanwise acoustic sources for this small oblique interaction angle, results in a higher frequency content at the  $120.9^\circ$  microphone azimuthal location (Fig. 3.22) and slightly lower frequencies at the microphones at  $107^\circ$ , compared to the parallel interaction. The frequency content of the measured noise at the microphones at higher azimuths, particularly for the topmost microphone, is higher compared to the parallel interaction.

Fig. 3.23 shows the peak noise levels observed at the various microphone locations for the tip Mach number of 0.702. As before the pressure values have been scaled using  $1/R$  law to a distance of  $3R$  from the rotor hub. The small change in interaction angle results in quite a different directionality profile when compared to the parallel interaction (Fig 3.16). While the parallel interaction had a sharp peak in the azimuthal direction, the small oblique interaction has a much shallower peak, falling off more slowly with changes in azimuth, particularly towards higher azimuth angles. The peak noise level has also shifted to a higher microphone azimuth for the top most microphone, compared to the parallel interaction.

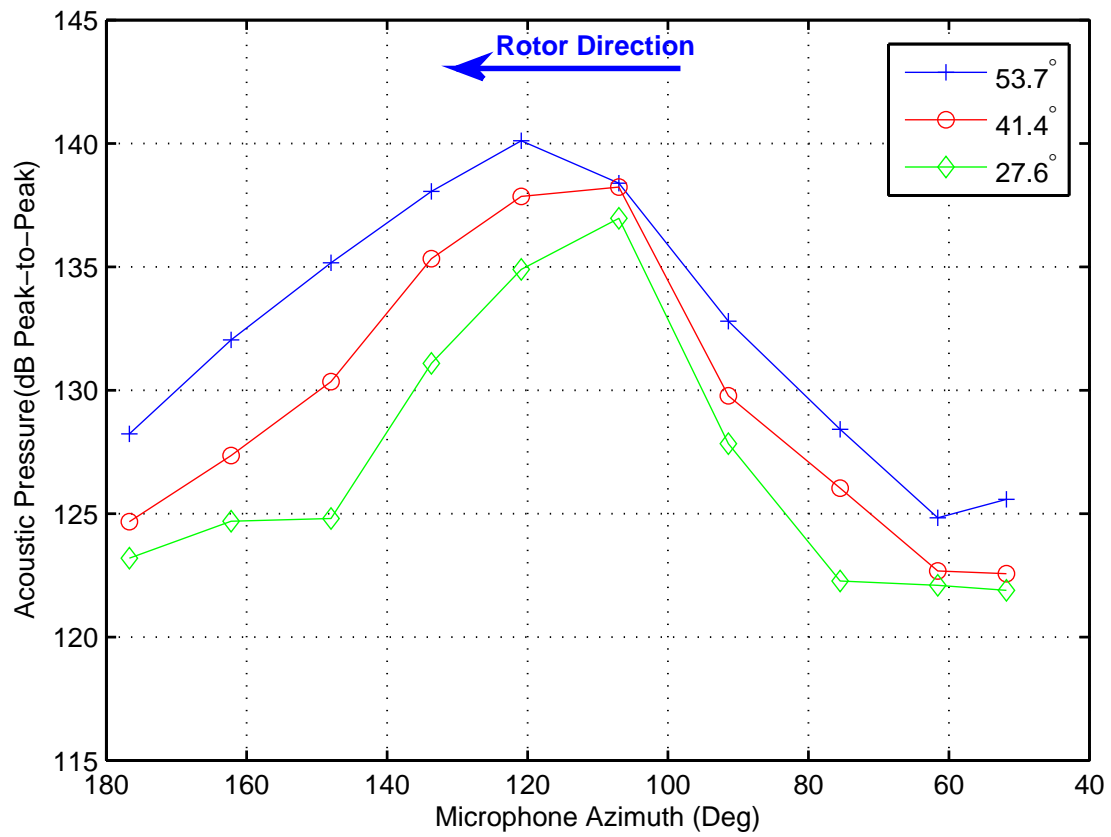


Figure 3.23: Directionality trends for Case 2 ( $3.3^\circ$  Oblique Interaction) at  $M_T = 0.702$

### 3.4.2 Case 3 — 8.8° Oblique Interaction

Fig. 2.22(c) shows an in-plane schematic of the second oblique interaction angle which starts out at 8.8° at the tip of the blade and proceeds inboard. The corresponding trace Mach number shown in Fig. 2.22(d) is supersonic throughout the entire interaction, just as in Case 2. The corresponding sketch of the radiating wavefront in the rotor plane is shown in Fig. 3.24. This suggests that the azimuthal phasing of the spanwise sources would be similar to the previous case discussed. However, the trace Mach number for the Case 3 oblique BCDI is much lower than the previous case. Thus, for the topmost microphone location, the component of the trace Mach number will become subsonic. When the trace Mach number becomes 1, the acoustic sources are triggered at the speed of sound, and hence the waves emanating from these sources would all collect in the medium and radiate outwards to the microphone (similar to a sonic boom). However, for the particular interaction angle under consideration, the trace Mach number is low enough for the component above the rotor plane to become subsonic only at around the 50% blade span location, which does not have a significant contribution to the acoustics (due to the very low Mach number at the blade section).

Fig. 3.25 and Fig. 3.26 show the time histories and the frequency spectrum at the microphones. As expected the trends are similar to Case 2 oblique BCDI, as the trace Mach number profiles are similar. Just as in the previous case, at azimuths greater 107° there is a lesser extent of destructive interference compared to the parallel interaction resulting in higher noise levels. The frequency content (Fig. 3.26) at the microphones at  $\psi = 120.9^\circ$  is higher than the parallel interaction case — similar to Case 2.

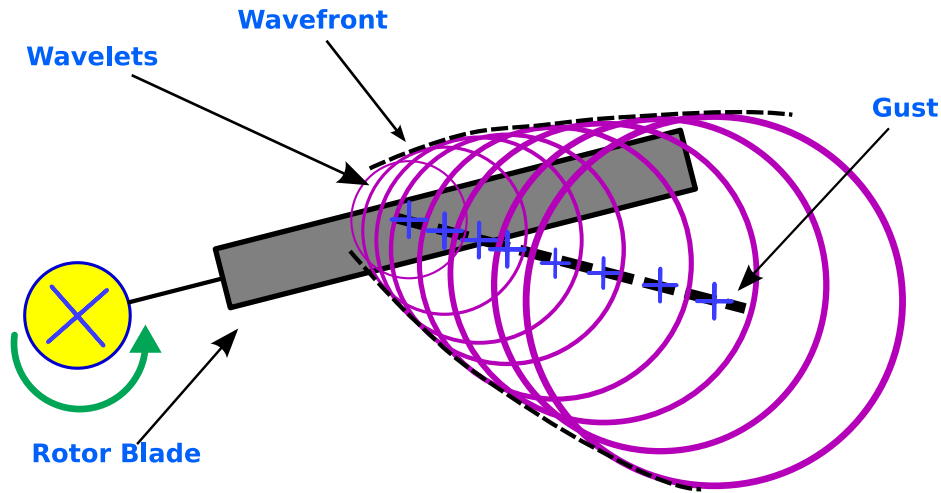


Figure 3.24: Top view of acoustic of the wavefronts for Case 3 oblique BCDI

The peak noise levels in decibels for this interaction angle for a tip Mach number of 0.702 are shown in Fig. 3.27. The asymmetry in the azimuthal direction is much more prominent for this interaction than was for the two previous interactions discussed. The reason for this, once again, is the phasing of the spanwise sources radiating from the blade at the time of the interaction. It is interesting to note that although the peak noise level ( $\psi = 120.9^\circ$ ) has reduced from the parallel interaction case, the noise levels at higher azimuth have in fact increased compared to the parallel interaction.

### 3.4.3 Case 4 — $15.3^\circ$ Oblique Interaction

The third oblique interaction angle (Fig. 2.22(e)) starts out at an angle of  $15.33^\circ$  at the tip and proceeds inboard as the blade rotates. For the case of the blade spinning with a tip Mach number equal to 0.702, the in-plane trace Mach number is supersonic for the outboard blade sections,

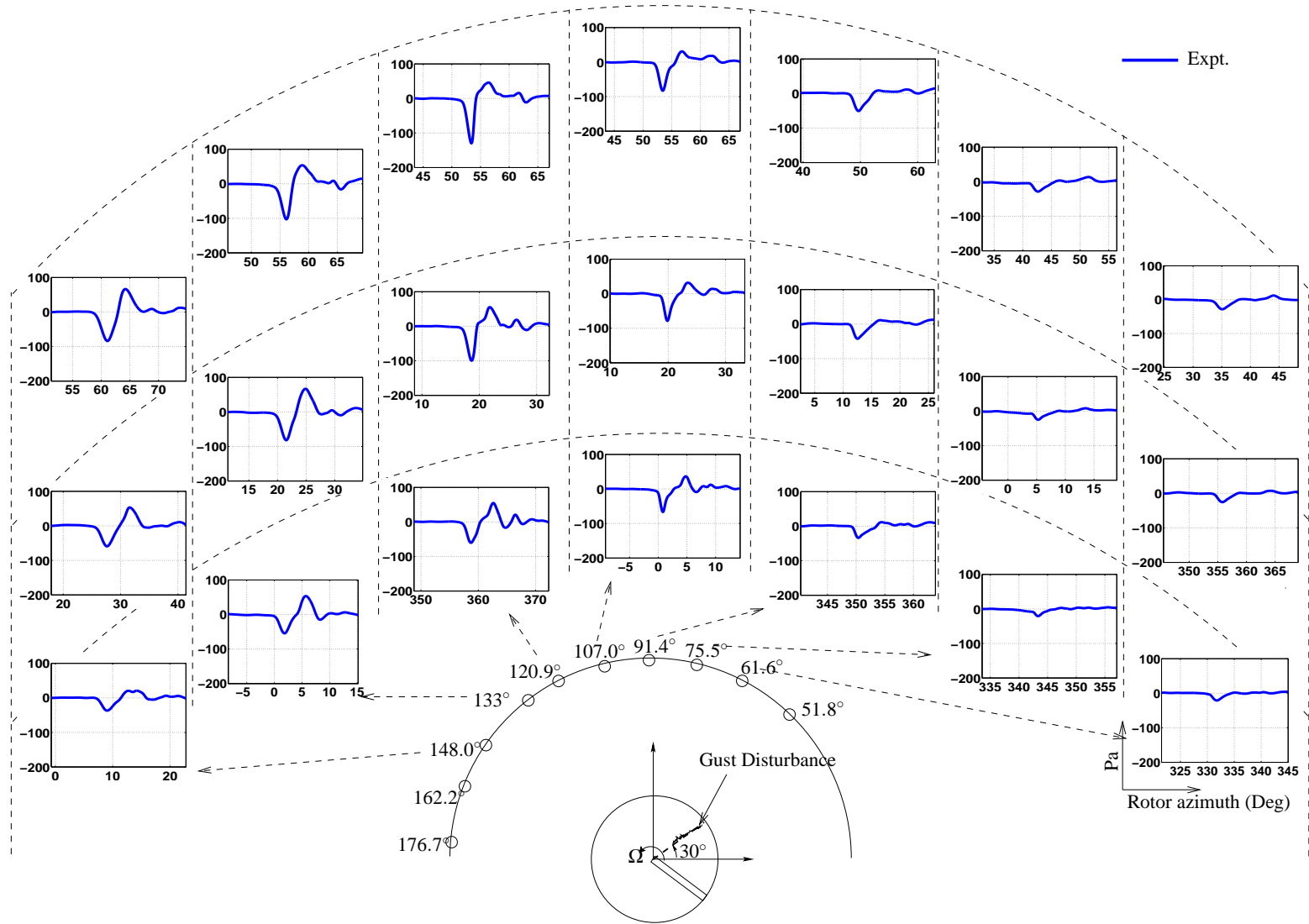


Figure 3.25: Acoustic time histories at the various microphones in terms of Acoustic Pressure (in Pa) vs. Rotor Azimuth (in Deg)

— Case 3 ( $8.8^\circ$  Oblique Interaction  $M_T = 0.702$ )

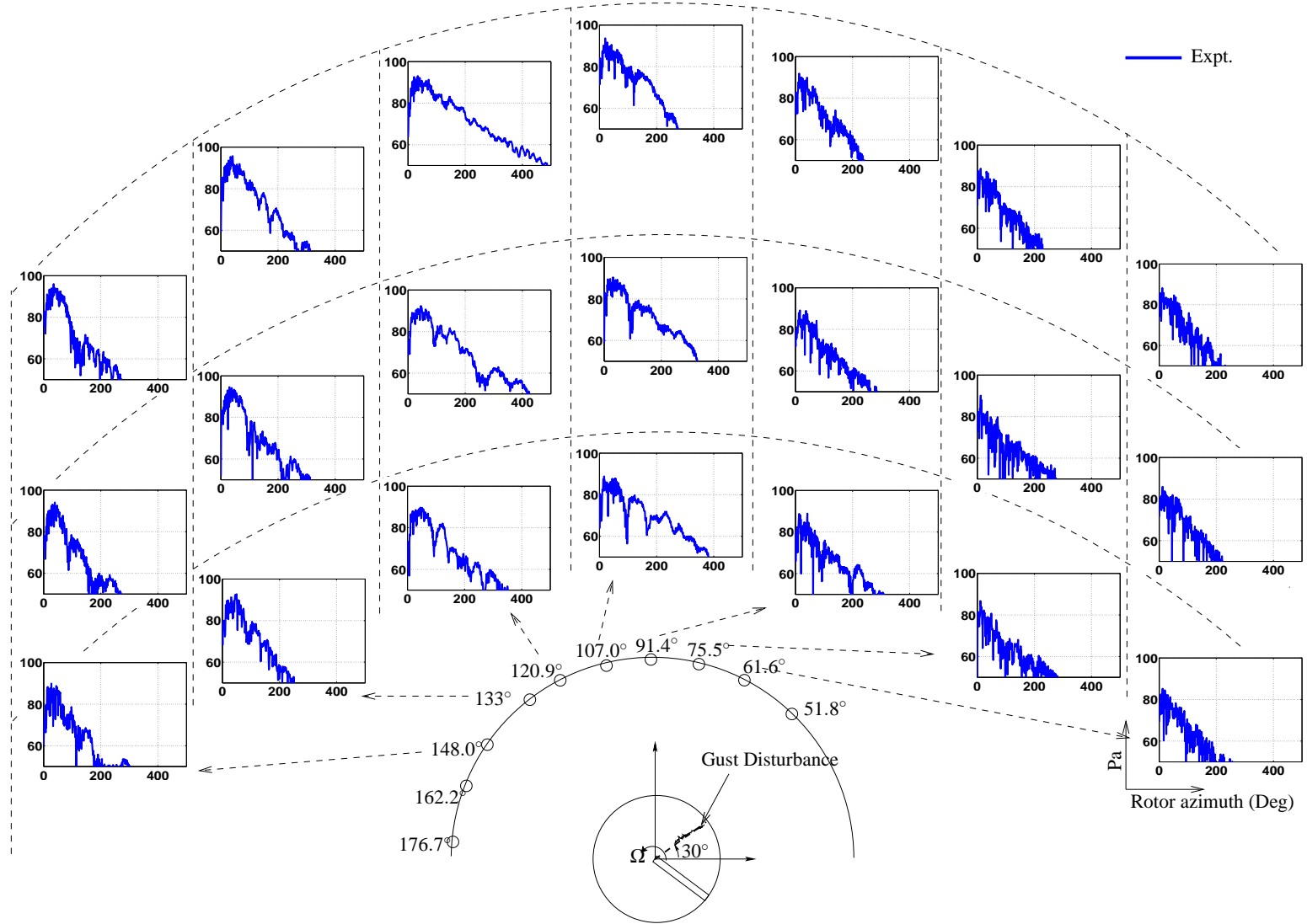


Figure 3.26: Frequency spectrum of noise at various microphones — Sound pressure in dB vs. Single-blade rotor harmonics —  
Case 3 ( $8.8^\circ$  Oblique Interaction  $M_T = 0.702$ )



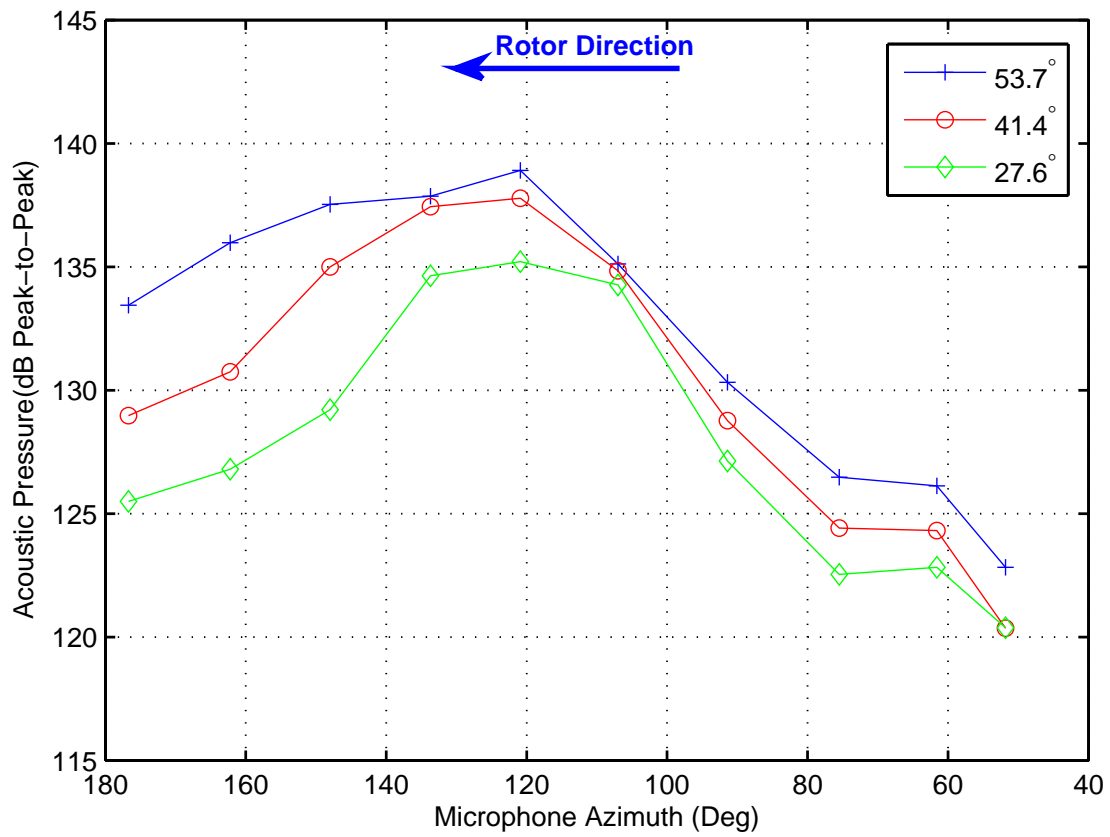


Figure 3.27: Directionality trends for Case 3 ( $M_T = 0.702$ )

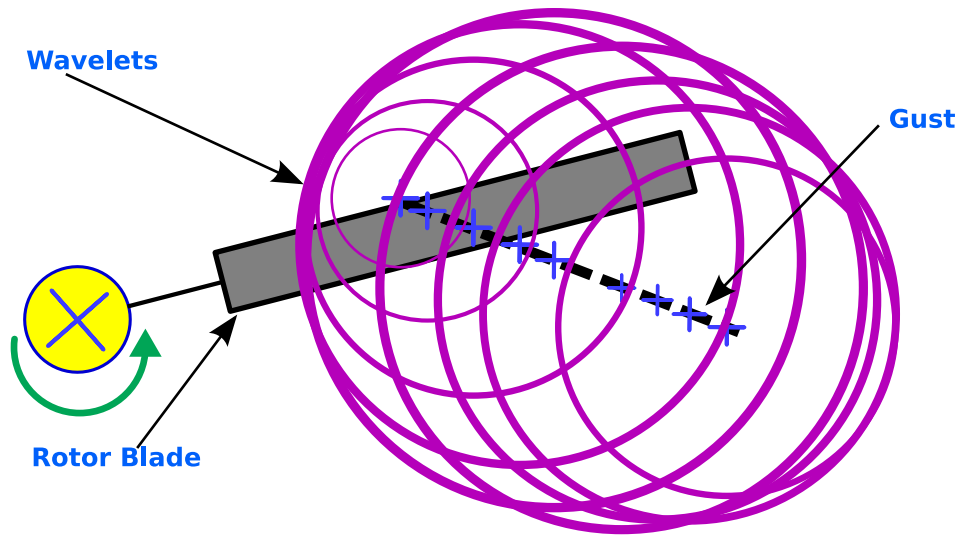


Figure 3.28: Top view of acoustic of the wavefronts for Case 4 oblique BCDI

but crosses 1 and becomes subsonic close to the 60% blade span location. This implies that the waves emanating from the triggered spanwise sources, collect close to the 60% blade span location (Fig. 3.28). These waves then propagate in the medium resulting in increase in the noise level. However, the fact that for the 0.702 tip Mach number, this process occurs at 60% blade span — where the contribution to the acoustics is relatively low — means that the final effect of this process is relatively small.

The acoustic waveform for the interaction consists of negative peak followed by a positive peak (Fig. 3.29). The negative peak is a result of the sharper edge of the gust velocity profile and hence has a higher frequency content compared to the positive side of the waveform, which is a result of the more gradual velocity gradient. Because of the wider waveform shape on the positive side of the pulse (because of the lower frequency content), there is a greater possibility of constructive interference. Thus, even if the waves from the spanwise sources are slightly out of phase, there is

a greater possibility of these waves summing up on the positive side of the waveform. This effect is seen at the  $107^\circ$  azimuth (Fig. 3.29). The positive peak for the microphone at  $27.6^\circ$  is slightly higher compared to the topmost microphone, and this results in the slightly higher peak noise levels observed from Fig. 3.31. This is also more clearly visible at the  $120.9^\circ$  azimuth location where the lowest microphone once again has a higher positive peak compared to the topmost. The microphone at  $41.43^\circ$  however, has higher negative peak compared to the other two microphones because of fortuitous constructive interference at that location.

It can be seen from Fig. 3.30 at  $120.9^\circ$  azimuth location, the microphone at  $41.4^\circ$  has a greater energy at the higher frequencies compared to the other two microphones at that azimuth. Also the frequency content is significantly higher for the microphones at the higher azimuth angles compared all the previous cases discussed this far.

Fig. 3.31 shows the variation in peak noise level expressed as decibels. Two things stand out when compared to the results of the previous interactions. Firstly, the azimuthal asymmetry is significantly higher than all the previous cases. Secondly, for some microphone azimuths, the lower microphones actually, record a greater noise level. This is purely because of the simultaneous and in-phase addition of the waves from a greater region of the blade span at the lower microphones than at the higher ones.

For the microphones at  $120.9^\circ$  azimuth the acoustic waves from the last 10% of the blade span arrive simultaneously at the microphone that is  $41.4^\circ$  location resulting in higher noise levels. At the other elevations the acoustic waves from the blade tip arrive somewhat out of phase, resulting in higher noise levels at the second microphone at the  $120.9^\circ$ .

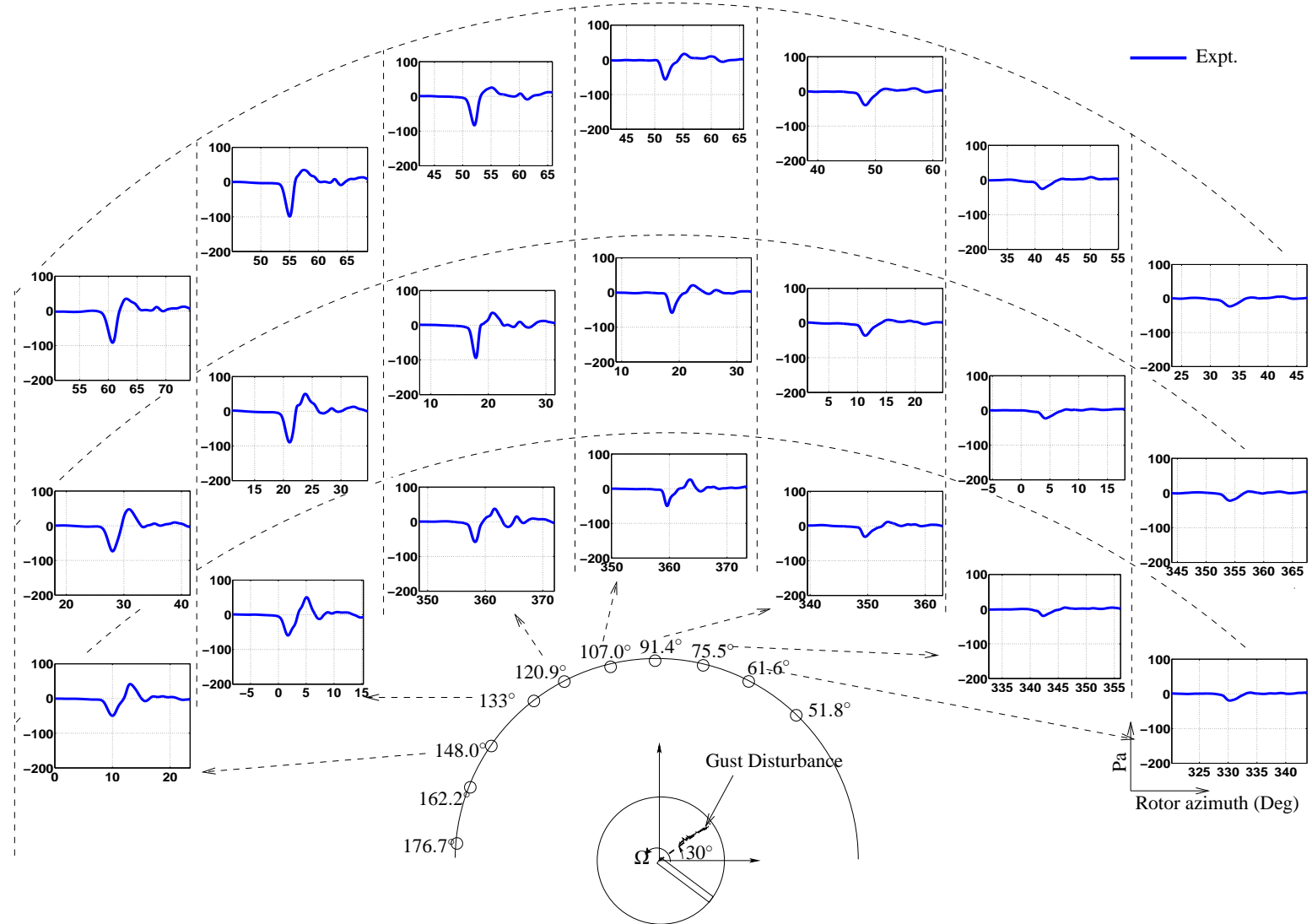


Figure 3.29: Acoustic time histories at the various microphones in terms of Acoustic Pressure (in Pa) vs. Rotor Azimuth (in Deg)

— Case 4 ( $15.3^\circ$  Oblique Interaction  $M_T = 0.702$ )

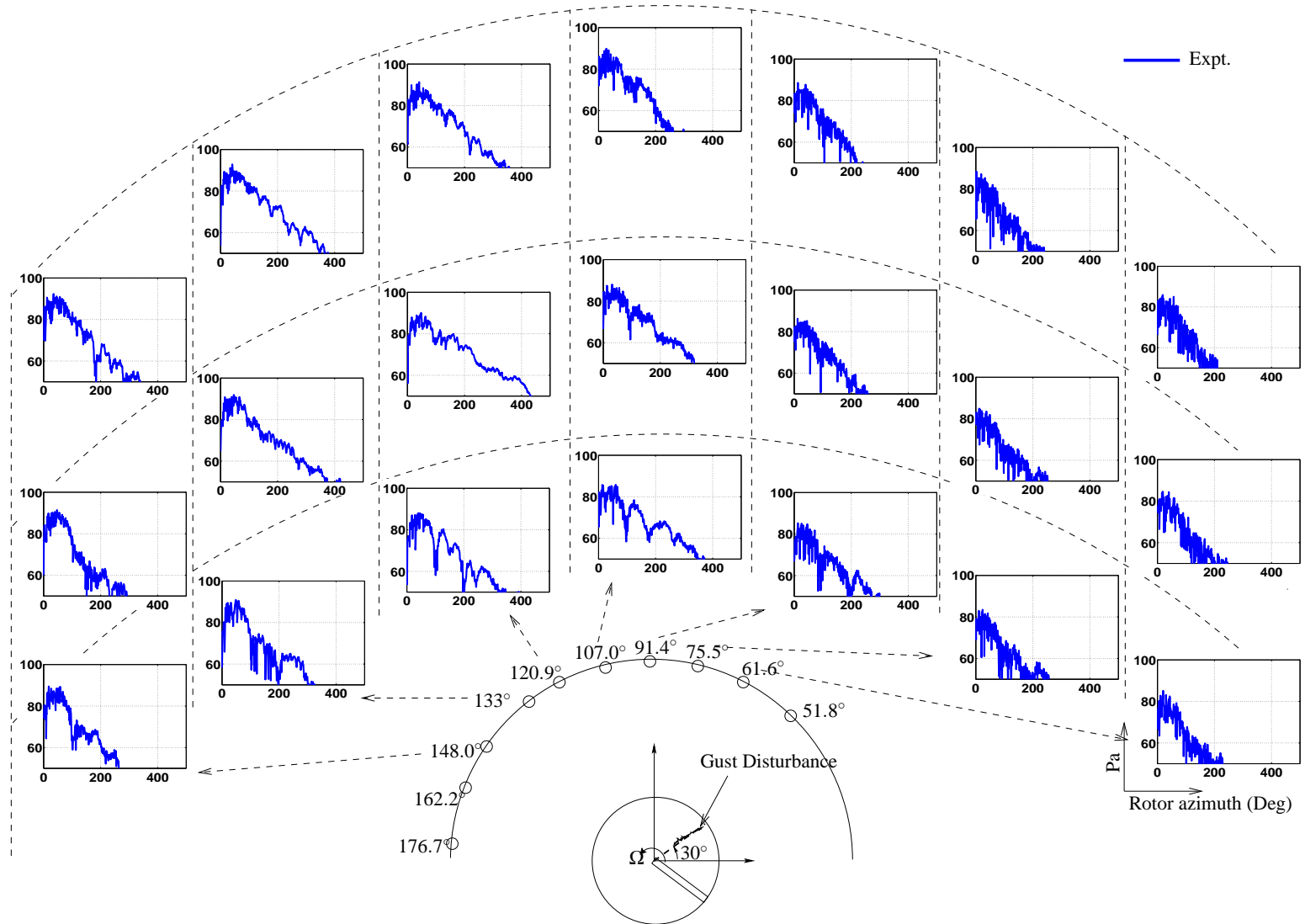


Figure 3.30: Frequency spectrum of noise at various microphones — Sound pressure in dB vs. Single-blade rotor harmonics —

Case 4 ( $15.3^\circ$  Oblique Interaction  $M_T = 0.702$ )

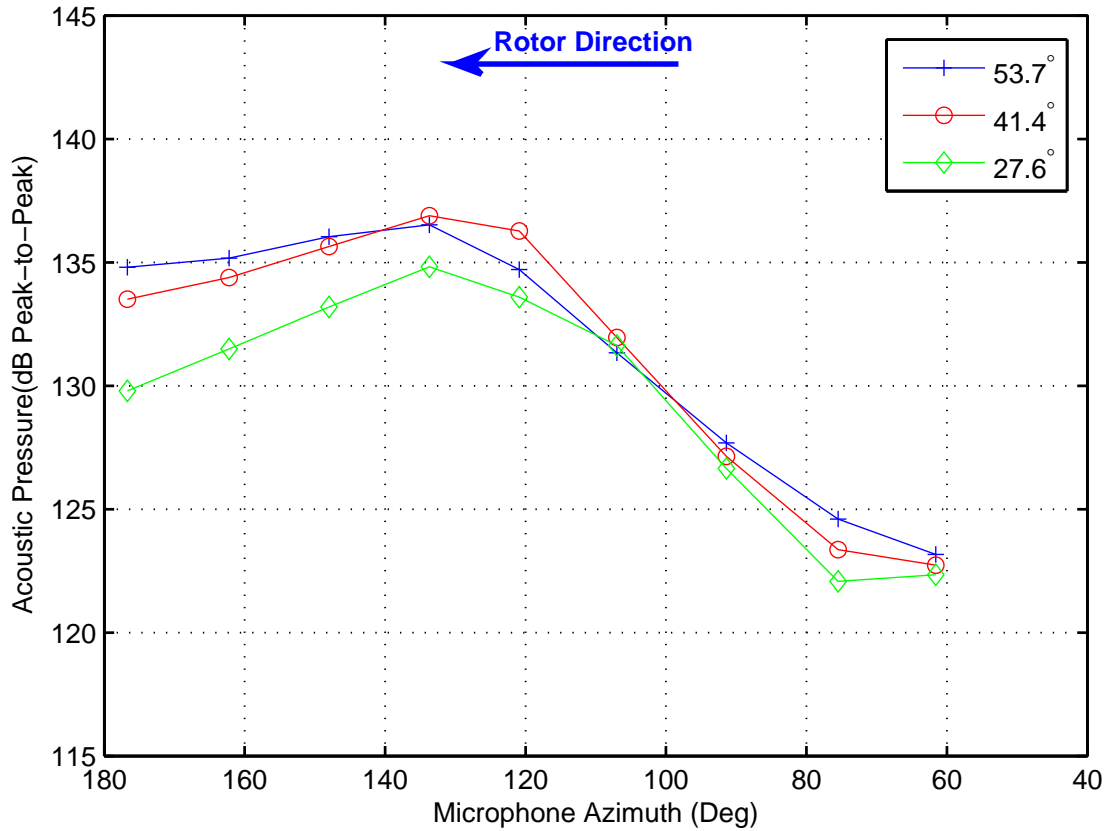


Figure 3.31: Directionality trends for Case 4 ( $M_T = 0.702$ )

A similar situation occurs at  $107^\circ$  azimuth resulting in the lowest ( $27.6^\circ$ ) elevation microphone having a higher noise level compared to the topmost microphone ( $53.7^\circ$ ).

### 3.5 Effect of Interaction Angle on Noise Levels

Previous researchers have studied the acoustics and the aerodynamics of the parallel interaction in controlled environments of the wind tunnel. For the first time, in this experiment a comparison between various interaction angles can be performed.

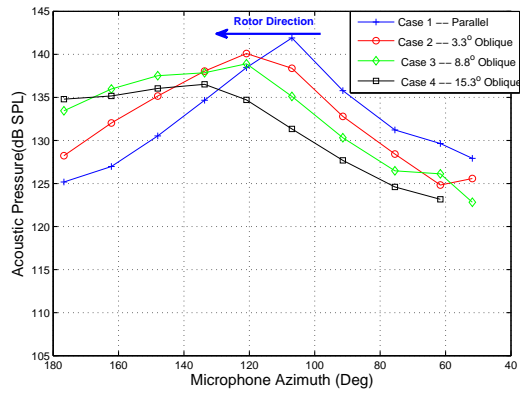
As before the tip Mach number of 0.702 is used for this comparison. Fig. 3.32 shows the vari-

ation with interaction angle for all the microphone locations. Clearly, for a given elevation above the rotor plane, the parallel interaction has the maximum peak noise level across the azimuthal angles. However, the parallel interaction has a sharp peak at the  $107^\circ$  azimuth and then falls off rapidly on either side for all elevations.

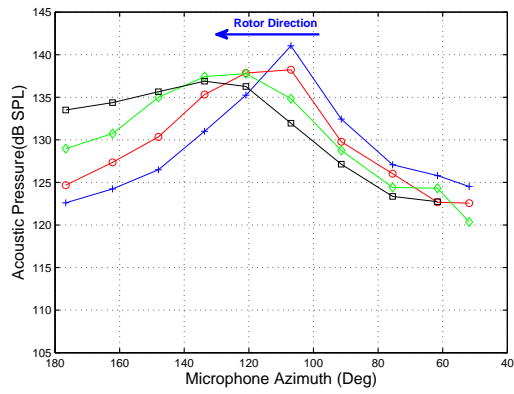
The oblique interactions have a lower peak noise level at a given elevation, but the azimuthal variation is shallower and the noise levels tend to fall off less rapidly, particularly along the direction of the trace Mach number. With the oblique interaction starting out at  $15.3^\circ$  at the blade tip (Case 4), the peak noise levels roll off very slowly at higher microphone azimuths. In fact, the noise levels are higher for higher interaction angles at microphone azimuth locations greater than about  $120^\circ$ . The acoustic energy is therefore, spread out over much wider azimuthal area (towards the direction of the acoustic trace velocity). Moreover, as noted earlier, as the interaction angle increases, the noise levels at the lower elevations can increase above that at the higher elevations (Fig. 3.31).

### **3.6 Effect of tip Mach number on Case 4 ( $15.3^\circ$ ) Oblique BCDI**

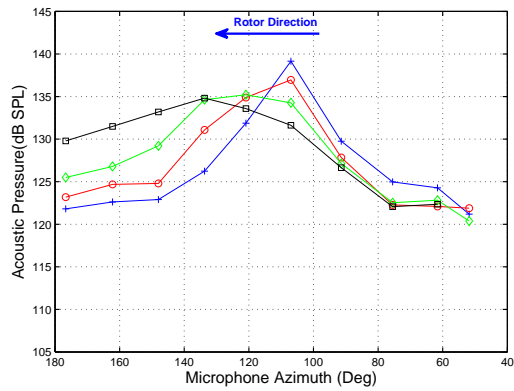
The acoustics directivity is a strong function of the tip Mach number for the parallel interaction. As discussed earlier, the noise level increases with increase in tip Mach number. It did not result in any significant change in the directionality patterns, either along the azimuthal or elevation directions. The noise level trends in the elevation direction were directly related to the dipole nature of the spanwise acoustics sources. The  $53.7^\circ$  elevation microphone always had the highest noise level, followed by the  $41.4^\circ$  and the  $27.6^\circ$  elevations microphones, at any given azimuthal location. The noise levels were affected because increase in the impulsiveness of the event as the



(a) Microphone elevation =  $53.75^\circ$



(b) Microphone elevation =  $41.43^\circ$



(c) Microphone elevation =  $27.60^\circ$

Figure 3.32: Variation of peak-to-peak noise levels with interaction angle ( $M_T = 0.702$ )



tip Mach number was increased. The oblique interaction, however, is different. Changing the tip Mach number when keeping the interaction angle constant, changes the trace Mach number and hence phasing. This results in differences in directionality trends both along the azimuth and elevation.

Fig. 3.33 shows the trace Mach number for the five tip Mach numbers studied. As the tip Mach number decreases, the percentage of the blade near the sonic region of the trace Mach number also increases. More importantly, the trace Mach number crosses the sonic point closer to the tip of the blade as the tip Mach number is reduced. Thus, the relative contribution of the acoustic sources in phase increases closer to the rotor plane with the reduction in tip Mach number for a given interaction angle.

Fig. 3.34 shows the directionality trends for four of the tip Mach numbers — 0.614, 0.658, 0.702 and 0.768, respectively. It can be seen that for tip Mach numbers of 0.614 (Fig. 3.34(a)) and 0.658 (Fig. 3.34(b)), the noise levels at the  $41.4^\circ$  elevation microphone are greater than at other elevations over much larger azimuthal range compared to both the  $M_T = 0.702$  (Fig. 3.34(c)) and  $M_T = 0.768$  (Fig. 3.34(d)). Moreover, the noise levels at the  $27.6^\circ$  elevation microphone and the  $53.7^\circ$  microphone are close to each other over a wider azimuthal range. Once again, as explained earlier, this is due to the phasing of the spanwise acoustic sources.

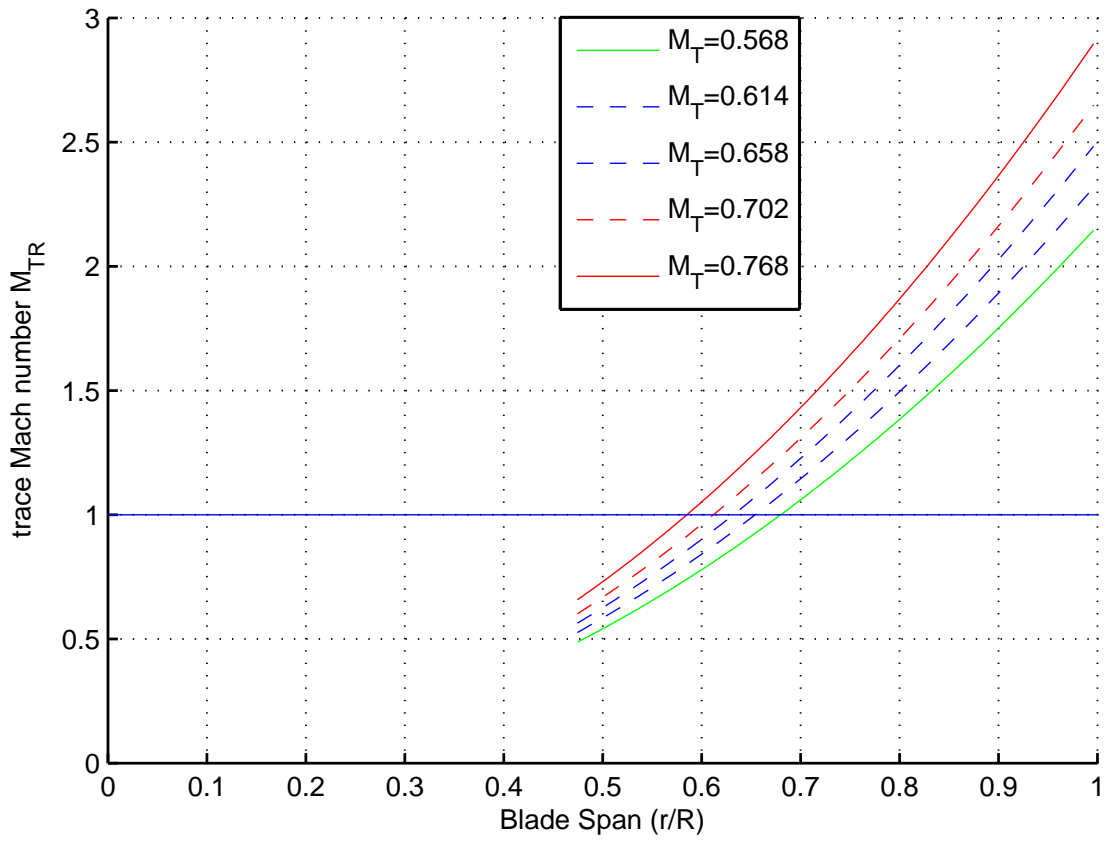
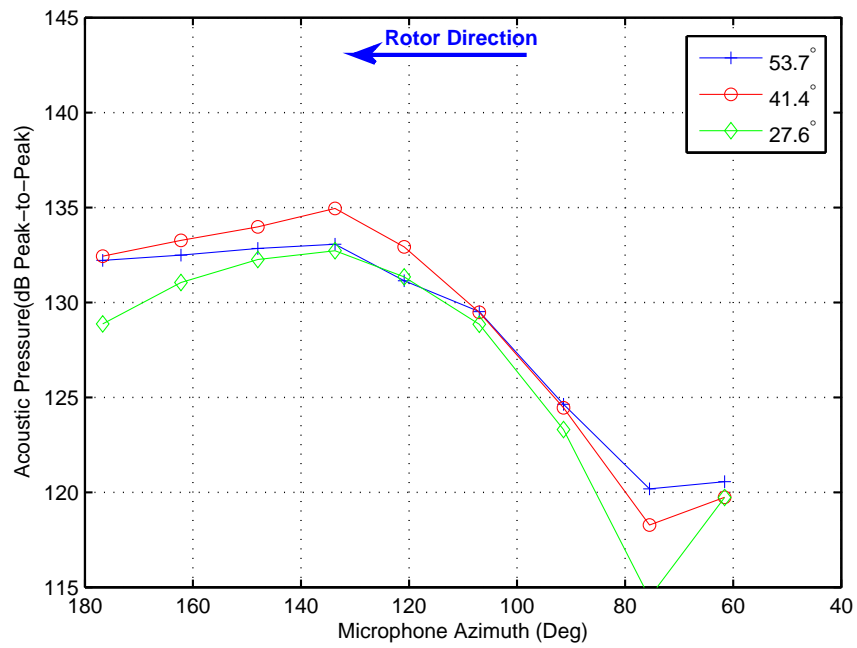
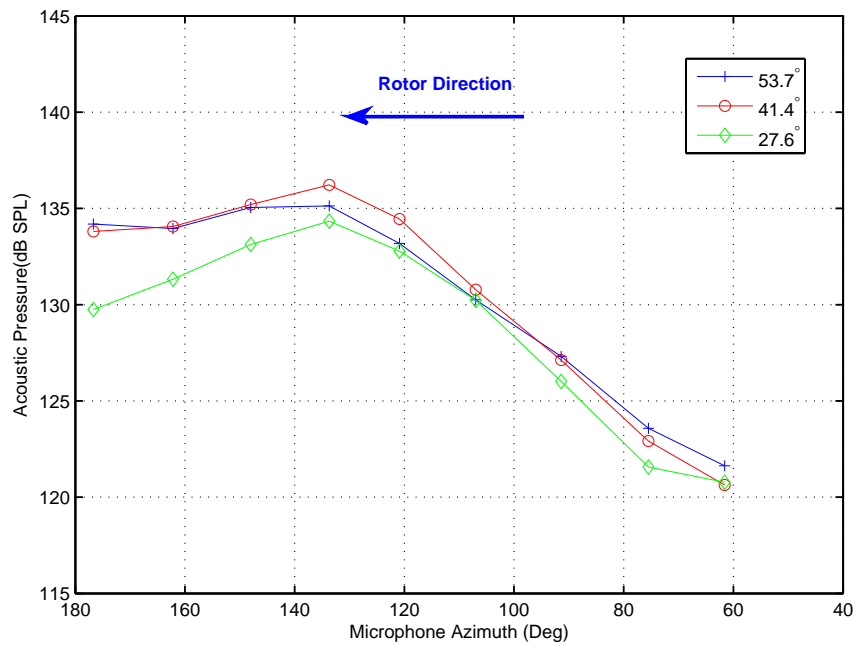


Figure 3.33: Variation of trace Mach number as function of tip Mach number — Case 4 oblique

BCDI

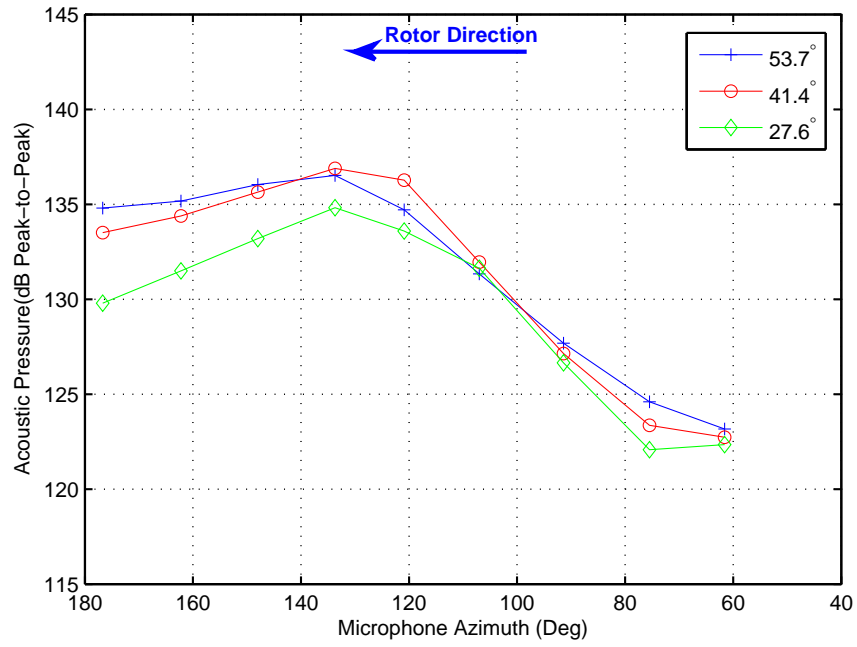


(a)  $M_T = 0.614$

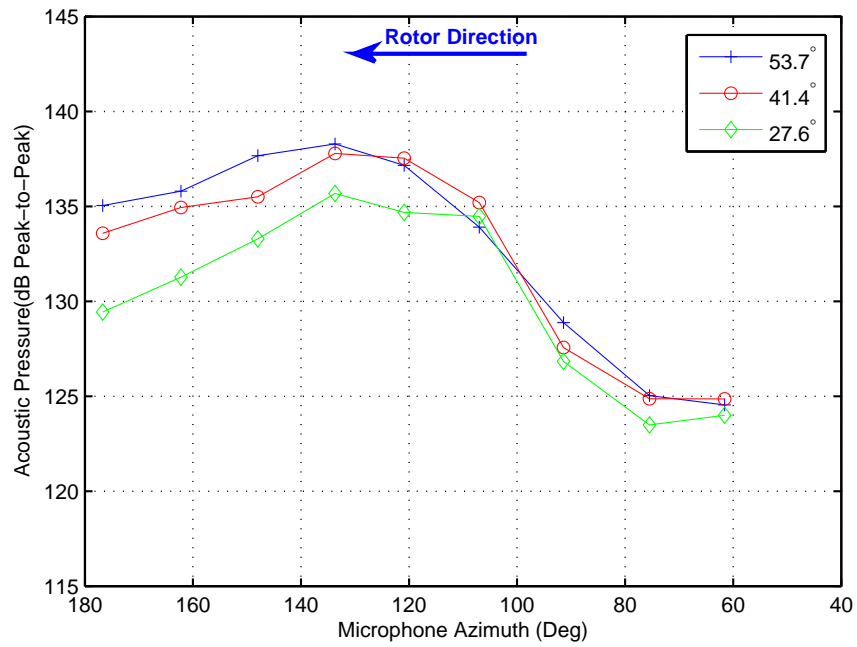


(b)  $M_T = 0.658$

Figure 3.34: Acoustic directivity variation with tip Mach number — Case 4 ( $15.3^\circ$  Oblique BCDI)



(c)  $M_T = 0.702$



(d)  $M_T = 0.768$

Figure 3.34: (Cont'd) Acoustic directivity variation with tip Mach number — Case 4 ( $15.3^\circ$  Oblique BCDI)

## Chapter 4

### Theoretical Comparison

#### 4.1 Theoretical Approach

The experimental results presented in Chapter 3 show that the acoustics is a very strong function of the phasing of the spanwise sources distributed on the blade during the time of the interaction. Using the data recorded from the microphones alone, it is not always possible to understand clearly the contributions of the blade span-sections to acoustic time histories. Understanding the phasing of these blade spanwise acoustic sources, could have implications to quiet blade designs — both passive and active techniques — by modifying the relative phasing of the sources to reduce noise radiation in certain directions. A thorough investigation of the radiation characteristics during BVI requires a comprehensive and detailed understanding of the unsteady surface pressure distribution on the rotor blade. This requires a comprehensive three-dimensional CFD analysis of the experiment, followed by a solution to the Ffowcs-Williams and Hawking's equation (Eqn. 1.6) using the off-surface formulation, and is beyond the scope of this dissertation. However, simpler

approaches such as the indicial method has been used in the past to understand BVI aerodynamics and acoustics. It has been shown [28, 29] to predict with reasonable accuracy the magnitude and pulse shape of the acoustic pressure for the parallel interaction. This approach is used here to study the acoustics as it is easier to implement as well as being much faster than a CFD simulation.

#### 4.1.1 Linear Unsteady Indicial Aerodynamics

A simpler approach, geared primarily towards understanding the phasing effects of the acoustics, can be implemented using a simpler unsteady aerodynamics approach which provides integrated sectional loads on the blade rather than a full surface pressure history. One such approach is the unsteady indicial approach developed used initially by Beddoes [27], and later extended by Leishman [28, 29] for studying helicopter BVI noise. The unsteady indicial theory involves estimating the two-dimensional airfoil response to a step change in induced velocity on the airfoil. This indicial function can then used to calculate the blade loads for an arbitrary induced velocity using the Duhamel's integral.

The indicial function used on the present study is one derived by Leishman [29] and is of the form:

$$\phi_g(s) = 1 - G_1 e^{-g_1 t} + G_2 e^{-g_2 t} \quad (4.1)$$

where  $G_1$ ,  $G_2$ ,  $g_1$  and  $g_2$  are the indicial coefficients, and  $\phi_g(s)$  is the indicial response as a function airfoil semi-chord,  $s$ . By choosing the indicial coefficients judiciously, compressibility effects at moderately high Mach numbers can be accounted for. The indicial coefficients used in this study (Table 4.1) are those derived by Leishman [29] by comparing the step response of the airfoil

using two-dimensional CFD analysis of the Kitapliouglu and Caradonna [84] wind tunnel BVI experiment. The Duhamel's integral for the change in lift coefficient is solved using a recursive

$G_1$	$g_1$	$G_2$	$g_2$
0.67	0.1753	0.33	1.637

Table 4.1: Coefficients of the Indicial gust function,  $\phi_g$

algorithm [15]:

$$Z_1(s) = Z_1(s - \Delta s)e^{-g_1\beta^2\Delta s} + G_1 [w_g(s) - w_g(s - \Delta s)] \quad (4.2)$$

$$Z_2(s) = Z_2(s - \Delta s)e^{-g_2\beta^2\Delta s} + G_2 [w_g(s) - w_g(s - \Delta s)] \quad (4.3)$$

$$\Delta C_l(t) = \frac{2\pi}{\beta} \frac{1}{V} [w_g(s) - Z_1(s) - Z_2(s)] \quad (4.4)$$

where,  $\beta$  is the Glauert factor given as

$$\beta = \sqrt{1 - M_\infty^2} \quad (4.5)$$

To capture the effect of the spanwise distribution of lift, the outer 50% of the blade is divided into 50 spanwise lifting elements. The three-dimensionality due to the tip vortex is accounted for by employing the Weissinger-L approach [87], a schematic of which is shown in Fig. 4.1. The Weissinger-L model is a vortex method with one horseshoe vortex for each blade section. The vortex is placed at the quarter chord location and the induced velocity is evaluated at the three-quarter chord location of the airfoil. This approach accounts for the three-dimensional effect of the tip vortex. The induced velocity on the blade used for the aerodynamic calculations is the measured vertical velocity field at the blade passage location, presented earlier in section 2.3.2 (Fig. 2.13(a)).

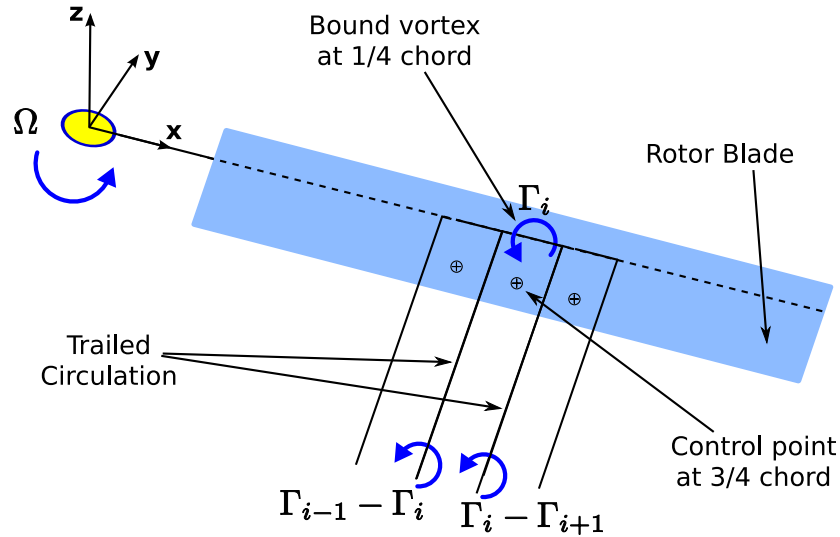


Figure 4.1: Weissinger-L lifting line model for the rotor blade

#### 4.1.2 The Acoustics Formulation

As discussed later in Chapter 3 the process of subtracting the effect of the nozzle also removes the thickness noise from the the resulting acoustics. Thus for comparison, only the acoustic contribution from the blade loading needs to be calculated. The sectional lift coefficient can be directly used to estimate the radiated noise using the loading noise terms of Farassat's formulation 1A [55]. This formulation of the Ffowcs-Williams and Hawking's equation is dependant on the force exerted by the body on the surrounding medium (which is equal and opposite to the lift force on the airfoil), and is dependant only on the source time (equal to rotor angular velocity in rad/s divided by the rotor azimuth in radians). The acoustic pressure at the observer location is calculated by repeated evaluation of the integrands in Eqn. 4.6 at the correct retarded time [55] over the blade surface for each spanwise blade element and summed up to arrive at the acoustic pressure at the



required observer time.

$$\begin{aligned}
4\pi p_L(\vec{x}, t) &= \frac{1}{a} \int \left[ \frac{\dot{l}_i \hat{r}_i}{r_{obs}(1-M_r)^2} \right]_{ret} dS + \int \left[ \frac{l_r - l_i M_i}{r_{obs}^2 (1-M_r)^2} \right]_{ret} dS \\
&+ \frac{1}{a} \int \left[ \frac{l_r (r_{obs} \dot{M}_i \hat{r}_i + a M_r - a M^2)}{r_{obs}^2 (1-M_r)^3} \right]_{ret} dS
\end{aligned} \tag{4.6}$$

where  $l$  is the sectional load on the blade, and the dots on  $l_i$  and  $M_i$  denote the derivative with respect to source time. The integrands are bracketed within  $[\dots]_{ret}$  to reinforce the fact that the terms are to be evaluated at the correct retarded times. The first term in the equation varies as  $1/r_{obs}$  with the observer distance from the source, and decays more slowly compared to the other two terms, which decay as  $1/r_{obs}^2$ . The first term is therefore, referred to as the far-field term, while the last two terms are referred to as the near-field term and do not have a significant contribution far away from the source, although the actual computational results includes all the terms.

When evaluating the surface integral in Eqn. 4.6, if the blade is discretized only along the spanwise direction, the acoustic representation is said to be “non-compact” (distributed) in span, and “compact” (acting at a point) in chord. A more detailed acoustic representation is to distribute the acoustic sources in the chord-wise direction, as well as in the spanwise direction. This acoustic modeling of the problem is said to be “non-compact” in both the spanwise and chord-wise directions. Strictly speaking, the unsteady aerodynamics and the acoustics of the problem should be consistent at all levels. This requires that the unsteady aerodynamic solutions be fully three-dimensional and “non-compact” when non-compact solutions to the acoustic problem are employed. However, this approach has not been studied in this thesis because of the added complexity involved. Nevertheless, some of the important effects of acoustic compactness can be explored by assuming a chordwise pressure distribution over the blade surface. Various pressure

distributions including triangular distribution [88], two-point chordwise distribution and the analytical flat plate pressure distribution in incompressible flow [28] have been used by previous researchers. In this dissertation, the sectional lift coefficient obtained from the indicial model was converted to a chordwise differential pressure distribution on the mean chord using a flat plate model, and is given by:

$$\Delta C_P = \frac{2C_l}{\pi} \sqrt{\frac{1-x}{x}} \quad (4.7)$$

where  $x$  is the chordwise station non-dimensionalized with respect to the local airfoil chord.

Distributing the acoustic sources over the chord result in a non-zero time interval between the arrival of the acoustic waves at the microphone from the successive chord-wise sources. For the case of the parallel interaction, this results in a wider waveform of lesser magnitude compared to the compact chord acoustics, as can be seen in Fig. 4.2. The non-compact chord predictions are much closer to the measured data, both in magnitude and pulse width. However, the non-compact formulation does not have the same effect at all microphone locations. Microphones near the peak impulsive noise azimuth angle and those located nearer to the plane of rotation see the largest reduction. Microphones located away from the peak level directivity see much lower reductions in pulse amplitude.

A microphone at  $\psi = 107^\circ$  and in the plane of the rotor would see the chordwise section “straight on” resulting in a finite time interval between the arrival of the chord-wise pulses. While a microphone at the same azimuth but out of the rotor plane would see the blade such that the chord-wise sources are almost equidistant from the microphone resulting in an almost simultaneous arrival of the pulses. Thus, this case would result in a lesser difference between the compact

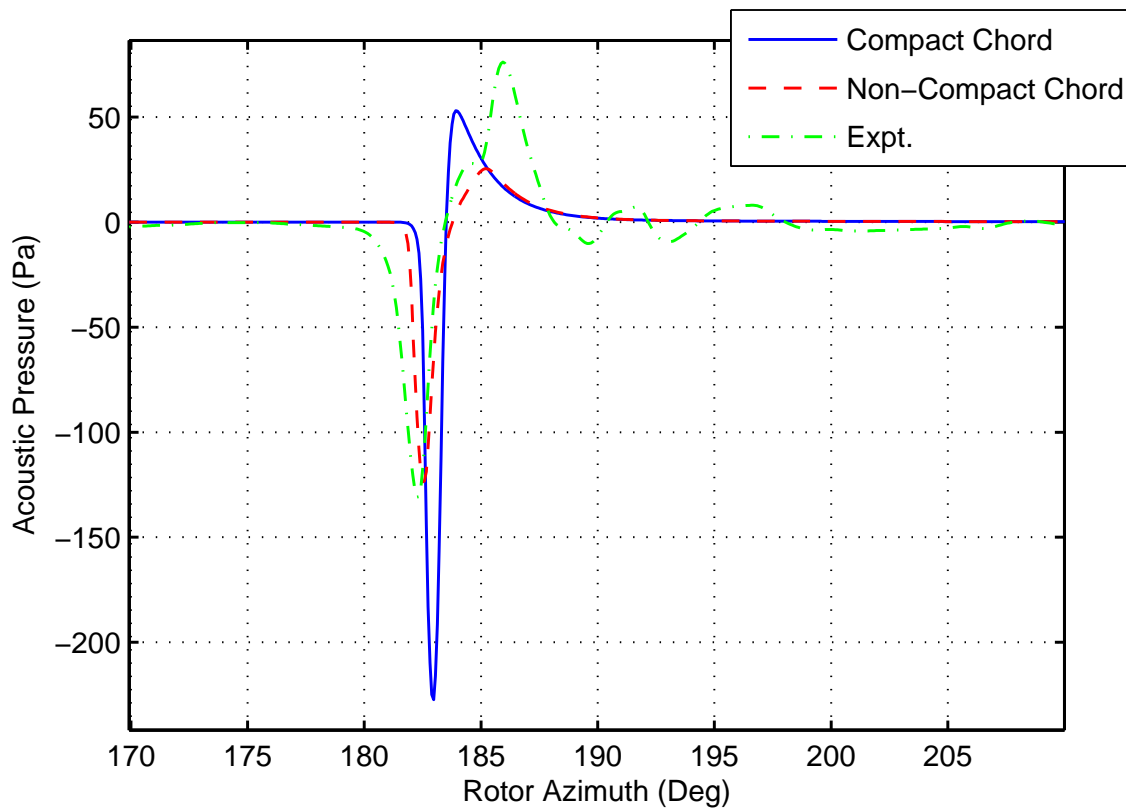


Figure 4.2: Comparison between compact and non-compact chord approaches — Parallel Interaction at  $M_T = 0.702$  ( $\psi = 107^\circ$  &  $\theta = 53.75^\circ$ )

and non-compact chord predictions compared to the microphone nearer to the rotor plane. A similar argument can be applied for variation in the azimuth location of the microphone. This result is presented in Fig. 4.3 as a plot of the difference in sound pressure level between the compact and non-compact approaches versus microphone azimuth angle for the three elevations. At the peak noise azimuth, the difference could be as much as 5dB at lower elevation levels. The difference between the compact and the non-compact chord approach reduces slightly as the interaction becomes more oblique, but the difference remains as high as 5dB for the lowest microphone even for the Case 4 BCDI (Fig. 4.4). At higher microphone elevations, the spanwise phasing becomes more important for the oblique interaction and the difference between the compact chord approach and non-compact chord approach reduced significantly. See Appendix D for time history comparisons between the compact and non-compact chord formulations.

## 4.2 Comparison with Experiment — Parallel Interaction

Fig. 4.5 shows the time history comparisons at some of the microphone azimuths at the three different elevation angles. For some cases, in particular for microphones at  $\psi = 107^\circ$  and  $\psi = 120.9^\circ$ , the time histories from the theoretical predictions do not overlap with the experimental observations precisely. This is possibly a result of inaccuracies in the measurement of the microphone coordinates with respect to the rotor during the interaction. There is an error of up to  $3^\circ$  of rotor azimuth in the time histories. For the case under consideration in Fig. 4.5, the rotor is spinning at a frequency of 40Hz. This translates to an error of 2.5% in the distance from the microphone to the rotor hub. Although great care was taken to accurately, position the microphone,

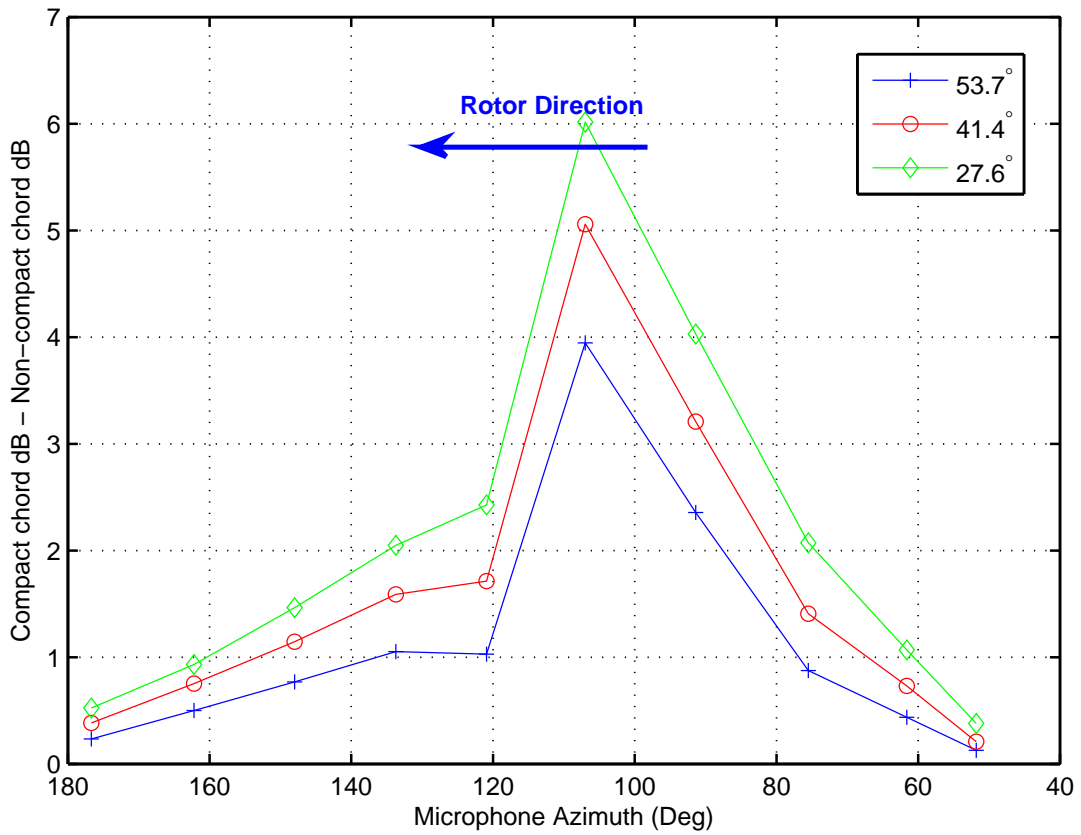


Figure 4.3: Difference in peak-to-peak sound pressure between compact and non-compact approaches — Case 1 parallel BCDI at  $M_T = 0.702$

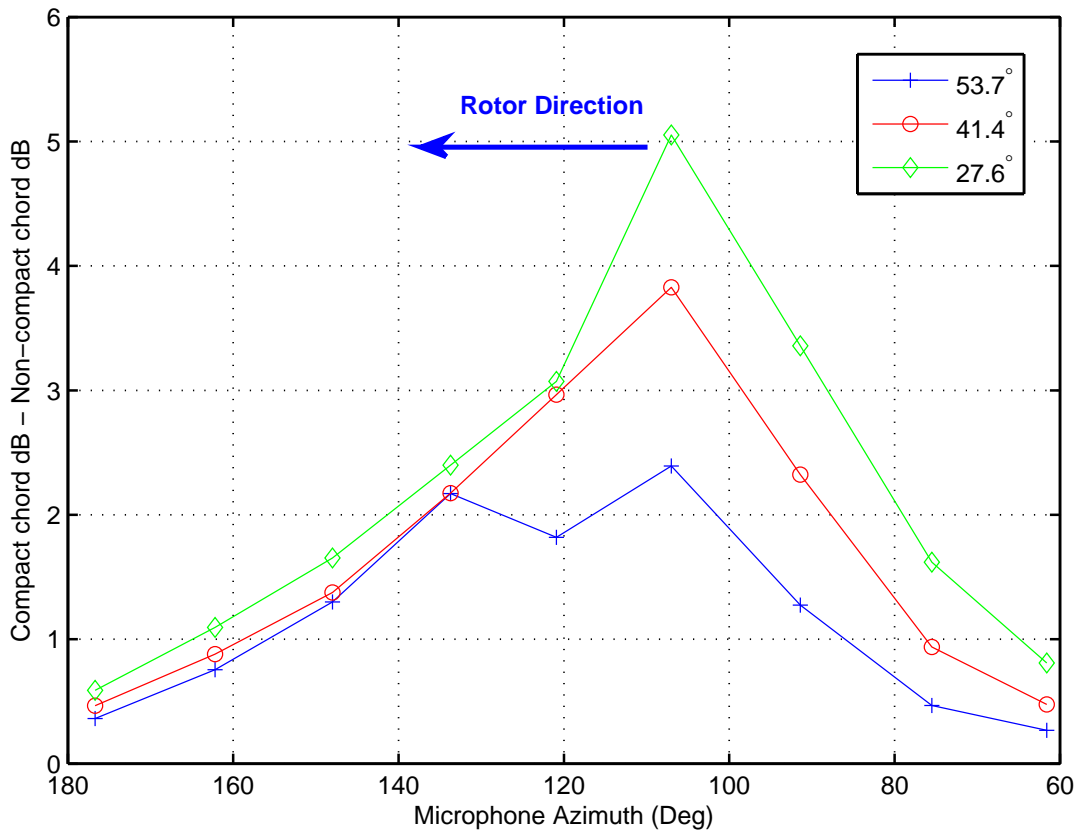


Figure 4.4: Difference in sound pressure between compact and non-compact approaches — Case 4 (15.3° Oblique BCDI) at  $M_T = 0.702$

the fact that the microphone array needed to be moved frequently, resulted in some inaccuracies in the positions. However, as can be seen, these errors are still within acceptable range to make reasonable comparison between the theory and the experiment.

As discussed earlier, the pulse shapes obtained in the experiment, have a strong negative peak followed by a positive peak. The positive peak is most prominent close to the peak noise azimuth of  $107^\circ$  and is smaller in magnitude for other microphone azimuths. The theory tends to predict the negative peak very closely for all the microphone locations. However, the positive peak is under predicted for all the cases. It should be noted that the width of the gust is about half the blade chord, implying that there is a point of time during the interaction when the chord stations ahead of the quarter chord point experience no gust field, while stations behind the quarter chord location experience a strong upwash from the gust. The unsteady indicial model, being a compact chord aerodynamic approach cannot account for such steep gradients along the chordwise direction. The indicial approach nevertheless, captures the negative pulse of the acoustic history as this event is dominated by the leading edge of the airfoil.

Fig. 4.6 shows the directionality trends computed using the linear indicial theory approach for the parallel interaction for the tip Mach number of 0.702. Firstly, for the parallel interaction case, the general azimuthal directionality at the three elevations are captured reasonably well by the non-compact chord theoretical approach. The peak noise occurs at the same azimuth ( $\psi = 107^\circ$ ) location for all the elevations as in the experimental case. The azimuthal directivity has a sharper peak at  $\psi = 107^\circ$  and rolls off more rapidly compared to the experimental results.

The theoretical results, however, under predict the noise. For microphone positions that are at

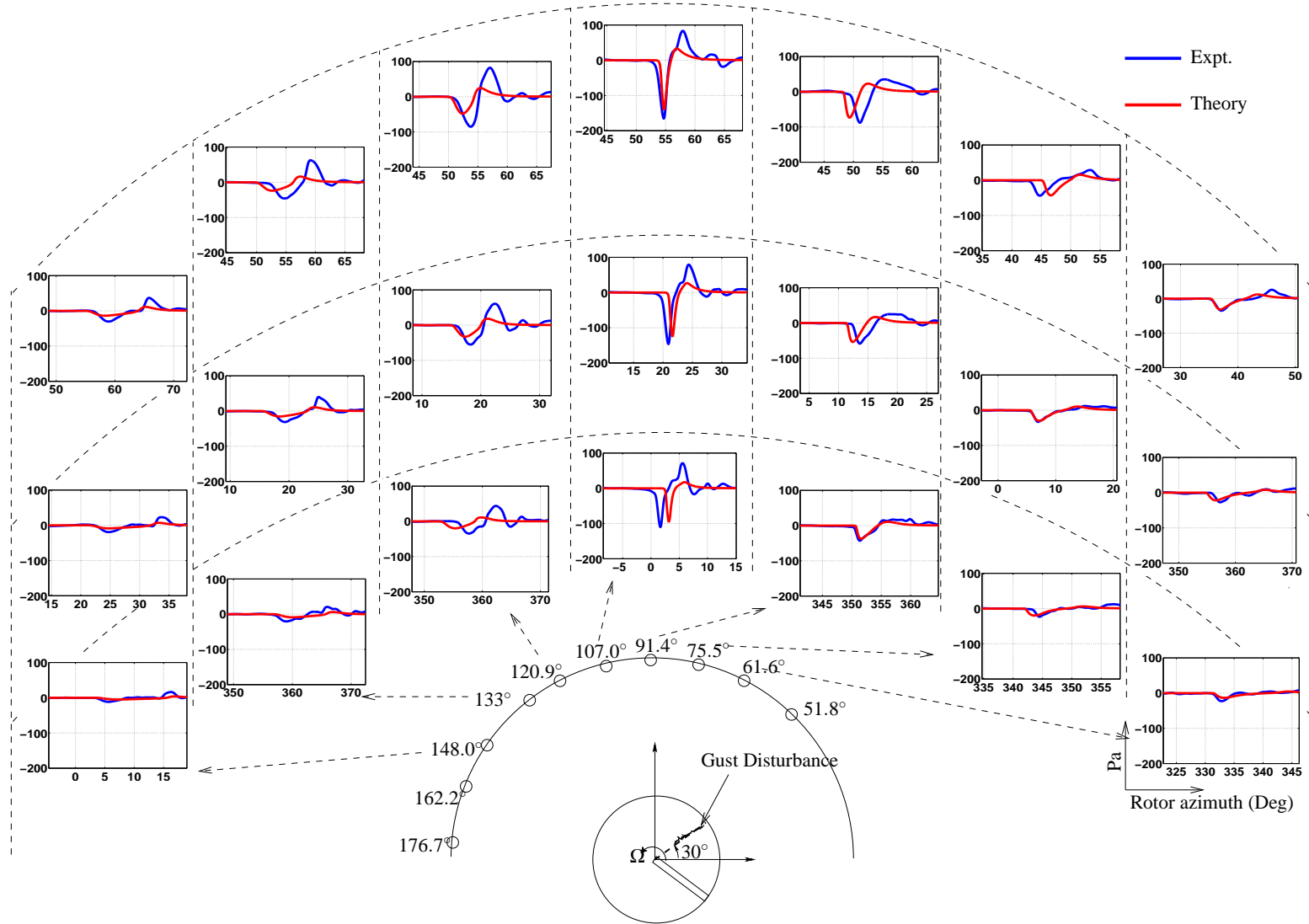


Figure 4.5: Acoustic time histories at the various microphones in terms of Acoustic Pressure (in Pa) vs. Rotor Azimuth (in Deg)

( $M_T = 0.702$  — Parallel Interaction)



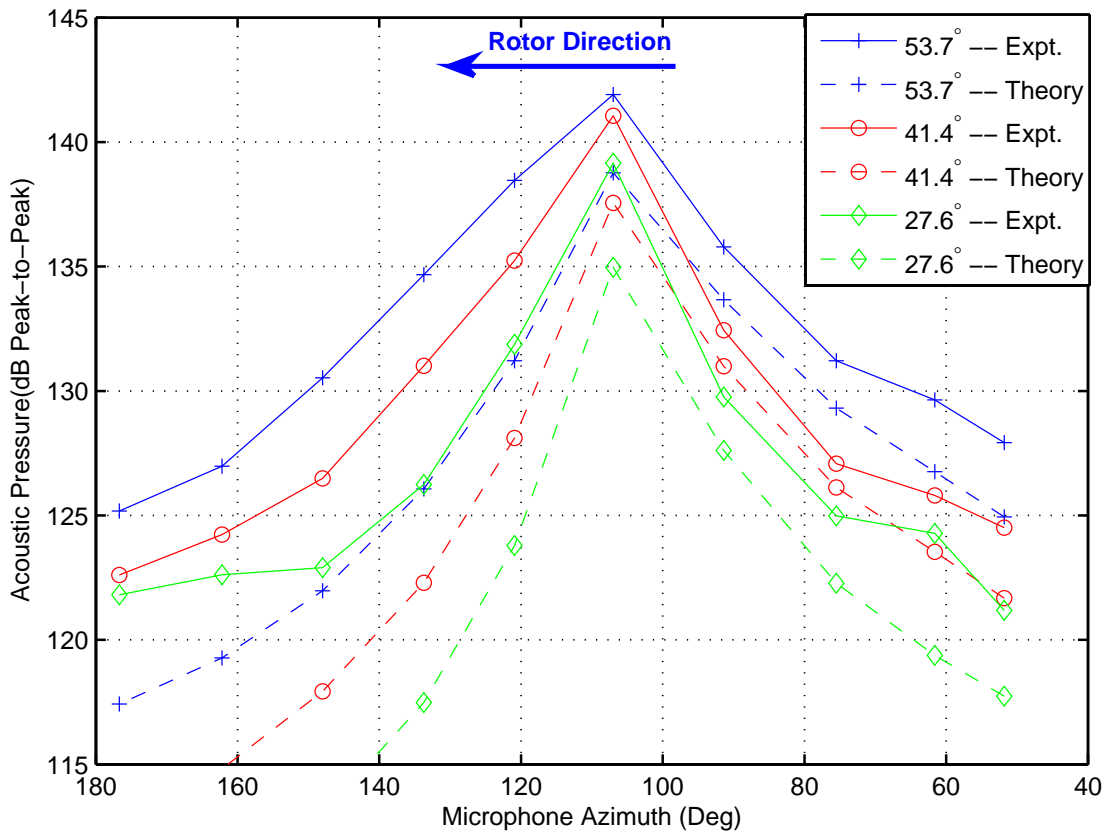


Figure 4.6: Comparison of the directionality trends between theory and experiment for the parallel interaction ( $M_T = 0.702$ )

lower azimuth angles compared to the peak noise azimuth, i.e.  $\psi \leq 107^\circ$ , the theory under predicts by less than 3dB. However, for microphone azimuths above  $107^\circ$ , the difference increases and can be as high as 6dB in some cases. This difference between the theory and experiment is mostly because the theory does not predict the second positive peak in the acoustic time history.

One of the main advantages of using a simple theoretical formulation is the ability to study the spanwise phasing and its effect on the radiation pattern of the acoustic energy. Fig. 4.7 shows the spanwise contribution for blade elements at 5% spanwise distance from the each other (every fifth element start on the rotor blade). As can be seen in all the figures, the contribution from the blade element at 95% span station is slightly smaller than the contribution from the 90% span station. This is due to three-dimensional effect of the tip vortex modelled by the Weissinger-L approach. Apart from the contribution from the element near the blade tip, all the other contributions scale directly with the local sectional Mach number. As can be seen, the blade sectional element at 50% span contributes a significantly lesser amount to the over all noise levels, due to the lower sectional Mach number. The acoustics of inner 50% of the blade span is not computed as the contribution is very small. Moreover, in the experiment, the inner 50% of the blade does not experience the gust interaction.

Figs. 4.7(a)-4.7(c) correspond to the microphone just to one side of the peak noise azimuth. It can be seen that the acoustic waves from the blade tip arrive at this microphone azimuth location earlier than from further inboard of the blade. At the peak noise azimuth location ( $\psi = 107^\circ$ ) shown in figs. 4.7(d)-4.7(f), all the waves from the spanwise sources arrive simultaneously, resulting in the sharp acoustic time history seen in Fig. 4.5. This microphone location corresponds to the

wavefront of the acoustic wavelets sketched in Fig. 3.13. The arrival of these pulse is the same at all the three microphone elevations because the trace Mach number is infinity for this case. The simultaneous in-phase summing of the pulse at this location results in strong and sharp acoustic pulse.

At microphone azimuth locations greater than  $107^\circ$  (Figs 4.7(g)-4.7(l)), the acoustic waves from the inboard blade section arrive earlier than from the tip of the blade. This results in the overlapping of the positive acoustic peak from the spanwise sections further inboard with the negative peaks of the waves from the sections closer to the tip of the blade. This results in some destructive interference leading to the reduction in noise. A similar situation occurs for the microphones at  $\psi = 133.7^\circ$ . The difference in the interference of the spanwise acoustic waves, before and after the peak noise azimuth explains to some extent the asymmetry (the sharper fall off noise for  $\psi > 107^\circ$ ) observed in Fig. 4.6.

## **4.3 Oblique Interactions**

### **4.3.1 Case 2 — $3.3^\circ$ Oblique BCDI**

A comparison of the time histories in Fig. 4.8 shows that negative peak of the acoustic pulses is reasonably well captured at most location, except at the lowest microphone location for  $\psi > 120^\circ$ . However, just as in the parallel interaction case, the positive peak of the acoustic pulse is notably under-predicted by the theory, and results in the smaller decibel value shown in Fig. 4.9. Moreover, the predicted pulses at the peak noise azimuth is sharper compared to the experiment. This can also

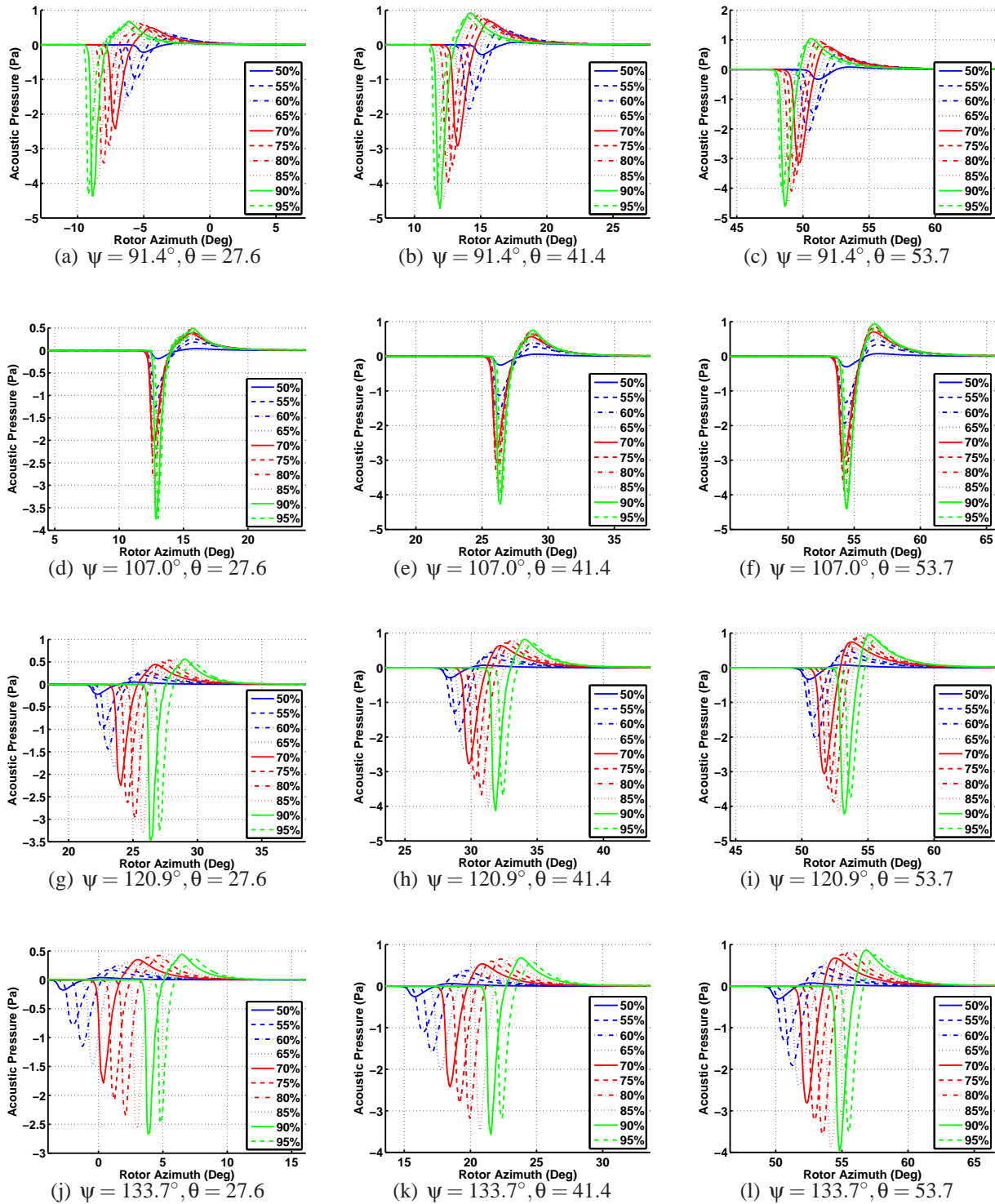


Figure 4.7: Spanwise acoustic phasing effect for the parallel interaction ( $M_T = 0.702$ )

be seen from the larger amplitudes of high frequencies in the frequency spectrum plots in Fig. E.2.

Fig. 4.9 shows a comparison of the noise levels expressed in decibels between theory and experiment for Case 2 oblique BCDI at  $M_T = 0.702$ . The peak azimuth location is captured for the lower two microphone elevations, but the peak azimuth locations is different for the highest microphone elevation. Once again, similar to the parallel interaction case, the theoretical predictions are closer to the experimental results for microphone azimuths less than  $107^\circ$ . At the higher microphone azimuths, the difference between the experiment and theory is now about 10dB.

Fig. 4.10 shows the spanwise acoustic contributions to some of the microphones for the Case 2 oblique interaction. For the microphones at  $91.4^\circ$  azimuth, the acoustic waves from the blade tip arrive earlier than from the inboard blade sections. This slight difference in phasing leads to a certain amount of destructive interference between the positive peaks of the spanwise waves from the tip and the negative peaks of the inboard sections, resulting in an almost complete removal of the positive peak in the final acoustic pulse (see Fig. 4.8). At the peak noise azimuth locations the spanwise acoustic waves no longer arrive perfectly in-phase, unlike in the parallel interaction case. For the lowest microphone, most of the waves from near the blade tip arrive almost simultaneously, but are slightly out of phase with the waves from further inboard. As the microphone elevation increases, the outboard waves too arrive somewhat out of phase resulting in some destructive interference. However, due to their dipole nature, the spanwise acoustic sources tend to radiate more acoustic energy out of plane. Nevertheless, this difference is insufficient to differentiate between the final acoustic levels at the  $53.7^\circ$  and the  $41.4^\circ$  elevation microphones at

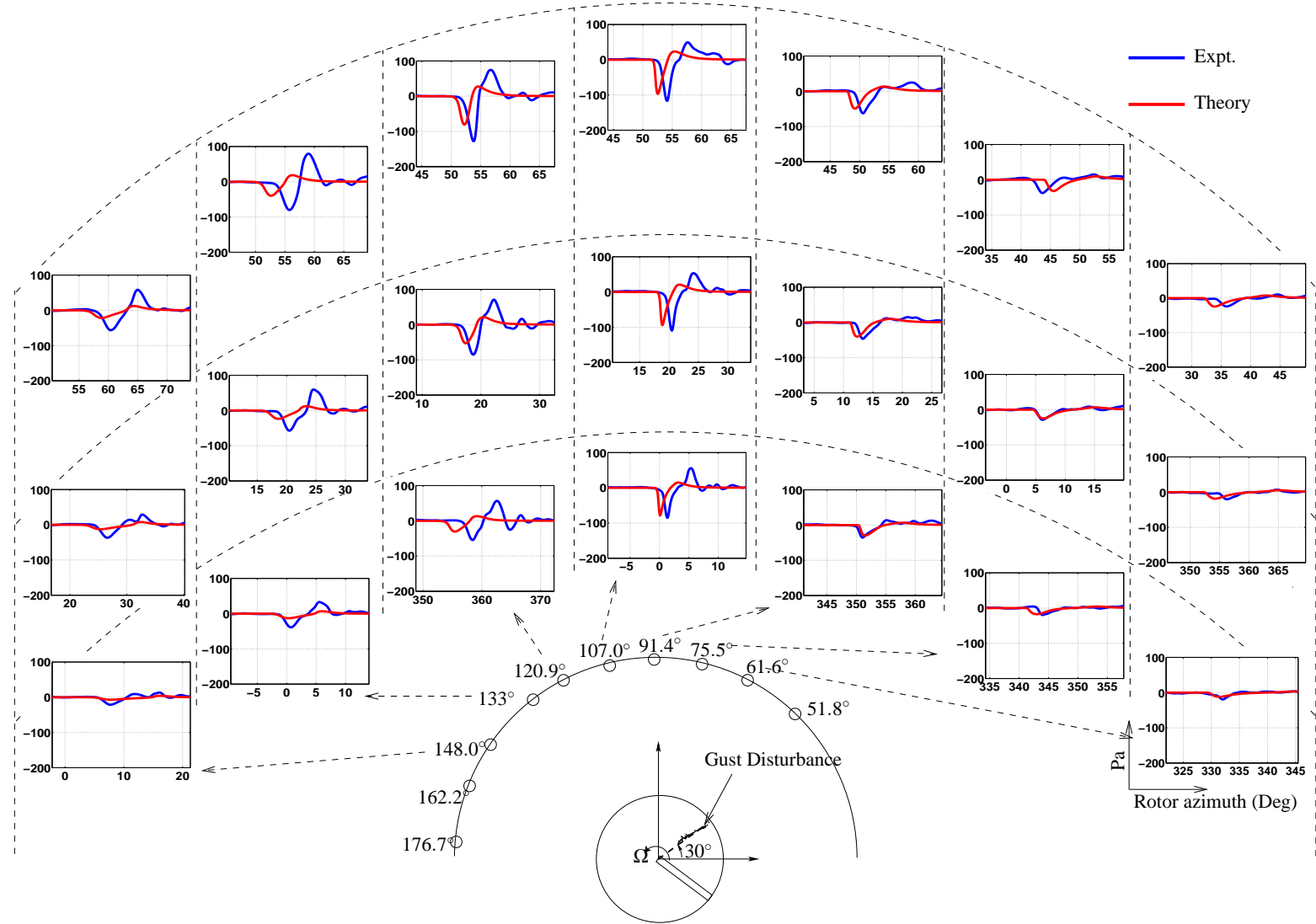


Figure 4.8: Acoustic time histories at the various microphones in terms of Acoustic Pressure (in Pa) vs. Rotor Azimuth (in Deg)

— Case 2 ( $3.3^\circ$  Oblique BCDI;  $M_T = 0.702$ )

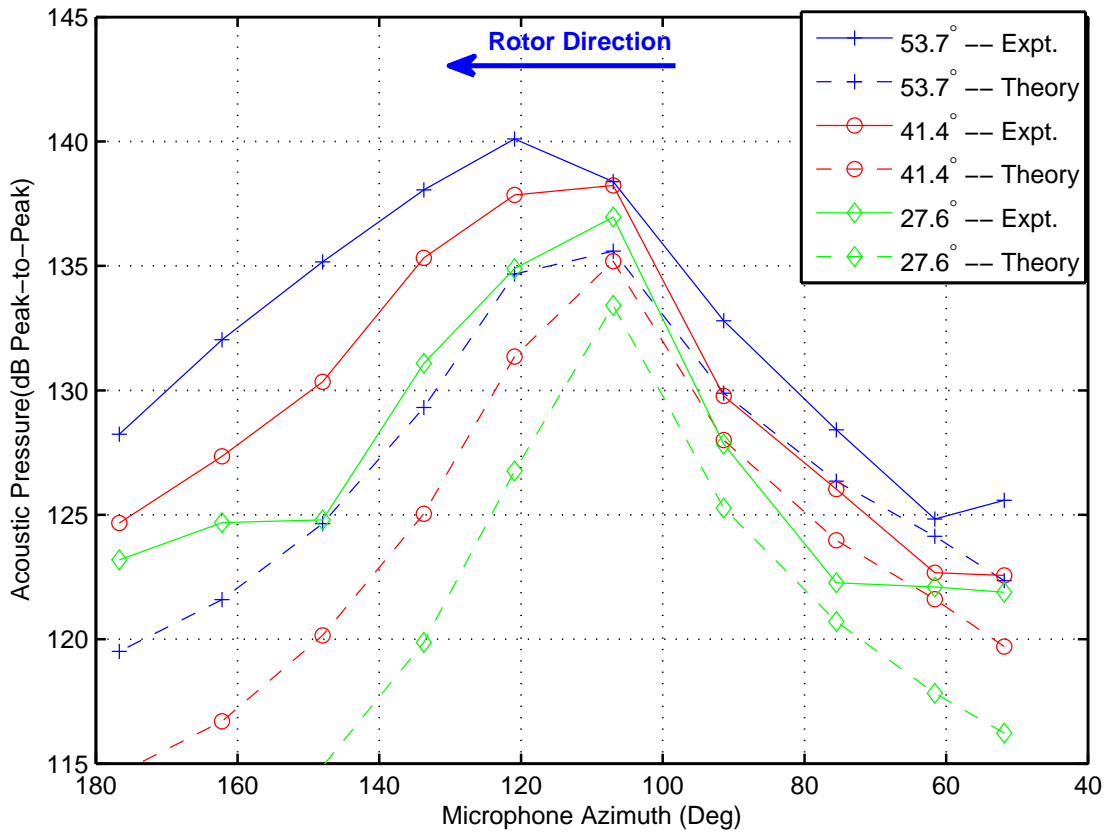


Figure 4.9: Comparison of the directionality trends between theory and experiment — Case 2 ( $3.3^\circ$ )

Oblique BCDI;  $M_T = 0.702$ )

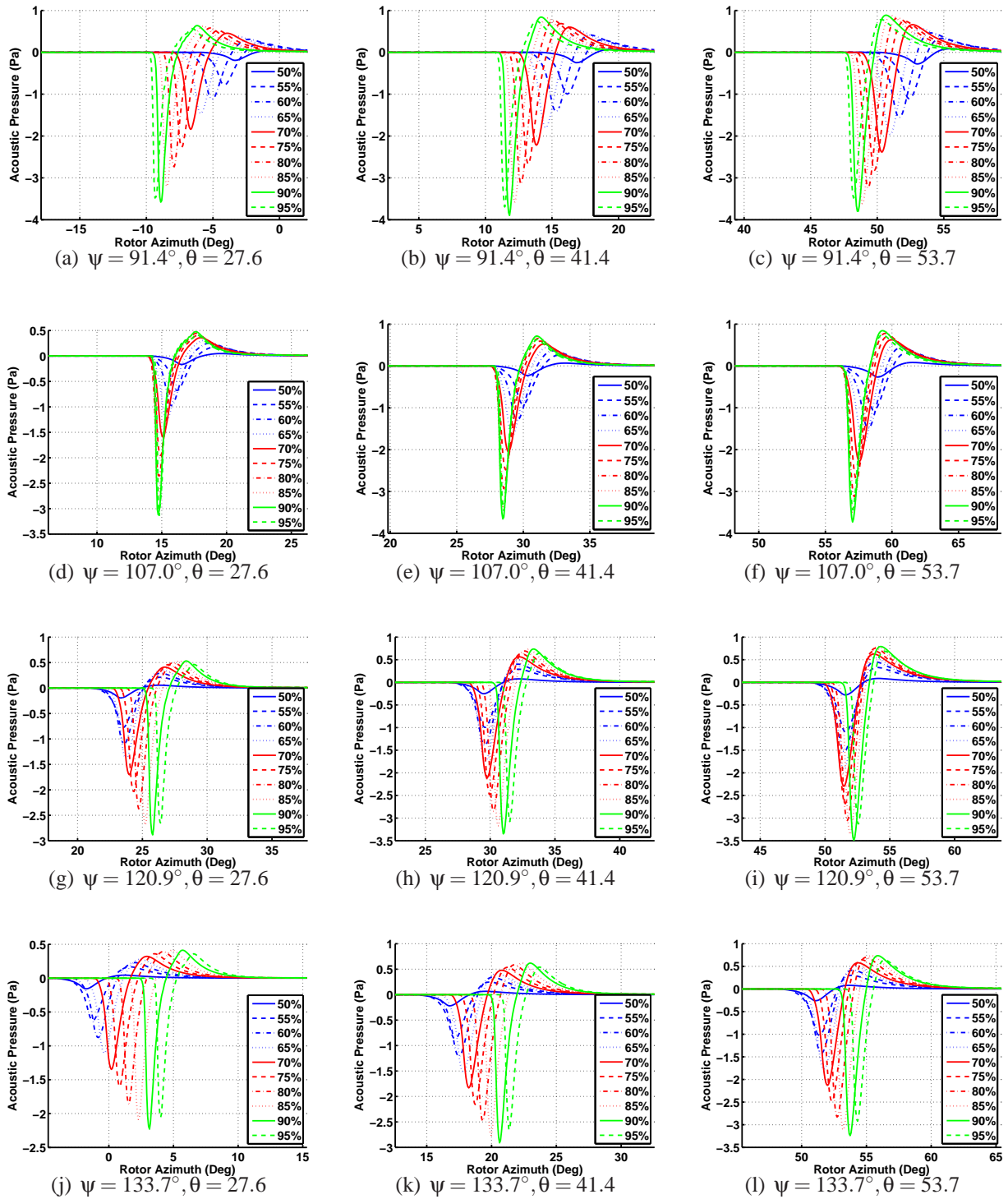


Figure 4.10: Spanwise acoustic phasing effect — Case 2 ( $3.3^\circ$  Oblique BCDI) at  $M_T = 0.702$



$\psi = 107^\circ$ . The two microphones record almost the same noise levels (Fig. 4.9) due to the slight difference in phasing of the waves alone.

At the  $\psi = 120.9^\circ$  microphone azimuth, the acoustic waves from the inboard blade sections arrive earlier than from near the blade tip for the lower two microphones. However, for the highest microphone (Fig. 4.10(i)), some of the waves from the inboard blade sections arrive almost simultaneously, followed a little later by the waves from closer to the blade tip. This in-phase arrival of the waves results very slight change in the final noise level (Fig. 4.9) between highest microphone at  $\psi = 120.9^\circ$  and  $\psi = 107^\circ$  azimuth, in the theoretical predictions. Even a slight change in either the microphone or the interaction location could lead to a stronger in-phase summing of the waves, resulting in higher noise levels.

As for the parallel interaction case, for the microphone azimuth of  $133.7^\circ$ , the waves from the inboard section arrive earlier than from the blade tip, resulting in a destructive interference of the positive side of the acoustic time history.

The summation of the acoustic waves from the spanwise blade sections is a function of the interaction geometry as well as the location of the microphones. While the trace Mach number profile (see Chapter 2) determines the summation of the waves in the rotor plane, the component of the trace Mach number in the direction along each microphone is representative of the spanwise summation process discussed above (Fig. 4.10). Figure 4.11 shows the trace Mach number profile along the radiation direction for four azimuthal microphone locations. The trace Mach numbers remain supersonic over a large portion of the blade for microphone azimuth greater than  $120.9^\circ$  suggesting that the acoustic waves from the outboard section arrive later than the from the inboard

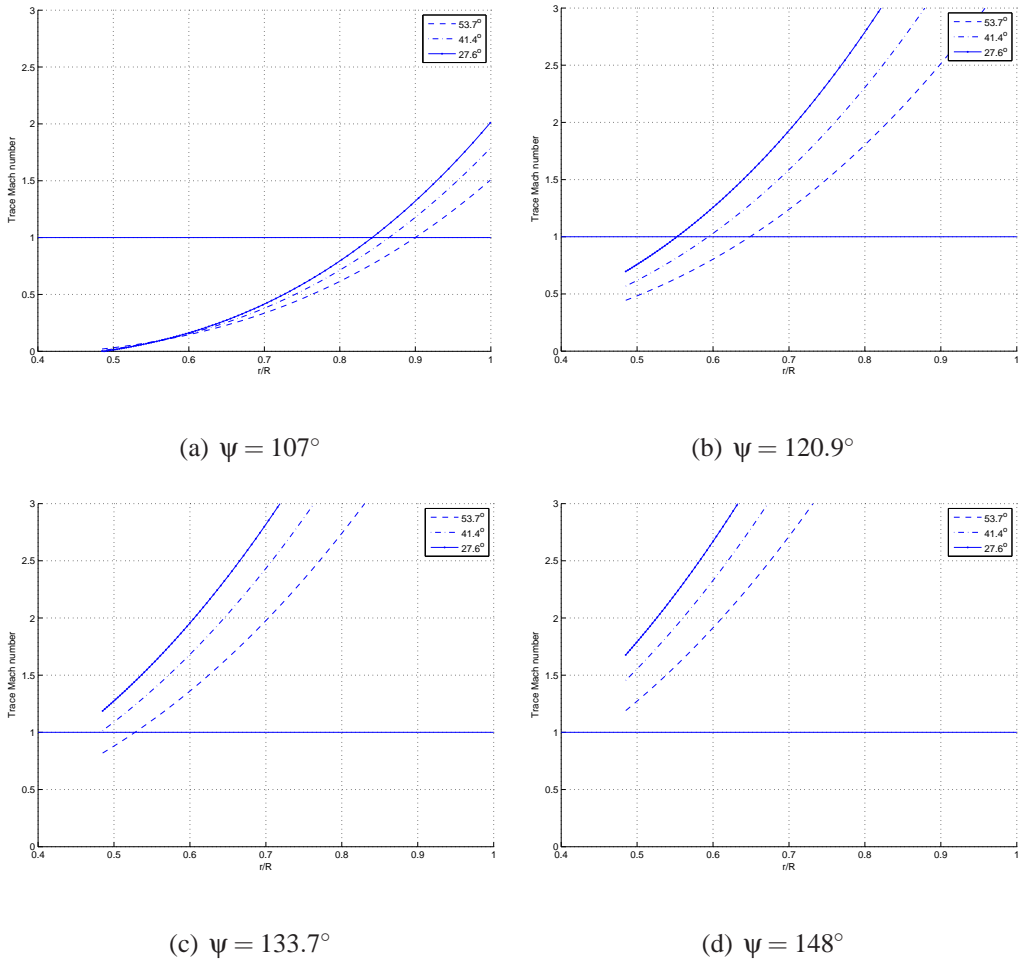


Figure 4.11: Trace Mach number along the radiation direction for Case 2 ( $3.3^\circ$  Oblique BCDI) sections. For microphones at  $107^\circ$  azimuth, the trace Mach number (Fig. 4.11(a)) becomes equal to 1 close to the blade tip, implying that waves from this portion of the blade arrive in-phase at the microphone azimuth leading to increase in noise levels.

### 4.3.2 Case 3 — $8.8^\circ$ Oblique BCDI

Fig. 4.12 shows the acoustic time histories comparisons for the theory and experiment for the  $8.8^\circ$  oblique interaction at  $M_T = 0.702$ . The theoretical results under predict the acoustics signif-

icantly at many the microphone locations, particularly for microphones at  $\psi > 107^\circ$ . Part of this is probably due to the increasing three-dimensional effect on the aerodynamics as the interaction angle increases. Moreover, while in the experimental results, the magnitude of the positive peak increases relative to the negative peak, the theory misses the positive peak altogether. This results in some significant underprediction in the peak-to-peak noise levels as shown in Fig. 4.13. Nevertheless, the relative noise levels at the different microphone locations are similar for the theoretical and experimental cases. The peak noise azimuth is the same, and the azimuthal asymmetry are similar in both cases.

For Case 3 BCDI event, the peak noise azimuth is at  $120^\circ$ . As before, for the microphone azimuths  $\psi < 120.9^\circ$ , the acoustic waves from near the blade tip sections arrive earlier than from the inboard section. However, unlike the previous cases, at the  $\psi = 120.9^\circ$  azimuth locations, there is a significant amount of destructive interference between the spanwise waves at all the three elevations. At the lowest elevation microphone (Fig. 4.14(d)), the acoustic wave from the close to the 70% blade span section arrives first followed simultaneously, by acoustic waves from the sections on either side of the blade. At  $41.4^\circ$  (Fig. 4.14(e)) elevation, the most of the waves from the outboard blade section arrive in-phase resulting in a constructive interference. At the highest microphone locations at  $\psi = 120.9^\circ$ , the outboard waves arrive earlier than from the further inboard of the blade. While, the trace Mach number describes to some extent the spanwise phasing along the azimuthal direction, clearly, spanwise phasing plays a significant role in determining the noise trends along the elevation as well. Similar trends occur for the other azimuth microphone locations shown in Fig. 4.14. The difference in the phasing of the spanwise waves at the different

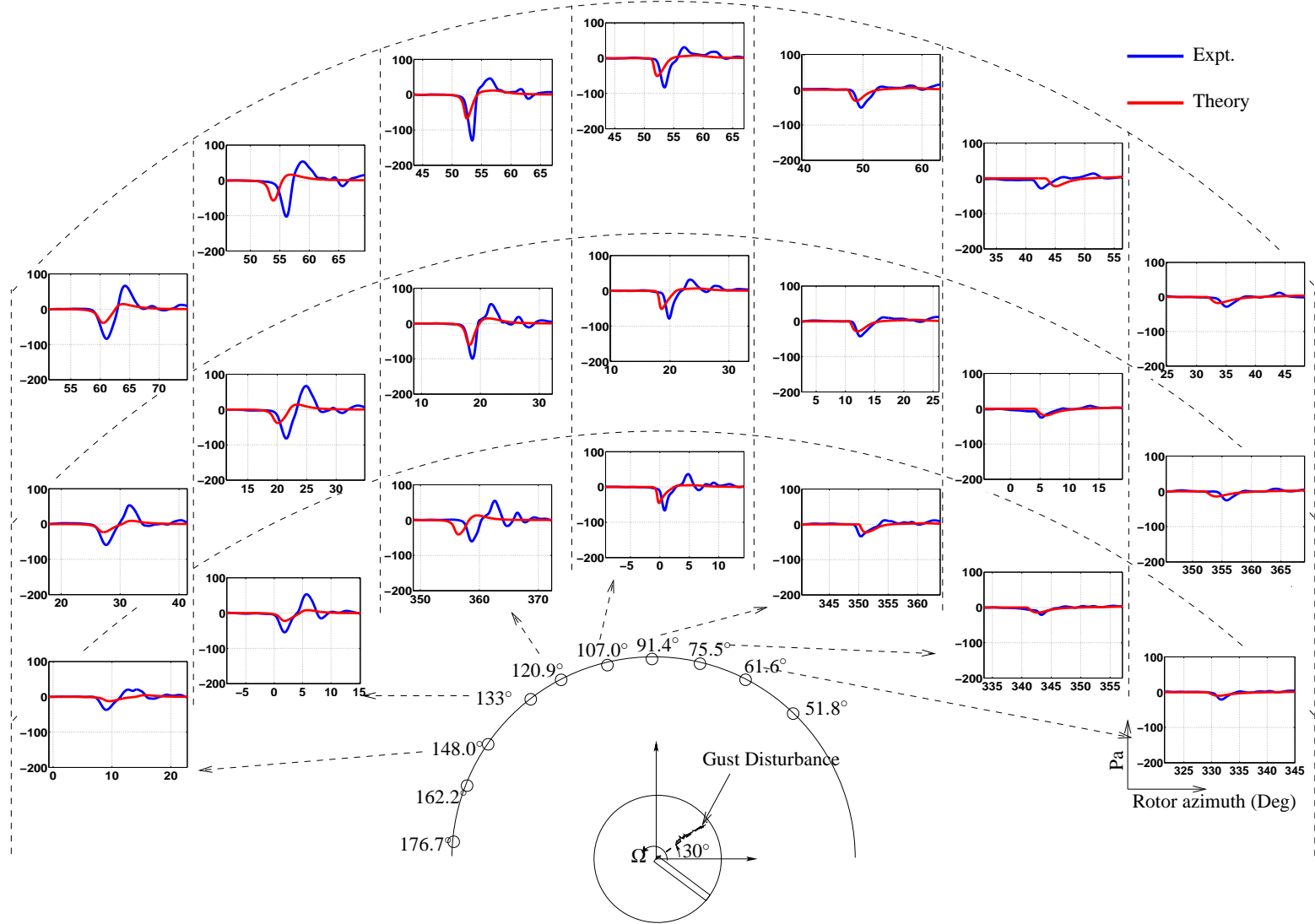


Figure 4.12: Acoustic time histories at the various microphones in terms of Acoustic Pressure (in Pa) vs. Rotor Azimuth (in Deg)

(Case 3 – 8.8° Oblique BCDI) at  $M_T = 0.702$

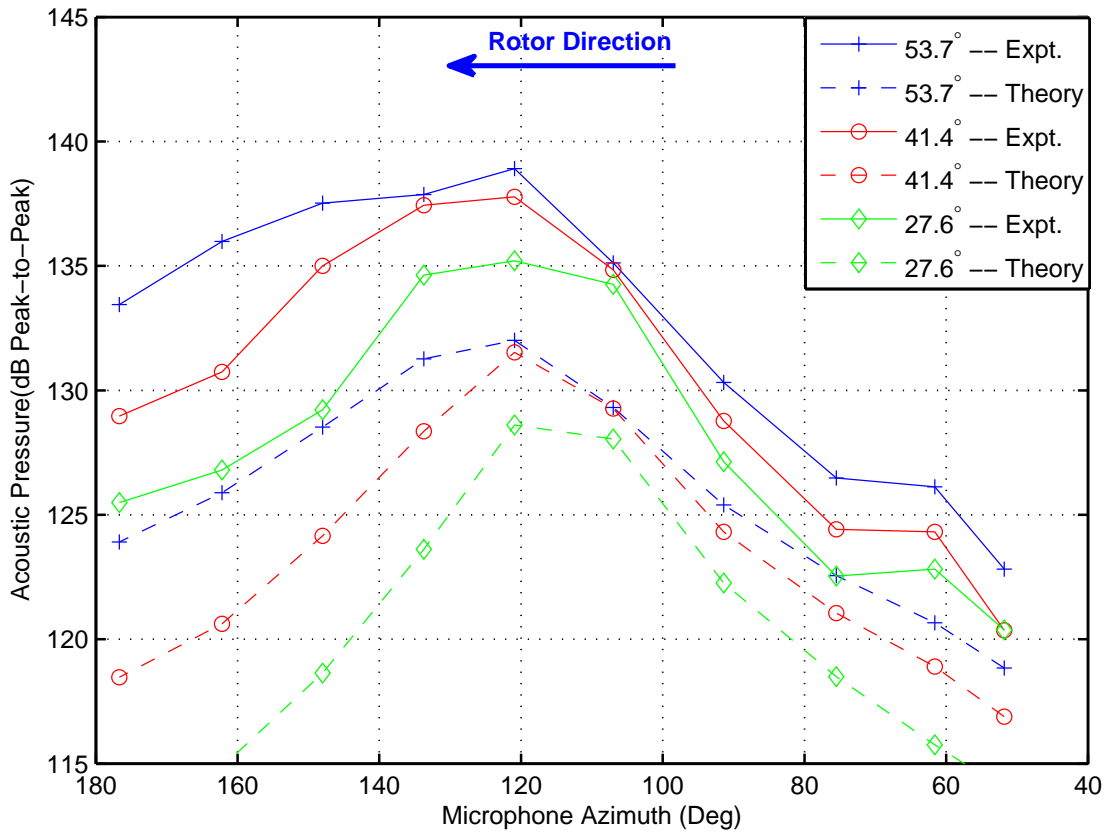


Figure 4.13: Comparison of the directionality trends between theory and experiment — Case 3

(8.8° Oblique BCDI) at  $M_T = 0.702$

microphone azimuth, clearly determines the azimuthal variation.

The trace Mach number profiles along the microphone directions are shown in Fig. 4.15. The trace Mach number profile at the  $107^\circ$  azimuth location (Fig. 4.15(a)) is subsonic for the microphones at the higher elevations. For the two highest microphones it becomes equal to one for the outboard blade sections at the  $120.9^\circ$  azimuth suggesting that the peak noise levels would occur at this azimuth (Fig. 4.13). For the microphone at  $27.6^\circ$  elevation, the trace Mach number becomes equal to 1 close to the blade tip at the  $107^\circ$  microphone azimuth. At the  $120.9^\circ$  azimuth, the trace Mach number becomes 1 at the outboard sections for the lower microphone elevation and has a higher subsonic value over the rest of the blade when compared to the  $107^\circ$  location. This results in a greater number of the spanwise sources being in-phase at the  $120.9^\circ$  azimuth compared to  $107^\circ$  azimuth for the lower elevation microphone (Figs. 4.14(c) & 4.14(f)). This results in the noise levels at these two locations being very close to each other as can be seen in Fig. 4.13.

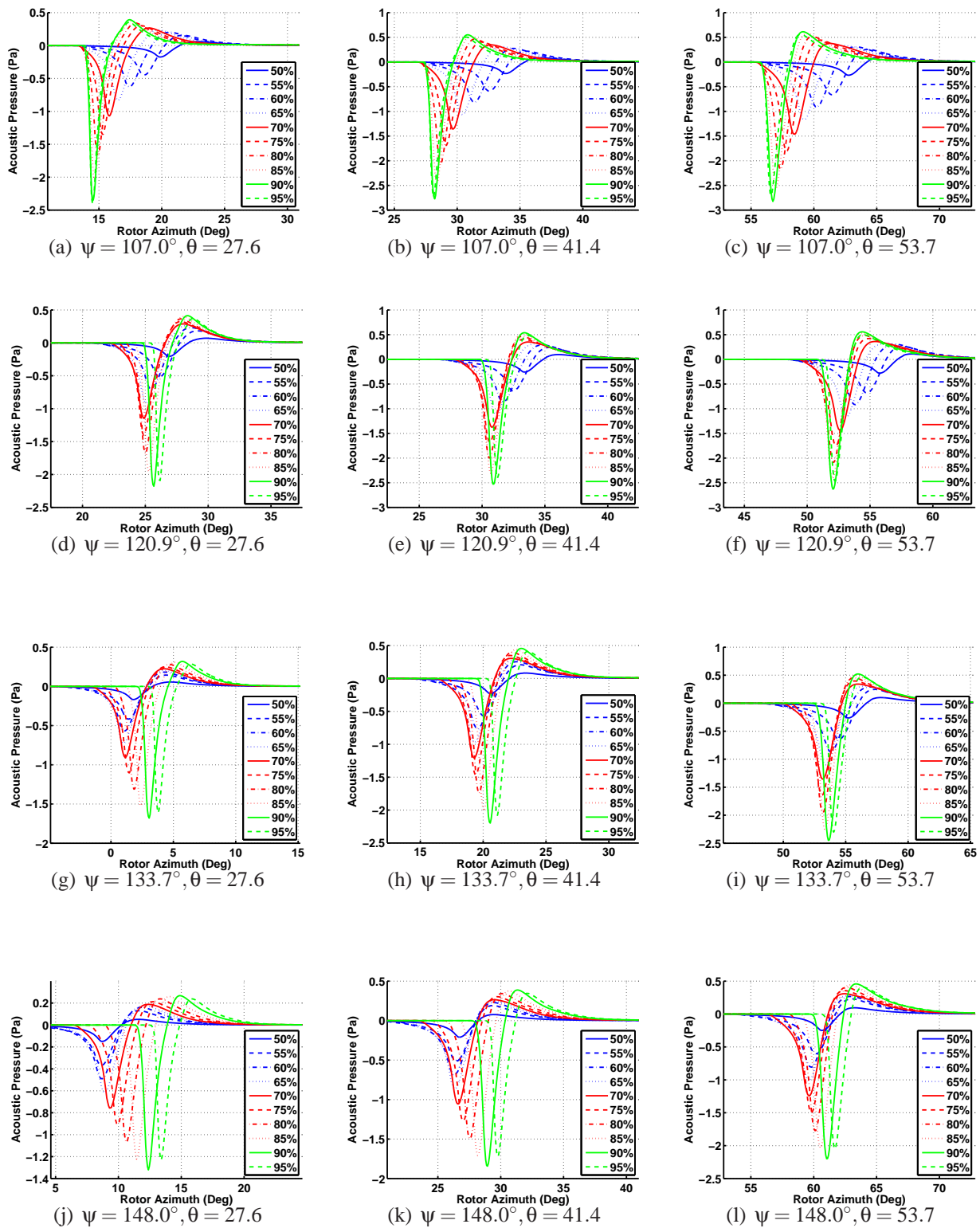
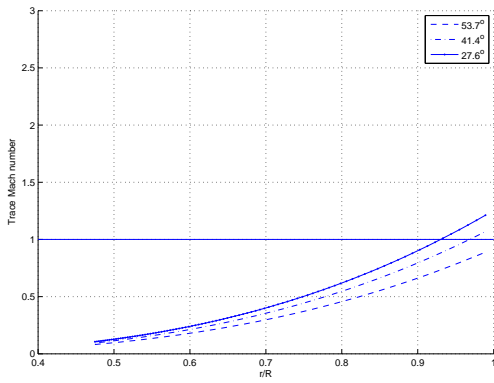
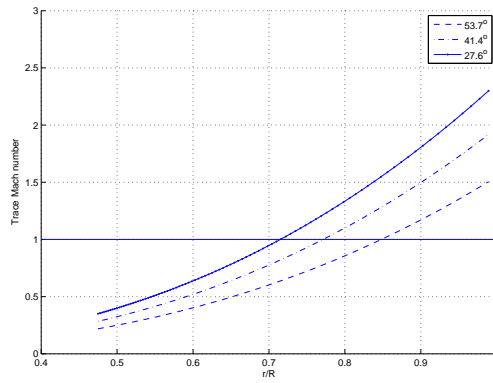


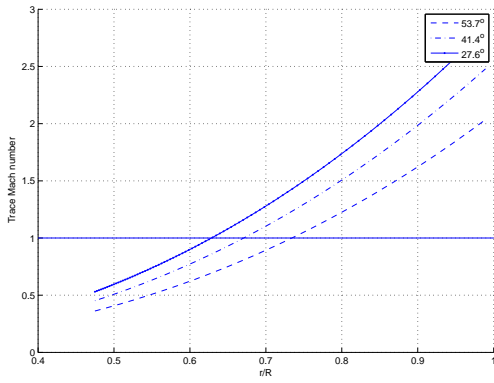
Figure 4.14: Spanwise acoustic phasing effect — Case 3 ( $8.8^\circ$  Oblique BCDI;  $M_T = 0.702$ )



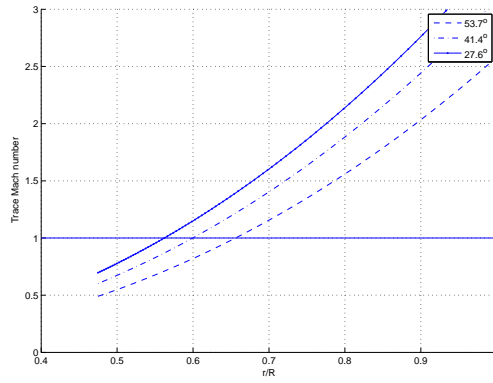
(a)  $\psi = 107^\circ$



(b)  $\psi = 120.9^\circ$



(c)  $\psi = 133.7^\circ$



(d)  $\psi = 148^\circ$

Figure 4.15: Trace Mach number along the radiation direction for Case 3 ( $8.8^\circ$  Oblique BCDI)



### 4.3.3 Case 4 — 15.3° Oblique BCDI

Figs. 4.16 and 4.17 show the comparison between the experiment and theory for the Case 4 BCDI event (15.3° at the blade tip) at a tip Mach number of 0.702. Once again, the theory under predicts significantly — 8dB-12dB depending on the microphone location. The general trends of the radiation directionality, both along the azimuth as well as the elevation are picked up by the theory for most of the microphone locations. The peak noise levels occur at slightly different azimuth locations for the lower two microphones as predicted by the theory. Nevertheless, the theory does manage to pick up the effect of the 41.4° elevation microphone recording a higher noise level at the 120.9° microphone azimuth.

Fig. 4.18 shows the phasing of spanwise acoustic waves at some microphone locations. Clearly, the maximum in-phase arrival of the spanwise waves at the microphone has moved to higher microphone azimuth angles. However, unlike the previous cases, there is no single location where all the waves arrive in-phase. Most waves from the outboard span locations arrive close to each other at 120.9° microphone azimuth. At this azimuth location, there is higher in-phase summation of the waves at the lowest elevation. However, the spanwise waves themselves at this low elevation are lower in magnitude compared to the radiation at higher elevations. The summing of the waves at the 41.4° microphone elevation for this azimuth location results in a higher noise level than the highest microphone. The fact that this trend is carried over to the next microphone azimuth ( $\psi = 133.7^\circ$ ) in the experiment, but not in the theoretical predictions, could be attributed to the lower predicted positive peaks. A higher magnitude positive peak from the spanwise sources, could result in significant increase in the noise levels.



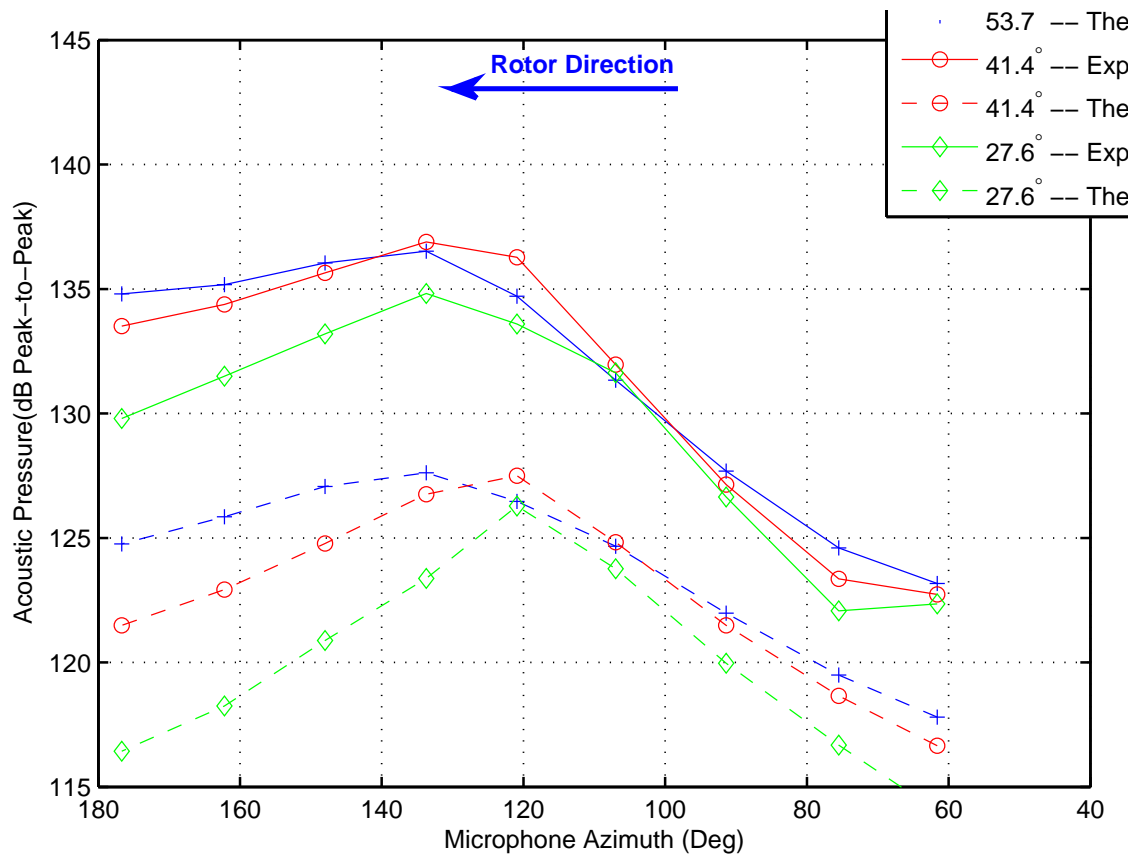


Figure 4.17: Comparison of the directionality trends between theory and experiment — Case 4

(15.3° Oblique BCDI;  $M_T = 0.702$ )

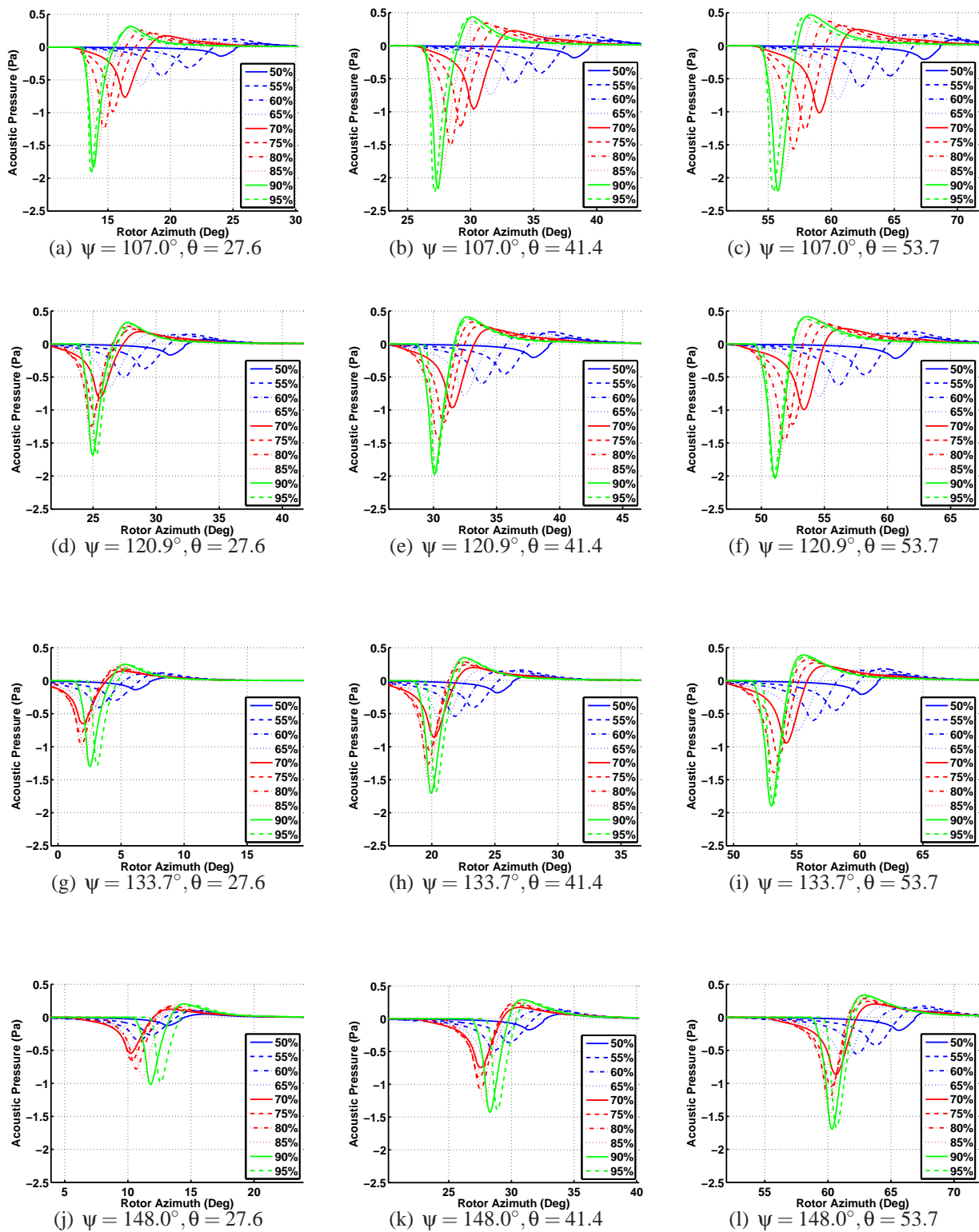
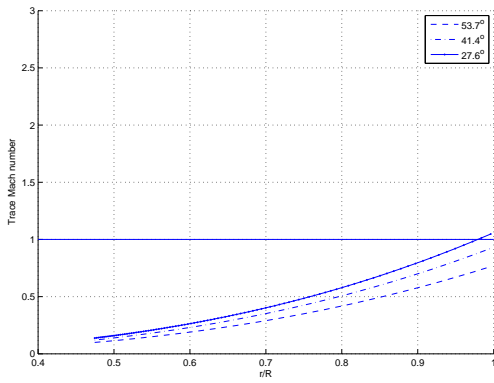


Figure 4.18: Spanwise acoustic phasing effect — Case 4 (15.3° Oblique BCDI;  $M_T = 0.702$ )

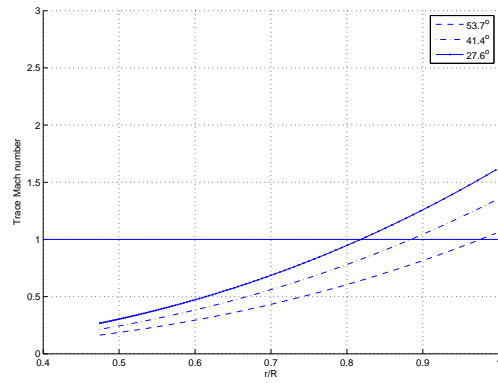
Figure 4.19 shows the trace Mach number profiles along the radiation direction for the  $15.2^\circ$  oblique BCDI. Note that for the  $107^\circ$  azimuth location the profiles almost entirely subsonic, suggesting that this is not the peak noise azimuth any longer. At the  $120.9^\circ$  azimuth, the trace Mach number remains subsonic for the highest microphone (at  $53.7^\circ$  elevation), but crosses 1 close to the blade tip for the lower elevations. This helps explain why the peak noise elevation moves closer to the rotor plane at this azimuth (as seen in Fig. 4.17). Moreover, the trace Mach number profiles are very similar for the microphone azimuths greater than  $120^\circ$ , resulting in similar phasing of the spanwise sources at these microphone locations (Fig. 4.18). This also helps explain the reason for the distribution of acoustic energy over a larger azimuthal region for this oblique interaction.

## 4.4 Summary of Results

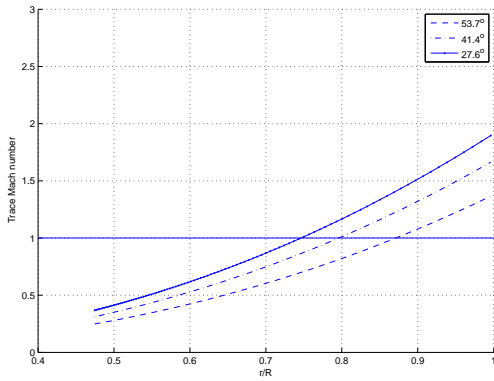
Indicial aerodynamics, combined with a non-compact chord rotor acoustic formulation predicts the acoustic pulse shape reasonably well for the parallel and near-parallel interaction angles. The negative peak of the pulse is well predicted, however, the positive peak is not captured sufficiently. Moreover, it is seen that using a non-compact chordwise aerodynamic approach is essential to capture the noise levels adequately, particularly for the peak noise microphone locations. The acoustic predictions become more divergent from the experiment as the obliqueness of the interaction increases, and under-predict the noise levels. Nevertheless, the relative negative peak noise levels and the trends at the different microphone locations are captured reasonably well. In particular, the general trend of the broadening of azimuthal directivity towards the direction of the trace Mach number with increasing BVI obliqueness is captured to some degree. Moreover, it is seen that the



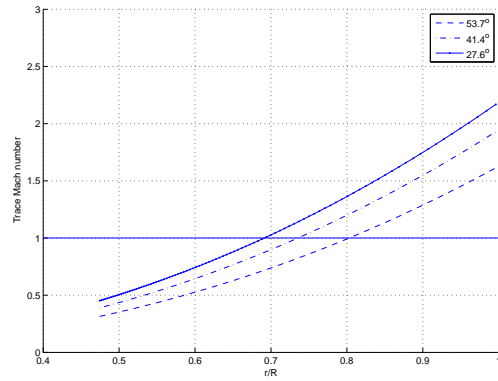
(a)  $\psi = 107^\circ$



(b)  $\psi = 120.9^\circ$



(c)  $\psi = 133.7^\circ$



(d)  $\psi = 148^\circ$

Figure 4.19: Trace Mach number along the radiation direction for Case 4 ( $15.3^\circ$  Oblique BCDI)

phasing of the spanwise acoustic waves plays an important role in the spatial distribution of the acoustic energy and could result in the peak noise elevation levels moving closer to the plane of the rotor as the interaction angle increases. This resulting distribution of the acoustic energy can be explained in terms of the trace Mach number profiles in the radiation direction.

## Chapter 5

### Summary and Conclusions

This chapter discusses the conclusions that been arrived at from the experimental investigations and measurements discussed in the previous chapters. The main purpose of the present work was to better understand the physics of the blade-vortex interaction and their effect on noise radiation characteristics. The present fundamental work decouples the interacting vortex parameters from the blade parameters, by replicating the vortex parameters in a controlled manner. In essence, the BVI problem is transformed into an experimental simulation called the Blade-Controlled Disturbance-Interaction (BCDI) that captures the major features of the BVI event but allows independent evaluation of the important governing parameters.

A unique and novel experimental facility has been developed from the ground up in order to study the BVI acoustics in a controlled manner. This experiment now facilitates a true comparison of the blade response — both aerodynamic and acoustic response — when blade planform is modified or rotor parameters are changed. Previous experiments which similarly decoupled the vortex parameters from the rotor parameters focused primarily on the parallel interaction, despite



the fact that real helicopter BVIs are never truly parallel. For the first time in the present work, oblique BVIs at different interaction angles have been studied. This experimental facility offers the ability to study in detail the effect of passive and active blade design changes on BVI noise.

## 5.1 The BCDI Facility

A unique experimental facility has been developed, calibrated and used to understand the fundamental mechanism involved in the helicopter BVI noise generation. The BCDI experiment consists of a single-bladed hovering rotor that is capable of operating at high tip Mach numbers passing through a controlled two-dimensional gust field. The rotor tip Mach numbers that are capable of being tested cover the full operational range of modern helicopters.

The gust field that the rotor passes through has been designed to simulate the vertical velocity field induced by a vortex filament, the strength and orientation of which are close to a typical vortex filament during a BVI event. A special “gust generator” has been designed, built and calibrated to generate this controlled disturbance. Detailed measurement of the gust field using hotwire anemometry has shown that the gust field is predominantly two-dimensional in nature, with a negligible velocity in the blade’s chordwise direction and capable of simulating the BVI. A residual acoustic response of the rotor blade due to the close passage of the rotor blade to the nozzle lip was identified as an additional source of acoustic radiation and a possible limitation of this approach. A superposition technique was developed that effectively removes this source of error from the BCDI acoustic time histories.

The BCDI testing space has been acoustically treated to lessen the reflection of the BCDI

acoustic pulses from the surrounding walls and apparatus, being recorded by the microphones. A suite of microphones has been positioned in this acoustically treated testing chamber to measure the acoustic directivity, including time histories and power spectrum of the radiated noise.

The successful development of this facility brings a new research tool to the helicopter acoustic community to help understand the basic mechanisms involved in BVI noise. The facility can also be used for applied research to study the effect of different blade design changes, such as planform or even some active control techniques on the BVI noise radiation.

## **5.2 BCDI Experimental Findings**

Some basic mechanisms of the BVI have been explored using the BCDI facility. The BCDI experimental acoustic results present a first quantitative simulation of the oblique BVI problem and a method of isolating the key governing parameters. The measured acoustic pulse consists of two distinct pulses – a negative pulse followed by a smaller positive pulse.

The geometry of the interaction is shown to play a significant role in the acoustic waveform and directivity of the radiated noise – a good part of the effect being a result of the phasing of the acoustic signals over the span of the rotor blade. Acoustic signals from the parallel BCDI emanate from the blade in-phase, resulting in the largest overall pulse in a direction perpendicular to the rotor span, with the levels decreasing on either side. Measured noise levels in this case, were highest out of the plane of the rotor due to the dipole nature of the acoustic sources. Their detailed pulse shapes did not change character with decrease in microphone elevation angles.

Noise levels for the oblique BVI are generally slightly less in peak magnitude, but spread the

acoustic energy over wider azimuth angles. A small non-zero interaction angle results in a more acoustic energy being distributed to higher azimuth angles compared to the parallel interaction. The peak noise directivity for the oblique interaction angle is primarily along the direction of the BVI trace velocity.

For a given interaction angle, as the tip Mach number is decreased, the point where the trace Mach number becomes one moves further outboard along the blade. This results in an increase in the effective strength of spanwise waves that arrive at a near in-plane microphone in phase. For very higher BVI interaction angles, the noise levels at lower microphone elevation angles increase because this effect becomes larger at lower elevations than at higher elevation.

### **5.3 Indicial Aerodynamics and Acoustic Predictions**

Indicial aerodynamic theory (when corrected for compressibility and three-dimensional effects) and when combined with a Green's function solution of the three-dimensional wave equation for fixed sources in space, predicts the acoustic pulse shape reasonably well for parallel BVI. It is necessary to treat the acoustic sources on the rotor blade as a non-compact source to bring the predicted peak noise levels more in-line with the measured data. However, this approach does not predict the smaller positive pulse adequately.

Acoustic predictions using indicial aerodynamics become more divergent from the experimental measurements with increasing BVI obliqueness. However, the general trend of broadening directivity with increasing BVI obliqueness is captured to some degree, but theoretical calculations substantially under-predict the noise levels.

Acoustic time tracing methods show that distinct events on the blade are related to the measured pulse shape and help develop a more complete understanding of the mechanism of the BVI. This approach has shown that span-wise phasing of the acoustic waves plays a significant role in determining the directionality both along the azimuth as well elevation direction. It is also seen that the trace Mach number in the radiation direction plays a significant role in the spanwise phasing of the acoustic sources at the corresponding observer locations, and hence also determines the distribution of the total acoustic energy due to the interaction event.

## **5.4 Recommendations for Further Research**

The BCDI experimental facility provides an ideal condition for testing the blade response to known velocity disturbance field for a variety of blade parameters. The parameters used in the present study can easily be extended to include higher tip Mach numbers and different interaction geometries. Some of recommendations for future work in this facility as listed below:

- Most helicopter BVIs occur at higher transonic tip Mach numbers where compressibility become important. The experimental setup developed in this work can be used to study the BCDI at higher transonic tip Mach numbers. This will provide valuable information regarding the effect of the aerodynamic non-linearity in BVI noise.
- Moreover, it would be interesting and very useful to study higher oblique interaction angles at these high transonic tip Mach numbers as the trace Mach number becomes 1 closer to the blade tip. The resulting collection of strong spanwise acoustic waves on the blade could re-

sult in interesting acoustic as well as aerodynamic phenomena, and might play an important role in the final generated noise.

- As a natural extension of the work so far, it is suggested that curved interaction geometries to closely match the real trace Mach numbers be tested. This is also important since the spanwise acoustic phasing would be differ from the straight interaction cases and could have an effect on the resulting acoustics.
- In order to understand the acoustics completely, it is essential to understand the detailed aerodynamic events occurring on the blade. It is therefore, suggested to test rotor blades instrumented with a sufficient number of pressure transducers placed at carefully chosen locations to capture important aerodynamic events, particularly those associated with the wave collection process on the blade at higher transonic tip Mach numbers.
- As mentioned already, one important advantage of the present approach is the ability to objectively compare the aerodynamic and acoustic response of different blade designs to a given velocity disturbance. Thus different passive, as well as active blade designs could be tested in this facility.
- The Weissinger-L lifting line approach used to correct the indicial aerodynamics for three-dimensional effects needs further research to make it applicable for oblique BVI cases. A more complete theory that resolves the pressure distribution over the blade chord, as well as along the span, is required for accurate oblique BVI predictions.
- A CFD approach could be used to model the experiment and be validated against the exper-

imental data. Either pressure measurements on the blade surface (if available), or hotwire and pressure measurements in the near-field of the blade could be used to validate the CFD.

## Appendix A

### Gust Generator Fabrication and Operational Details

The Gust Generator consists of various sections which aid in achieving a clean flow with less turbulence. A brief description of the sections are given here.

**Fan Blower** The fan-blower assembly was sized as per the procedure laid out in Pope's Wind-Tunnel Design and Testing [89], keeping in mind the losses due to the screens and various sections of the gust generator and the final required peak velocity of the flow. The fan-blower is placed outside of the chamber in order to prevent contamination of the acoustic environment within the chamber due to the fan.

**Diffuser section** A long rectangular section with a small divergence angle to slow the flow. The divergence angle is kept small to prevent flow separation along the walls. It also consists of screens to smoothen the flow and reduce the turbulence levels. The diffuser section was also built, keeping in mind the chamber dimensions to ensure that the fan-blower assembly remains outside the chamber.

**Corner Section** Since the flow starts out horizontal, it needs to be turned by  $90^0$  as the final velocity required is in the vertical directions perpendicular to the rotor plane. This section primarily consists of vanes which were designed based on [90, 91] to achieve the required flow rotation.

**Turn-table Sections** An important design criteria for the gust generator was the ability to orient the nozzle at any angle with respect to the blade to simulate oblique BVIs. This was achieved by fabricating two sections such that the interface between the two was circular. One section was a transition from a square to a circular cross-section, and the other was a transition from a circular to rectangular cross-section. The dimensions of these two sections were based on keeping the divergence angle to a minimum to prevent flow separation along the walls. The top section along with all the sections above it can be oriented at any angle.

**Settling Chambers** Two settling chambers – one after the diffuser and one after the turn-table sections equipped with screens reduce the turbulence levels and allow the flow to settle.

**Nozzle** The nozzle is the most critical section of the gust generator as it decides the velocity profile of the ensuing gust at the nozzle outlet. The detailed design of the nozzle is discussed in the following section.

### **Nozzle Design**

The dimensions of the gust are chosen to match a typical BVI for Mach-scaled rotor blade of radius  $38.125in$ . The DNW tests [92] have shown that a typical vortex shed from a blade has a core radius( $r_c$ ) of  $0.05c$  and vorticity ( $\Gamma$ ) of  $5.46ft^2/s$ , giving rise to a peak velocity of about



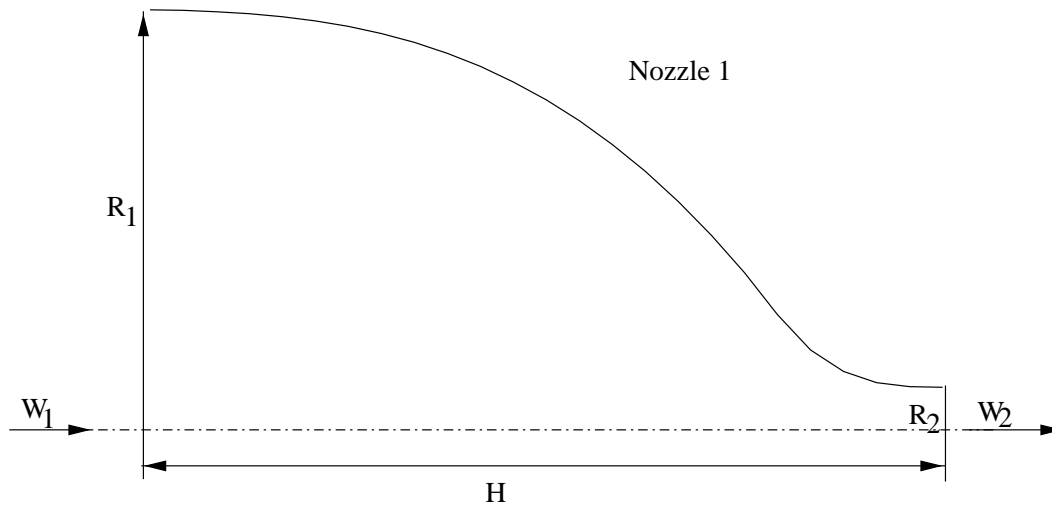


Figure A.1: Schematic of early nozzle design

$150 - 170 \text{ ft/s}^1$ . In order to minimize the three dimensional effects of the nozzle edges, the blade would be run such that one edge of the nozzle lies outside the blade radius, while the other edge sits within 50% of the blade radius. These criteria require that the nozzle dimensions be  $24 \text{ in.} \times 1 \text{ in.}$

Various nozzle designs were attempted before the current one was realized. In most of the designs, the two walls of the nozzle were parallel to each other at the outlet. On the curved wall, it was postulated that the boundary layer would be thicker as the flow has to travel a greater distance. This reduces the velocity gradient on the curved wall, thus causing an asymmetry in the velocity profile. Moreover, the negative static pressure gradient has the advantage of preventing boundary layer separation and reducing turbulence in the shear layer. A schematic of the this nozzle design is shown in Fig. A.1. However, pitot probe measurements of flow on this nozzle (Fig. A.2) showed that the asymmetry between the flows on either wall, was not sufficient enough to generate the required velocity profile. However, building this nozzle demonstrated that a span-wise uniform

<sup>1</sup>Based on OLS rotor [92]

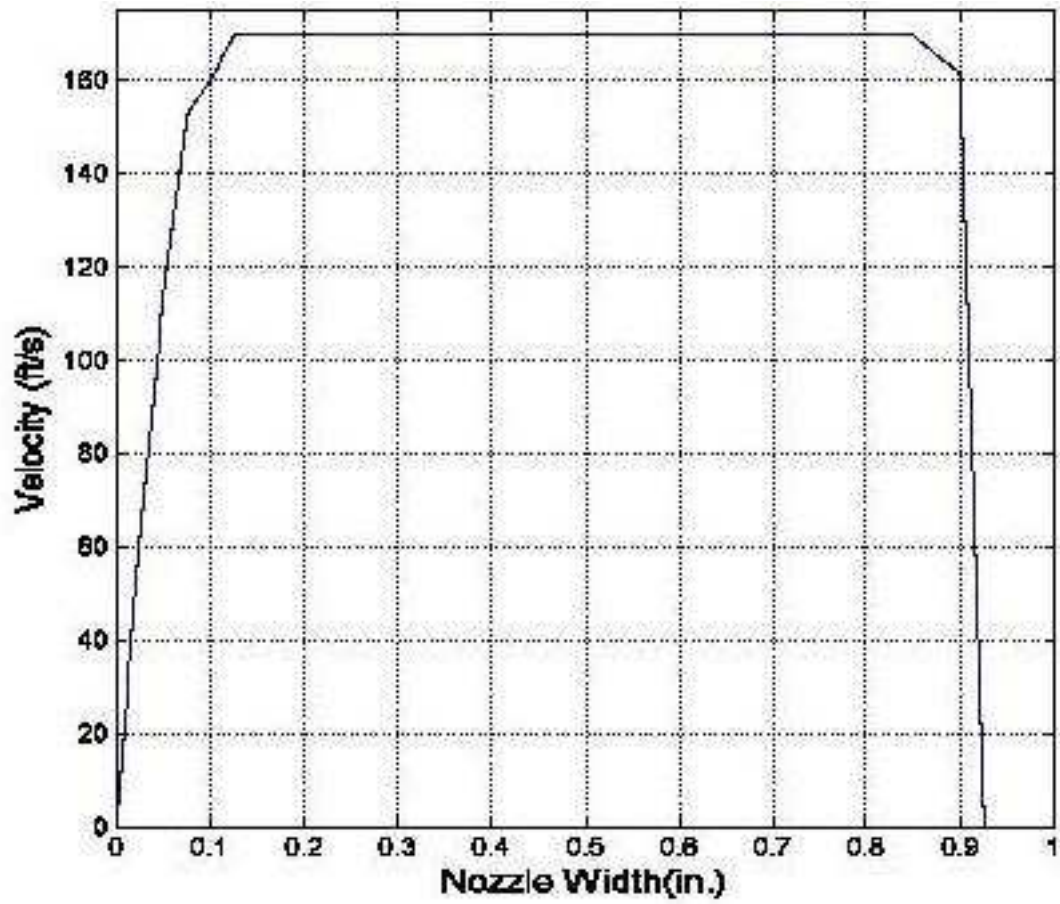


Figure A.2: Velocity profile obtained from the first nozzle design

flow was achievable with the present gust generator design, and that the flow was effectively two-dimensional.

### **Gust Turbulence Characteristics**

The rotor blade, when passing over the gust is also affected by the turbulence present in the gust. Since, the mean velocity profile is generated by exploiting mixing regions, there is a tendency for the turbulence to be high when the mixing region is long. Thus it is necessary to characterize the turbulence and study its contribution to the radiated noise, to show that the main features of BVI noise can be replicated by the current experiment. Measurements were carried out using a TSI 1241-20 two component Hotfilm sensor probe and a TSI 1050 series anemometer. A sampling rate of 12800Hz was used to cover a wide range of frequencies that might affect the blade response, including possible BVI frequencies. The obtained data was averaged over 75 frames of 0.32 seconds. In situ calibration was considered impractical, given the rapid change in velocity along the nozzle width. The calibration was carried out in the Glenn L. Martin Calibration Facility Wind Tunnel over the velocity entire velocity range that encompasses the a single gust velocity profile.

The turbulence levels, measured by  $w'$  and  $u'$  are also uniform across the nozzle length, suggesting that the flow is effectively two-dimensional. The RMS values of the turbulent velocities are shown in Fig. A.3. The trend shown is typical of mixing flows. The first peak represents the mixing layer developed on the flat side of the nozzle, while the second corresponds to the mixing layer on the curved side ( $x = 1in$ ). Since the mixing length on this side is higher as compared to that for  $x = 0$ , this is to be expected. Nevertheless, the RMS values are significantly lower than the mean

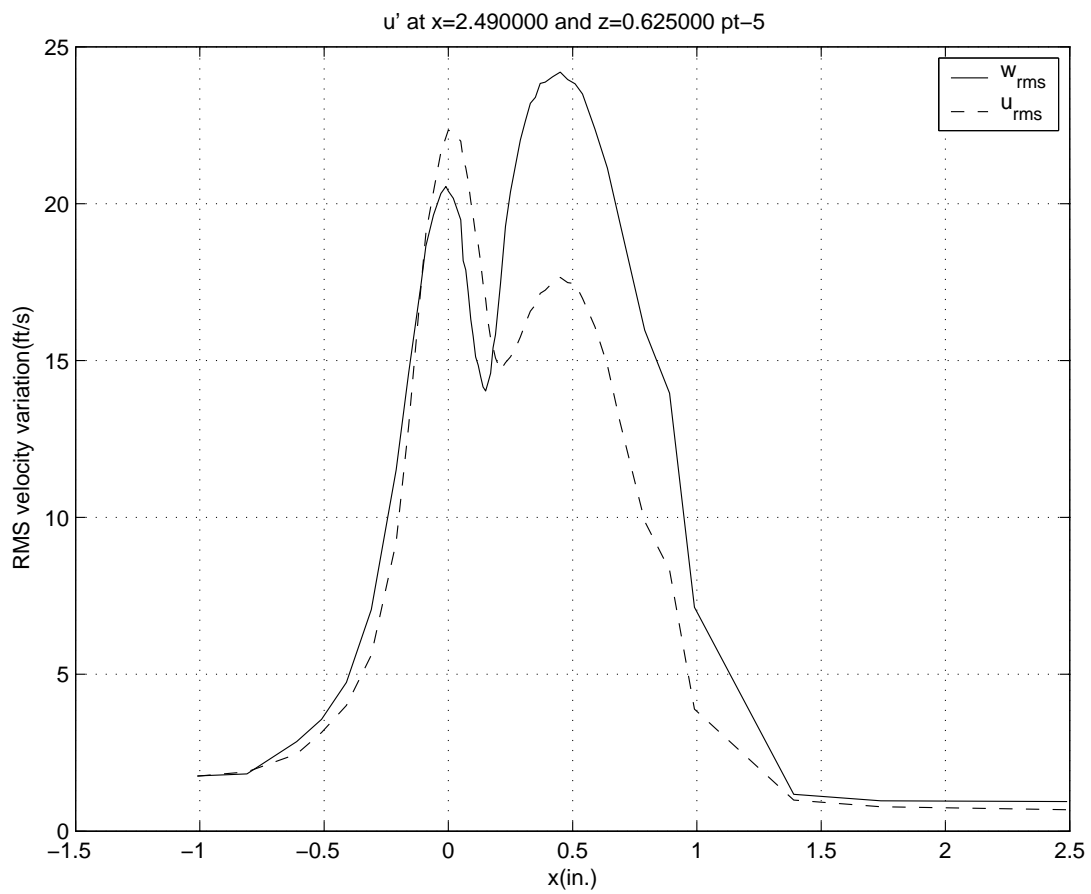
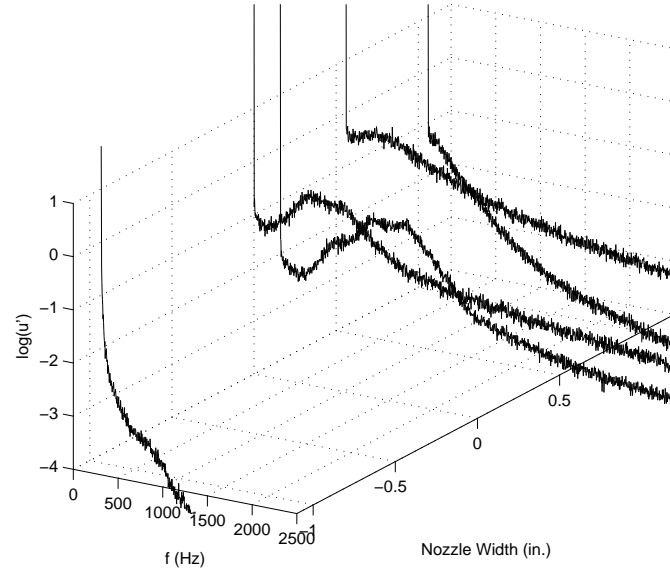


Figure A.3: RMS variation of velocities across nozzle width

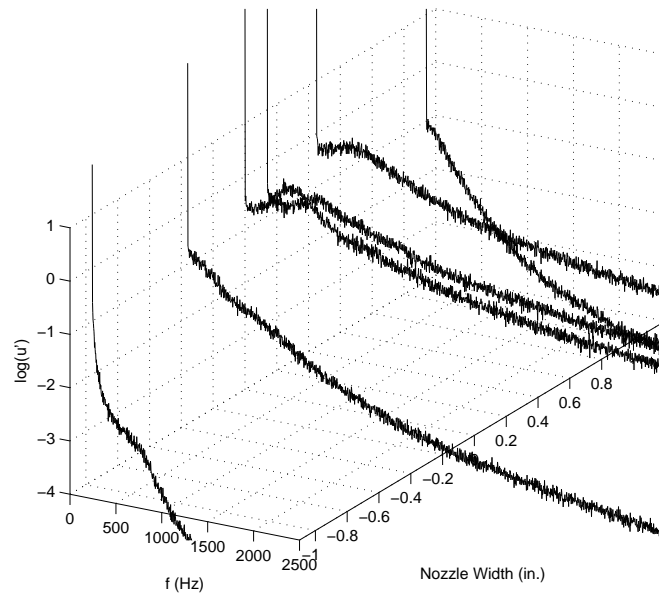
velocity. The dip in the turbulence level near  $x = 0$  is purely due to wind tunnel turbulence and has little contribution from the mixing. The wind tunnel itself has significantly lower turbulence levels because of the screens placed in the two settling chambers.

Fig. A.4(a) and Fig. A.4(b) show frequency domain representation of the data after a Fast Fourier Transform at  $0.625in$  and  $1.275in$  above the nozzle. The bumps in the graphs between  $500Hz$  and  $1000Hz$  correspond to some coherence in the mixing layers. The disturbances corresponding to  $500Hz$  and  $1000Hz$  appear at  $1.275in$  above the nozzle as well. However, across the nozzle width the variation in amplitude appear to be less than that at  $0.625in$ .

While the mean and turbulence levels are only statistical quantities, the blade “sees” something different. When the blade moves over the gust, the instantaneous values of the velocity are quite different from the mean values. However, one can view the turbulence fluctuations ( $u'$ ) as a high frequency signal superimposed over the mean velocity ( $\bar{u}$ ). Now, the aerodynamic response of the blade is such that it acts as a low pass filter, responding strongly to lower frequencies – in the range of the mean velocity profile – and not so strongly to the higher frequencies – associated with the turbulence fluctuations. Thus, the turbulence in the gust would not result in significant effect on the acoustics of the blade, in the frequency range associated with the BVI. However, it would be interesting to see what the effect is on the higher frequencies, and broadband noise in general.



(a) 0.625in above Nozzle



(b) 1.275in above Nozzle

Figure A.4: Frequency distribution of turbulence at various locations

## Appendix B

### Rotor Test Stand Dynamics

It is important to establish the smoothest operating conditions of the motor/rotor dynamical system during the operation. Every complex dynamical system has resonance like operating conditions that should be avoided. Strike tests with an impulse hammer were performed at key locations on the rotor stand while recording accelerometer data in order to identify these resonant like fundamental frequencies of the rotor stand. The modes corresponding to these frequencies could be excited when the rotor is spinning at the corresponding RPMs and are to be avoided or passed through quickly. Fig. B.1 shows the natural frequencies of the stand. The impact hammer strike test suggests that Rotor RPMs close to 1200 and 3600, (corresponding to 20Hz and 60Hz, respectively) are to be avoided. With the shaft spinning (without the rotor blade), two more stand frequencies show some resonance like characteristics at about 42Hz (2520RPM) and 84Hz (5040RPM). Out of the four critical frequencies, the one closest to the operating range is the one at 42Hz, and so the rotor was not operated close to 2520RPM for any of the experiments.

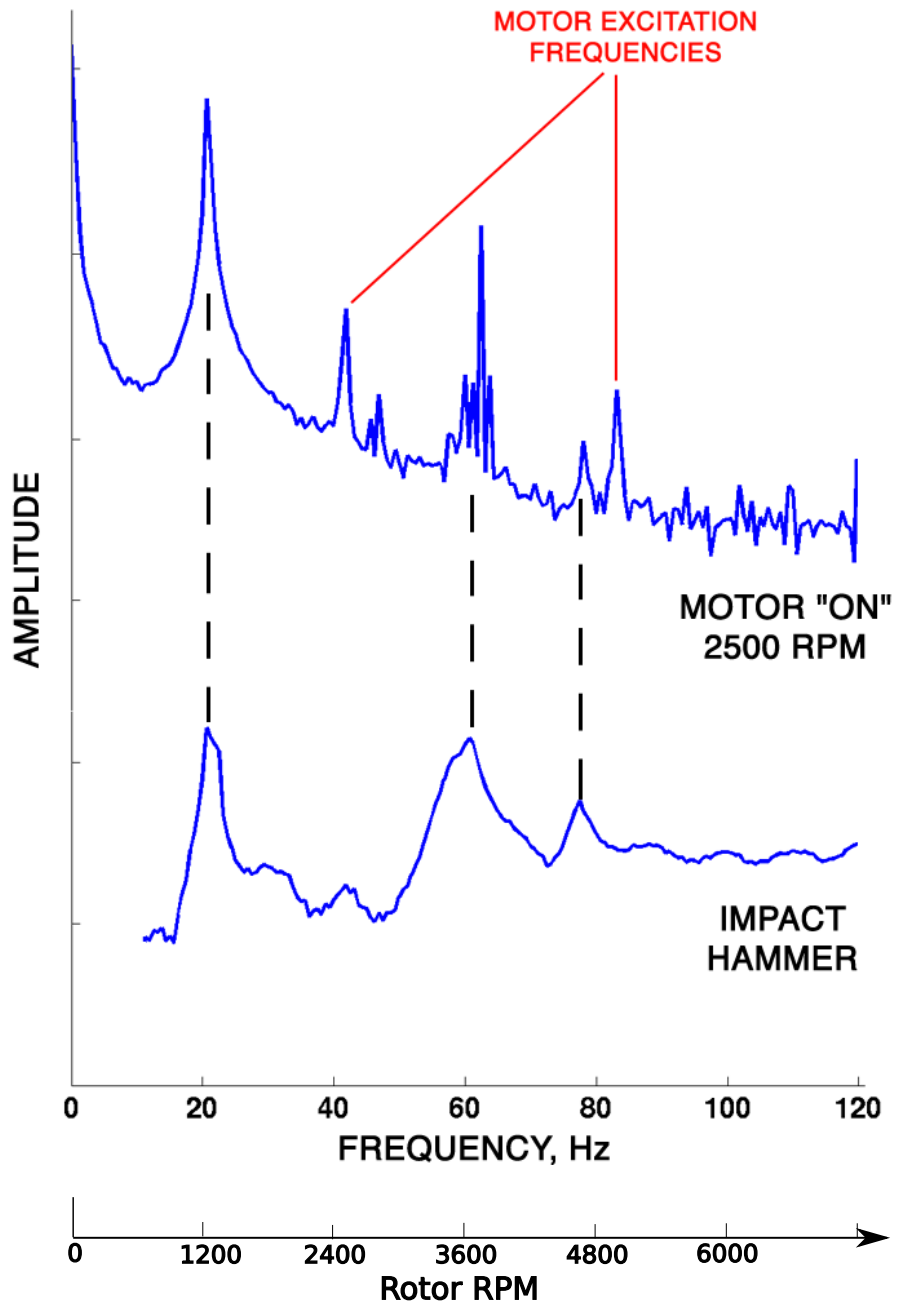


Figure B.1: Resonant frequencies associated with the RTS



## **Appendix C**

### **Effect of Nozzle Interference on the Acoustic Time**

#### **Histories**

As mentioned in Chapter 3, the proximity of the nozzle lip to the rotor blade results in some noise radiation by itself. This radiation is impulsive and occurs over the same time interval as the main BCDI event, possibly limiting the scope of the experiment. The acoustic pulse radiated from the rotor blade due to the nozzle presence alone is significantly lower than the main BCDI pulse and its effect is removed from the acoustic data by subtracting it from the total noise radiated. The radiation of noise resulting from the nozzle's proximity to the rotor blade peaks azimuthally at the same microphone location as the BCDI event. However, it seems to be directed more in the plane of the rotor, suggesting it is not due to impulsive lift on the blade. At this point, the reason for this noise is speculated to be a result of the fluid dragged along the by the blade having to accelerate over the nozzle wall. For completeness, the time histories of this acoustic event is presented here in Figs. C.1-C.4 for all the microphones at a rotor blade tip Mach number of 0.702.

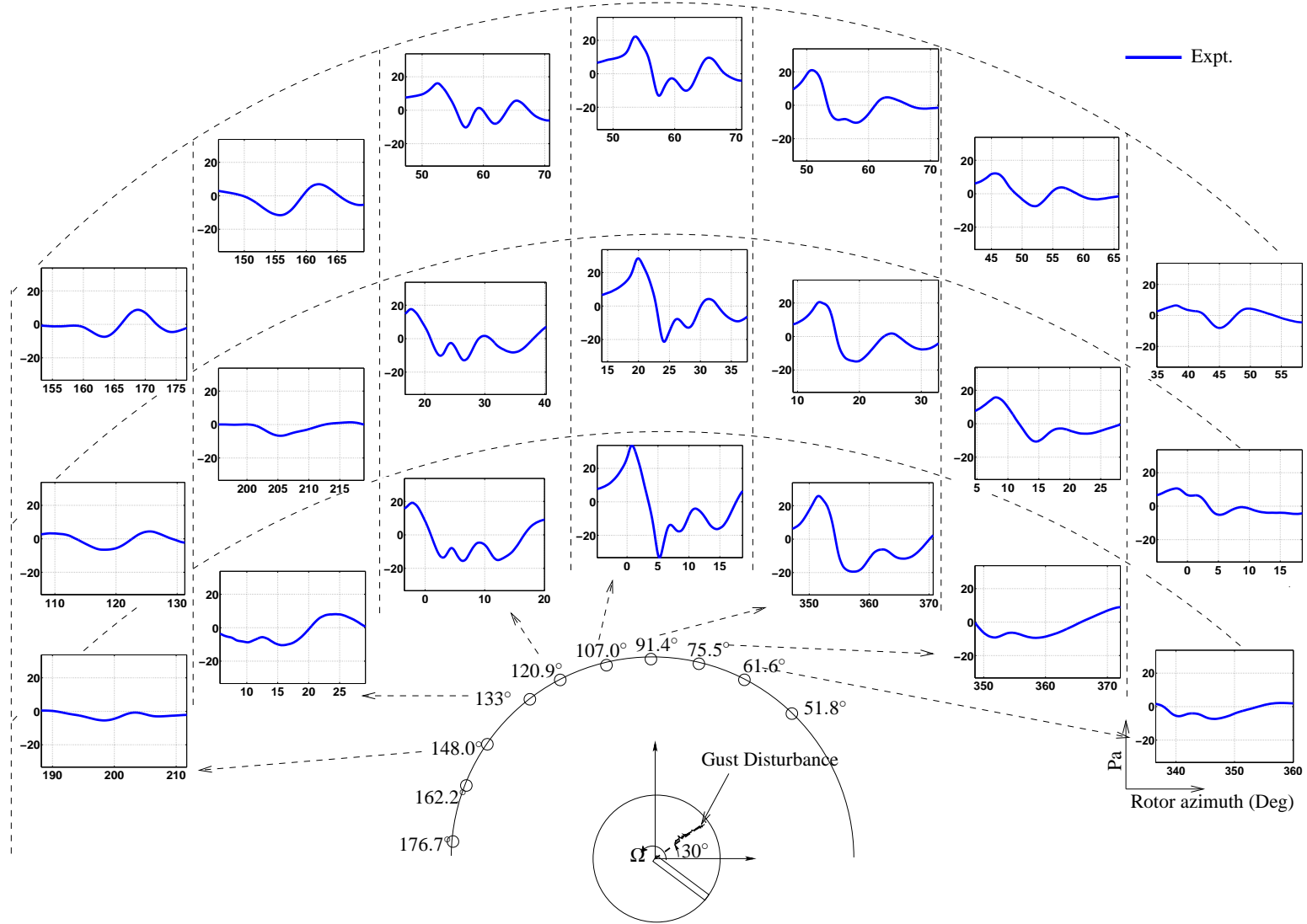


Figure C.1: Acoustic time history due to nozzle alone (No gust) ( $M_T = 0.702$  — Parallel Interaction)

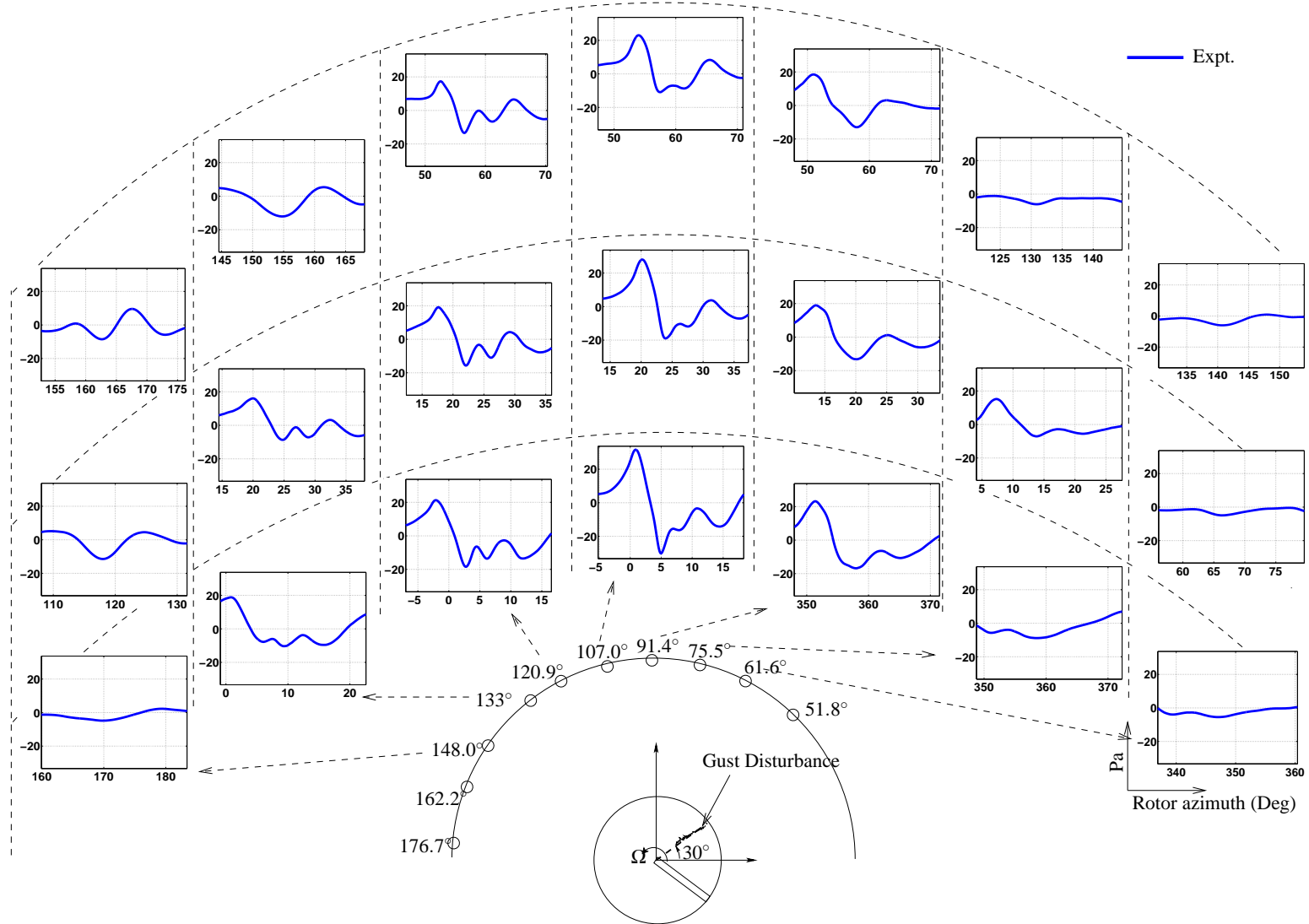


Figure C.2: Acoustic time history due to nozzle alone (No gust) ( $M_T = 0.702$  — Case 2)

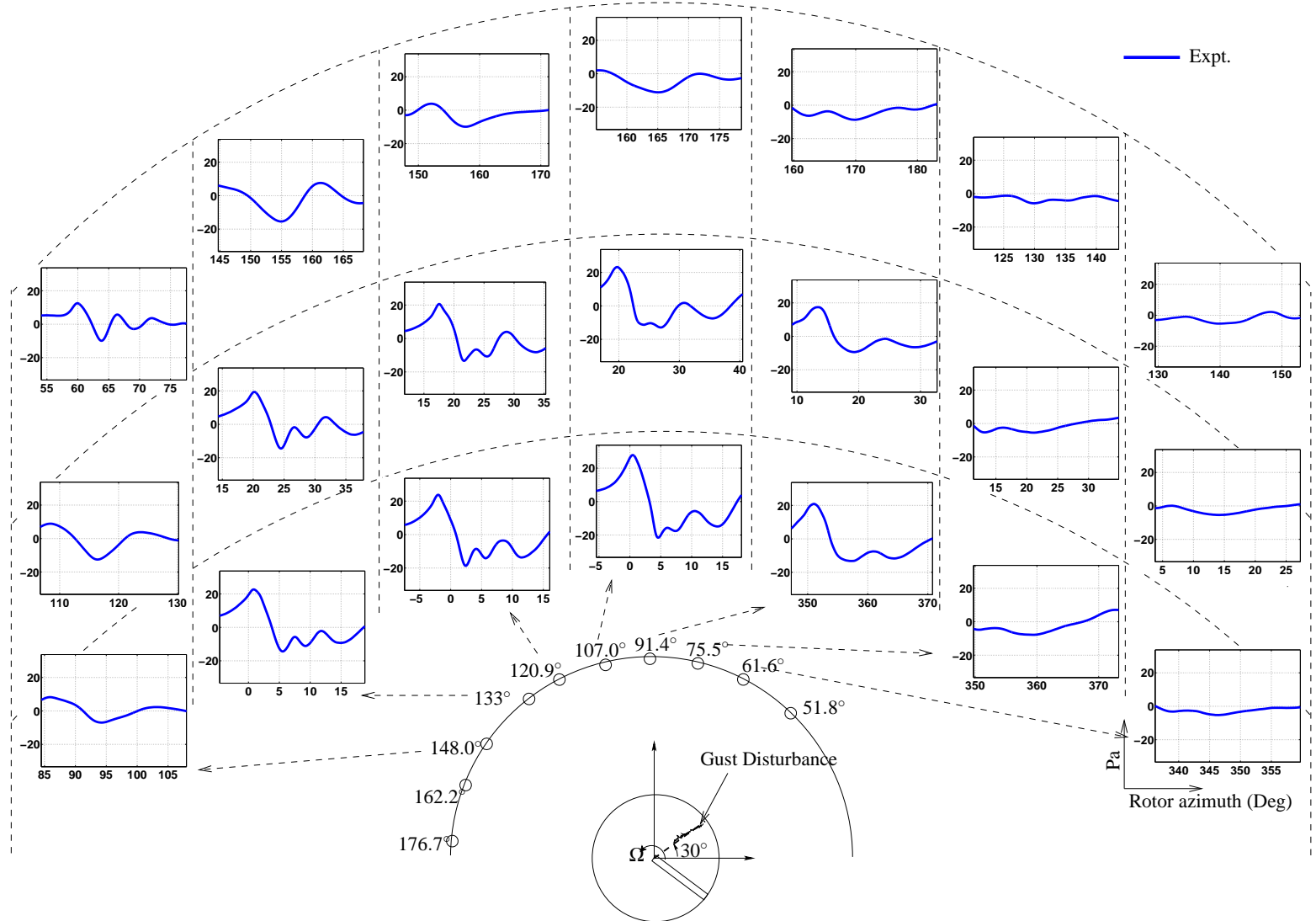


Figure C.3: Acoustic time history due to nozzle alone (No gust) ( $M_T = 0.702$  — Case 3)

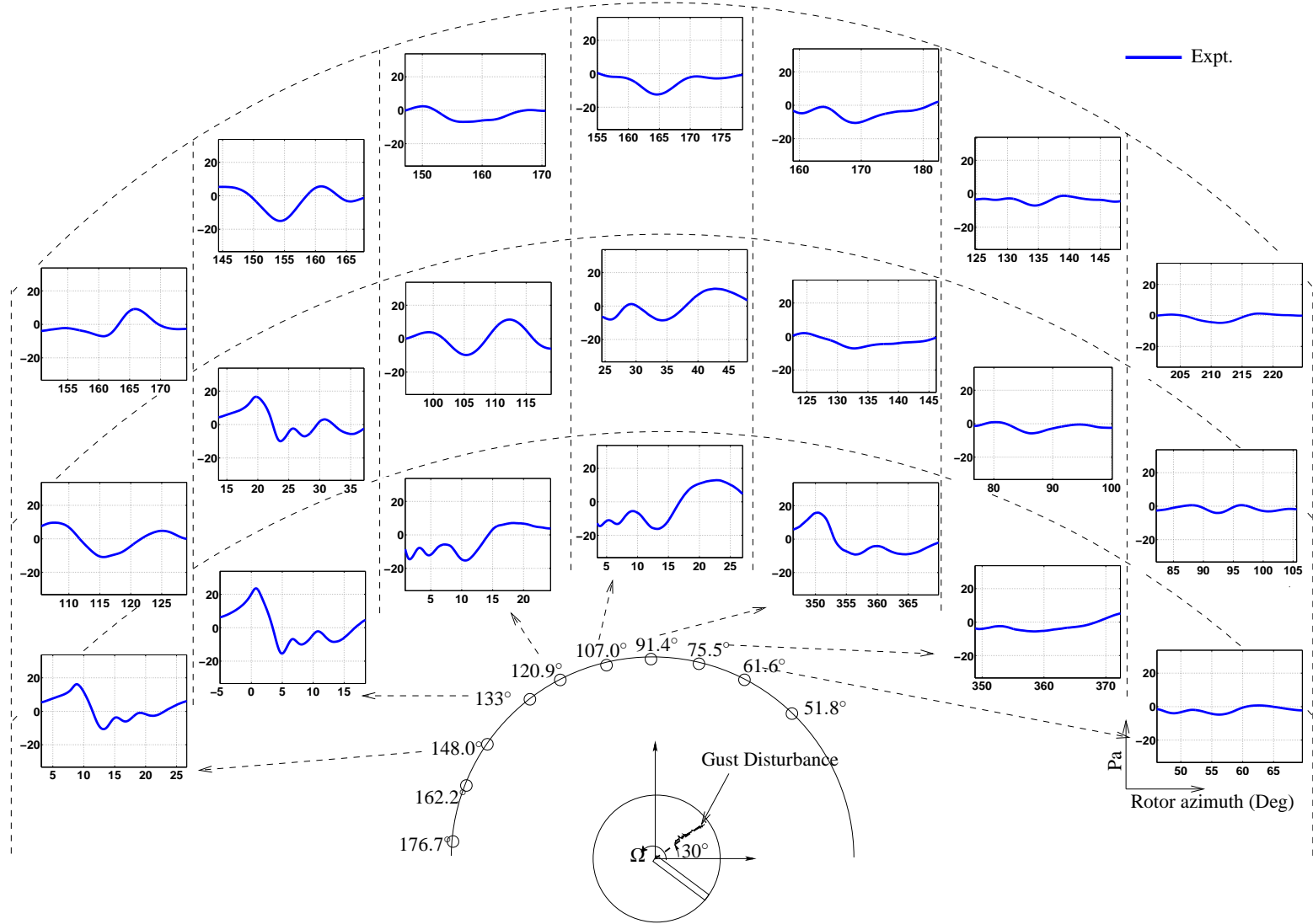


Figure C.4: Acoustic time history due to nozzle alone (No gust) ( $M_T = 0.702$  — Case 4)

## **Appendix D**

# **Comparison Between Compact and Non-Compact Acoustic Formulations**

The acoustics formulation used in Chapter 4 is a non-compact formulation, which distributes the lift over the blade chord using a steady flat-plate assumption (Eqn. 4.7). This approach provides for better prediction of negative peak of the BCDI event. As discussed earlier, for a parallel interaction, the non-compact chord formulation results in a slightly wider pulse width and lower magnitude at the  $107^\circ$  microphone azimuth. This effect is most prominent at the peak noise azimuth at the lower elevation. The difference between the compact and non-compact formulation decreases for the microphones on either side as was shown in Fig. 4.3. The acoustic time history comparisons between the compact and non-compact formulations for the various microphone locations are shown here in Figs. D.1-D.4.

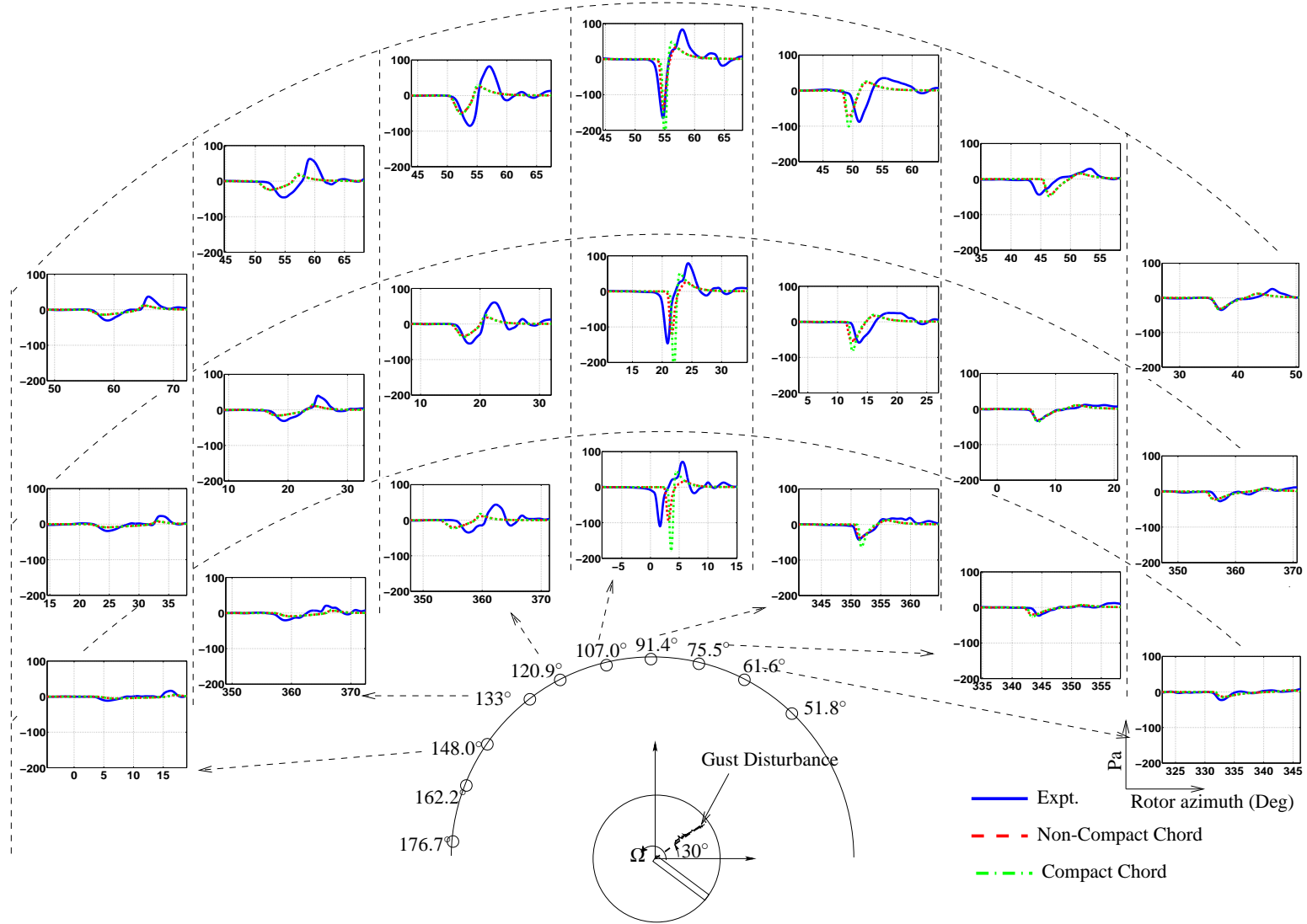


Figure D.1: Comparison between Compact and Non-compact chord formulations ( $M_T = 0.702$  — Parallel Interaction)

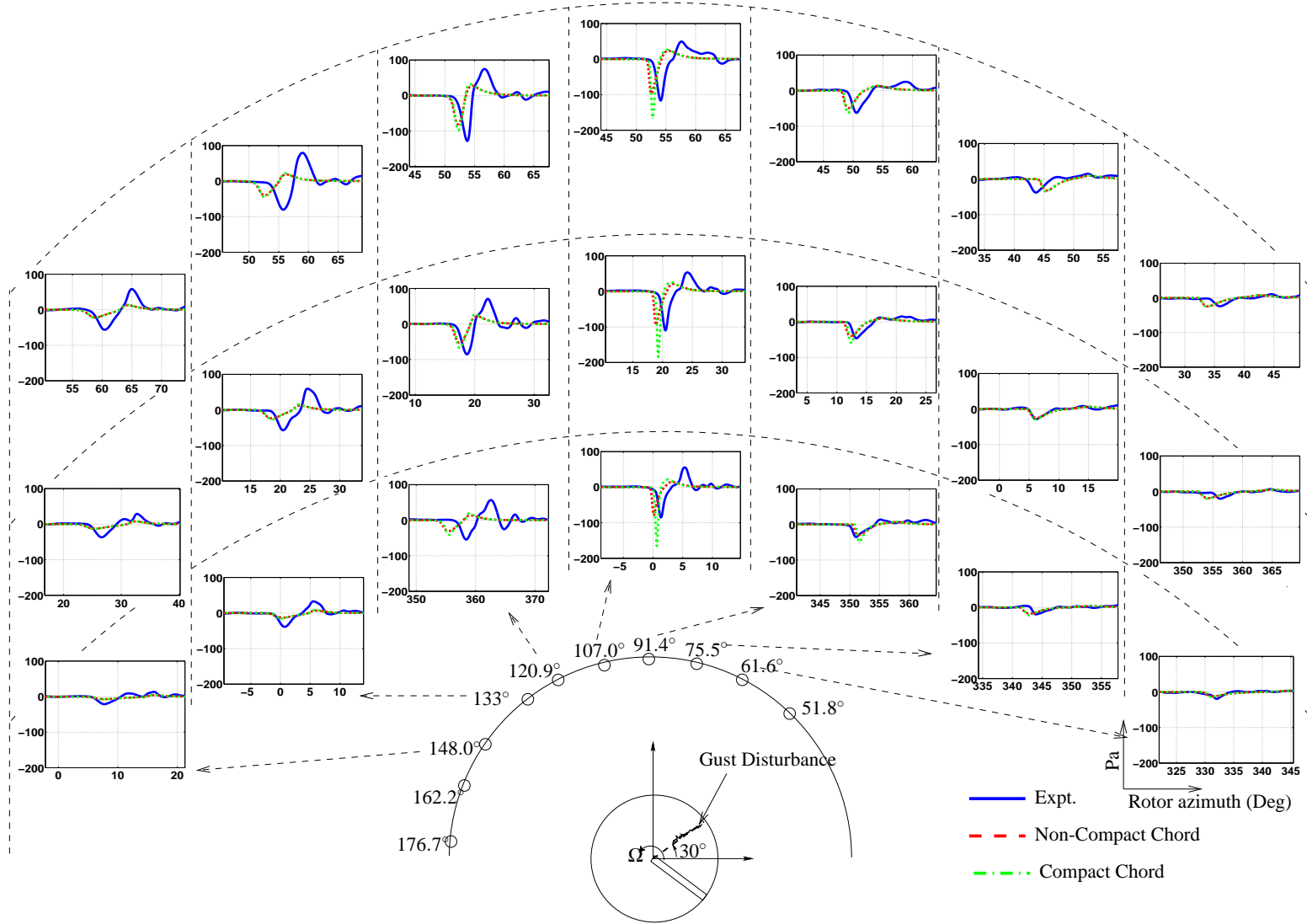


Figure D.2: Comparison between Compact and Non-compact chord formulations ( $M_T = 0.702$  — Case 2)



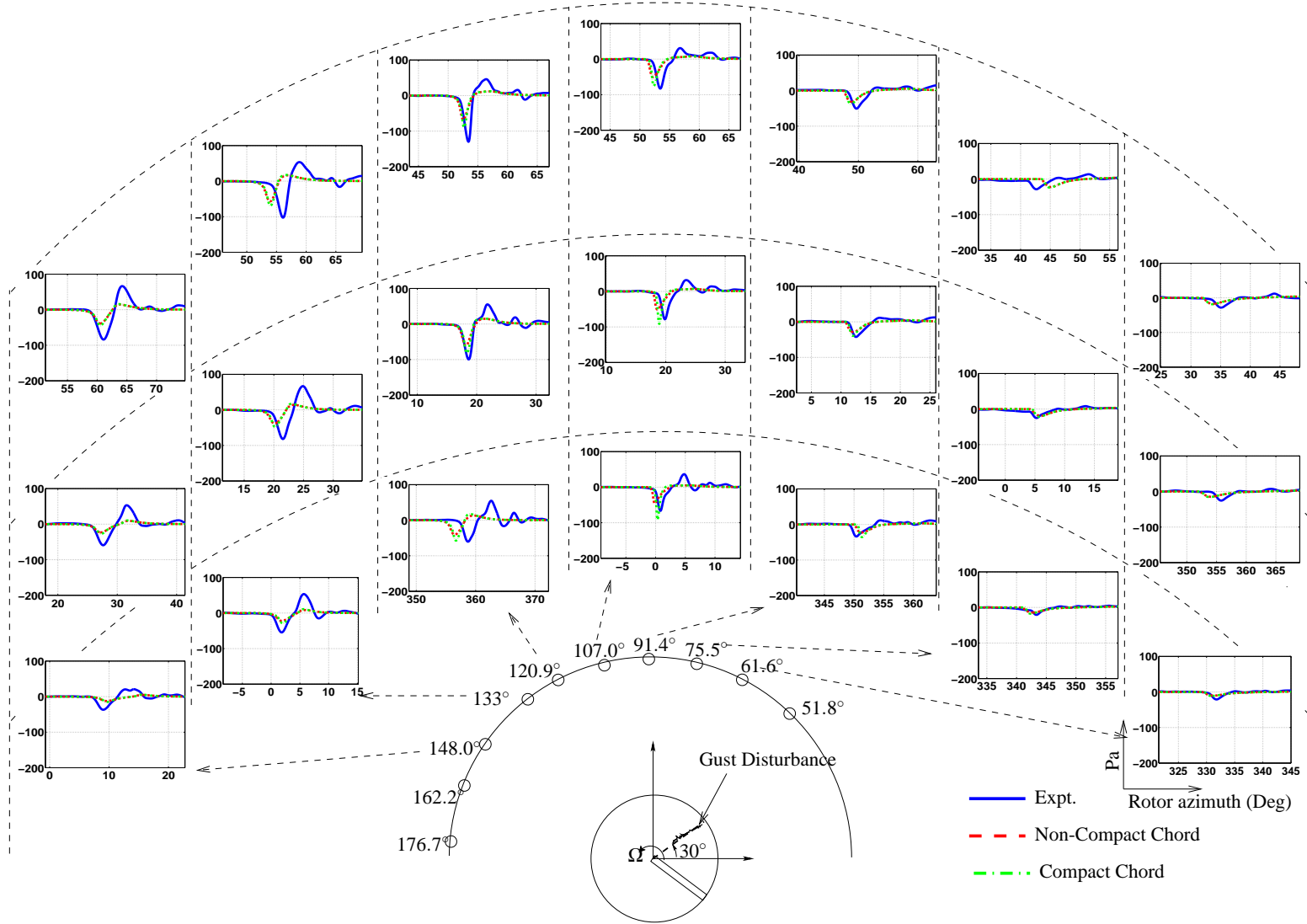


Figure D.3: Comparison between Compact and Non-compact chord formulations ( $M_T = 0.702$  — Case 3)

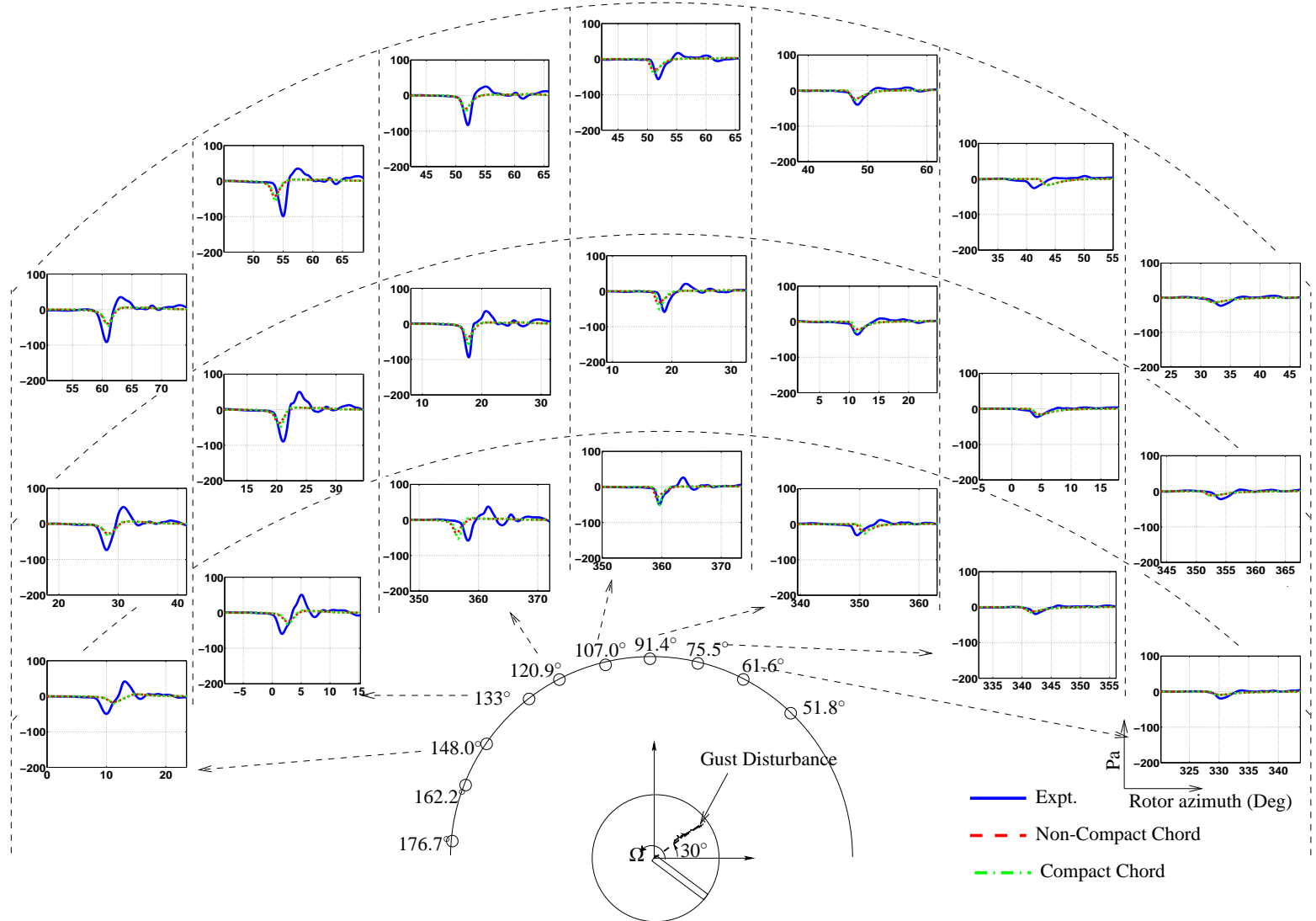


Figure D.4: Comparison between Compact and Non-compact chord formulations ( $M_T = 0.702$  — Case 4)

## Appendix E

# Comparison of Frequency Spectrum Between Theory and Experiment

Figs. E.1-E.4 show a comparison of the frequency spectrum between the theory and experiment for the different interaction angles at  $M_T = 0.702$ . The theory tends to under predict the magnitude of the frequencies for the corresponding peak microphone azimuths. This corresponds in the time history plots (Figs. 4.5, 4.8, 4.12 & 4.16) to a wider pulse width predicted by theory at the corresponding microphones. Part of the reason could be a strong tip vortex predicted by the Weissinger-L model based on the two-dimensional indicial results. Since the indicial aerodynamics is assumed a compact chord approach (which might not be true in reality) the strength of the tip vortex and hence the contribution to the acoustics from the blade tip might actually be higher than that predicted by the theory.

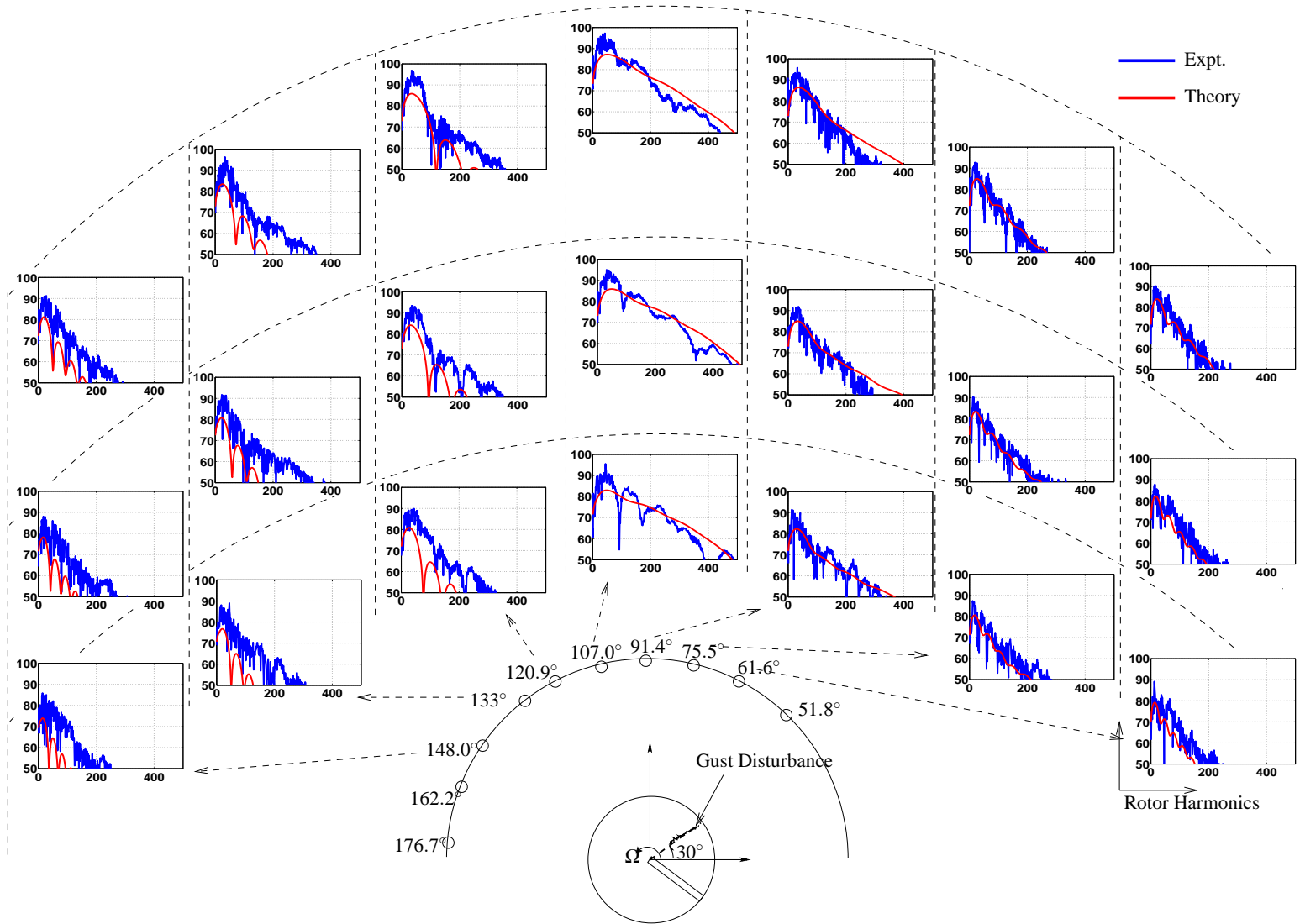


Figure E.1: Acoustic time histories at the various microphones in terms of Acoustic Pressure (in Pa) vs. Rotor Azimuth (in Deg)

( $M_T = 0.702$  — Parallel Interaction)

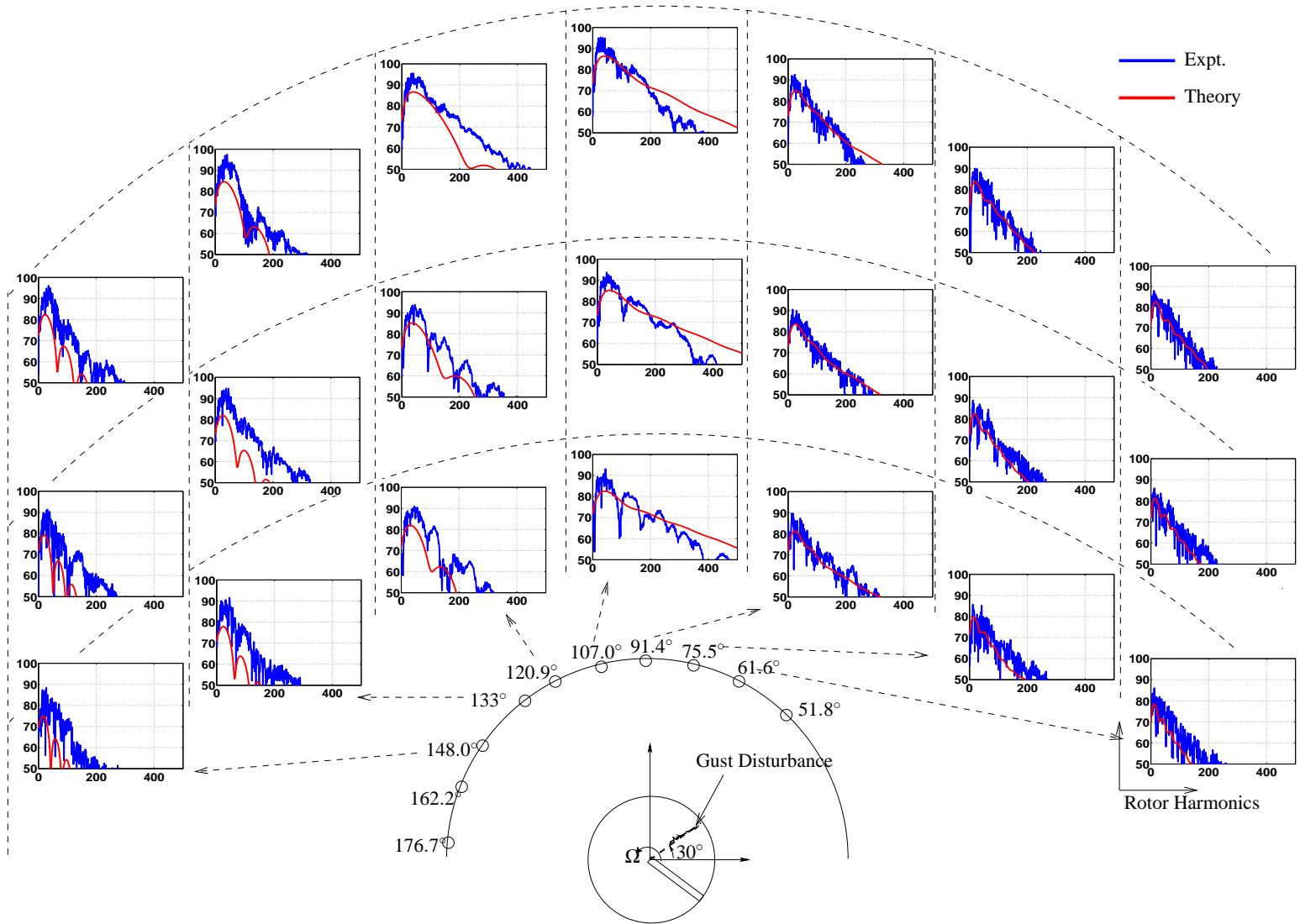


Figure E.2: Acoustic time histories at the various microphones in terms of Acoustic Pressure (in Pa) vs. Rotor Azimuth (in Deg)

( $M_T = 0.702$  — Case 2)

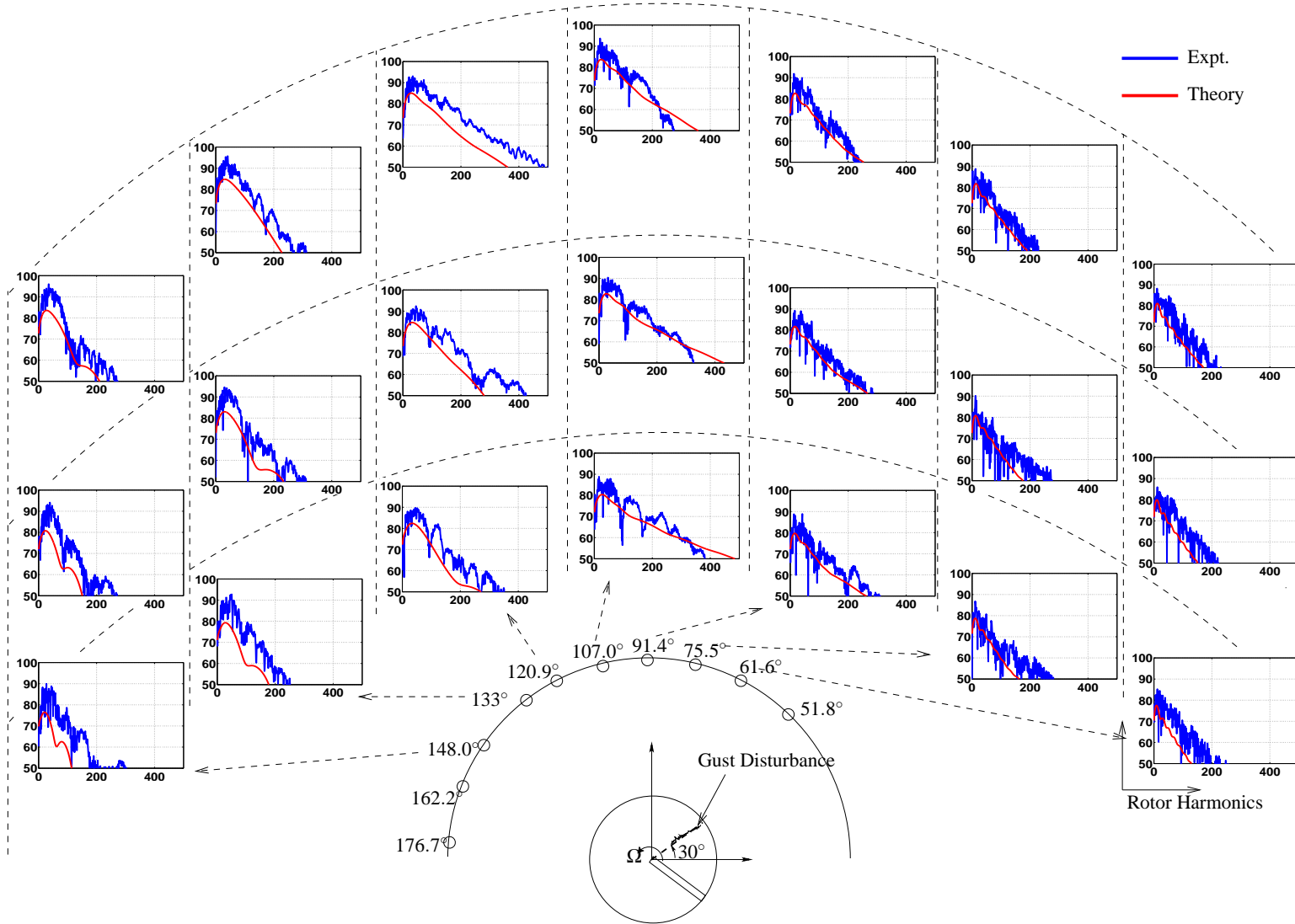


Figure E.3: Acoustic time histories at the various microphones in terms of Acoustic Pressure (in Pa) vs. Rotor Azimuth (in Deg)

( $M_T = 0.702$  — Case 3)

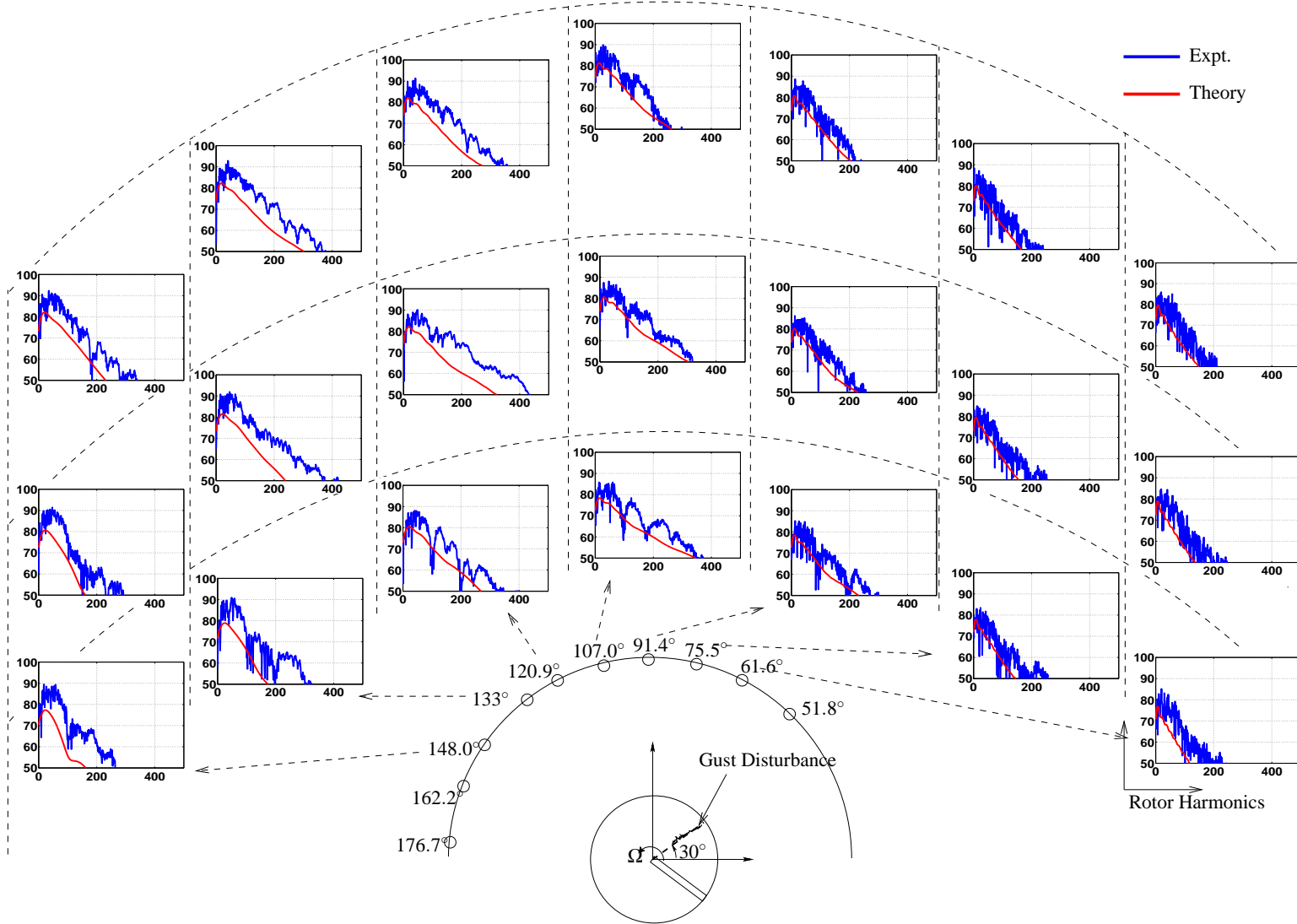


Figure E.4: Acoustic time histories at the various microphones in terms of Acoustic Pressure (in Pa) vs. Rotor Azimuth (in Deg)

( $M_T = 0.702$  — Case 4)

# Appendix F

## Scaling of the Acoustics Data

### F.1 Choice of Scaling Origin

The experimental and theoretical results have been scaled to a distance of  $3R$  from the hub, for easier comparison, as has been mentioned in the thesis. As discussed earlier, the parallel interaction peaks about a line drawn perpendicular to the blade at the 80% span location during the interaction event. Moreover, most of the noise is radiated from the outboard region of the blade for all the interaction angles, as the sectional Mach number is higher at those sections compared to the inboard sections. Thus, one could also scale the results about a location that is not the hub, but rather a point on the outboard section of the blade during the interaction, as it would be more representative of the source of sound. For a truly far-field observer, this choice of scaling would have a very negligible effect. However, given the size of the chamber, the microphones cannot be considered truly far-field with respect to the spanwise sources.

Figures F.1,F.3,F.5 & F.7 show the measured peak-to-peak noise expressed in decibels when



scaled about the 80% blade span location during the interaction. The corresponding plots with the measured data scaled about the hub are also shown for easy comparison (Figs. F.2,F.4,F.6 & F.8. Although there is some difference in the noise levels, for the two choices of scaling origin, the overall azimuthal trends do not change. Moving the origin of scaling to the 80% blade section at the interaction, increases the distance between the microphones from the effective sound source. Thus, the scaling results in an increase in magnitude, when compared to the values scaled with respect to the hub.

For different interaction angles, the 80% span section of the blade undergoes the interaction event at a different azimuth. This makes it difficult to compare the noise levels across different interaction angles.

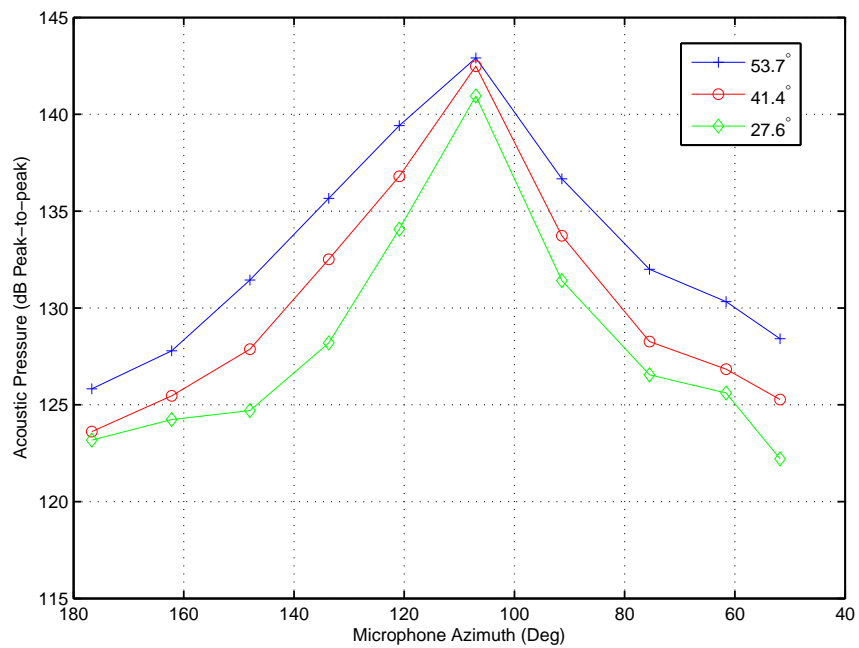


Figure F.1: Directionality trends for parallel BCDI when scaled about 0.8R ( $M_T = 0.702$ )

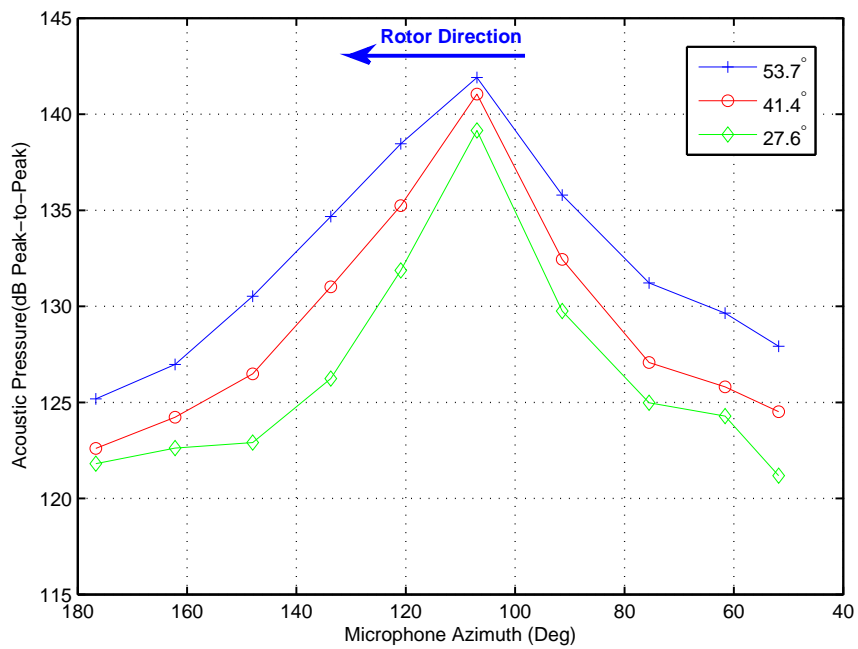


Figure F.2: Directionality trends for parallel BCDI when scaled about the hub ( $M_T = 0.702$ )

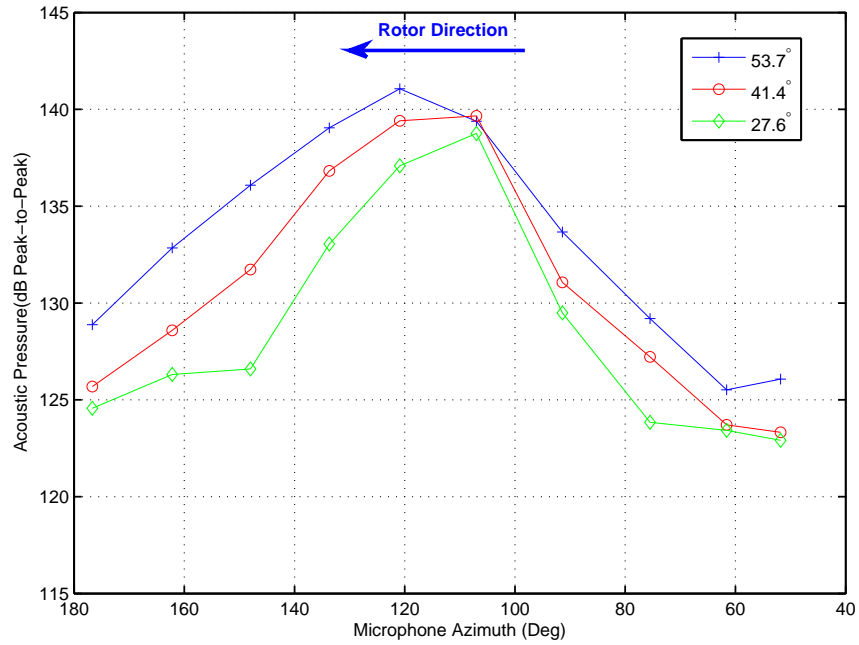


Figure F.3: Directionality trends for the 3.3° oblique BCDI when scaled about 0.8R ( $M_T = 0.702$ )

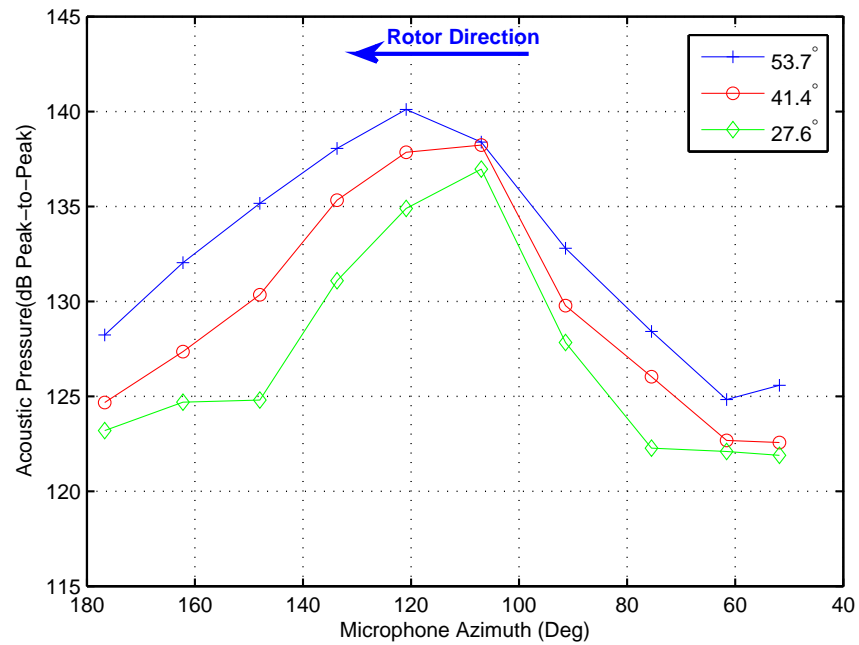


Figure F.4: Directionality trends for the 3.3° oblique BCDI when scaled about the hub ( $M_T = 0.702$ )

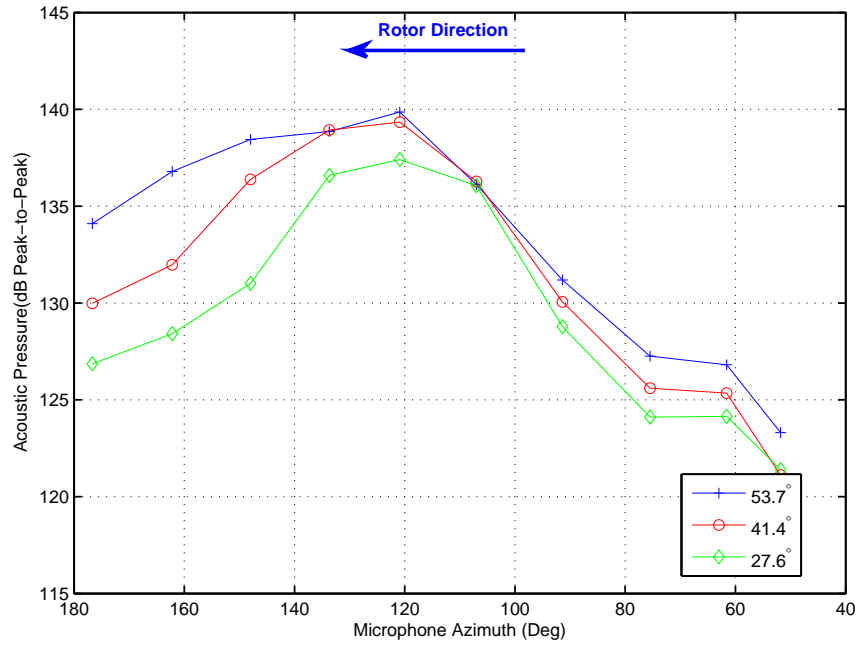


Figure F.5: Directionality trends for the 8.8° oblique BCDI when scaled about 0.8R ( $M_T = 0.702$ )

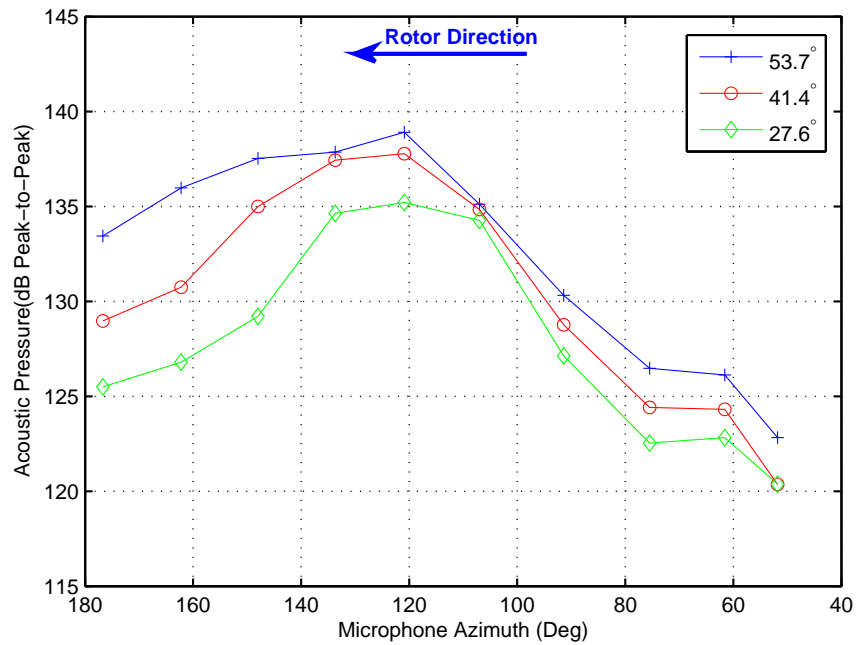


Figure F.6: Directionality trends for the 8.8° oblique BCDI when scaled about the hub ( $M_T = 0.702$ )

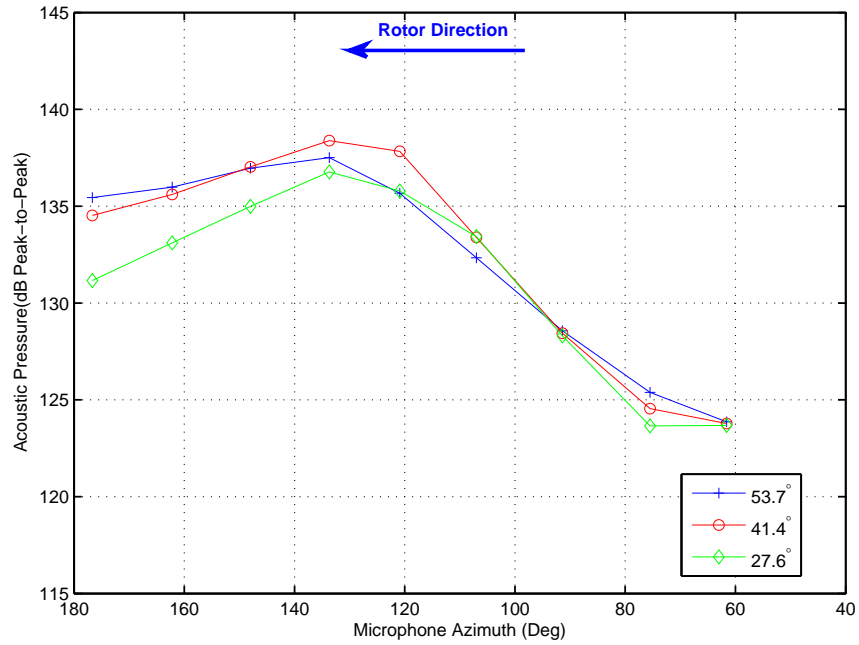


Figure F.7: Directionality trends for the 15.3° oblique BCDI when scaled about 0.8R ( $M_T = 0.702$ )

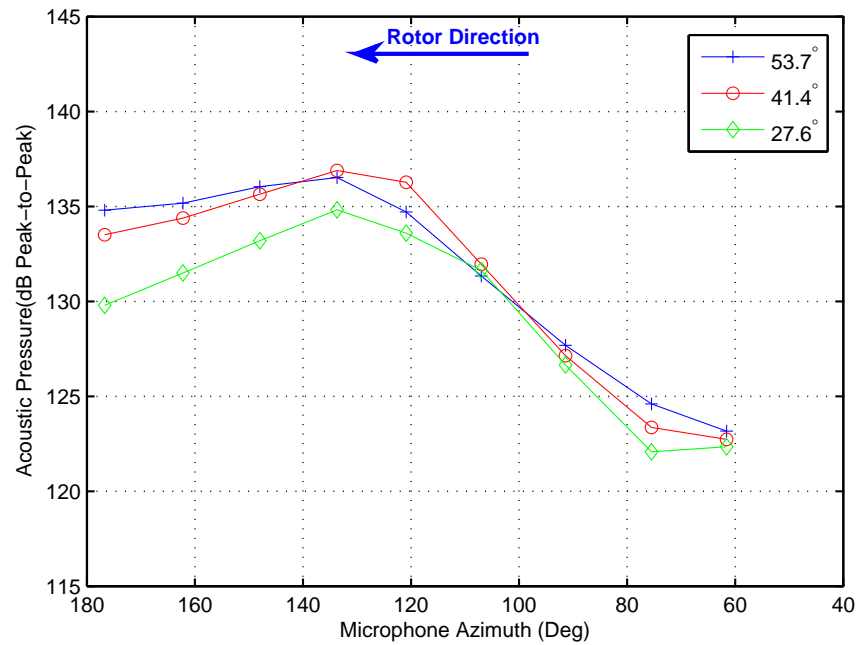


Figure F.8: Directionality trends for the 15.3° oblique BCDI when scaled about the hub ( $M_T = 0.702$ )

## References

- [1] Pike, A.C., and Leverton, J.W., “Understanding Helicopter Noise – Implications of Design and Operation,” 24<sup>th</sup> European Rotorcraft Forum, Marseilles, France, 1998.
- [2] Allongue, M., Marze, H.J., and Potdovin, F., “The quiet Helicopter: From Research to Reality,” Proceedings of the 55<sup>th</sup> Annual Forum of the American Helicopter Society, Montreal, Canada, 1999.
- [3] Niesl, G., and Arnaud, G., “Low Noise Design of the EC 135 Helicopter,” Proceedings of the 52<sup>nd</sup> Annual Forum of the American Helicopter Society, Washington, D.C., May 1996.
- [4] Brentner, Kenneth S., and Farassat, F., “Modelling Aerodynamically Generated Sound of Helicopter Rotors,” *Progress in Aerospace Sciences*, 2003.
- [5] Cox, C.R., “Subcommittee chairman’s report to membership on aerodynamic sources of rotor noise,” Proceedings of the 28<sup>th</sup> Annual Forum of the American Helicopter Society, May 1972.
- [6] Schmitz, F.H., and Yu, H.Y., “Theoretical Modelling of High-Speed Impulsive Noise,” Proceedings of the 3<sup>rd</sup> European rotorcraft and Powered Lift Aircraft Forum, 1977.

- [7] Yu, Y.H., Caradonna, F.X., and Schmitz, F.H., “The Influence of Transonic Flow Field on High-Speed Impulsive Noise,” Proceedings of the 4<sup>th</sup> European rotorcraft and Powered Lift Aircraft Forum, Stresa, Italy, 1978.
- [8] Schmitz, F.H., and Boxwell, D.A., “In Flight Measurement of Helicopter Impulsive Noise,” *Journal of the American Helicopter Society*, Vol. 21, No. 4, October 1976, pp. 2–16.
- [9] Schmitz, F.H., and Yu, Y.H., “Helicopter Impulsive Noise: Theoretical and Experimental Status,” *Journal of Sound and Vibration*, Vol. 109, No. 3, 1986.
- [10] Lowson, M.V., Byham, G., Perry, F.J., and Hawkings, D.L., “Rotor Tip,” US Patent 4077741, 1976.
- [11] Brentner, K.S., “Modelling Aerodynamically Generated Sound: Recent Advances in Rotor Noise Prediction,” 38<sup>th</sup> Aerospace Sciences Meeting and Exhibit, Reno, NV, 2000, AIAA 2000-0345.
- [12] Yu, Y.H., “Rotor-Blade Vortex Interaction Noise,” *Progress in Aerospace Sciences*, Vol. 36, No. 2, February 2000, pp. 97–115.
- [13] Lowson, M.V., “Progress Towards Quieter Civil Helicopters,” 17<sup>th</sup> European Rotorcraft Forum, Berlin, September 1991.
- [14] Schmitz, F.H., *Aeroacoustics of Flight Vehicles: Theory and Practice*, Vol. 1 1991, Ch. Rotor Noise.

- [15] Leishman, J.G., *Principles of Helicopter Aerodynamics*, 1<sup>st</sup> ed., Cambridge University Press, 2000.
- [16] Boxwell, D.A., Schmitz, F.H., Splettstoesser, W.R., and Schultz, K.J., “Helicopter Model Rotor-Blade Vortex Interaction Impulsive Noise: Scalability and Parametric Variations,” *Journal of the American Helicopter Society*, Vol. 32, No. 1, January 1987.
- [17] Widnall, S.E., “Helicopter Noise due to Blade-Vortex Interaction,” *J. Acoustical Society of America*, Vol. 50, No. 1, 1971, pp. 354–365.
- [18] Leishman, J.G., “Acoustic Focusing Effects Generated by Parallel and Oblique Blade Vortex Interactions,” American Helicopter Society Technical Specialists’ Meeting for Rotorcraft Acoustics and Aerodynamics, Williamsburg, VA, October 1997.
- [19] Lowson, M.V., “Helicopter Noise: Analysis Prediction and Methods of Reduction,” AGARD Report LS-63, 1973.
- [20] Sim, B.W., George, A.R., and Yen, S.J., “Blade-Vortex Interaction Noise Directivity Studies Using Trace Mach Number,” American Helicopter Society Aeromechanics Specialists Conference, Connecticut, October 1995.
- [21] Open, C.J., and Patrick, R.J., “Directionality of Blade Vortex Interaction Noise,” 17<sup>th</sup> European Rotorcraft Forum, Berlin, Germany, September 1991.



- [22] Sim, B.W., and Schmitz, F.H., “Acoustic Phasing and Amplification Effects of Single Rotor Helicopter Blade-Vortex Interactions,” Proceedings of the 55<sup>th</sup> Annual Forum of the American Helicopter Society, Montreal, Canada, May 1999.
- [23] Theoderson, T., “General Theory of Aerodynamic Instability and the Mechanism of Flutter,” NACA Report 496, 1935.
- [24] Sears, W.R., “Operational Methods in the Theory of Airfoils in Nonuniform Motion,” *Journal of Franklin Institute*, Vol. 230, 1940, pp. 95–111.
- [25] Sears, W.R., and Sparks, B.O., “On the Reaction of an Elastic Wing to Vertical Gust,” *Journal of Aeronautical Sciences*, Vol. 9, No. 2, 1941, pp. 51–64.
- [26] Miles, J.W., “The Aerodynamic Force on an Airfoil in a Moving Gust,” *Journal of Aeronautical Sciences*, Vol. 23, No. 11, 1956, pp. 1044–1050.
- [27] Beddoes, T.S., “Practical Computation of Unsteady Lift,” *Vertica*, Vol. 8, No. 1, 1984, pp. 55–71.
- [28] Leishman, J.G., “Subsonic Unsteady Aerodynamics Caused by Gusts Using the Indicial Method,” *Journal of Aircraft*, Vol. 33, No. 5, September-October 1996.
- [29] Leishman, J.G., “Aeroacoustics of 2-D and 3-D Blade Vortex Interaction Using the Indicial Method,” Proceedings of the 52<sup>nd</sup> Annual Forum of the American Helicopter Society, Washington D.C, June 1996, Vol. 2, American Helicopter Society.

- [30] Chu, S., and Widnall, S. E., “Prediction of Unsteady Airloads for Oblique Blade-Gust Interaction in Compressible Flow,” *AIAA Journal*, Vol. 12, No. 9, 1974, pp. 1228–1235.
- [31] Martinez, R., and Widnall, Sheila E., “Unified Aerodynamic-Acoustic Theory for a Thin Rectangular Wing Encountering a Gust,” *AIAA Journal*, Vol. 18, No. 5, 1980, pp. 638–645.
- [32] Widnall, S. E., Harris, W. L., Lee, Y. C. A., and Drees, H. M., “The development of experimental techniques for the study of helicopter rotor noise,” NASA CR 137684, 1974.
- [33] Lee, A., Harris, W.L., and Widnall, S.E., “An Experimental Study of Helicopter Rotor Rotational Noise in a Wind Tunnel,” *Journal of Aircraft*, Vol. 14, No. 11, 1977.
- [34] Egolf, T.A., and Landgrebe, A.J., “Helicopter Rotor Wake Geometry and its Influence in Forward Flight, Vol. 1 — Generalized Wake Geometry and Wake Effects in Rotor Airloads and Performance,” NASA CR 3726, October 1983.
- [35] Beddoes, T.S., “A Wake Model for High Resolution Airloads,” 2<sup>nd</sup> International Conference on Basic Rotorcraft Research, Triangle Park, NC, 1985.
- [36] Ananthan, S., *Analysis of Rotor Wake Aerodynamics During Maneuvering Flight Using a Free-Vortex Wake Methodology* PhD thesis, University of Maryland, College Park, 2006.
- [37] Leishman, J.G., Bhagwat, M.J., and Bagai, A., “Free-Vortex Methods for Helicopter Rotor Wake Analyses,” *Journal of Aircraft, Special Edition on Rotorcraft Wakes*, Vol. 39, No. 5, 2002, pp. 759–775.

- [38] Datta, Anubhav, Nixon, Mark, and Chopra, Inderjit, “Review of Rotor Loads Prediction with the Emergence of Rotorcraft CFD,” 31<sup>st</sup> European Rotorcraft Forum, Florence, Italy, September 2005.
- [39] Sitaraman, J., Baeder, J., Datta, A., and Chopra, I., “Coupled CFD/CSD Prediction of Rotor Aerodynamic and Structural Dynamics Loads of the Three Critical Flight Conditions,” Proceedings of the 31<sup>st</sup> European Rotorcraft Forum, Firenze, Italy, September 2005.
- [40] Strawn, R.C., and Barth, T.J., “A Finite-Volume Euler Solver for COmputing Rotary-Wing Aerodynamics on Unstructured Meshes,” Proceedings of the 48<sup>th</sup> Annual Forum of the American Helicopter Society, Washington, D.C., June 1992.
- [41] Strawn, R.C., Duque, E.P.N., and Ahmad, J., “Rotorcraft Aeracoustics Computations with Overset-Grid CFD Methods,” *Journal of the American Helicopter Society*, Vol. 44, No. 2, July 1999.
- [42] Steinhoff, J.S., Yonghu, W., Mersch, T., and Senge, H., “Computational Vorticity Capturing — Application to Helicopter Rotor Flow,” AIAA 30<sup>th</sup> Aerospace Sciences Meeting, Reno, NV, January 1992.
- [43] Lyrintzis, A.S., Koutsavdis, E., and Strawn, R.C., “Technical Note – A Comparison of Aeroacoustic Prediction Methods,” American Helicopter Society, 2<sup>nd</sup> Aeromechanics Specialists’ Conference, Bridgeport, CT, October 1995.

- [44] Lyrintzis, A.S., “Surface Integral Methods in Computational Aeroacoustics — From the (CFD) Near-Field to the (Acoustic) Far-Field,” *International Journal of Aeroacoustics*, Vol. 2, No. 2, 2003.
- [45] Gutin, L., “On the Sound of Rotating Airscrew,” *Z Tech Fiz* [translated as NACA TM 825 1948], 1936, pp. 889–909.
- [46] Demming, A.F., “Noise from Propellers with Symmetrical Sections at Zero Blade Angle,” NACA TM 679, 1938.
- [47] Ernsthausen, W., “The source of propeller noise,” *Luftfahrtforschung* (translated as NACA TM 825), 1936.
- [48] Garrick, I.E., and Watkins, C.E., “A Theoretical Study of the effect of forwards speed on the free-space sound pressure field around propellers,” NACA Report 1198, 1954.
- [49] Lowson, M.V., “The sound of singularities in motion,” *Proceedings of the Royal Society A*, 1965, pp. 559–572.
- [50] Wright, S.E., “Sound radiation from a lifting rotor generated by assymmetric disc loading,” *Journal of Sound and Vibration*, Vol. 9, No. 2, 1969, pp. 223–240.
- [51] Lighthill, M.J., “On Sound Generated Aerodynamically,” *Philosophical Transactions of the Royal Society. Series A*, Vol. 211, No. 1107, March 1952, pp. 564–587.

- [52] Lighthill, M.J., “On Sound Generated Aerodynamically. II. Turbulence as a Source of Sound,” *Proceedings of the Royal Society of London. Series A*, Vol. 222, No. 1148, February 1954, pp. 1–32.
- [53] Ffowcs William, J.E., and Hawkins, D.L., “Sound Generated by Turbulence and Surfaces in Arbitrary Motion,” *Philosophical Transactions of the Royal Society. Series A*, Vol. 264, No. 1151, 1969, pp. 321–342.
- [54] Farassat, F., “Linear Acoustic Formulas for Calculation of Rotating Blade Noise,” *Journal of the American Institute of Aeronautics and Astronautics*, Vol. 19, No. 9, September 1981, pp. 1122–1130.
- [55] Farassat, F., “Theory of Noise Generation from Moving Bodies with and Application to Helicopter Rotors,” NASA TR R-451, 1975.
- [56] Brentner, K.S., “Prediction of Helicopter Rotor Noise - A Computer Program Incorporating Realistic Blade Motions and Advanced Formulations,” NASA TM 87721, 1986.
- [57] Singh, R.K., *Transonic Effects on Aerodynamics and Acoustics of Blade-Vortex Interaction* PhD thesis, University of Maryland, College Park, 1999.
- [58] Farassat, F., and Myers, M.K., “The Kirchoff Formula for Supersonically Moving Surfaces,” 1<sup>st</sup> CEAS/AIAA Aeroacoustic Conference, Munich, Germany, 1995.
- [59] Farassat, F., and Myers, M.K., “Extension of Kirchoff’s Formula to Radiation from Moving Surfaces,” *Journal of Sound and Vibration*, Vol. 123, No. 3, 1988.

- [60] Duque, E.P.N., Strawn, Roger C., Ahmad, Jasim, and Biswas, Rupak, “An Overset Grid Navier-Stokes/Kirchhoff-Surface Method for Rotorcraft Aeroacoustic Predictions,” 34<sup>th</sup> Aerospace Sciences Meeting and Exhibit, Reno, NV, January 1996.
- [61] di Franciscantonio, P. “A New Boundary Integral Formulation for the Prediction of Sound Radiation,” *Journal of Sound and Vibration*, Vol. 202, No. 4, 1997, pp. 491–509.
- [62] Morgans, A.S., Karabasov, S.A., Dowling, A.P., and Hynes, T.P., “Transonic Helicopter Noise,” Proceedings of the 59<sup>th</sup> Annual Forum of the American Helicopter Society, Phoenix, Az, May 2003.
- [63] Gopalan, G., Sitaraman, J., Baeder, J. D., and Schmitz, F. H., “Aerodynamic and Aeroacoustic Prediction Methodologies with Application to the HART II Model Rotor,” Proceedings of the 62<sup>nd</sup> Annual Forum of the American Helicopter Society, Phoenix, Az, May 2006.
- [64] Caradonna, F.X et al “Methods for the Prediction of Blade-Vortex Interaction Noise,” *Journal of the American Helicopter Society*, October 2000.
- [65] Kitaplioglu et al “Study of BVI Aeroacoustics Using Independantly Generated Vortex,” AGARD Fluid Dynamics, 1994.
- [66] Yokishima, S., “Flight Operations: Noise Test of Eight Helicopters,” Federal Aviation Authority, USDoT FAA-EE-85-7, August 1985.

- [67] Conner, D.A., and Page, J., “A Tool for Low Noise Procedures Design and Community Noise Impact Assessment: The Rotor Noise Model (RNM),” AHS International Meeting on Advance Rotorcraft Technology and Life Saving Activities, HeliJapan, Japan, 2002.
- [68] Boxwell, D.A., and Schmitz, F.H., “Full-Scale Measurements of Blade-Vortex Interaction Noise,” *Journal of the American Helicopter Society*, Vol. 27, No. 4, October 1982, pp. 11–27.
- [69] Burley, C.L., and Martin, R.M., “Tip-path Plane Angle Effects on Rotor Blade-Vortex Interaction Noise Levels and Directivity,” Proceedings of the 44<sup>th</sup> Annual Forum of the American Helicopter Society, Washington, D.C., June 1988.
- [70] Splettstoesser, W.R., Lehmann, G., and van der Wall, B., “Higher Harmonic Control of a helicopter model rotor to reduce Blade-Vortex Interaction Noise,” *Z. Flugwiss Weltraumforsch*, Vol. 14, 1990, pp. 109–116.
- [71] Splettstoesser, W.R., Kube, R., Wagner, W., Seelhorst, U., Boutier, A., Michelia, F., Mercker, E., and Pengel, K., “Key results from a higher harmonic control aeroacoustic rotor test (HART),” *Journal of the American Helicopter Society*, Vol. 42, No. 1, 1997.
- [72] Yu, Y.H., Gmeling, B., Heller, H., Philippe, J.J., Mercker, E., and Preisser, J.S., “HHC aeroacoustics rotor test at the DNW – the joint German/French US HART project,” 20<sup>th</sup> European Rotorcraft Forum, Amsterdam, Netherlands, 1994.

- [73] Lim, J.W., Tung, C., and Yu, Y.H., “Prediction of blade-vortex interaction airloads with higher-harmonic pitch controls using the 2GCHAS program,” Heli Japan 98, Gifu, Japan, 1998.
- [74] Yu, Y.H., Tung, C., and Low, S., “Blade aeroelastic effect on rotor blade-vortex interaction noise,” Proceedings of the 52<sup>nd</sup> Annual Forum of the American Helicopter Society, Washington, D.C., 1996.
- [75] Yu, Y. H., Tung, C., van der Wall, B., Pausder, H.J., Burley, C., Brooks, T., Beaumier, P., Delrieux, Y., Mercker, E., and Pengel, K., “The HART-II test. Rotor wakes and aeroacoustics with higher-harmonic pitch control (HHC) inputs - The joint German /French/Dutch/U.S. project,” Proceedings of the 58<sup>th</sup> Annual Forum of the American Helicopter Society, Montreal, Canada, June 2002, pp. 1984–1994.
- [76] Yamauchi, G.K., Signor, D.B., Watts, M.E., Hernandez, F.J., and LeMasurier, P., “Flight Measurements of Blade-Vortex Interaction Noise Including Comparisons with Full-Scale Wind Tunnel Data,” Proceedings of the 49<sup>th</sup> Annual Forum of the American Helicopter Society, St. Louis, MO, May 1993.
- [77] Sim, B.W., Beasman, T., Schmitz, F.H., and Gopalan, G., “In-Flight Blade-Vortex Interaction Noise Measurements using a Boom-Mounted Microphone Array,” Proceedings of the 60<sup>th</sup> Annual Forum of the American Helicopter Society, Baltimore, Maryland, 2004.
- [78] Leverton, J.W., “Helicopter Noise – Blade Slap, Part 1: Review and Theoretical Study,” NASA CR 1221, October 1968.



- [79] Leverton, J.W., "Helicopter Noise – Blade Slap, Part 2: Experimental Results," NASA CR 1983, October 1972.
- [80] McCormick, B.W, and Surendraiah, M., "A Study of Rotor Blade-Vortex Interactions," Proceedings of the 26<sup>th</sup> Annual Forum of the American Helicopter Society, Washington, D.C., June 16-18 1970.
- [81] Visintainer, J.A., Burley, C.L., Marcolini, M.A., and Liu, S.R., "Acoustic Prediction using Pressures from a Model Rotor in the DNW," Proceedings of the 47<sup>th</sup> Annual Forum of the American Helicopter Society, Phoenix, AZ, May 1991, pp. 791–806.
- [82] Joshi, M.C., Liu, S.R., and Boxwell, D.A., "Prediction of Blade-Vortex Interaction Noise Using Measured Blade Pressures," 11<sup>th</sup> AIAA Aeroacoustics Conference, Sunnyvale, CA, October 1987.
- [83] Schultz, K.J., and Spletstoeser, W.R., "Prediction of Helicopter Rotor Impulsive Noise Using Measured Blade Pressures," Proceedings of the 43<sup>rd</sup> Annual Forum of the American Helicopter Society, May 1987.
- [84] Kitapliouglu, C., and Caradonna, F, "Aerodynamics and Acoustics of Blade-Vortex Interaction Using and Independantly Generated Vortex," American Helicopter Society Aeromechanics Specialists Conference, San Fransisco, CA, January 19-21 1994.
- [85] Kitaplioglu, C., Caradonna, F.X., and Burley, C.L., "Parallel Blade-Vortex Interactions: An Experimental Study and Comparison with Computations," American Helicopter Society 2<sup>nd</sup> International Aeromechanics Specialists' Conference, Bridgeport, Connecticut, 1997.

- [86] Schmitz, F.H, and Sim, B, “Radiation and Directionality Characteristics of Helicopter Blade-Vortex Interaction Noise,” *Journal of the American Helicopter Society*, Vol. 48, No. 4, October 2003, pp. 253–269.
- [87] Weissinger, J., “Lift Distribution of Swept-Back Wings,” NACA TM 1120, 1947.
- [88] Baeder, J.D., and Sim, B.W., “Blade Vortex Interaction Noise Reduction by Active Trailing Edge Flaps,” Proceedings of the 54<sup>th</sup> Annual Forum of the American Helicopter Society, 1998.
- [89] Rae, H.W., and Pope, Alan, *Low-Speed Wind Tunnel Testing* John Wiley & Sons, 1984.
- [90] Morel, Thomas, “Comprehensive Design of Axisymmetric Wind Tunnel Contractions,” *Journal of Fluids Engineering*, 1975.
- [91] Morel, Thomas, “Design of Two-Dimensional Wind Tunnel Contractions,” *Journal of Fluids Engineering*, 1977.
- [92] Brooks, T.F., Marcolini, M.A, and Pope, D.S, “Main Rotor Broadband Noise Study in the DNW,” *Journal of the American Helicopter Society*, Vol. 34, No. 2, April 1989, pp. 3–12.